



HAL
open science

Characterization and multiscale modeling of textile reinforced composite materials considering manufacturing defects

Keerthi Krishna Parvathaneni

► **To cite this version:**

Keerthi Krishna Parvathaneni. Characterization and multiscale modeling of textile reinforced composite materials considering manufacturing defects. Materials. Ecole nationale supérieure Mines-Télécom Lille Douai, 2020. English. NNT : 2020MTLD0016 . tel-03893942

HAL Id: tel-03893942

<https://theses.hal.science/tel-03893942v1>

Submitted on 12 Dec 2022

HAL is a multi-disciplinary open access archive for the deposit and dissemination of scientific research documents, whether they are published or not. The documents may come from teaching and research institutions in France or abroad, or from public or private research centers.

L'archive ouverte pluridisciplinaire **HAL**, est destinée au dépôt et à la diffusion de documents scientifiques de niveau recherche, publiés ou non, émanant des établissements d'enseignement et de recherche français ou étrangers, des laboratoires publics ou privés.

THÈSE

présentée en vue d'obtenir le grade de

DOCTEUR

en

Mécanique des solides, des matériaux, des structures et des surfaces

par

KEERTHI KRISHNA PARVATHANENI

DOCTORAT DE L'UNIVERSITÉ DE LILLE DELIVRÉ PAR IMT LILLE DOUAI

**CHARACTERIZATION AND MULTISCALE MODELING OF TEXTILE REINFORCED
COMPOSITE MATERIALS CONSIDERING MANUFACTURING DEFECTS**

Soutenance le 11th Décembre 2020 devant le jury d'examen

Président	COUTELLIER Daniel, Professeur	INSA Hauts-de-France
Rapporteur	HOCHARD Christian, Professeur	Ecole Centrale de Marseille
Rapporteur	LAIARINANDRASANA Lucien, Directeur de recherche	Mines ParisTech
Examinatrice	DAGHIA Federica, Maître de conférences HDR	ENS Paris-Scalay
Directeur	PARK Chung-Hae, Professeur	IMT LILLE DOUAI
Co-encadrant de thèse	VASIUKOV Dmytro, Maître de conférences	IMT LILLE DOUAI

Laboratoire d'accueil

Centre d'Enseignement, de Recherche et d'Innovation (CERI) Matériaux et Procédés de IMT Lille Douai
Ecole Doctorale SMRE 104 (U. Lille, U. Artois, ULCO, UPHF, Centrale Lille, Chimie Lille, IMT Lille Douai)

"We may regard the present state of the universe as the effect of its past and the cause of its future. An intellect which at any given moment knew all of the forces that animate nature and the mutual positions of the beings that compose it, if this intellect were vast enough to submit the data to analysis, could condense into a single formula the movement of the greatest bodies of the universe and that of the lightest atom; for such an intellect nothing could be uncertain and the future just like the past would be present before its eyes."

— Marquis Pierre Simon de Laplace

"Prediction is difficult, especially the future."

— Niels Bohr

“I dedicate this thesis to my grandmother: Narukulla Thummala Sathya Narayanamma”

ACKNOWLEDGEMENTS

I want to thank my thesis Director Prof. Chung-Hae PARK for his constant guidance which helped to achieve the correct direction for this research. He made me realize how a leader should be rich in knowledge and energetic.

I can never thank enough my thesis supervisor Dr. Dmytro VASIUKOV. I will remain grateful for his help in every step of my journey during this thesis. It is an absolute pleasure working along with him and I cannot ask for a better supervisor.

I would like to thank, Prof. Christian HOCHARD and Dr. Lucien LAIARINANDRASANA for their acceptance to review this thesis. I would also like to thank Prof. Daniel COUTELLIER and Dr. Federica DAGHIA for accepting to be a part of the jury for this thesis.

I would like to thank all my gentle lab colleagues. I want to extend a special thanks to Dr. Masoud BODAGHI for his friendly and enriching talks, Dr. Mylène LAGARDERE for her warm smiles and Mr. Patrice HULOT, Mr. Xavier DORCHIES: my go-to persons for any technical difficulties during experiments.

I want to thank my family, brother Tulasi Krishna and my parents Sridhar and Prameela who always rooted for my well begin and success. I would like to thank all my friends (a numerous never-ending list). However a few deserve special mention. Thank you to my best friends Harika and Chandra. Thank you Anurag for our intellectual discussions. Thank you Amulya for all your caring and support. Thank you Aniket for sharing your knowledge on a lot of documentaries. Thank you, Ivana for being there when I felt low in life. Thank you Xiao for our scientific discussions. A special thank you to the late comer Rowshni.

Last but not least, I want to thank numerous beer and coffee makers in this world. Special thanks to Charles and Agathe for choosing Douai to have their bar Baragouin. I also want to thank NETFLIX and YOUTUBE.

Table of content

1	General Introduction	9
1.1	Context	9
1.2	Motivations.....	10
1.3	Objectives.....	10
1.4	Outline.....	11
2	State of the art	14
2.1	Composites and processing defects.....	14
2.2	Manufacturing of composites.....	15
2.2.1	Autoclave	15
2.2.2	Liquid composite molding with emphasis on RTM.....	16
2.3	Void type defects.....	17
2.3.1	Void formation	17
2.4	Geometrical characteristics of voids	19
2.4.1	Void volume fraction	19
2.4.2	Void size.....	20
2.4.3	Void shape.....	20
2.4.4	Void distribution	21
2.4.5	Void characterization techniques	22
2.5	Effect of voids on the mechanical properties of composites.....	23
2.5.1	Interlaminar shear strength.....	23
2.5.2	Tensile properties	25
2.6	Methods for prediction of elastic properties	27
2.6.1	Analytical methods.....	27
2.6.2	Numerical simulations.....	29
2.6.3	Microscale (Yarns).....	30
2.6.4	Mesoscale (Architecture)	32
2.6.5	Macroscale	36
2.6.6	Numerical homogenization	36
2.7	Conclusions	39
3	Materials, Manufacturing, and Characterization	41
3.1	Introduction	41
3.2	Materials and manufacturing method.....	41

3.2.1	Materials.....	41
3.2.2	Manufacturing method	41
3.2.3	Specimen extraction	42
3.3	Characterization of volume fractions for each constituent.....	43
3.3.1	Characterization of total fiber volume fraction and total void volume fraction...	44
3.3.2	Characterization of yarn constituents	45
3.4	Micro-computed tomography.....	56
3.5	Mechanical characterization.....	57
3.6	Results and discussion.....	62
3.7	Conclusions	67
4	Microscale modeling of yarns with void type defects	68
4.1	Introduction	68
4.2	Analytical methods to calculate the elastic properties	68
4.2.1	Stepping scheme for multiple inclusion	69
4.2.2	Results for stepping Mori- Tanaka’s scheme	71
4.3	Numerical homogenization	73
4.3.1	Generation of microstructure	73
4.3.2	FE simulations.....	83
4.4	Results and discussion.....	86
4.5	Conclusions	92
5	Mesoscale reconstruction and Multiscale Modeling.....	94
5.1	Introduction	94
5.2	Creation of the voxel models	94
5.2.1	Convergence study	97
5.2.2	Results of segmentation	98
5.3	Characteristics of inter-yarn voids (meso-voids)	100
5.4	Multiscale simulation to analyze the effect of voids on elastic properties.....	103
5.4.1	Finite element model description	103
5.4.2	Parametric study on the sensitivity of elastic properties concerning intra & inter-yarn voids.....	103
5.4.3	Validation of FE-solution with experimental results	109
5.5	Conclusions	111
6	Conclusions and perspectives	112
7	ANNEXES.....	115

7.1	A: Numerical homogenization	115
7.2	B: Burn-off test.....	118
7.3	C: Eshelby tensor for cylindrical and spherical inclusions	120
7.4	D: Microstructures that can be generated by modified NNA.....	121
8	Bibliography	123

1 General Introduction

1.1 Context

Composite materials have a wide range of applications in transportation, sports, civil structures, and medical fields. However, they have a major share in the aviation industry, in 1903 Wright brothers initiated an application for wood fabric composite, from recorded data in 1964 Royal Aircraft Establishment used carbon fiber composites to enhance the structural strength and in recent trends Airbus 380 which is one of the biggest passenger aircraft containing more than 50% composite structures to support its strength.

For industrial applications composites are manufactured by autoclave, resin transfer molding (RTM), infusion, compression molding, etc. Void type defects are unavoidable and observed in every manufacturing process. This will result in the reduction of mechanical properties or undesired behavior. For instance, due to this reason, the composites with the void volume fraction greater than 0.02 are rejected for aerospace applications. However, not all applications require this standard, thus increasing the application range for composites with voids. Hence,

- Understanding the influence of void on the mechanical properties will provide cost savings and design advantages.
- Studying the effect of void characteristics such as size, shape, location (inside or between the yarns) as well as volume fraction, on the mechanical properties of composites will help to provide a guideline for selecting good manufacturing parameters.

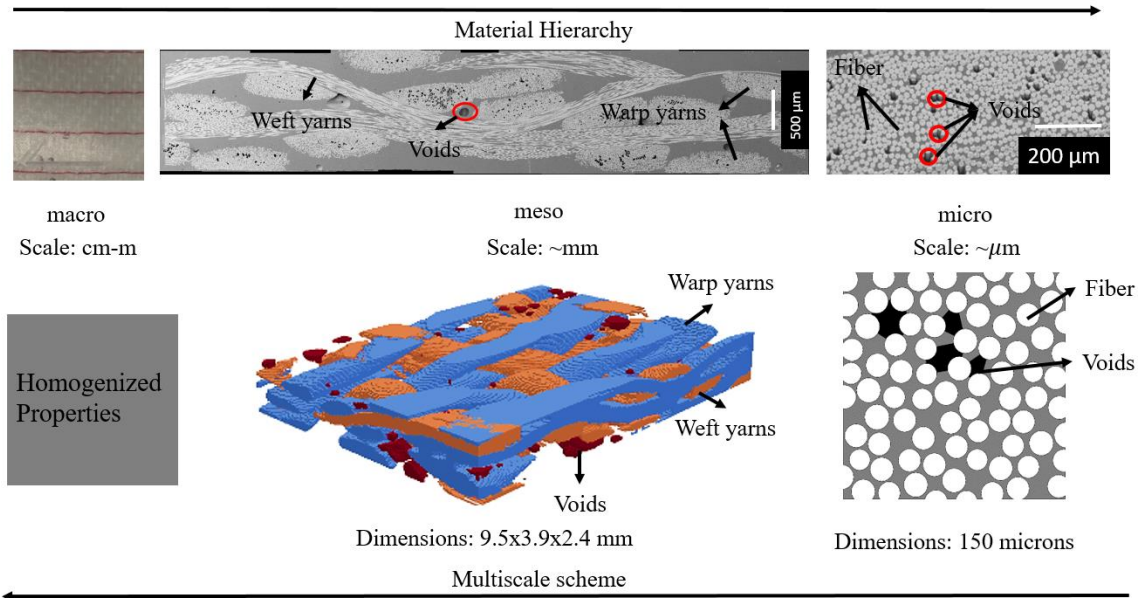
This subject was under investigation since the 1970s. Because of the lack of experimental techniques, in most of the cases composite behavior was directly related to the void volume fraction. Which is always not an effective parameter. As we will show, it leads to very coarse approximation and sometimes may lead to wrong conclusion.

Recent developments of the imaging techniques provided a detailed insight into the micro world of composites which allowed researchers to measure the void's geometry such as shape and size. In the literature, void characteristics were used to estimate the elastic properties of the composites with help of analytical or numerical techniques. It is found that void characteristics also should be taken into account in modeling.

The void characteristics depend on the type of reinforcement and manufacturing process parameters. In addition, depending on the reinforcements voids can have a dual scale nature. For example, in textile composites, the voids occur inside the fiber yarns and also in-between the yarns. To understand the influence of such voids, a multi-scale investigation should be carried out.

1.2 Motivations

The material hierarchy of the textile composites, calls for a multi-scale numerical method. The representation of this phenomenon and numerical method for textile composites are presented in the following figure.



- In microscale (in yarns) voids have irregular shapes and have special spatial distribution. Fibers have a circular cross-section and unique spatial arrangement.
- In mesoscale (reinforcement) voids have near-spherical shapes and the yarn has irregular cross-section and paths.

The influence of these parameters on mechanical properties was not completely covered in the literature. In recent studies, the effect of void aspect ratio and size have been investigated. However, parameters such as void spatial distribution is still an open question. Moreover, most of the studies are confined to the unidirectional and laminated composites. There are no dedicated microstructure generators to produce a Representative Volume Element (RVE) containing voids. This may be the reason for approximating the void shapes as a regular geometry such as a sphere in the literature. However, at meso-scale, a real structure with voids and yarn cross-section can be reconstructed from micro-computed tomography (μ CT) data.

1.3 Objectives

In this work, we present the multi-scale numerical homogenization to predict the elastic properties of the 3D textile composite. However, this method can be adapted to any other types of composites. This task contains combined experimental methods and a numerical approach.

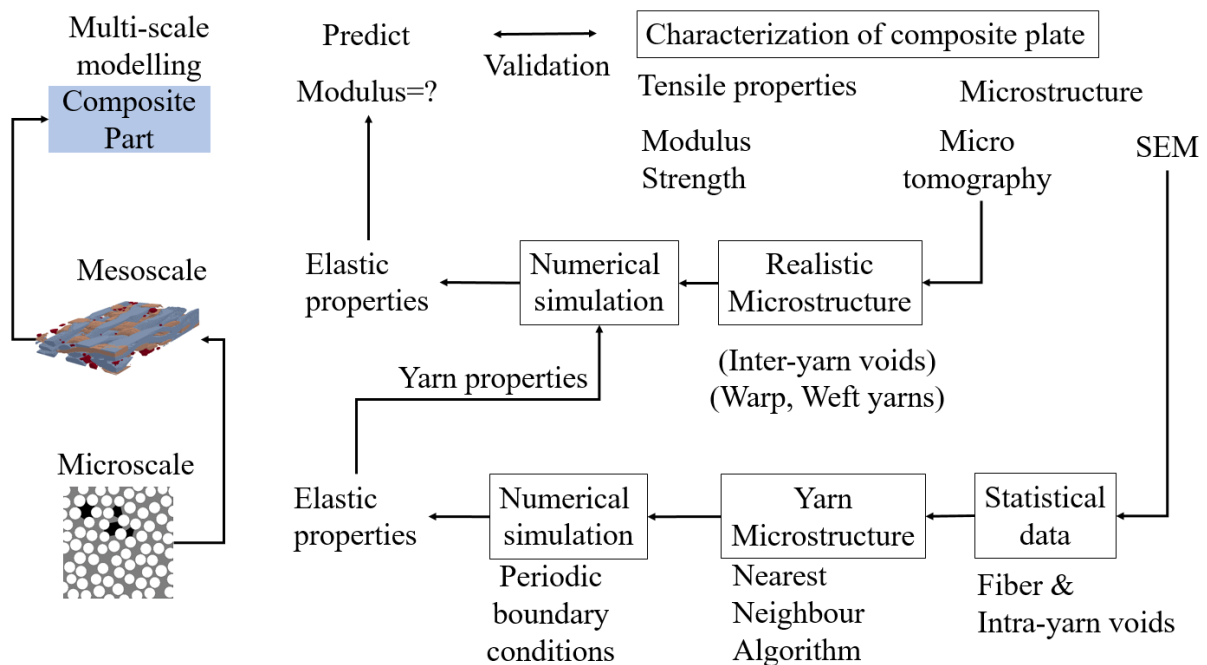
Experimental:

- Manufacturing of the 3D textile composite with a controlled void volume fraction.
- Characterizing the mechanical properties of the composite.

- Characterization of the void volume fraction, intra-yarn characteristics (fiber area fraction, and void area fraction).
- μ CT of the composite to capture the inter-yarn voids and textile reinforcement.

Numerical:

- Develop a tool to generate fibers in yarns respecting fiber radius and spatial distribution.
- Develop a tool to generate the voids inside and between the yarns considering all possible void characteristics.
- Carry out a multi-scale homogenization to predict the elastic properties of the 3D textile composite. The complete multi-scale scheme is presented in the following figure.



1.4 Outline

This thesis is organized as follows. The second chapter focuses on the mechanism of void formation, different void characteristics, and their characterization techniques. Here we also present, a literature survey covering the effect of void on the mechanical properties of the composites and the state of art techniques to predict their effect. This chapter also serves as the motivation for the developments presented in the next chapters.

Composite manufacturing methods and characterization are explained in the third chapter. It starts with the introduction to textile reinforcements used in this study and composite manufacturing. Then we present the template for the extraction of the specimens to characterize the composite plate. Total fiber volume fraction and void volume fraction are measured by burn-off tests. The intra-yarn fiber area fractions and void area fraction inside warp and weft are obtained by microscopy. The specimens for the μ CT are extracted to obtain the scan data for the reconstruction of meso-structure which will be used in Chapter 4. Tensile tests are

carried out along the weft direction to quantify Young's modulus, strength, and failure strain. The chapter ends with a sensitivity study on tensile properties to total void volume fraction and intra-yarn (warp & weft) void area fraction.

Homogenization of the yarn properties and a parametric study to analyze the effect of void radius, shape and distribution on the elastic properties are conducted in the fourth chapter. The chapter starts with a stepping scheme to predict the effect of the spherical voids on the yarns. Next, the modified Near Neighbor Algorithm is presented. The statistical equivalence of the RVE is verified with the measured fiber radius and inter-fiber distance. Two more algorithms dedicated to generating the void in RVE are proposed. A convergence study is presented to choose the element size and RVE size for the numerical homogenization. Numerical homogenization is carried out by adopting approximate periodic boundary conditions. The chapter ends with a detailed discussion on the influence of void characteristics on the elastic properties of the yarns.

Chapter 5 starts with the explanation of the structure tensor based segmentation method to generate the real meso-structure from μ CT data and the converge study. Later, the results of segmentation for μ CT data acquired during this study are presented. An algorithm is developed to generate artificial inter-yarn voids. Using this algorithm meso-structure with different inter-yarn void volume fraction are created. A parametric study is carried out to understand the sensitivity of composite elastic properties to void characteristics. A complete multi-scale simulation is carried out at end of the chapter and the results are validated with the experiments carried out in the third chapter.

Conclusions and perspectives are presented in Chapter 6.

2 State of the art

In this chapter, we present a general introduction to composites and their manufacturing processes. In particular, we state the importance of studying the effect of manufacturing induced defects on the mechanical properties of composites and modeling techniques to predict composite behavior. The chapter begins with a quick introduction of composites and processing defects in Section 2.1. Section 2.2 presents industrial composite manufacturing techniques like autoclave and resin transfer molding (RTM). This section also explains the different defects induced during manufacturing in composites, particularly void type defects. In Section 2.4, we present the characterization techniques to measure void characteristics such as void volume fraction, size, shape, and spatial distribution. Section 2.5 discusses the influence of the voids on the mechanical properties. The analytical and numerical methods to predict the impact of void on the mechanical properties of composites are presented in section 2.6. Finally, in section 2.7, we discuss the summary of chapter 2 and present the road map for the next chapters.

2.1 Composites and processing defects

Fiber-reinforced composites have a high strength to weight ratio, making them an optimal choice in various engineering applications in aerospace, automotive, marine, civil, chemical processing equipment, sporting, land transportation, and leisure sectors. In this work, we focus on the fiber-reinforced polymer matrix composites, containing the reinforcements made of synthetic fiber (glass, carbon, etc.) or natural fibers (flax, jute, etc.). The composites can be sub-classified as random, unidirectional (UD), laminated, and textile composites based on the reinforcement architecture. The reinforcement choice depends on the application, the manufacturing technique, cost, and type of matrix. However, anomalies can be created in composites at different steps of manufacturing called process-induced defects. A detailed explanation of such defects is presented following section.

Process induced defects: Composites are an effective solution for producing high strength composite parts. However, the final properties of the composite parts depend on the type of matrix and manufacturing process. Notably, defects induced during composite manufacturing will result in an undesired behavior of the part. They can be classified into matrix, fiber, and interface defects [1,2]. The 2D schematic representation of the manufacturing defects (fiber and matrix) is presented in Figure 1.

- Fiber defects include fiber misalignments, waviness, and broken fibers. The cause of the fiber defects can be fiber curving during manufacturing, faulty textile machines.
- Interface defects are fiber/matrix separation, caused by improper sizing of the fiber or bad choice of matrix, resulting in improper adhesion between fiber and matrix.
- Matrix defects include matrix cracks (improper matrix curing), dry spots, and voids.

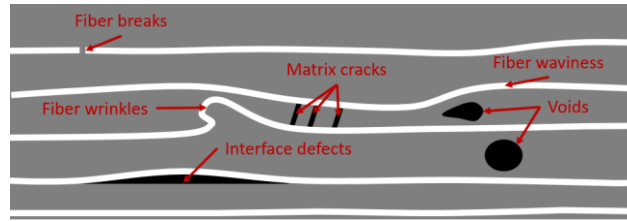


Figure 1: Different types of manufacturing defects in composites.

Dry spots are caused due to insufficient resin in the system, whereas void can be due to entrapment of air during resin injection or curing. Hence dry spots can be removed by optimizing the manufacturing strategy. Out of the defects mentioned above, voids are the most common and unavoidable during most of the manufacturing processes. Hence, in the following Section 2.2, we present the industrialized manufacturing processes, like autoclave and resin transfer modeling techniques and the mechanism of the void formation/nucleation, respectively. Voids are the most significant defect type, and the creation of the part without void is highly expensive and not often possible. Thus quantifying the effect of voids on composite properties will provide a tradeoff between mechanical performance and manufacturing cost [3].

2.2 Manufacturing of composites

Composites manufacturing is assembling two or more non-miscible materials (reinforcements and matrix) to obtain a final part. There are different types of manufacturing techniques available to produce a composite part. Depending on the resin flow during the manufacturing of fiber-reinforced composites, the processes can be classified into two types.

- Flow processes, where resin flows into a stationary porous medium.
- No-flow processes where the resin does not flow through the preform but gets consolidated under the external pressure and temperature [4].

There are different manufacturing processes utilized in the production of a composite part. However, selecting the correct manufacturing technique depends on the material choice, time of manufacturing, and the required properties of the composite part. Autoclave and resin transfer modeling (RTM) are two widely used manufacturing processes in the composite industry.

The autoclave molding is mostly utilized in producing composite parts for aerospace applications but not a cost-effective solution for mass production. On the other hand, RTM has gained interest in the industry because of its cost-effectiveness [5]. Thus, the manufacturing process (Autoclave, RTM) and the phenomenon leading to voids are explained in the following Sections 2.2.1 and 2.2.2, respectively.

2.2.1 Autoclave

The process starts with cutting the prepregs sheets into the desired shape and stacking them in a sequence on an open mold. Then it is vacuum bagged and the air will be removed (Layup). The layup is placed inside an autoclave then compaction pressure and temperature are applied for consolidation of the part. The steps under which the temperature and pressure can be varied

are called cure cycles. After the prescribed cycle time, the part will be moved out of the autoclave and the final product can be collected. Figure 2 represents the schematic of the autoclave stacking sequence and vacuum bagging.

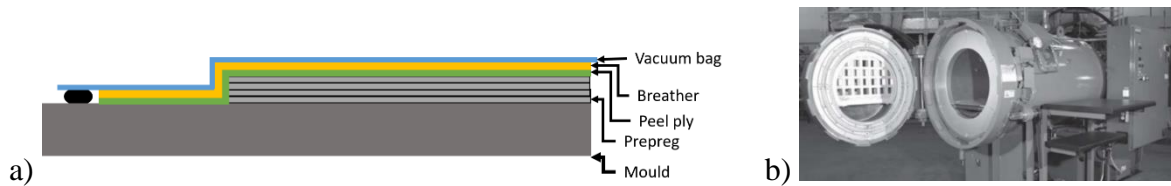


Figure 2. a) Prepreg layup sequence for Autoclave b) An industrial scale autoclave [4].

2.2.2 Liquid composite molding with emphasis on RTM

Impregnation of resin under controlled conditions (resin velocity, inlet pressure) into a dry fibrous medium is the working principle of the liquid composite molding (LCM) processes. It comprises different techniques such as Compression Resin Transfer Molding (CRTM), Resin Transfer Molding (RTM) and Vacuum Assisted Resin Transfer Molding (VARTM), etc. [6]. The schematic representation of the RTM process is shown in Figure 3. The process starts with cutting the fiber or textile and placing it in a closed mold. The mixture of resin is prepared separately and injected into the preform under controlled parameters like constant pressure or flow rate and constant temperature. Once the resin is solidified, the mold is opened and the final part can be collected. In comparison to the autoclave, RTM is cost-effective for large-scale productions. The cycle time of the parts is comparatively shorter, as there is no preparation for vacuum bagging. The advantages and disadvantages of the RTM process are presented in Table 1.

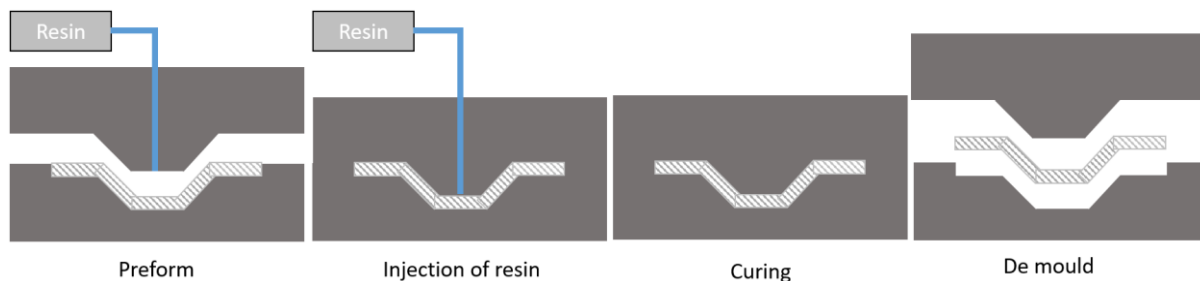


Figure 3. Different steps involved in manufacturing composite by RTM.

Advantages	Disadvantages
<ul style="list-style-type: none"> • Best geometrical control on the produced part. • A higher surface finish can be achieved. • Take less time when compared to autoclave. • Prototyping with high accuracy is possible. • Low manufacturing cost compared to the autoclave. • Better control of void percentage. 	<ul style="list-style-type: none"> • Possible leaks during the process due to improper molds. • For a part with large dimensions, production tooling cost can be higher. • The void volume fraction is higher

Table 1 Advantages and disadvantages of the RTM process [4].

After comparing both processes (autoclave & RTM) RTM is selected as the better process because of its adaptability for mass production and ease of manufacturing complex shapes. However, composites manufactured by RTM processes always have voids, and it is impossible to avoid their formation. Moreover, in the case of dual-scale reinforcements like textiles, void also occurs in two scales (see Figure 5 b) intra-tow voids and inter-tow voids). Hence, in Section 2.3 we will present the mechanism of void formation in the autoclave process and dual scale void formation in textile composites during the RTM process.

2.3 Void type defects

The formation and evolution of voids in the textile composites depends on the manufacturing technique, textile architecture, and type of matrix. Since void formation is a local phenomenon, it is impossible to control its occurrence during the manufacturing process. However, the understanding of the void formation mechanism will help us to control the void formation to some extent. For example, by controlling the injection pressure in RTM and cure cycles in Autoclave we can produce composites with different void volume fractions [7–9]. A detailed understanding of this mechanism can further help us to control certain void characteristics like the location of void formation. Hence, the void formation mechanism in autoclave and RTM processes is explained in the following sections.

2.3.1 Void formation

During an autoclave process, voids can occur due to various reasons such as the air entrapment during the layup, the volatile gas during the curing of the matrix, existing air bubbles in the prepregs, and matrix shrinkage during curing [4]. As the temperature increases, the small voids move and settle near the top layer and bigger voids get trapped in between the layers as shown in Figure 4.

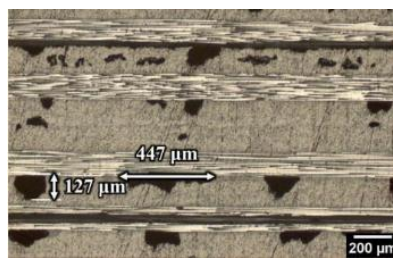


Figure 4. Through thickness void distribution of a UD laminate (0/90) [10].

In the RTM process the formation of voids can be due to mechanical entrapment of air during resin flow [11], volatile gas created during curing [12], and nucleation of the dissolved gas in the resin [13]. Out of all the phenomena, the major contribution to the void formation is the entrapment of the air, which is caused due to the non-uniform resin flow in non-homogeneous fiber preform. Even the macroscopic resin velocity seems to be smooth, the local velocity at the microscale can vary from point to point. This results in the formation of the void in different scales (see Figure 5 b)) intra-yarn voids and inter-yarn voids). There are different nomenclature used in the literature for voids at different scales. Micro void refers to void located in yarns called “yarn void”, “intra-yarn voids”, “intra-bundle voids”, whereas the meso-voids refer to the void in between yarns “inter-yarn voids” or “inter-bundle voids”, “channel voids”. In this

thesis, we refer to the voids as intra-yarn void (voids in a yarn) and inter-yarn voids (voids in a channel).

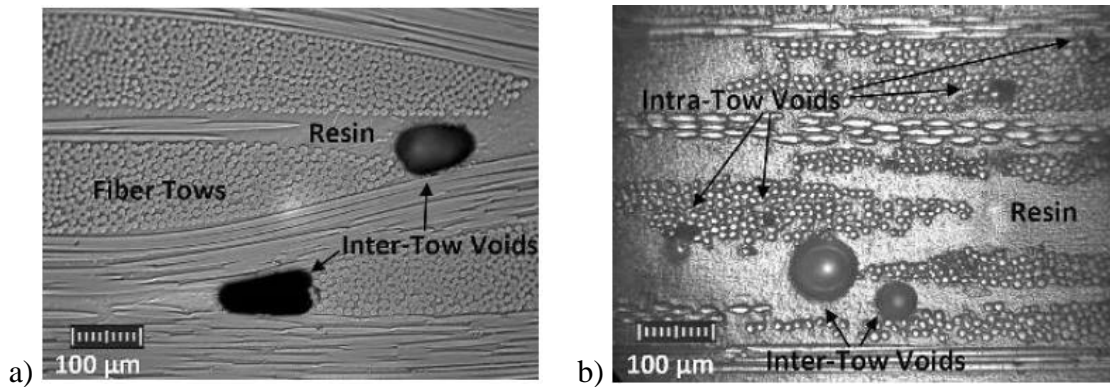


Figure 5: Void shapes in the composites manufactured by RTM a) In a textile composite and b) In the laminates [1].

The occurrence of intra-yarn voids and inter-yarn voids have a complex coupled physics. Therefore, this topic was highly studied [11,14–16], and the authors suggested a dual scale porosity distribution, which is a characteristic feature of the yarn based composites such as textile composites. In a textile composite, the pore size in a channel (meso-pores) is in the order of $\sim 100 \mu\text{m}$ to $\sim 1\text{mm}$, whereas pores inside the yarns are at an order of $\sim 1 \mu\text{m}$ to $\sim 10 \mu\text{m}$ [17]. Hence the resin flow in the channel is driven by the viscous flow and inside the yarns, the surface tension is predominant. Hence, flow in yarns is driven by capillary forces causing wicking. The formation of the inter-yarn and intra-yarn voids is determined as competition between these two flows. For example, if the capillary flow is dominant it results in the creation of inter-yarn voids as shown in Figure 6 b), d). Otherwise as presented in Figure 6 a), c) high viscous flow in the inter-yarn channels would result in the creation of intra-yarn voids.

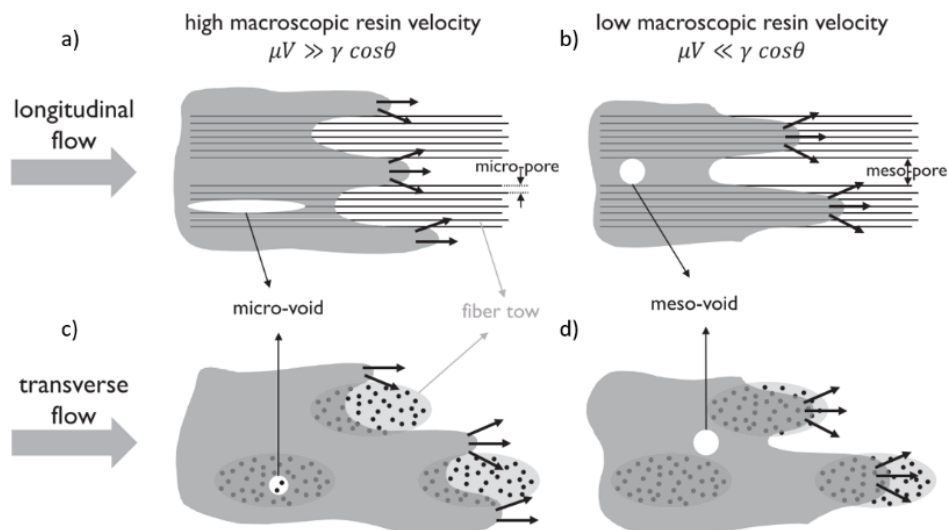


Figure 6: Formation of dual scale voids in textile composites a), c) Formation of a void in yarns and b), d) Formation of a void in channels [18] (μ resin viscosity, V resin velocity, γ surface tension resin, and θ contact angle).

To quantify the competition between the viscous flows and capillary wicking in yarns [16], the authors proposed the modified capillary number (C_a^*) which is the ratio of the viscous force to the surface tension as shown in Equation 2.1.

$$C_a^* = \frac{\mu \cdot V}{\gamma \cdot \cos \theta} \quad (2.1)$$

where μ is the resin viscosity, V is the resin velocity, γ is the surface tension of the resin, and θ the contact angle of resin with fiber. The modified capillary number suggests that, at smaller values of C_a^* (lower resin velocity) the inter-yarn voids are predominant and at higher C_a^* (high resin velocity) the intra-yarn voids are predominant [19]. There have been experimental and numerical works to relate the void formation and capillary number by an in-situ investigation [20–22]

It is worth mentioning that the final void content is also affected by other phenomena such as void migration and void compression. Once the air void is created it is constantly compressed by the resin surrounding it results in the reduction of the void volume and this phenomenon is called void compression. During the mold filling process the air bubbles continue to move along the flow this is called void migration.

Thus, the void formation in the textile composite is affected by architecture, processing conditions (flow velocity), resin properties such as viscosity and surface tension. In this thesis, we use this mechanism intentionally to induce a particular void distribution in the composite part.

Moreover, one can also observe that voids have different shapes, sizes, and spatial distribution. These parameters are termed as void characteristics and they influence the mechanical behavior of the composite. Thus, it is important to consider these constituent characteristics for the exact prediction of the material properties. Void type defects are generally characterized by void volume fraction. However, this parameter does not provide any information about the size, shape, and spatial distribution. Hence the techniques to characterize the geometrical features of the voids are explained in the Section 2.4

2.4 Geometrical characteristics of voids

In composite materials, the void characteristics correspond to void volume fraction (Section 2.4.1), size (Section 2.4.2), shape (Section 2.4.3), and distribution (Section 2.4.4). The review presented by [23] emphasizes the importance of the void characteristics to understand the composite behavior. Since, these void characteristics depend on the properties of reinforcement, matrix, and manufacturing parameters (pressure, time, and temperature), It is worth noting that the measuring of all void characteristics requires special characterization techniques which were explained in section 2.4.5.

2.4.1 Void volume fraction

It is the most frequently used void characteristic and is mostly addressed in the literature to quantify the effect of voids on the mechanical properties [24]. It is calculated as the ratio of the total volume of air in the composites to the total geometrical volume of the composite part.

$$\text{Void volume fraction} = \frac{\text{Volume of air in composite part}}{\text{Volume of the composite part}} \quad (2.2)$$

However, there are enough works to support that total void volume fraction is not a single parameter to relate the behavior of composite with voids. Hence, the other void characteristics such as void size, shape, and distribution should be characterized.

2.4.2 Void size

It can be related to the cross-section area (A) of the void when observations are performed on the 2D slices of composite and volume (V) of the void in the case of 3D reconstruction. To remove the ambiguity of the size measurement, in [25] was introduced an equivalent void radius. They observed for a UD composite, this value can range from ~10 to 450 microns. The equation to calculate the equivalent void radius (r_{eff}) by using cross-section is given in Equation 2.3 and utilizing void volume is presented in Equation 2.4 [10].

$$r_{eff} = \sqrt{\pi/A} \quad (2.3)$$

$$r_{eff} = \sqrt[3]{3V/4\pi} \quad (2.4)$$

Void size has been a difficult parameter to determine. Firstly high variation of void size results in difficulty in determining the good parameter for void identification. Secondly, the measured void size can be varied with respect to the characterization techniques[26]. There are considerable studies conducted to determine the statistics of void size in UD composites. Micro-CT along with image segmentation was the common tool utilized in determining the void size [27,28].

In a UD composite manufactured by autoclave [29] it has been observed, in the specimens with high void volume fraction contained bigger voids than the specimens with lower void volume fraction. However, the void size can highly depend on the cure cycles. For example, observations made on composites manufactured out of autoclave [30] reported a void size of 8-30000 micron², whereas [31] reported 3-15000 micron². Hence, it is important to obtain the void size for each composite even if they are manufactured by the same process. In the studies of [10], the authors presented void effective diameter/size as the efficient parameter than total void content to study the effect of voids on inter-laminar properties.

2.4.3 Void shape

Morphology of voids can be influenced by the manufacturing process [32,33], the architecture of the reinforcement, and the layup sequence. Classically the void shape is indicated by the parameter called aspect-ratio (AR). The AR of the void is defined as the ratio of the length of the major axis to the length of the minor axis, presented in Equation 2.5. This is a measure to specify elongation of the void, smaller AR mean voids shapes are spheroids [34] and large AR means they are elliptical [35]. Depending on the AR, there are several morphological terms

utilized to describe the void shapes, such as flattened, coins shapes [32], cylindrical-shaped, cigar-shaped, rod-like shapes, elliptical cylinders, and large-long shapes [29].

$$AR = \frac{\text{Length of major axis}}{\text{Length of minor axis}} \quad (2.5)$$

The shape of the void is measured by using imaging techniques such as microscopy and μ CT. Microscopy can only provide the 2D morphological information of the void. However, the observation on the multiple slices can give adequate information on the 3D morphology of the void [36]. Since the proper investigation is only possible by analyzing the 3D void morphology, several studies in the literature have used micro Computed Tomography (μ CT) aided with image segmentation tools to analyze the void characteristics. In the literature, most of the studies are dedicated to UD composites manufactured by autoclave. Research from various sources can be concluded that small voids ($\sim 5\mu\text{m}^2$) are volatile induced voids and have spherical shapes. Meanwhile the larger voids formed by air-entrapment in between laminates have flattened and elongated shapes with $\sim 50\text{-}250\mu\text{m}^2$ and an aspect ratio of about 40 [25,32]. The voids in laminates are dominantly elongated in the fiber direction and always in contact with the adjacent fibers [27,37]. In textile composites manufactured by RTM, the void have near-spherical shapes in matrix rich zone and elongated cylindrical shapes inside the fiber yarns [38,39]. The description of different void shapes observed in the literature is presented in Table 2.

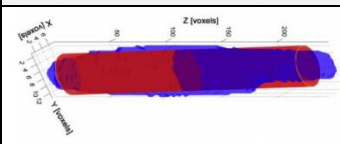
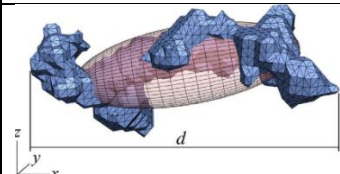
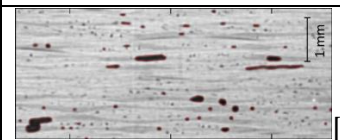
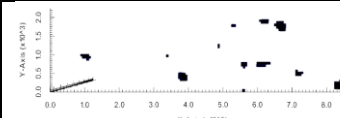
Void schematic	Shape description	Location	Composite type
 [37]	Elongated Cigar shapes- irregular cross- section	Inside the yarns	Textile, UD
 [40]	Voids with irregular cross- section	In matrix	2D,3D textile
 [41]	Flat disk shapes	In between plies	UD, Textile Laminate
	Spherical	In resin-rich zones	Textile

Table 2: Description of shapes and their location observed in composites.

2.4.4 Void distribution

Voids can be concentrated in a certain zone or uniformly distributed in a large zone. This spatial distribution of voids will influence the state of stress distribution thus affecting the material's mechanical response. The spatial distribution of the void can be affected by the manufacturing method, processing parameters, and architecture of the textile. For example in laminated

composites, depending on the process parameters, voids can be concentrated in between plies or inside the ply. In textile composites, they can be inter-yarn or intra-yarn. Several studies were conducted to observe the position of the void as the function of processing parameters. For an LCM process, [42] observed the position of the void with respect to the resin velocity. In the autoclave process, through-thickness void distribution studies were conducted in [30,37]. Several other works also presented the distribution of the void position in the composite. However, there are no works found investigating the spatial distribution of the voids such as homogeneous, random, and cluster distribution. Hence the effect of void distribution will be evaluated in our study along with other void characteristics. For this, in Chapter 4 a novel algorithm based on the near neighbor distance will be proposed to generate a microstructure with the controlled spatial distribution of the voids.

2.4.5 Void characterization techniques

Now we present the different characterization techniques available to evaluate all the void characteristics discussed above. There are four major characterization techniques to obtain the void characteristics in a composite part, namely burn-off test, ultrasonic method, gravimeter/density test, and image-based analysis (Microscopy/ μ CT). The choice of the technique depends on the material type and scale of the required data. For example, the burn-off test cannot be used for composites reinforced with the fiber having the degradation temperature lower than the matrix (e.g. natural fiber composites), whereas, in the case of the synthetic fibers burn-off is highly utilized. Conversely, the burn-off test does not provide any other void parameters such as shape, size, and distribution. Hence, every test has its advantages and limitations. It is recommended to understand the methodology, application, and limitations of these techniques so that one can choose the right technique. The comparison of different techniques available in the literature is presented in Table 3.

Technique	Density method	Burn-off test	Images based analysis	Ultrasonic
Methodology	Archimedes principle	Matrix dissolution	Pixel counting (Microscopy/Micro-CT)	Acoustic
Type	Non-destructive	Destructive	Non-destructive	Non-destructive
Void (size, shape, and distribution)	No	No	Yes	Yes
Scale	Macro	Macro	Macro/Meso/Micro	Macro/Meso
Speed of test	Quick	Quick	Slow	Slow

Table 3: Comparison of the different void characterization techniques.

In this thesis, we will use the burn-off test to obtain the total void volume fraction and scanning electron microscopy (SEM) to measure the intra-yarn void characteristics and Micro-CT to characterize the inter-yarn void volume fraction.

2.5 Effect of voids on the mechanical properties of composites

This has been a broadly studied topic in the field of composites and is still under exploration. The main interest in characterizing the voids in structural composites is to quantify their effect on the mechanical behavior. Depending on the characteristics of the void, even a small volume fraction of voids can have dramatic effects on composite behavior, in particular on the matrix-dominated properties (interlaminar shear strength, transverse properties). Many studies have tried to relate the mechanical properties of composite with respect to the total void volume fraction, to list a few [24,29,43–47]. However, there are several studies [30,41,48–51] concluded that the void volume fraction is not a sufficient parameter to understand the effect of voids. In some of these works, the authors proposed that specimens with void volume fraction less than 0.005-0.01 do not affect the mechanical properties, hence this void volume fraction is called critical void volume fraction. It is important to note that, particular void characteristics have a detrimental effect on the specific mechanical property. Hence in this section, the effects of void characteristics on mechanical properties like interlaminar shear strength (ILSS) and tensile properties are presented.

2.5.1 Interlaminar shear strength

The effect of voids on the interlaminar shear strength ILSS is one of the most-studied topics and the early research date from 1968. This is simply because the ILSS is dominated by the matrix and matrix fiber interface properties which are highly affected by voids. However, most of the available literature was only limited to laminated composites. After a large number of studies, the effect of void on ILSS is reported in terms of total void content as a linear or non-linear decrease or by following empirical relations.

In the works of Judd and wright [52], they obtained the critical void volume fraction for ILSS as 0.005. They also identified a linear relation between ILSS and void content: a 1% increase of void content will result in a 6% decrease of the ILSS. According to Ghiorse [53] for every 1% increase of void content will result in a 10% decrease in ILSS. This value is significantly higher than Judd and wright. This significant decline of ILSS is supported by the argument that the reduction of properties can also depend on the void characteristics. In the works of Tang et al. [46], Lui et al. [7], found the void sensitivity on ILSS increases at higher void content, the sensitivity was attributed to the reduction of the ply interface area because of high void content. Their observations also confirmed that a 1% increase in void content resulted in a 6% decrease in ILSS. An empirical exponential relation (see Equation 2.6) between the ILSS (σ) and the total void volume fraction (V_v) (correlated to the ultrasonic attenuation) was proposed by [54] as follows :

$$\sigma = \sigma_{max}e^{-BV_v} \quad (2.6)$$

where σ_{max} is the strength of void-free composite and B is the coefficient that depends on the void characteristics.

The recent research on the ILSS tried to attribute the reduction of ILSS to voids length [55] or their locations [51]. Olivier et al. [51] observed that during a short beam shear test voids in

between the plies trigger the failure of the composite. A more systematic study was conducted by Wisnom et al. [55] to relate ILSS to the void size (length), the increase of void length from 0.28 to 3.00 mm results in a reduction of 23% of ILSS in comparison with void-free composite. The effect of void size (radius) was also studied by Kousourakis et al. [56]. They created cavities for sensors in between the plies by using silicon tubes, they found that ILSS decreased linearly with an increase in the cavity size or number of cavities. Assuming that cylindrical voids are arranged in a regular pattern Hernández et al. [37] proposed a simple analytical net-section model to correlate the reduction of ILSS with respect to void content. They proposed that, depending on the void morphology, even at lower void content the ILSS can suffer a huge decline. To find the better parameter to signify the effect of void on ILSS, Gagauz et al. [10] compared the reduction of ILSS with respect to void volume (see Figure 7a) and effective void radius (see Figure 7 b)). The measurement with an effective void radius (Equation 2.4) provided a slightly higher correlation with a linear fit ($r=0.863$, see Figure 7-b) which suggests that this is a better morphological characteristic to be used when assessing the influence of voids on ILSS.

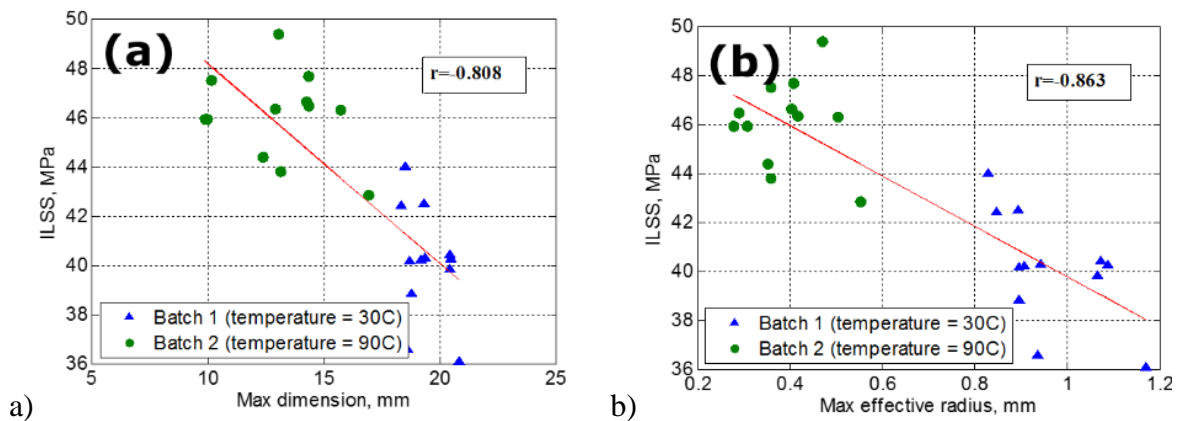


Figure 7. Effect of void characteristics on the reduction of ILSS a) Maximum void dimension and b) Maximum void volume measured in terms of effective radius [10].

The effect of voids on ILSS properties of woven-ply composites was also studied in the literature. Studies conducted by Jeong et al. [47] and Uhl et al. [57] recorded for the same void volume fraction the ILSS of UD composites has been more sensitive to the voids than woven-ply composites. This could be due to the natural resistance of the woven composites for crack propagation. They also assigned the variation to the difference in the void morphology. For a UD composite in resin-rich zones, the voids were elongated cylinders and spheres in textile composites. Moreover, Goodwin et al. [58] noted the difference in the response of the composites based on the textile. For a 1% increase of void content, the plain weave showed a 4% reduction, and 5-harness had a 7% reduction in ILSS. This was attributed to void shapes in 5-harness composites, the higher stress concentration at the corners of the void with a smaller radius.

Remarks:

- The void volume fraction is not an exclusive efficient parameter to correlate the effect of voids on ILSS.

- For better correlation, one can consider void morphological parameters such as effective void radius and length of the void.
- The ILSS also depends on the type of reinforcements. In general, for a UD composite, a 1% increase in void content results in a 6 % decrease in ILSS and textile composite it reduces to 4%. However, the percentage of reduction can vary depending on void characteristics.

2.5.2 Tensile properties

Young's modulus: In the early studies of Harper et al. [59] and Olivier et al. [51] it was found that in the UD ply composites, the fiber dominant elastic properties (i.e. longitudinal tensile modulus and Poisson's ratio) are less sensitive to voids. This phenomenon was also confirmed by Lui et al. [7], Zhan et al. [60], and Stamopoulos et al. [61]. This behavior was also analytical and numerically verified by Selmi et al. [62] Huang and Talreja [63]. But the matrix dominant properties like transverse tensile modulus and shear modulus decreases with an increase in void volume fraction. Experimental investigations by Gurdal et al. [25] showed that out of plane tensile modulus decreases by 10% for a 1% increase in void content. Varna et al. [64] found 5% of voids resulted in a 15% reduction of the transverse modulus and related the lower reduction of modulus to the difference in the reinforcements. Van Den Broucke et al. [65] found that in carbon/epoxy woven composite, a 1% increase in the void content results in the reduction of 5% in-plane tensile modulus and 7% out-of-plane tensile modulus. The reduction of the transverse tensile properties depends on the orientation of the fiber. Zhu et al. [66] conducted an experimental study on composites with the same void content and different fiber orientations. They found that composites with 0-degree orientation have a 14% reduction in properties whereas ± 45 degrees reduce by 8%.

Naganuma et al. [67] observed that the effect of voids on tensile modulus is dependent on the morphology of the void (created by residual solvents) in woven composites. They found that composites with flat regular cross-section voids between the plies in composites registered less reduction in properties than the composites with voids of the irregular cross-section. The effect of the void aspect ratio on the elastic properties of the UD composites was studied by Talreja et al. [63]. For a given aspect ratio, 5% void content resulted in 5 to 10% reduction of the longitudinal tensile modulus and (12-40) % reduction in transverse tensile modulus. For the same void content in plane-shear modulus reduced by 6 to 12% and the out of plane shear modulus reduced by 12 to 40%. They also conducted a comparison between analytical Mori-Tanaka solution and FE-simulation and found a good agreement at lower void content, whereas at higher void content Mori-Tanaka under-estimated the elastic properties.

The void sensitivity of 3D braided carbon/epoxy composite numerically was explored by Xu and Qian [68]. They concluded that at a given void content the elastic properties are smaller sensitive to the randomly distributed voids. The reduction of properties in the longitudinal direction is less than the transverse direction. However, the longitudinal tensile modulus starts decreasing with an increase in the braiding angle. A few numerical studies conducted by Shigang et al. [69] modeled the void by reducing the mechanical properties of the randomly chosen elements in the mesh. They showed that an increase in the intra-yarn void percentage resulted in the reduced tensile properties of the 3D textile composite.

Shear modulus: Longitudinal shear modulus of cylindrical (rod) made of UD carbon/epoxy specimen was measured in the torsion test by Hancox et al. [70]. The observations showed that 1.5% of void content resulted in a 10% reduction of the shear modulus and the theoretical estimates based on Mori-Tanaka showed that 1% of void content will result in a 10% reduction of shear modulus. In the experimental investigation, an increase of void content (~5%) lead to the rapid decrease of the shear modulus (70%). The author concluded this reduction can be because of the void morphology and distribution in specimens with higher void content.

The numerical simulations conducted by V.D.Broucke et al. [65] and found that a 1% increase of the randomly distributed voids results in a 4% and 10% reduction of in-plane shear modulus and out-of plane shear modulus respectively. In a 2D FEM simulation carried by Nikopour et al. [71] by considering the voids as the circles, they obtained that for a given void content the shear modulus reduced faster than the tensile properties. For braided composites, the numerical results presented by Xu and Qian [68] showed that out-of-plane shear modulus decreases faster than the in-plane shear modulus. The reduction of the properties was related to the fiber orientation. They found that increasing the braiding angle reduced the effect of voids on the out-of-plane shear modulus.

Remarks:

- The longitudinal (fiber-direction) tensile modulus is almost unaffected by the void content, whereas the transverse tensile modulus registered higher reduction. Based on the experimental investigation on UD composites presented in Section 2.5.2, an average increase of 1% in void content resulted in a 7 to 9% reduction of transverse tensile modulus. The uncertainty of the experiments was related to variation in void morphology and distribution.
- The results from FE-simulations [63] proved that transverse tensile modulus is highly affected by the aspect ratio of the void. For a void content of 5% depending on the aspect ratio the transverse tensile modulus by 12-40%.
- Similar behavior is also observed for shear properties. The in-plane shear modulus is less affected by the voids when compared to the out-of-plane shear modulus.
- The numerical investigation on the woven composites showed that shear modulus is more sensitive to the local fiber orientation. Shear modulus in direction of the fiber orientation is less affected by the voids.
- Shear modulus is highly affected in the presence of a void when compared to the tensile modulus. For 1% of void content, shear properties are reduced by 10 to 12% whereas the tensile modulus is reduced only by 7 to 9%. This effect is more predominant at higher void content.

Based on the literature survey we can conclude that experimental control on the void volume fraction, shapes, size, and distribution is not possible. The analytical models and numerical simulations have been utilized and proved to be an efficient tool to understand the effect of void on mechanical properties. Hence in Section 2.6, we present the different techniques to estimate the elastic properties of the composites.

2.6 Methods for prediction of elastic properties

The prediction of the elastic properties of the composites containing void was carried based on different analytical models (e.g. in the literature [37,62,63,71–73]) and numerical methods (e.g. in the literature [63,68,74,75]). The process of predicting the elastic properties of the final composites based on the constituent properties is called homogenization [76].

In an analytical method, for a UD composite, the elastic properties were calculated by inclusion methods based on the Mori-Tanaka solution [63] or by reducing the properties of the matrix [77]. For textile composites, approaches based on the method of cells, the mosaic model, and bridging models were used (e.g. in literature [78–81]). The methods based on the numerical approach make use of FE-solution (e.g. in the literature [3,68,82,83]).

For a UD composite, the elastic properties can be calculated in a single step. However, textile composites or layered composites use a multiscale approach to predict the properties of the composite [84]. A multi-scale simulation critically consists of two following homogenization steps one at micro-scale to obtain properties of yarns and the second is at the meso-scale to obtain final composite properties.

Regardless of the problem's scale, homogenization can be performed using analytical or numerical methods. The different analytical methods review applied to textile composites is presented in Section 2.6.1 followed by the numerical homogenization in Section 2.6.2.

2.6.1 Analytical methods

In this section, we present the different analytical models used to predict the homogenized stiffness of the textile composites and their limitations. As explained in the previous section the first step in the multiscale approach is the prediction of the elastic properties of yarns (micro-scale). The accuracy of results for analytical homogenization at the microscale is dependent on two key parameters.

- Yarn geometrical parameters (yarn cross-section, yarn width, fiber volume fraction, void volume fraction, etc.)
- Method of homogenization (Micromechanical models).

Homogenization at the micro-scale can be achieved by micromechanical models [85,86]. At the meso-scale, the homogenized composite properties are calculated based on the iso-strain assumptions, iso-stress assumptions, or inclusion methods. The available methods for macro-scale homogenization can be divided into four categories a) Classical Laminate Theory (CLT), b) iso-strain, c) iso-stress assumption models and d) inclusion methods. CLT-based models were proposed by Ishikawa et al. [87] to predict the elastic properties of the 2D laminates. Authors have proposed mosaic, undulation, and birding models. These three different models are explained in the following.

The mosaic model approximates the composites as a lay-up of cross-ply laminates. The final properties of the composite can be calculated by iso-strain or iso-stress conditions. This model yields lower and upper bounds of the in-plane elastic properties [87].

The undulation model is an extension of the mosaic model. The undulation of yarns in the loading direction is modeled by trigonometric function, and yarns in the transverse direction are considered to be straight. The undulated yarn is divided into sub-volumes and the stiffness of each block is evaluated considering fiber orientation as the direction of undulation. The whole system now can be assembled as a mosaic model and elastic properties can be calculated by using iso-strain/iso-stress methods. This method is applied in the literature to find the properties of 2D textile laminates [87].

In later works of Chou et al. [88] proposed the extension of the undulation model called the bridging model. This model can be applied to the composites with complex reinforcement architectures. The total volume is subdivided into three to five sub-volumes such as warp, weft, and binder yarns. Later these sub-volumes are assembled and homogenization is carried out under a combination of iso-stress and strain assumptions.

Using the bridging model Yanjun et al. [78] calculated the stiffness of the 3D interlock reinforced ceramic composites. Later Hage et al. [80] used a similar method to calculate the elastic properties of 3D woven textile reinforced composites. [89] used the iso-strain approach to calculate the stiffness of 3D angle interlock composites. The bridging models were also applied to complex architecture considering such a braided textile by Li et al. [90]. Further, these methods were used by Naik et al. [81,91] to calculate the properties of the 3D textile reinforced composites. In the review presented by Hallal et al. [92] the qualitative comparison of the predictive models shows that analytical models based on iso-strain assumption have an over prediction of the in-plane elastic properties and only a reasonable prediction on the out-of-plane module and Poisson's ration is almost out of bounds.

In recent three-stage homogenization (3SHM), models were proposed by Hallal et al. [89] where they presented an improved comparison of elastic properties concerning the experimental data from Hage et al. [80]. The 3SHM is based on the homogenization at three scales micro-, meso- and macro- scales. At first, the properties of the yarns are evaluated, in the second step the yarns are divided into sub-volumes where the properties of each sub-volume are calculated based on the fiber orientation. Now the sub-volumes are assembled to calculate the properties of the yarns at mesoscale. Finally, in step three, the homogenized composite properties are calculated by the iso-strain approach. The simplicity of this model facilitates the application to complex architectures.

Apart from the presented models the inclusion methods based on mean-field homogenization were also used in the literature to calculate the elastic properties of the textile composites. [93] used the Mori-Tanaka model on different textile reinforced composites. In this method, the yarns are subdivided into regions of elliptical cross-section and the effective properties of each sub-region are calculated by Eshelby's inclusion methods [94]. In the end, the homogenized sub-cells were assembled to calculate the properties of the composite. This method is also used by Lomov et al. [95] to calculate the properties of the textile composite with different reinforcements and presented that the longitudinal Young's modulus and in-plane shear modulus are close to numerical simulations. However, the transverse modulus has a deviation of more than 15%, and this was associated with the inaccurate geometrical modeling of the yarns in the analytical formulation.

Method of cells (MOC) has gained recent popularity in the homogenization of textile composites [96]. In this approach, the sub-volumes contain the yarn layers and matrix layers, where the properties of the yarn layers can be calculated by the micromechanical models such as Chamis, modified rule of mixtures, and Halpin-Tsai [97].

The comparison of elastic properties calculated by different analytical models with the experimental results is presented in Table 4. Micromechanical methods and inclusion based methods have a smaller percentage of error than the iso-strain/iso-stress methods. The source of error can be related to the approximation in the yarn geometry and local fiber volume fraction and fiber orientation. The analytical solution cannot take into account the defects/anomaly in the composite parts in the geometrical modeling and, this results in the inaccurate prediction in the mechanical properties of the 3D composites [98].

Ref.	Architecture	Method	Material Properties in GPa										
			Comparison	E_{11}	E_{22}	E_{33}	G_{12}	G_{13}	G_{23}	ν_{12}	ν_{13}	ν_{23}	
[98]	Knitted	Bridging	Experiment	10.28	-	-	-	-	-	-	-	-	-
			Bridging	13.12	-	-	-	-	-	-	-	-	-
[89]	Woven	3SHM Iso-strain	FEM	40.20	33.07	7.78	2.75	2.97	2.19	0.058	0.463	0.506	
			3SHM	43.94	30.47	8.19	2.913	3.14	2.26	0.063	0.519	0.524	
			Iso-strain	61.22	30.30	8.19	2.92	4.63	2.27	0.031	0.693	0.529	

Table 4: Comparative study on the different analytical methods to predict the elastic properties of the textile reinforced composites.

Modeling the effect of voids on mechanical properties: There are no dedicated analytical models available to consider the effect of voids on textile composites. Regardless of the MS framework, the effect of void on composites has been related to overall void content with help of empirical relation [70,73]. However, there a few works where the properties of the yarn are calculated by using micromechanical models such as Chamis, Halpin-Tsai, and Mori-Tanaka. Later yarn properties are used at the meso-scale to calculate the homogenized composite properties [99,100]. In a multiscale simulation framework, almost all the works in literature use a numerical approach to determine the effect of voids on the mechanical properties.

- The limitation of the analytical models such as consideration of real yarn geometry and manufacturing defects can be realized by numerical simulations presented in the following section.

2.6.2 Numerical simulations

It is a highly utilized method to understand the behavior of heterogeneous materials such as textile composites [84]. The key feature is that numerical modeling allows us to replicate the microstructure close to reality, to take into account the real yarn geometry and anomaly/defects in the material. The growing image-based characterization techniques such as micro-CT and computational capability have enabled the researcher to create exact microstructures and analyze the non-linear and linear behaviors of textile architectures [99,101]. However, a complete representation of microstructure from fiber to composite in a single structure is far out of the reach for the present computational capability. Thus, a multiscale numerical simulation has gained the popularity to bridge the gaps between different scales of material [102]. The term, numerical homogenization is generally associated with this process in the literature. The first order numerical homogenization has almost been the basis of the

homogenization process for the last 20 years and proved to be the best technique for the estimation of the linear material behavior at small strains and not only [103].

In this section, we present a multi-scale numerical simulation homogenization scheme to predict the behavior of the textile reinforced composites which requires a detailed description of the microstructure, material properties, and boundary conditions at each step/scale [84]. Thus, the first numerical homogenization is carried out at a micro-scale to calculate the properties of yarn and the second one at the meso-scale to calculate the properties of a composite.

In general, the workflow numerical simulation can be divided into three steps: 1) Definition of geometry, 2) Meshing and boundary conditions, and 3) Stress analysis and calculation of elastic properties. Geometry generation is the spatial arrangement of constituents which depends on the scale of the material. In the numerical homogenization of the 3D textile composites, at the micro-scale, the microstructure corresponds to the yarns, and at the meso-scale, it refers to the architecture of the textile. In this section, we present the different kinds of modeling techniques/algorithms adopted to generate microstructure at microscale and mesoscale.

2.6.3 *Microscale (Yarns)*

The microstructure of yarns corresponds to the distribution of the fibers and voids in a domain, such that it represents the behavior of the entire yarn. Then the microstructure can be called a Representative Volume Element (RVE). In the literature, there are numerous algorithms to generate fibers [104]. However, there were no dedicated algorithms for packing voids. In most of the studies considering the voids, their morphology was approximated to regular cylinders or elliptical cylinders [71,82,105–107]. These works considered micro-voids (intra-yarn voids) to be elongated cylinders along the fiber direction as shown in Figure 8 a), b). Unlike in reality the intra-yarn voids have very concave shapes and cannot be approximated to simple circular cross-sections (see Figure 8 c)). However, the approximation of the void cross-section will result in uncertainty in the prediction of the elastic properties, this phenomenon was presented by [63] already presented in section 1.4.2. Apart from the morphological indicator (aspect ratio), the shape of the void is also rendered important, [83] studied the effect of different void geometries (square, triangular and circular) and concluded that void geometry influences the strength of the UD composites. Also, the experimental works presented in the literature showed that at given void content the UD glass fiber composite has a different reduction in properties ranging between 12 and 40% this variation was directly associated to void shapes and distribution [32]. Hence it is important to consider the geometrical features of the void in the generation of RVE.

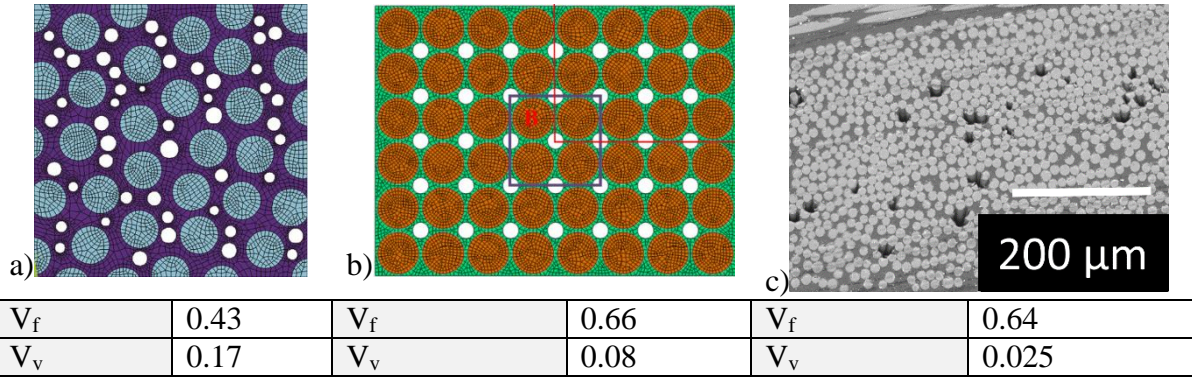


Figure 8: Approximation of the intra-yarn voids by a) [82], b) [71], and c) Void shapes observed in yarns.

Image-based modeling techniques are developed by Wu et al. [108], Qi et al. [74]. They used a segmented image to generate the microstructure containing the voids and calculated the mechanical properties of that particular image. However, this process needs images at high resolution and the choice of image is crucial, as every slice of an image cannot be representative of the entire composite. Hence image-based microstructures can be used for validation but cannot be treated as the representative for the whole composite.

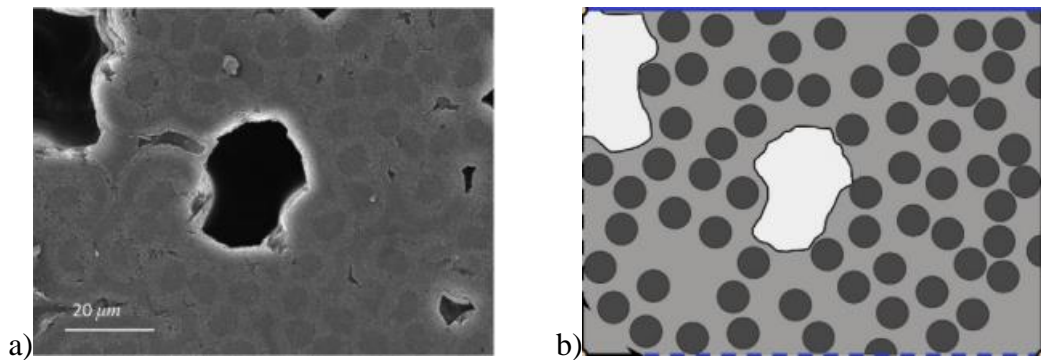


Figure 9: Generation of microstructure directly from SEM images [74].

Limitations of present microstructure generation algorithms at the microscale are:

- There are no works found, that the study about the effect of void spatial distribution on the mechanical behavior of the composites. And there are no algorithms that allow generating voids, either.
- Even the algorithms for the fiber generation are being developed for a long time, there was no possibility in the present algorithm to enforce the spatial distribution of the fiber, even though in literature it was found that the distance between fibers and the local packing, both play an important role in stress concentration, damage initiation, and elastic properties [109].

Motivation 1: Hence in this work, we propose an algorithm that can respect all the statistical parameters, which can be used to describe the yarn, such as fiber size and spatial distribution, and voids, spatial distribution, shape, and size. The detailed information regarding the microstructure generation will be presented in section 4.3.1.

2.6.4 Mesoscale (Architecture)

Textile composite architecture at mesoscale can be referred to as the modelling of the intertwined warp, weft yarns and manufacturing defects such as voids. There is a vast pool of research with numerous examples to model the woven composites, with several advancements into more complex 3D woven and braided structures. Elastic properties are calculated from mesoscale finite element calculations are proved to be reliable, provided a correct description of the yarn geometry and successful meshing [110–114]. Meso-scale yarn-based geometrical models can be generated by “Ideal” or “Realistic” numerical model.

Ideal models

These geometry generation algorithms have the assumptions [79,115–117] such as

- Simplified yarn cross-sections,
- Constant yarn cross-sections,
- Propagation path of the binder yarns, and
- Aligned warp and weft yarns.

Modeling of yarn can be carried by considering them as homogeneous anisotropic material. Whereas, their geometry can be achieved by generating yarn cross-section and yarn paths. Several solutions [76,118–120] have been proposed to create a geometry for these complex structures. Creating a coding [121,122] to describe the relative positions (above/under) of the yarns is one of the common approaches used to describe generate the yarns.

The yarn paths are given by the spatial positions of the centers of the yarn cross-sections. These yarn centers can be calculated from the microscopy observation [123,124] or mathematical functions [116,124,125]. These functions are defined for all the yarns in the unit cell by the geometrical model. When used in numerical calculations, all these functions are given as arrays of values for a set of points along the yarn midline, the quality of representation of the continuous yarn lines and especially the continuity of the tangent regulated by the fineness of the divisions of the yarn middle lines. The shape of the yarn cross-sections can be assumed elliptical, lenticular, etc [123,126–128]. Additionally corrected dimensions can be measured from microscopy observations.

Software like TexGen and WiseTex are considered as the alternative for the construction of 2D/3D textile geometry. TexGen was developed by the University of Nottingham and the working principle of this software was explained in [117]. It is also widely used to perform a numerical simulation [129]. WiseTex was developed in KU-Leuven and it works on the principle of minimization of energy and has better parameters that can take into account yarn distortions during the process. The common assumptions of the idealized models in that the geometry of the textile only depends on the key parameters such as the cross-section of the yarns and the spacing between the yarns remains constant.

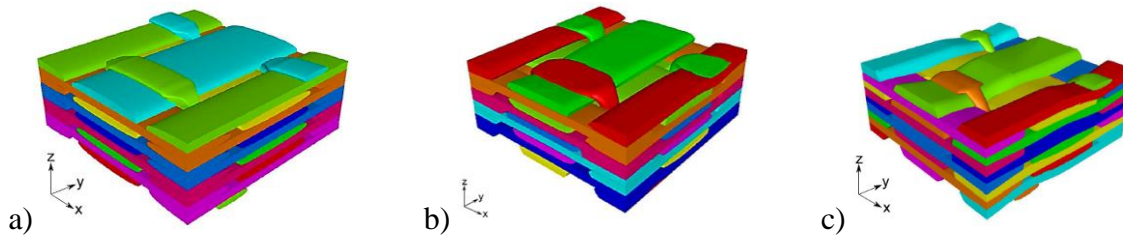


Figure 10: Modeling of the textile architecture by a) Idealized model generated by TexGen and b) Geometry modeled in TexGen and c) Analytical geometry modeled in TexGen [115].

The textile composites are also modeled by the Digital Element Method (DEM) geometry and analytical geometry. The main difference between idealized models and DEM is the consideration of the effect of the binder yarn on the warp and filler yarns. The geometry of the textile produced by this software (idealized) does not consider yarn waviness or yarn pinching, and these parameters play an important role in the resulting properties [130] [131]. Conversely the models (DEM & analytical) define a more realistic geometry that can reproduce the yarn undulations and varying cross-section.

The digital element method (DEM) was proposed by [132] and later developed by [133] based on the yarn kinematics of yarn during the textile deformation. Yarns are not considered as solid entities. Instead, they are treated as a bundle of 1D chains connected through frictionless joints which allows modeling the phenomenon such as yarn sliding, sticking, and compaction such that DEM allows modeling the textile architecture more in detail. However, to utilize the yarn sections in the numerical simulation they must have a continuous solid surface. Hence, [133] proposed the use of convex hull algorithms to construct the yarn surface. Similar methods are also implemented by [134]. A representative of the 3D woven textile model generated based on such an approach is shown in Figure 10. Although the higher accuracy of the geometry can be modeled by DEM, the time cost is also considerable. Due to the requirement of the FE simulation, it takes on average around 9 hours to generate a numerical model with the desired complexity [135].

An analytical approach to model the internal architecture of woven composite was proposed by [115]. This model was built by considering that the geometry of the textile, can be generated by interpolation of a few sections along the two orthonormal planes. The cross-section of the yarns can be continuously varied and the locus of the yarn path can be followed by trigonometric function. This mode is very simple to define and once the interpolation points are obtained the textile geometry can be modeled in TexGen. The comparative study presented by [115] showed that geometry generated by the analytical approach has the closest variation for micro-CT and the highest variation is observed on the model produced by modeling software (TexGen / WiseTex).

Unfortunately, although the predicted elastic properties using the ideal geometry agree well with the experimental results, the ability to study damage and failure mechanisms with the proposed model remains questionable. Because it is still an idealized model based upon the symmetry hypothesis about the middle planes of the Unit Cell (UC) which cannot be found in the real material. Alongside there is no reference to models found in the literature that can

accommodate the inter-yarn voids in the geometry. These drawbacks will be addressed in the realistic models.

Realistic models

These are an alternative to the ideal model to achieve realistic textile geometry with manufacturing defects like voids. These models are usually reconstructed from the micro-CT image. The realistic models can be generated either as 2D or 3D models. The first attempts for the generation of 2D-realistic models to evaluate the damage and crack propagation was presented by Faes et al. [136]. After image processing in a 2D slice, real yarn sections were outlined. The undulated yarn path was modeled by segments while the heterogeneity of local intra-yarn fiber volume fraction (V_{fy}) was determined by mapping the circular detection zone with a specified radius.

A structural tensor-based method was used by Naouar et al. [138] to generate the 3D-model directly from micro-CT data. The segmentation method is applied to each 2D slice to identify the matrix, warp yarns, and weft yarns. A skeleton scheme was applied to determine the locus of the yarn path and this was assigned to the local fiber orientation. Hence this model is called the backbone model. The octahedral mesh was adopted to conserve the yarn shapes. Since the model does not use the local fiber orientation from the μ CT data the results produced were much close to the analytical models.

Similar method based on supervised learning was proposed by Straumit et al. [139]. They preliminarily discretized the 3D domain into several cubic sub-domains (i.e. voxels). They defined a set of variables for each voxel termed as the feature vector. This vector is unique for each voxel and is calculated based on the structure tensor. The voxel can be segmented based on the probability of their feature vector with respect to training sets. For example, for the segmentation 3D textile [101] utilized a structure tensor containing three variables (the principal direction of anisotropy, the degree of anisotropy, and the averaged grey value). This method is simple to implement. However, the actuary of the solution depends on the definition training set for each constituent. This method was also used by Vasiukov et al. [100] to segment the inter-yarn voids in a 3D textile composite.

An example of segmentation result is shown in Figure 11. Where the warp, weft, and matrix phases are separated by imposing (anisotropy, in-plane orientation angle, AGV) as a feature vector.

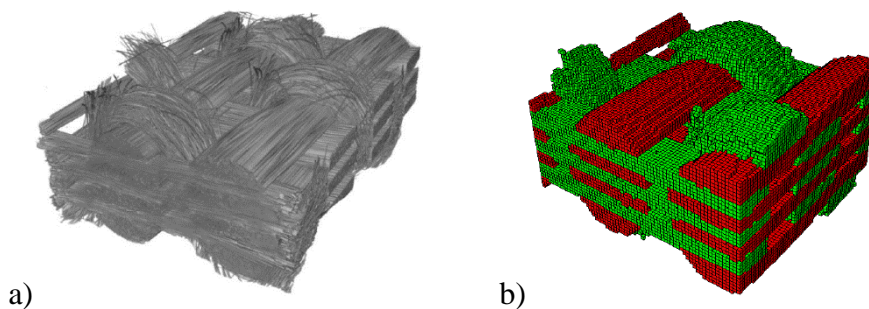


Figure 11: Generation of textile geometry from micro-CT data a) Micro-CT data, b) Voxel model generated by using VoxTex [140].

The yarn paths and cross-sections can also be directly reconstructed from the images acquired from μ CT data as shown in Figure 12. The next challenge is to address the variation in the local fiber volume fraction along with the yarns. One of the first attempts to solve this issue is proposed in [137], where authors presented methods to incorporate a variation of the local fiber volume fraction in the yarns.

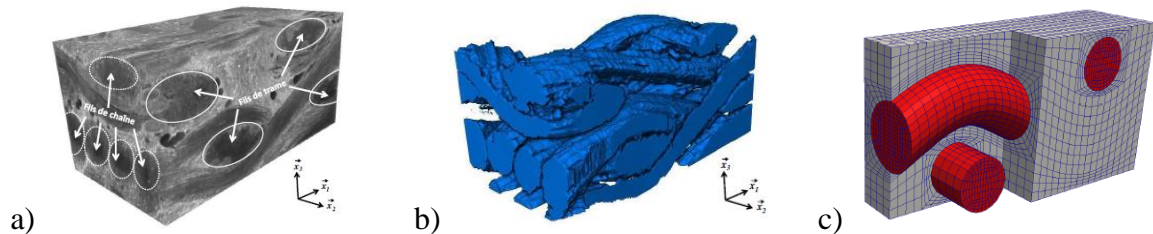


Figure 12: Yarn geometry a) μ CT data of 3D textile composite, b) Segmented yarns, c) Ideal RUC of a 3D textile composite [124].

Local fiber volume fraction (V_f): The distribution of fibers over a yarn cross-section is usually assumed uniform, and the value of V_f is the same in all the points on the cross-section (but may differ according to the cross-section) [141]. Non-uniform distribution may be important for damage analysis [121,142] in this case V_f will vary over the cross-section. The variation of the local fiber volume fraction along the yarns is addressed by modeling the variation of the yarn cross-section. Similar methods were used in [116,143].

Modelling interyarn voids: Currently, no work dealing with meso-voids generation algorithm has been identified. However, a few strategies to model the effect of the void are available in the literature. In the works of Laiarinandrasana et al, [144] the effect of the porosity on mechanical behavior is considered by modification of the constitutive modeling. It is considered that the non-linear behavior such as plasticity of the material is effected in the presence of voids. This kind of approach considers the effect of voids via a complex phenomenological non-linear material model without representing the geometry of void. Another strategy was selected by Shigang et al, [69], where authors modeled voids by reducing the properties of the randomly chosen mesh elements. This approach does not respect their morphology or spatial distribution. Similarly to microvoids, this drawback is overcome by image based modeling where the void can be directly segmented from the matrix [145,146]. The example of segmented voids segmented using μ CT data is presented in Figure 13.

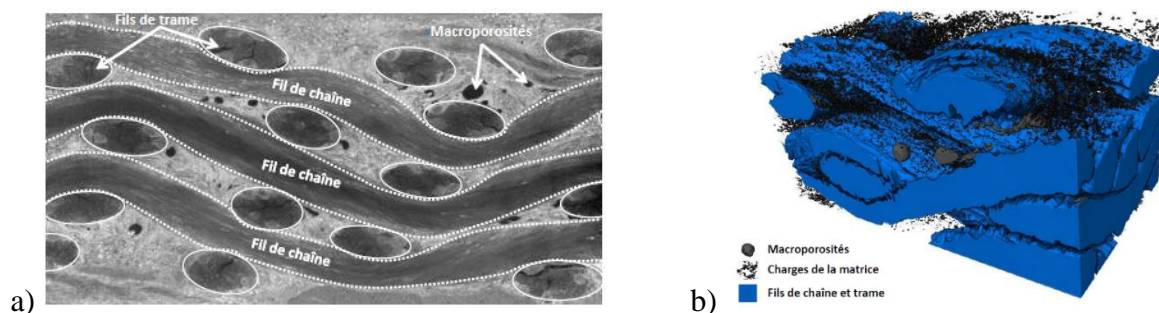


Figure 13: Segmentation of void in a meso-structure a) Image of 3D textile composite, b) Segmented interyarn voids in a 3D textiles composite [124].

Based on the methodology to create these geometrical properties, the modelling approaches can be classified into two types a) ideal models and b) realistic models.

Motivation 2: However, none of the algorithms to produce the ideal models presented in the literature deals with consideration of the inter-yarn voids. Thus, generation techniques for both the models and an argument for a reason to choose realistic models are presented below.

2.6.5 Macroscale

The anisotropic properties of the composite part can be predicted by the numerical homogenization at the meso-scale. However, the non-linear behavior in composites such as damage is a local phenomenon, thus depends on the arrangement of yarns. This phenomenon was well illustrated in the works of Hurmane [147]. In Figure 14 we can observe that the complex, heterogeneous meso-structure of the studied 3D textile composite was approximated by anisotropic non-linear material behavior. The absence of the local yarn geometry and material heterogeneity results in unrealistic crack prediction during the numerical simulation. These simulations showed the importance of considering the local yarn geometry, fiber volume fraction and orientation of the fibers [148]. Hence to address the realistic yarn geometry, voids and fiber orientation we will use the realistic models in our study.

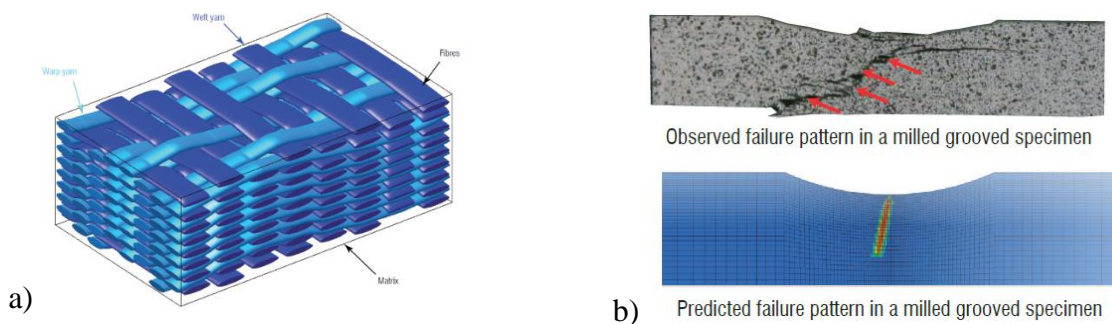


Figure 14: Effect of meso-structure on the non-linear behavior of 3D textile composites [147]: a) Representation of 3D textile, b) Propagation of crack in experiment vs numerical simulation.

2.6.6 Numerical homogenization

It is a process to find an equivalent homogeneous medium that has the same mechanical response for a given heterogeneous microstructure. The standard methodology is to connect macroscopic quantities through the volume averaging of their microscopic counterparts over the RVE [149]. The implementation of the Hill-Mandel macro homogeneity theory was available in several works to calculate the elastic properties. Hence, the formulation is included in Annexe (see section 7.1).

Meshing

Meshing corresponds to the discretization of the material geometry, described by geometrical features (yarns/matrix/voids) into subdomains called finite elements. For an FE-mesh free from topological errors and defects, the FE-solution should be independent of the mesh. To name some, elongated elements, interpenetrated volumes, and high density mesh in a certain location are major defect types noticed in the meshing. The presence of such errors will result in the

local mesh distortion which will affect the FE-solution. Usually, the FE-packages like ABAQUS produces the conformal mesh to conserve the geometry of the structure and are mostly used in FE-simulations.

For FE-simulations at the microscale, the geometry is well defined and this facilitates having a uniform mesh. On the other hand, at meso-scale the complex topology of the yarns results in local over-density of the mesh and this results in heavily distorted elements during a simulation [150]. These challenges lead to the development of an alternative called voxel mesh [151]. Voxel meshing has been used in a biomedical application for simulations on trabecular bones reconstructed from μ CT data [152]. Applying a similar method to the micro-CT data of textile composite will help to develop a voxel model avoiding yarn interpenetration and other difficulties. This can be achieved by using VoxTex an image segmentation tool developed by Straumit et al. [139]. A voxel mesh is an even rectangular discretization of space into perfect hexahedral elements. This allows us to model the yarn as explicit non-interpenetrating surfaces. A finer mesh can be achieved by increasing the spatial resolution. Due to this simplicity, it is used in the FE-simulations of the textile composites [140]. However, due to the simple geometry of the mesh, it produces non-physical stress concentrations at the edge of the yarn geometries, as reported by Doitrand et al. [153]. At the same time, averaging techniques were proposed by Fanget al. [154] to smooth the stress concentrations caused by the voxel element, such that extending the application to predict the elastic properties and non-linear behavior of the composites.

Boundary conditions

Boundary conditions (BC's) are a set of constraints applied to the boundary of the domain. They have a decisive effect on the behavior and convergence of the solution. In the literature, there are three kinds of boundary conditions utilized to homogenize the properties of the composite at micro-scale and meso-scale. The BC's can be listed as 1) uniform displacement boundary conditions (KUBC's), uniform traction boundary conditions (SUBC's), periodic boundary conditions (PBC's), and mixed boundary conditions [155].

BCs have a direct effect on the prediction of mechanical properties, and the comparison of different boundary conditions on effective properties was found in the literature [156,157] reported that KUBC's overestimate the elastic properties and SUBC's underestimate. However, a study conducted by [158] showed that for a sufficiently large domain size the effect of BC's can be removed. They found for an RVE of length ($L=50R$) 50 times of fiber radius (R_f) the effect of BC's is no more be observed. On another hand, PBC's and mixed boundary conditions have convergence to the solution at small domain sizes which makes them an optimal choice for numerical homogenization. The deformation field of boundary conditions is schematically represented in Figure 15. In a numerical solution, the macroscopic stress $\bar{\sigma}_{ij}$ (see Equation 2.7) and strain $\bar{\epsilon}_{ij}$ (see Equation 2.8) for volume V can be expressed as the average over microscopic stress σ_{ij} and strain ϵ_{ij} on volume dV .

$$\bar{\sigma}_{ij} = \frac{1}{V} \int_V \sigma_{ij} dV \quad (2.7)$$

$$\bar{\epsilon}_{ij} = \frac{1}{V} \int_V \epsilon_{ij} dV \quad (2.8)$$

KUBC's can be imposed as a Dirichlet boundary condition ($u_i = \bar{\epsilon}_{ij}X_j$) applied directly on the boundary of the volume V . SUBC's can be imposed as the Neumann boundary condition $t_i = \bar{\sigma}_{ij}n_j$, where t_i is the applied traction and n_j is the normal representing surface on which traction is applied. PBC's can be applied to the structures with the in-plane periodicity like 2D woven composites with a small thickness. In computational homogenization, PBC can often be termed as micro fluctuation in opposite faces [159]. Let $\bar{\epsilon}_{ij}$ represents the average strain in the volume of RVE, u_i^+ and u_i^- represents the displacement field on the opposite faces of the RVE, such that

$$u_i^+ = \bar{\epsilon}_{ij}X_j^+ + \tilde{u}_i \quad (2.9)$$

$$u_i^- = \bar{\epsilon}_{ij}X_j^- + \tilde{u}_i \quad (2.10)$$

Subtracting Equation 2.9 from Equation 2.10 gives the micro fluctuation of the displacement field on the opposite faces (see Equation 2.11).

$$u_i^+ - u_i^- = \bar{\epsilon}_{ij}(X_j^+ - X_j^-) \quad (2.11)$$

Boundary Conditions	Remark
KUBC's	In structures with one-dimensional periodicity RUC (In-plane strain).
SUBC's	Can be used in along with other boundary condition.
PBC's	Periodic structures.
MBC's	Good choice for the laminates with several layers.

Table 5: Remarks on boundary conditions.

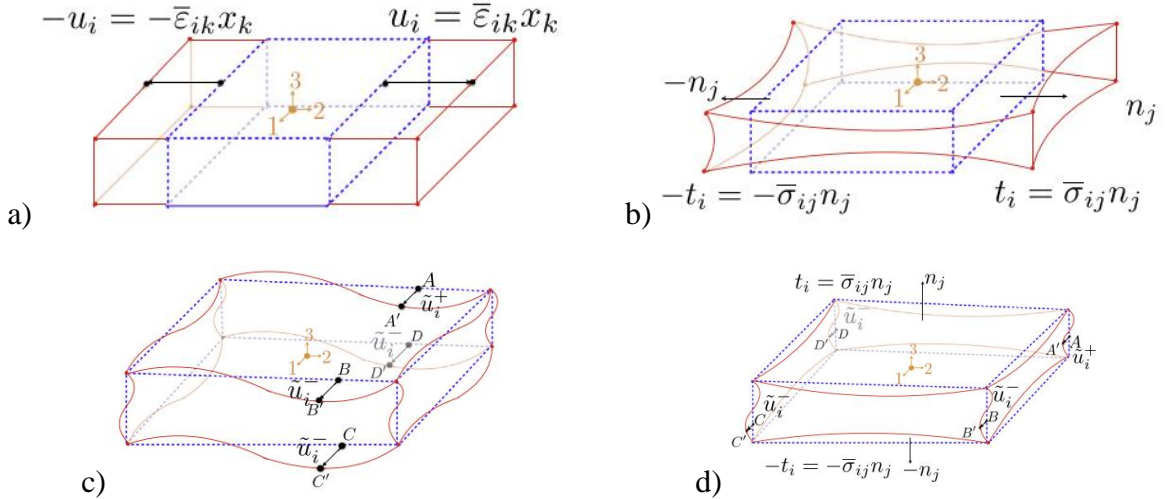


Figure 15. Boundary conditions in computational homogenization a) Uniform Displacement boundary condition, b) Uniform Traction boundary condition c) periodic boundary condition and d) mixed boundary condition [155].

MBC's are used for the problems where the out-of-plane traction can be zero i.e. different mixture of in-plane and out-of-plane boundary conditions possible in the problem as presented in Figure 15 d). At first, the in-plane PBC is solved considering the out-of-plane traction condition as zero. Secondly, the out-of-plane stress can be calculated considering the in-plane displacements.

Application of PBC's needs a periodic geometry of RVE. However [160] compared periodic and non-periodic structures and concluded that PBC can be applied to non-periodic structures. This type of boundary condition is called approximate periodic boundary conditions (APBC's). APBC are equally effective as complete periodic boundary conditions. This saves the extra effort to generate the exact periodic structure for the numerical homogenization. Moreover, the application of APBC solves an important issue of reconstructed geometries from μ CT data which are generally not strictly periodic.

Motivation 3: Hence in this work, we use the APBC's both at the microscale and mesoscale homogenization. Since commercial software like ABAQUS does not facilitate an inbuilt tool for APBC's, an automated python script was developed to apply the PBC's on any given box-shaped structures.

2.7 Conclusions

In this chapter, we introduced state-of-the-art manufacturing induced void type defects in composites and the mechanism of their formation in RTM, and void characterization techniques. The formation of voids is an unavoidable phenomenon and was extensively studied in the literature. From the understanding of the modified capillary number, we proposed a manufacturing technique that is explained in detail in Section 3.2 to obtain a part dual scale void distribution.

It was observed that void content is not always an effect parameter to determine the effect of void on mechanical properties. A detailed literature survey about the effect of voids on the elastic properties and interlaminar shear strength was presented. It was observed that the void characteristics such as volume, aspect ratio, and distribution affect the elastic properties of UD composites, yarns, and textile composites. Hence, in this thesis, we present the correlation of the elastic properties with the total void volume fraction and intra-yarn void volume fraction. The burn-off test will be used to characterize the total void content in the composite part and microscopy will be performed on the intra-yarn void cross-section to determine the void size, aspect ratio, and distributions. Moreover, we propose two parametric studies to understand the influence of the void characteristics on the elastic properties of 1) yarns at the micro-scale and 2) textile composite at the meso-scale.

Since numerical homogenization facilitates representing the real geometry of composites, it is a better approach for the homogenization of composites. The multi-scale numerical approach is proved as a better homogenization technique in the literature to predict the elastic properties of the textile composites. This approach needs the description of the yarn geometry (microscale) and composite geometry (mesoscale). Since constituent characteristics in the yarn have a decisive effect on their behavior, they should be respected while generating the microstructure. For, example interlaminar properties are highly affected by void size,

transverse tensile properties are affected by void aspect ratio. Void spatial distribution was seldom studied in the literature.

Moreover, most of these studies were limited to UD composites and do not consider realistic void shapes or distribution. Moreover, there are no efforts found to enforce the statistical parameters of the fiber and voids to generate the microstructure. Hence in this study, we propose a novel algorithm to generate a statistically equivalent RVE for yarns. To conduct a parametric study at meso-scale we present a new approach to generate voids at meso-scale in a meso-structure reconstructed from μ CT data. At the microscale, the geometry is generated as a solid structure containing fibers and voids. Hence a conformal mesh, produced by ABAQUS will be adopted. For mesoscale FE-simulation a voxel model can be constructed from μ CT data and boundary conditions are applied under the framework of approximate periodic boundary conditions.

3D textile composites were chosen to show the applicability of multi-scale numerical simulation presented in this thesis to predict the elastic properties of the textile composites (this method can be equally applied to any textile composites).

3 Materials, Manufacturing, and Characterization

3.1 Introduction

In this chapter, we present the materials, the manufacturing method of composites plates, and their characterization. Materials and manufacturing process are explained in Section 3.2, followed by the characterization of the total fiber volume fraction (V_{FT}), total void volume fraction (V_{VT}), and intra-yarn fiber fraction (V_{fy}), intra-yarn void volume fraction (V_{vy}) in Section 3.3. X-ray micro tomography was performed on several composite specimens to reconstruct the internal architecture of the 3D textile composites at the mesoscale (yarn level). The parameters of scanning and reconstruction of radiographs are presented in Section 3.4. Finally, the experimental setup to evaluate the tensile properties along the direction of the weft yarns is presented in Section 3.5. The observation and correlations of the material behavior with respect to the void characteristics are presented in Section 3.7.

3.2 Materials and manufacturing method

3.2.1 Materials

The 3D textile reinforcements used in this study are modified layer to layer satin and twill interlocks. These textiles were manufactured at ENSAIT (Roubaix, France). The architecture of three 3D layer to layer interlock (Satin, Twill, 2nd Twill) textiles generated in TexGen are presented in Figure 16.

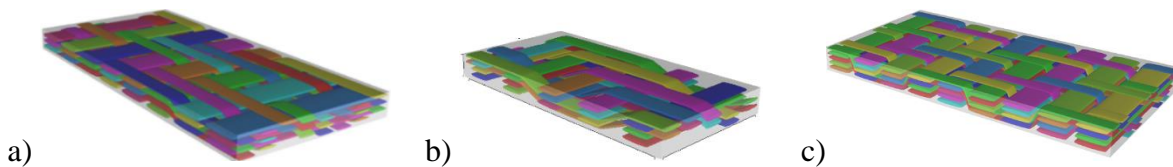


Figure 16: The architecture of 3D textiles a) Satin b) Twill and c) 2nd Twill.

The yarns of each textile are spun from E-glass fibers with a density $\rho_f = 2.61 \text{ g/cm}^3$, Young's modulus $E = 72 \text{ GPa}$ and Poisson's ratio $\nu = 0.22$. Textiles were impregnated with a thermoset epoxy matrix. The resin was prepared by mixing the 100 grams of epoxy (prime 27) with 28 grams of hardener (prime 20). This mixture results in the cured epoxy with a density $\rho_m = 1.11 \text{ g/cm}^3$, Young's modulus $E = 3.3 \text{ GPa}$, and Poisson's ratio $\nu = 0.375$.

3.2.2 Manufacturing method

Resin transfer molding was used to produce composite plates with dimensions of 190 mm x 290 mm x 2.3 mm. A fabric with dimensions of 190 mm x 290 mm was cut from the textile with a layer thickness of 2.4 mm. It will be placed in a prepared mold and a gap greater than two centimeters was left in the injection edge to ensure the rectilinear flow. The press applied the pressure of 20 bar to the mold, compressing the fabric with the accuracy of 0.1 mm in terms of mold cavity height. By following this process we could ensure that there would be no race tracking inside the mold. Later, epoxy was prepared in a beaker by mixing resin and hardener in proportions of 100:28 and stirring until the mixture was homogeneous, then it was degassed

for 20 minutes. The resin mixture was injected into the preform under constant pressure. The mold design used in the RTM process is presented in Figure 17. The injection pressure applied for manufacturing and time took to fill the mold of each plate are presented in Table 6.

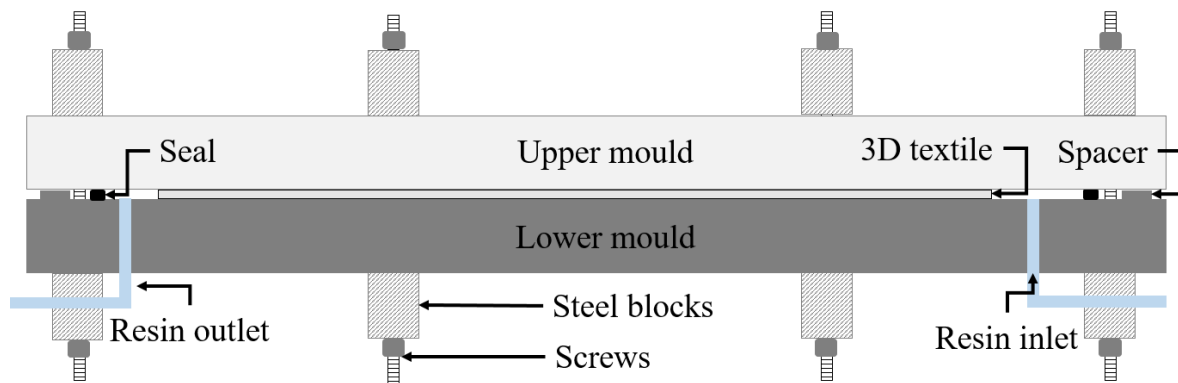


Figure 17: Mold design for the RTM process.

Textile	Satin	Twill	2 nd Twill -P1	2 nd Twill -P2	2 nd Twill -P3
Injection pressure (bar)	2.0	1.5	0.5	1.0	1.5
Number of plates	1	3	3	3	3
Fill time (s)	64	220 ± 40	380 ± 34	280 ± 23	198 ± 36

Table 6: Parameters for the RTM manufacturing process.

Both the resin inlet and outlet vents were closed as soon as the resin once appeared near the outlet. This ensured no resin flow in the mold after the mold filling. As specified in the technical data sheet from the supplier, the resin was left to cure at room temperature for 17 hours. This setup would ensure a straight linear flow front during the mold filling. Therefore the advancing flow front does not have any effect on the void formation in the transverse direction of the flow front advancement. Hence, it was assumed that the void volume fraction have negligible variation along the transverse direction. Hence, the specimens were extracted along the same direction which was also along with the weft yarns in the textile architecture. The layout of specimen extraction for manufactured composite plates is presented in the following section.

3.2.3 Specimen extraction

The scheme of specimen extraction for Twill and Satin is illustrated in Figure 18. Y-axis represents the direction of resin flow during injection and alignment of the warp yarns, while the weft yarns are aligned along the X-axis. The entire composite plate is divided into two zones: starting from the injection edge to the middle of the plate is called upstream and from the middle to the edge of the injection is called downstream (see Figure 18).

The variation of total void volume fraction (V_{VT}), which is the sum of the void volume fraction inside and outside the yarns in a specific position, was obtained by conducting a burn-off test [161] at 9 different locations on the plate. Burn-off specimen is indicated by B {1, 2, 3} {L, R, M}. {1, 2, 3} denotes the position of the specimen along the direction of the resin flow (Y-Axis) and {L, R, M} (Left, Middle and Right) represents the position of the specimen in the X-axis. At a given point, for an ideal situation, the resin velocity is the same along X-axis (uniform flow) such that it has a negligible variation in the void volume fraction along the X-

axis. On the other hand, the void content may increase along the Y-axis from B1-B3 due to the phenomenon of void migration along with the resin flow (upstream to downstream) [11].

To understand the effect of void volume fraction on the tensile properties of textile composites, six tensile specimens (T1 to T6) were extracted along the direction of the resin flow for each composite plate. The variation of void volume fraction and the void characteristics were measured by both burn-off tests and microscopy.

Burn-off tests can only provide the global trend of the void volume and fiber volume fractions. However, in a textile composite, the total void volume fraction can be split into intra-yarn voids and inter-yarn voids. Imaging techniques were used to obtain the complete information of the local constituents' (i.e. fiber, matrix, and void) characteristics and their volume fractions at the micro and meso scales. Microscopic observations were performed on the warp (blue in layout) and weft (red in layout) yarns to evaluate the constituents' characteristics in each yarn. X-ray μ CT was performed on the specimens at the upstream and the downstream (colored orange in Figure 18). This data was used to reconstruct the internal geometry at the mesoscale (yarn profiles and inter-yarn voids). The characterization of the fiber and void volume fractions at different scales is presented in the subsequent sections.

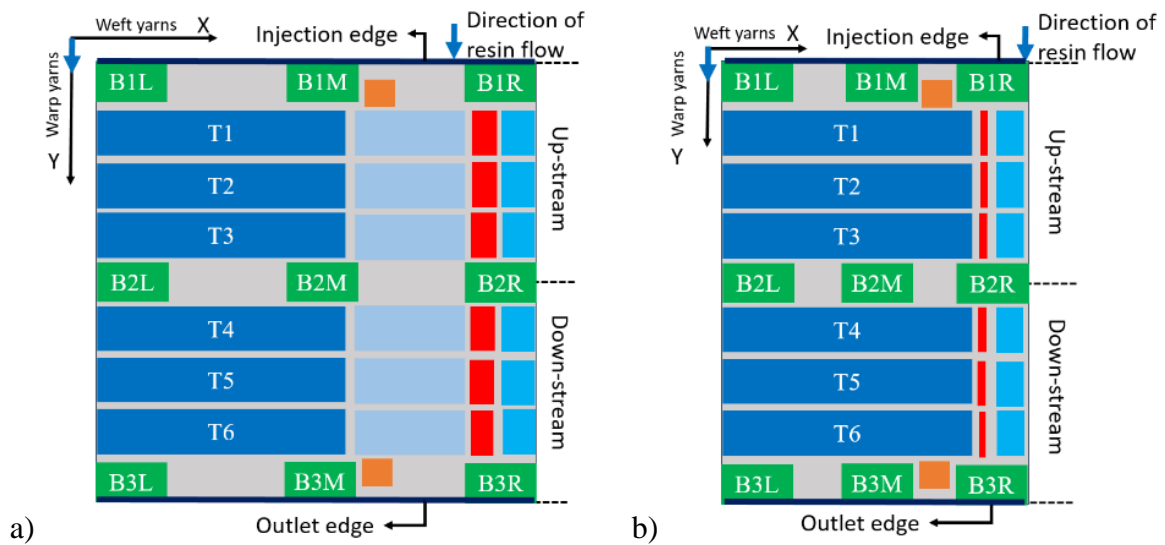


Figure 18. Specimen extraction criterion for a) Satin 3D and b) Twill 3D.

3.3 Characterization of volume fractions for each constituent

The constituents of composites correspond to fiber, matrix, and voids. Since composites are a multiscale material, each constituent volume fraction can be sub-classified depending on the scale of the material. At the macro-scale, we can consider total fiber area fraction (V_{FT}) and total void volume fraction (V_{VT}). At the micro-scale in the yarns, we can take into account intra-yarn fiber area fraction (V_{fy}) and intra-yarn void area fraction (V_{vy}). In this section, we present a methodology to obtain the constituent volume fractions at the macro-scale and the micro-scale.

3.3.1 Characterization of total fiber volume fraction and total void volume fraction

The total volume fractions of void and fiber in the composite plate were measured by conducting burn-off tests. The measurement process is presented in the Annexe (see Section 7.2). The results of V_{VT} for the plates manufactured with different injection pressure are presented in Figure 19. The total void volume fraction is observed to increase from the edge of injection to the vent, this kind of behavior was also observed in the literature [8]. The fiber volume fraction has a negligible variation from the upstream to the downstream. The results for fiber volume fraction of all three different composite plates are presented in Table 7.

The composite part with 3D satin reinforcement manufactured with 1.0 bar injection pressure exhibits an increase of 30% in total void volume fraction from the upstream to the downstream, whereas the 3D twill reinforced composite has an increase of 35%. In the case of 2nd-twill reinforced composites manufactured by 0.5 bar injection pressure, V_{VT} varied only by 0.3%. Hence, it is conclusive to consider it homogeneous in terms of total void volume fraction from the upstream to the downstream. However, for the injection pressure of 1.0 bar, V_{VT} increased by 20%, and for the injection pressure of 1.5 bar, the variation was further increased to 23%. Hence, we can state that the total void volume fraction in a composite part manufactured by RTM depends on the injection pressure and also the type of reinforcement.

Reinforcement, injection pressure		V_{TF}		Dimensions in mm
		Up-stream	Down-stream	
Satin, 2.0 bar		0.34 ± 0.021	0.35 ± 0.011	$270 \times 270 \times 2.4 \pm 0.2$
Twill, 1.0 bar		0.35 ± 0.015	0.36 ± 0.01	$270 \times 270 \times 2.4 \pm 0.2$
2 nd Twill	0.5 bar	0.42 ± 0.012	0.42 ± 0.007	$190 \times 270 \times 2.2 \pm 0.09$
	1.0 bar	0.42 ± 0.019	0.42 ± 0.009	$190 \times 270 \times 2.2 \pm 0.08$
	1.5 bar	0.42 ± 0.009	0.42 ± 0.007	$190 \times 270 \times 2.2 \pm 0.06$

Table 7: Total fiber volume fraction in composites plates used in this study.

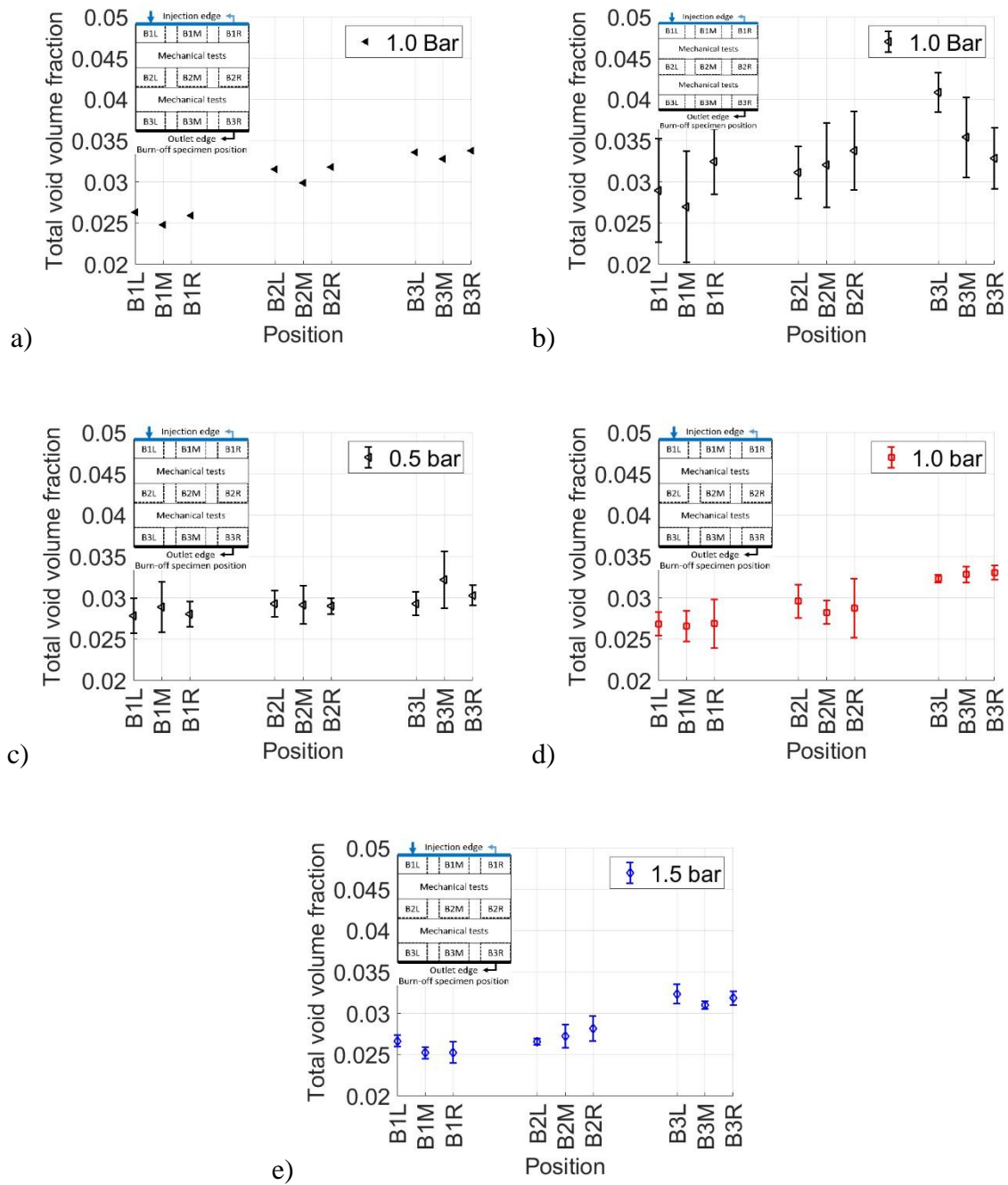


Figure 19: Void volume fraction measured by burn-off test on specimens manufactured at different injection pressures a) Satin layer to layer b) Twill layer to layer and c-e) 2nd Twill layer to layer interlock manufactured by injection pressure of 0.5, 1.0, and 1.5 bar respectively.

3.3.2 Characterization of yarn constituents

Now at the microscale, intra-yarn fiber volume fraction, and intra-yarn void fraction are characterized by image processing of SEM observations on the local slices. Intra-yarn fiber volume fraction (V_{ff}) and intra-yarn void volume fraction (V_{vy}) are crucial in determining the behavior of the yarn, as well as the statistical parameters such as fiber radius distribution and

inter-fiber distance (explained in detail in Section 0). As mentioned in Section 2.5.2, the void parameters such as shape, size, and spatial distribution also play a decisive role to determine the properties of the yarn. These parameters can be measured either by μ CT or microscopy. μ CT may help to capture the complete 3D information of the yarn, while its image acquisition is costly and it has limits for higher resolution. Moreover, its reconstruction at the yarn-level is computationally expensive. On the other hand, microscopy helps to reach a higher resolution at a relatively low cost and requires no reconstruction for the analysis whereas it provides the 2D information of yarn geometry. In this study, we use a scanning electron microscopy (SEM) technique to acquire the 2D micrographs of the yarn cross-section.

Image acquisition

The intra-yarn fiber and intra-yarn void volume fraction were obtained from the images acquired by SEM using JOEL (NEO-SPACE). The probe power was set to 10Kv and images were acquired at 100 \times magnification at a resolution of 0.96 μ /pixel. Figure 20 shows the cross-section composite specimen containing warp yarns, weft yarns, inter-yarn voids and intra-yarn voids.

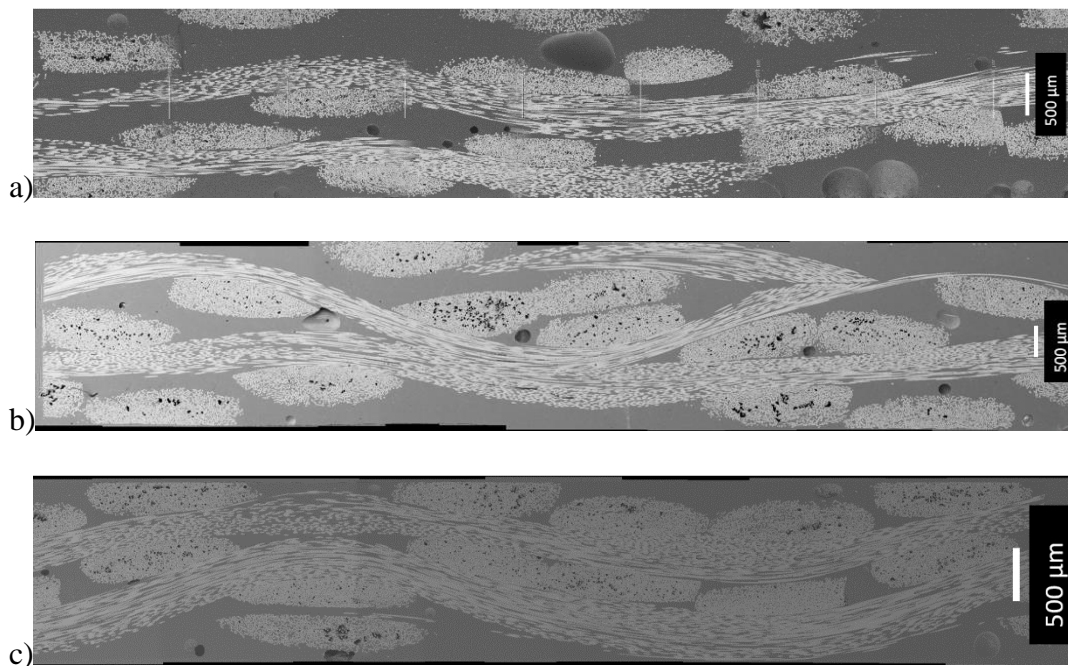


Figure 20: SEM observation for all three different architectures studied in this work a) Satin, b) Twill and c) 2nd Twill.

In the subsequent sections, we provide the methods to detect the fiber centers and the fiber radius directly from an SEM image. Once fiber position and radius are identified, a statistical descriptor called inter-fiber distance is measured to analyze the spatial distribution of the fibers. Utilizing a threshold-based segmentation, the micrographs from upstream and downstream in warp and weft directions are analyzed to obtain the statistical data on intra-yarn void area fraction, size, shape, and spatial distribution.

Algorithm for the detection of the fiber centers and radius

The most famous method to identify the fiber centers and measure fiber radius is the Hough Circle Transform (HCT) which is usually performed by the plugin provided in image processing tools like FIJI [162,163]. However, the HCT might be time-consuming (large images) and also requires noise-free high-resolution images for the detection of the fiber centers and radius. Thus, in this work, we developed an algorithm in MATLAB to map the fiber centers and measure the fiber radius based on the Voronoi tessellation.

To adapt micrographs for the post-processing, the image was treated with a low pass filter to remove isolated pixel noise and increase the contrast between the fiber and the matrix. Then the binarization of the image was carried out by considering all the pixels having a gray value higher than 135 as the fibers and the remaining pixels were identified as the matrix [26]. Then, a watershed algorithm was performed on the images to remove any fiber interconnectivity and a Euclidean space transform was applied to the image result in the intensity map of the fiber centers. Finally, the obtained image was overlapped with the original image to identify the high-intensity zones which were the fiber centers as shown in Figure 21 d). A Voronoi tessellation was performed on this fiber centers and the fiber radius (R_f) was defined as the least distance (L_i) from the fiber center to the Voronoi cell wall as shown in Figure 22 ($R_f = \min\{L_i\}$).

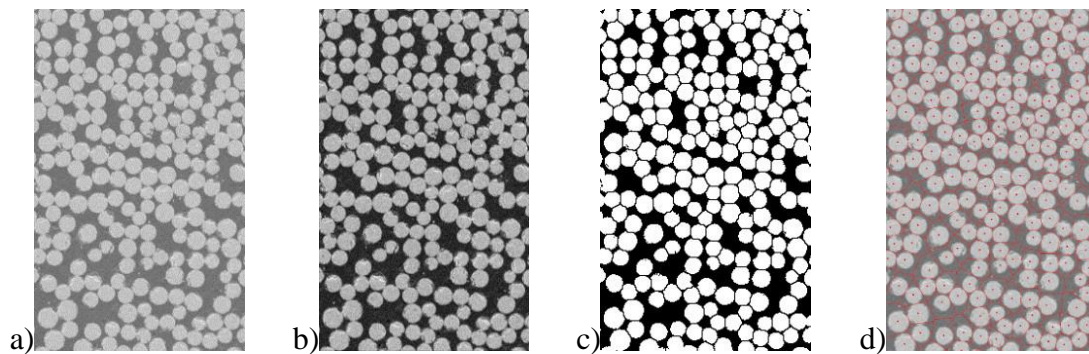


Figure 21: Algorithm to identify the fiber centers demonstrated on a single micrograph: a) SEM image with resolution 0.96 μm , b) Result of low pass FFT filter, c) Watershed to remove the fiber interconnectivity, and d) Evaluated fiber centers and Voronoi tessellation.

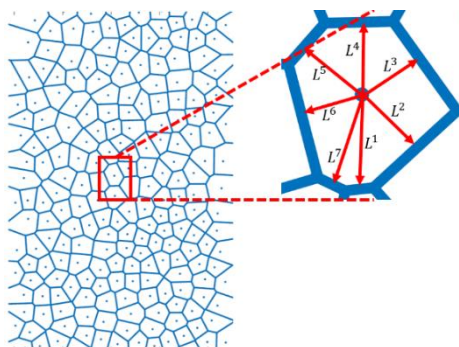


Figure 22: Calculation of the fiber radius based on the Voronoi tessellation.

The fiber radius can also be measured by using a “particle analysis” plugin in FIJI. This plugin was developed by ILLINOIS Carl R. Woese Institute for Genomic Biology to analyze the particle shape, radius in the image [164,165]. The comparison among the HCT, particle analysis and the algorithm developed in this work is presented in Figure 23. The mean fiber radius measured using the algorithm differed by 0.5% when compared to the HTC and 2.4% to particle analysis in FIJI. To further extend the validation, the algorithm was also tested on the microstructure presented in the work of [162] where they use the HCT to detect the fiber center, and the results are presented in Figure 23 d), e). The results differ by a negligible margin of 0.1%. HCT predicted a few cases of fiber overlap (Figure 23 a)) which is physically impossible. Even though particle analysis has no fiber overlaps, since this method requires manual operation, it is not ideal for large data sets. Hence, in this work, we will use the algorithm proposed in Section 0. The fiber radius has a normal distribution measured over 749 fibers as presented in Figure 25, which has a mean value of 7.9 microns and a standard deviation of 0.85 μm . It is important to notice that, the calculation of fiber radius based on Voronoi tessellation performs better for densely packed fibers with a low variation of the fiber radius.

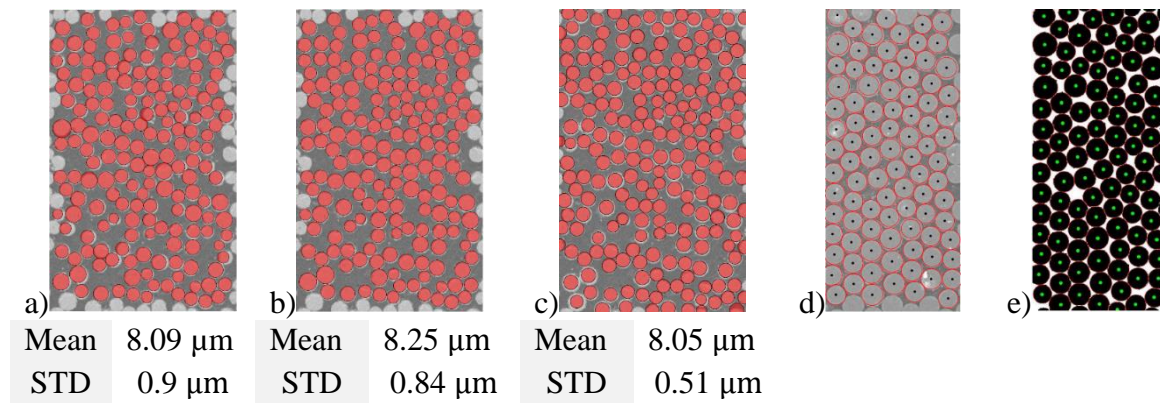


Figure 23: Comparisons of fiber detection by a) Hough circle transform, b) Particle analysis and c) Algorithm proposed in this work, d) Present algorithm, and e) HCT presented in [162].

Once the fiber centers and radii were measured, the next step is to evaluate the fiber spatial distribution. For this, one needs to determine the inter-fiber distance which is based on the nearest neighbor distance. This procedure will be explained in the following section.

Nearest neighbor distance

Nearest neighbor distance is a spatial descriptor to study the distribution of the distance between the particles and it is given by the 1st, 2nd, and 3rd nearest neighbor. The detailed analysis of these parameters can be helpful for the detection of clusters of fibers in a given domain. For any given fiber (F_i), the closest of all the fibers is called the 1st nearest neighbor. Similarly, 2nd and 3rd neighbors correspond to the second and the third closest fibers respectively. To find the closest fibers, inter-fiber distance (IFD) between the fibers is calculated. IFD can be defined as the distance between the circumferences through the shortest distance for any pair of fibers and is calculated based on the schematic presented in Figure 24. If R is the radius of the current fiber, x_c and y_c represents the fiber center coordinates and R_i is the radius of the n^{th} fiber. Then the IFD of the fiber with respect to remaining fibers is given by $\text{IFD} = D - (R + R_i)$ where D is the nearest distance between the fiber pair.

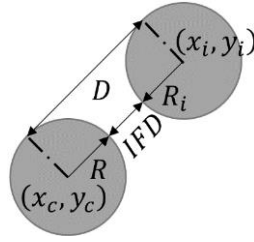


Figure 24: Formulation to calculate the inter-fiber distance (IFD) between two fibers.

An average of five micrographs collected from five yarns combined to have 749 fibers were used in this study. From statistical data, it was found that the 1st inter-fiber distance was equal to zero and most of the fibers were in contact with the neighbor fibers. The zero 2nd inter-fiber distance and 3rd inter-fiber distance were usually observed in the areas of high packing fraction. The distribution of the IFD is presented in Figure 26.

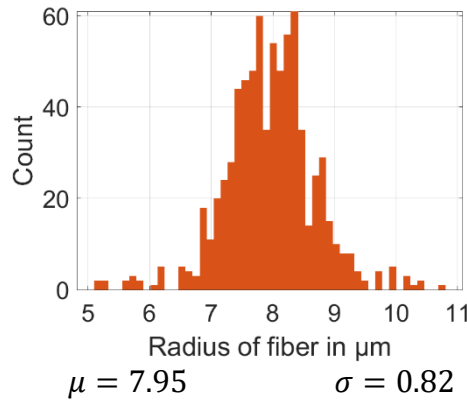


Figure 25: Fiber radius distribution.

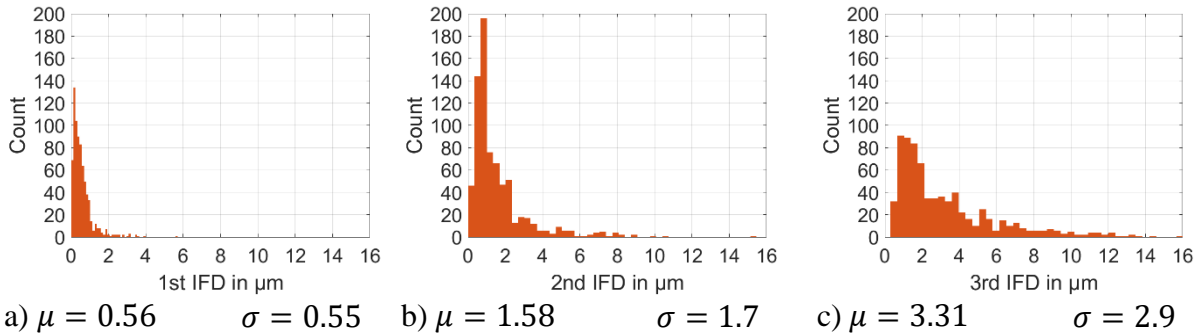


Figure 26: Distribution of the inter-fiber distances a) 1st b) 2nd and c) 3rd nearest neighbor.

As the statistical descriptors of the fiber radius and distribution are identified, the next step is to calculate the intra-yarn fiber volume fraction and intra-yarn void volume fraction.

Intra-yarn fiber and void volume fractions

In the literature, there are different methods to calculate the intra-yarn constituent fractions [115,166], such as the Fiber Count Method (FCM), the Pixel Counting Method (PCM), and Voronoi Cell Method(VCM). In this work, we proposed to improve the present VCM and this will help to determine the local fiber and void volume fractions and also to provide the information about the yarn geometry.

Fiber Count Method [166] (FCM) is an approximate method for the calculation of the intra-yarn fiber volume fraction (V_{fy}). If r_{fmean} represents the statistical mean fiber radius measured for a given yarn and N represents the number of complete fibers (fibers on the edges with circularity smaller than 1 are neglected) in an image with an area A_{image} , then the fiber volume fraction can be calculated by Equation 3.1.

$$V_{fy} = \frac{N\pi r_{fmean}^2}{A_{image}} \quad (3.1)$$

It is the fiber area fraction in the yarn cross-section. Assuming that all the fibers are unidirectional in the yarn, we can regard the fiber area fraction as the fiber volume fraction.

The Pixel Counting Method (PCM) is straightforward when compared to the FCM. It can be directly applied to the SEM image, and effectively used to measure the V_{vy} . The main idea is to perform segmentation to provide a binary image of fiber and matrix. For example, in Figure 27 c), the histogram-based segmentation by the Otsu method [167] was employed for identifying the fiber (see Figure 27 c)) and the matrix. All pixels corresponding to the matrix to be measured were assigned the value 0.0 and the remaining pixels were assigned 1.0. Then, the fiber volume fraction and void volume fraction could be identified as the ratio of the number of pixels with the corresponding value to the total number of pixels in the image as given in Equation 3.2. However, the measurements were highly affected by the noise in the images. Post-processing of an image with some special filter can reduce the noise but will affect the accuracy of calculation.

$$V_{fy} = \frac{\text{Number of fiber pixels}}{\text{Total number of pixels in an image}} \quad (3.2)$$

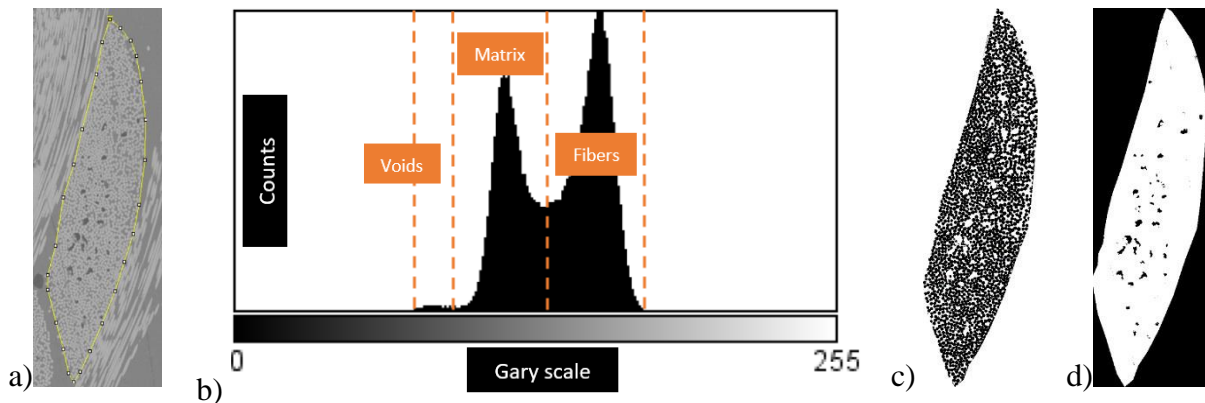


Figure 27: Histogram of the ROI from yarn to show the threshold for fiber, voids a) Cross-section of yarn from SEM image, b) Histogram of the yarn, c) Segmentation of fiber and d) Segmentation of the voids.

Voronoi Cell Method [168] (VCM) is a tessellation based method which was proposed recently. The whole ROI was discretized into Voronoi cells containing only one fiber. The open Voronoi cells on the boundary of the ROI were removed from the calculation to avoid the ambiguity in the calculation of the fiber volume fraction. The overall V_{fy} could then be estimated as the ratio of the total area occupied by the circles to the total area of the Voronoi cells in which fibers were identified. The equation for calculation of V_{fy} as follows:

$$V_{fy} = \frac{\sum_{i=1}^N \pi r_{if}^2}{\sum_{i=1}^N A_{iVP}} \quad (3.3)$$

Where A_{iVP} is the area of the Voronoi polygon, r_{if} (see Figure 28) represents the radius of the fiber in corresponding Voronoi polygon and N represents the total number of fibers.

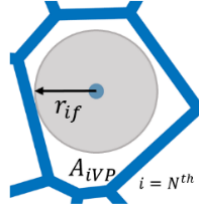


Figure 28: Identifying the fiber radius based on the VCM.

Since this method is built over the pre-identified centers and fiber radius, there is no effect of the isolated pixels which is unavoidable in the images. Hence this method is more robust than PCM and FCM. However, this method needs the pre-processing for the particle identification which needs high-quality microscopy images. Based on several resolutions used in this study, a magnification greater than 70 times should be sufficient to identify the fibers. Intra-yarn fiber volume fractions in warp and weft yarns are calculated by VCM for all the composites utilized in this study are presented in Table 8.

Reinforcement, injection pressure	Warp (V_{fy})		Weft (V_{fy})	
	Upstream	Downstream	Upstream	Downstream
Satin, 2.0 bar	0.60 ± 0.022	0.59 ± 0.05	0.60 ± 0.031	0.61 ± 0.029
Twill, 1.5 bar	0.61 ± 0.041	0.63 ± 0.03	0.60 ± 0.052	0.61 ± 0.03
2 nd Twill, 1.5 bar	0.62 ± 0.052	0.60 ± 0.044	0.62 ± 0.05	0.60 ± 0.036

Table 8: Distribution of intra-yarn fiber volume in upstream and downstream for 3 different architectures.

The methods like VCM, PCM and FCM allows to calculate the fiber volume fraction in a region of interest (ROI) in the yarn. However, they cannot provide the information on the packing density around each fiber (i.e. how closely fibers are packed). One of the example is shown in Figure 29 where both the microstructures a) and b) have the same fiber volume fraction but different **local fiber packing** (F_{LFP}). This is an important property and should be analyzed, especially in presence of defects. Thus, in this thesis, we provide the extension of the VCM method to calculate **local fiber packing** (F_{LFP}).

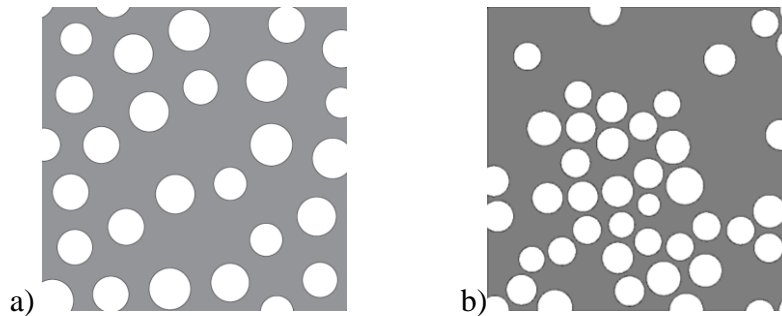


Figure 29: Microstructure with the same fiber volume fraction (0.3) but different local packing around fibers a) Homogeneously distributed fiber and b) Clustered fibers.

The proposed algorithm is based on Delaunay Triangulation to construct a discretized spatial domain where vertices of each triangle are connected to the neighboring fiber centers (see Figure 30 a)). Subsequently, the **local fiber packing** (F_{LFP}^i) around the i^{th} fiber is calculated as the weighted average packing of all the Delaunay triangles connected to the i^{th} fiber. The fiber volume fraction in each triangle is called **local fiber density** (T_{LFD}^i). The total area of each triangle can be the sum of the area occupied by the fibers and the area by the matrix. If the area of the triangle T^i is T_A^i and S_A^i is the area in a triangle occupied by fibers then $T_{LFD}^i = (\sum_{i=1}^n S_A^i) / T_A^i$. Similarly, the **local fiber volume** fraction at each fiber can be calculated by analyzing the T_{LFD}^i of all the triangles that share the common node. In Figure 30 d), triangles from 1 to 8, share a common node at the fiber (in blue) F^1 forming clusters represented in black lines. Then LFP of the fiber F^1 is calculated by $F_{LFP}^i = \sum_{i=1}^n \frac{T_A^i}{\sum_{i=1}^n T_A^i} T_{LFD}^i$.

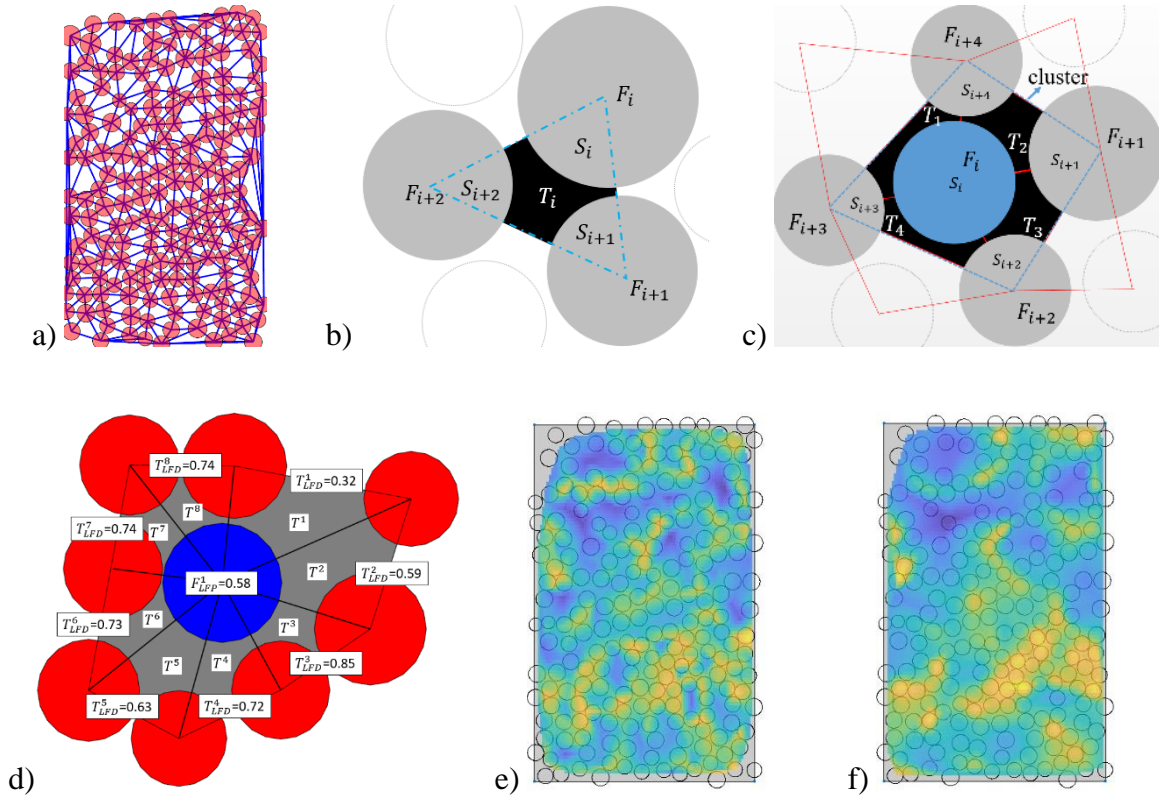


Figure 30: Calculation of the local fiber packing and local fiber density at each fiber center a) Delaunay triangulation, b) Illustration to calculate local fiber density T_{LFD}^i , c) Illustration to calculate local fiber packing F_{LFP}^i , d) Example of the T_{LFD}^i , F_{LFP}^i e) Distribution of T_{LFD}^i f) Distribution of F_{LFP}^i .

The improved VCM was applied to calculate the local fiber packing (F_{LFP}^i) and also local void volume fraction in yarns. The yarn profile can be outlined as the convex polygon passing through the centers of the outline fibers (fibers on the edges of the yarn). Results from modified VCM to the entire yarn is presented in Figure 31. Figure 31 a) represents a warp yarn cross-section of the 3D twill layer to layer interlock, b) shows the variation of the local fiber packing (F_{LFP}^i) and c) shows the local variation of the void area fraction.

A study was conducted to find the correlation between the occurrence of voids and the local packing fraction of the yarn. We observe that it is not possible to exactly predict the location for void creation since it is not only depends on the F_{LFP} . However, there is a likelihood of its occurrence. Moreover, the voids are only observed in the region having F_{LFP}^i in the range of (0.35-0.65).

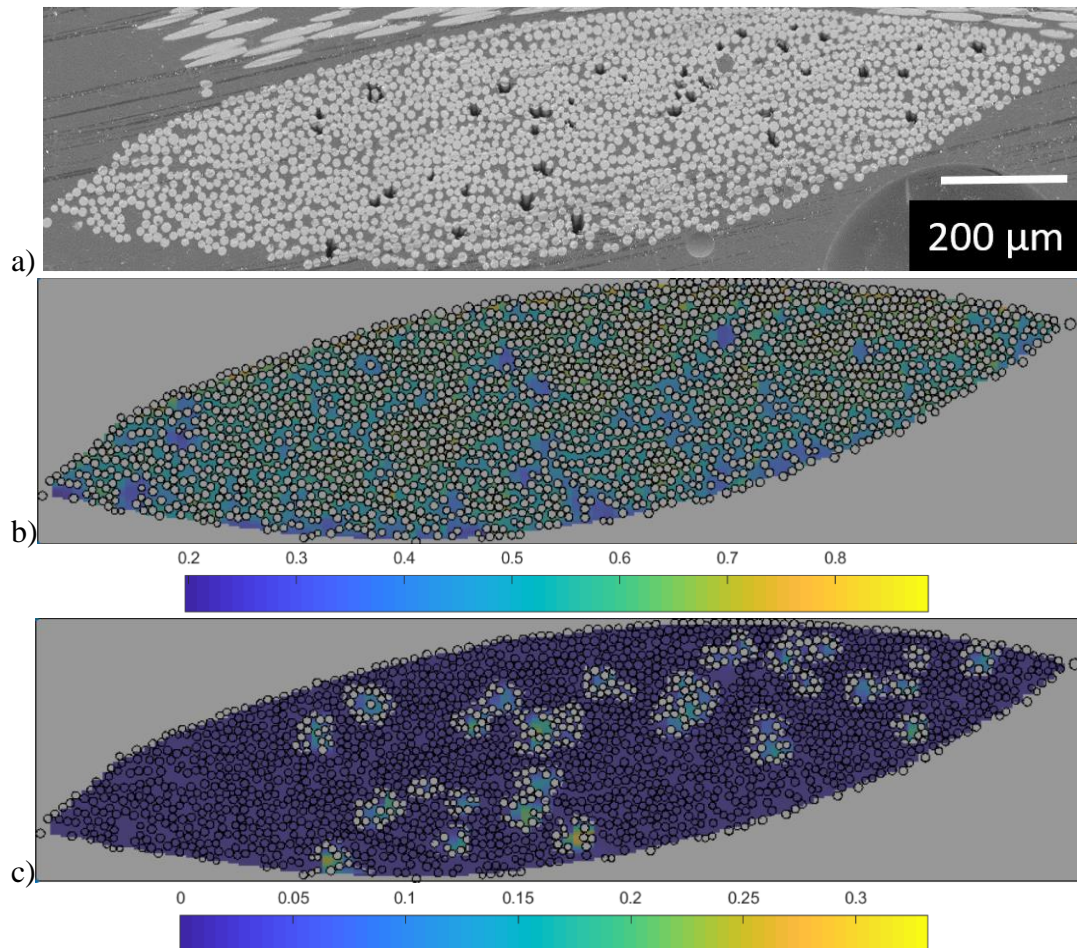


Figure 31: Results from modified VMC applied on entire yarn a) SEM observation of the yarn, b) Local fiber packing (F_{LFP}^i) in yarn and c) Local void area fraction in the yarn.

Area, radius, and aspect ratio of intra-yarn voids

In this study, we used the pixel counting method (PCM section 1.3.4) to measure the void volume fraction in a yarn. The void characteristics such as area, radius, and aspect ratio were calculated by segmentation of the yarn by using the image processing tool FIJI [26,169]. At first, the yarn profile was manually outlined and a threshold was applied with a maximum gray value of 50. This resulted in an image containing only voids and an inbuilt plugin of FIJI called analyze particle [26] was used to obtain the data such as void area, aspect ratio, and position as shown in Figure 32.

Additionally, a noise removal procedure was applied to the image. In this study, the noise was related to the unwanted information in an image such as isolated or clustered pixels after the application of threshold. The origin of such noise can be polishing defects, the dust settled during metallization, and the electronic fluctuations during the image acquisition, which will

cause wrong information of the measured data. The method of manual threshold cannot remove this kind of isolated noise without affecting the global measurement. To remove such noise, a numerical filter was applied to the calculated data during post-processing such that the least value with high repetition could be removed from the data before making the final data set. A similar technique was also adopted by Medhikhani et al. [170].

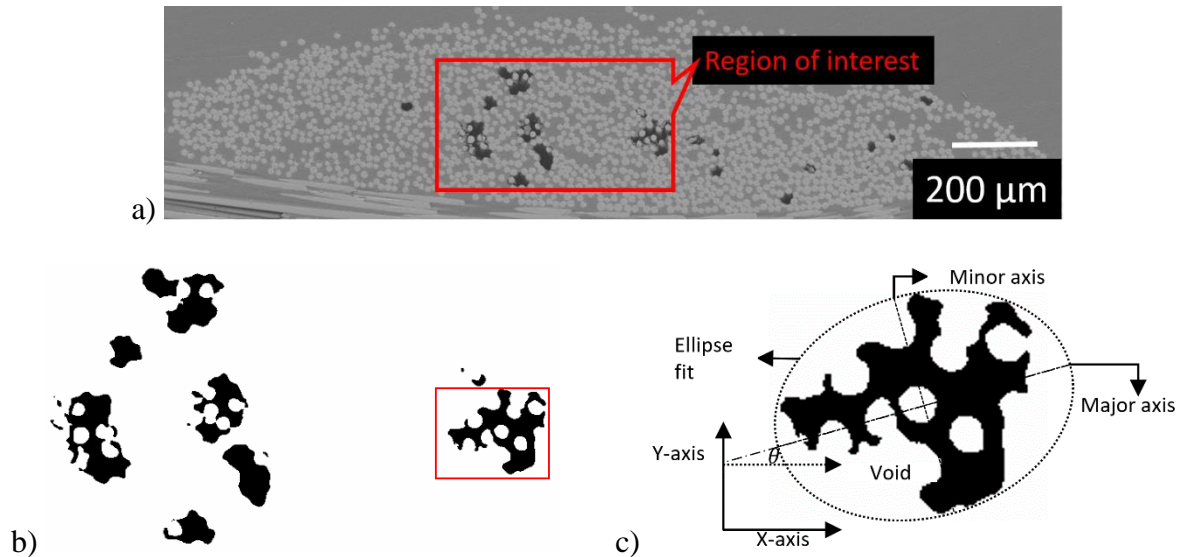


Figure 32: Steps to calculate void parameters a) Manual selection of the yarn cross-section, b) Threshold (max=50) to visualize the voids and c) Measurement of the void parameters (area, axis) by using “analyze particle” in FIJI, representing effective void fraction (A_{eff}) and the aspect ratio of the void (AR).

A total of 2069 voids were evaluated in this study out of which were 493 on the upstream warp, 601 on the upstream weft, 526 on the downstream warp, and 449 on the downstream weft. Intra-yarn void area fraction distributions at upstream and downstream in warp and weft yarns for three textile architectures are presented in Table 9. The intra-yarn void area fraction in both warp and weft yarns increases from upstream to downstream. This phenomenon is anticipated and was already explained in Section 2.3.1. The relatively high velocity of resin in upstream results a dominant resin flow in the channel, thus increasing the occurrence of the intra-yarn void. Conversely, in downstream the velocity of the resin is low and the capillarity of the yarns is significant enough to fill the yarns before the resin fills the inter-yarn channel. Thus, the low resin velocity in the downstream results in a small amount of intra-yarn voids.

Reinforcement, injection pressure	Warp (V_{vy})		Weft (V_{vy})	
	Upstream	Downstream	Upstream	Downstream
Satin, 2.0 bar	0.014 ± 0.002	0.012 ± 0.001	0.015 ± 0.001	0.012 ± 0.008
Twill, 1.5 bar	0.022 ± 0.009	0.015 ± 0.004	0.058 ± 0.0016	0.030 ± 0.002
2 nd Twill, 1.5 bar	0.025 ± 0.003	0.020 ± 0.001	0.028 ± 0.009	0.021 ± 0.002

Table 9: Distribution of intra-yarn void area fraction in upstream and downstream for 3 different textile architectures (Satin, Twill, and 2nd Twill).

In Figure 33, x-axis represents the void areal fraction of each void (A_{eff}) for the void cross-section area (A_v) and y-axis represents the count of voids having similar A_{eff} . The mathematical

relation for calculating A_{eff} is given in Equation 3.4, where A_{yarn} is the area of yarn. It is observed that the intra-yarn void area fraction has a log-normal distribution in both warp and weft yarns. The effective void radius can be calculated by approximating the area of the void as the area of a circle, and the effective radius of a void can be calculated from Equation 3.5.

$$A_{eff} = A_v/A_{yarn} \quad (3.4)$$

$$R_{eff} = \sqrt{A_v/\pi} \quad (3.5)$$

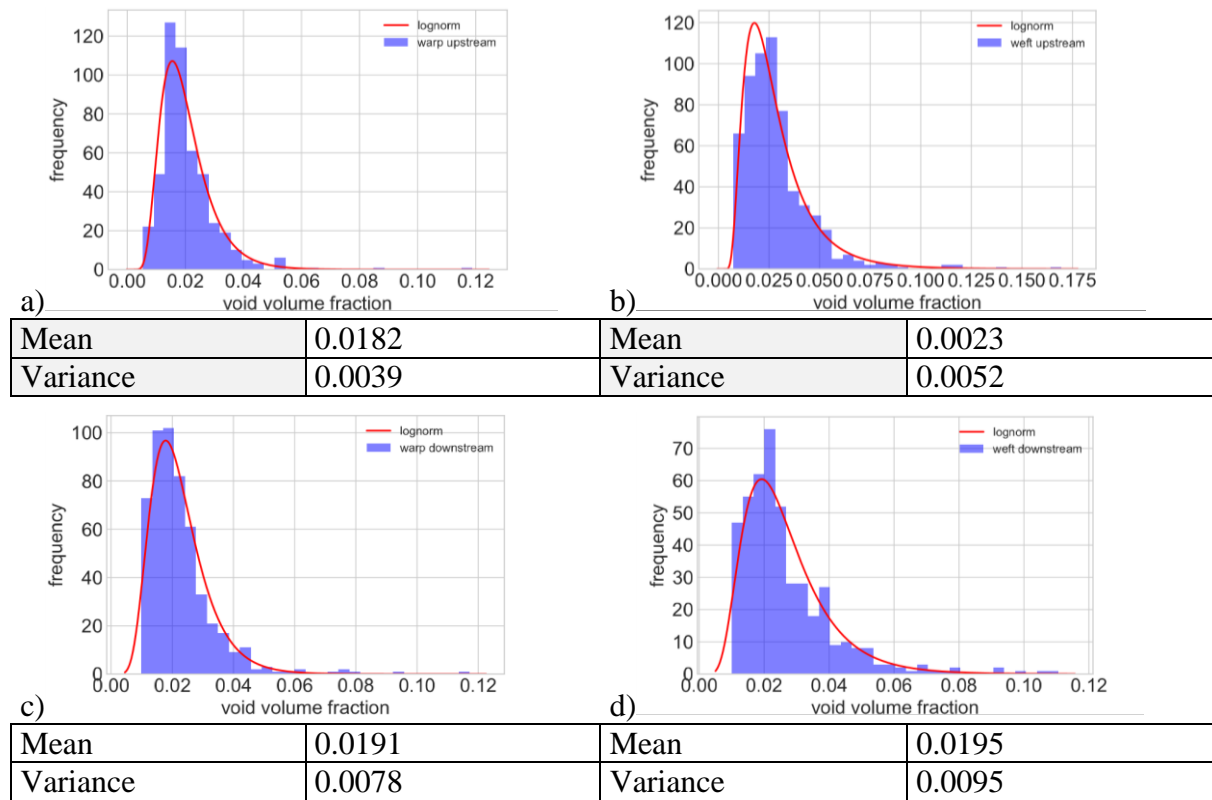


Figure 33: Intra-yarn effective void area/volume fraction (A_{eff}) distribution for warp yarns upstream a) Warp upstream, c) Warp downstream b) Weft upstream, d) Weft (for Twill-3D).

In upstream, it is observed that voids in weft yarns are 27.78 % bigger than voids in warp yarns. However, downstream, the variation is reduced to 2.63%. When a comparison is made between upstream and downstream, it is observed that voids for warp yarn have a similar size while the void in downstream for weft yarns is 26.8% smaller than voids in the upstream weft. Aspect ratio is the effective parameter to describe the shape of the void. It is calculated by:

$$AR = \text{major axis length}/\text{minor axis length} \quad (3.6)$$

High AR means, the void cross-section is elliptical, approaching flat disk shapes. If AR is one, the void cross-section is circular. In Figure 34, x-axis represents the aspect ratio (AR) of the void calculated by Equation 3.6 and y-axis represents the count of voids. In upstream, the AR of voids in weft yarns is 5.8% higher than that of voids in warp yarns. The void in upstream has a higher AR that in downstream.

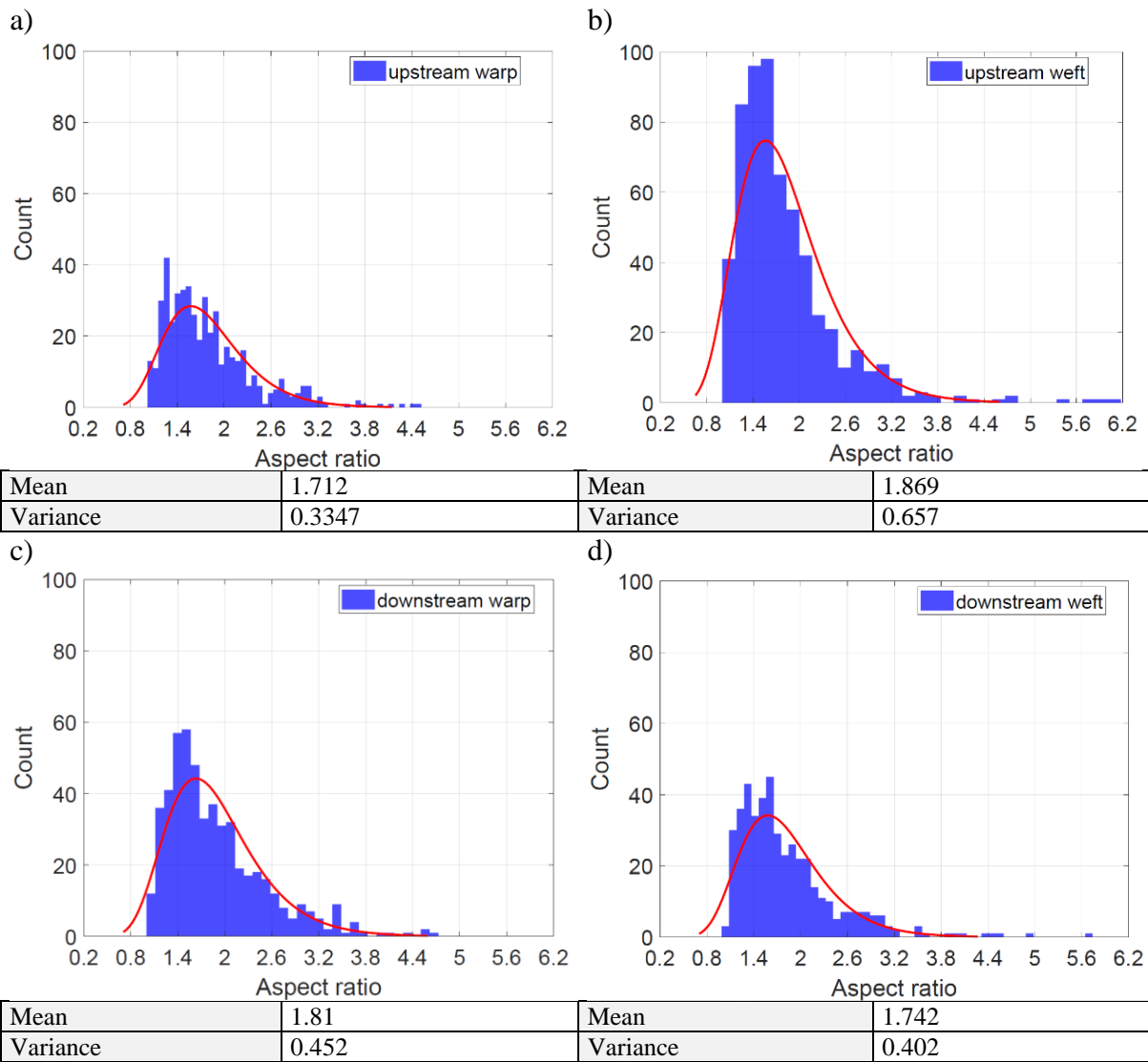


Figure 34: Intra-yarn void aspect ratio (AR) distribution in Twill-3D a) Warp upstream, c) Warp downstream, b) Weft upstream, d) Weft downstream.

3.4 Micro-computed tomography

Micro-CT is a 3D non-destructive technique to characterize material microstructure with a high spatial resolution at the micron level. X-ray beam plays a role as a penetrating probe so that, by monitoring the light identity variation before and after passing through the object, the constitutive phases and internal features can be distinguished by the different absorptivity of the material, which depends on the number (density) and type of atoms along the beam path. As illustrated in Figure 35, the electronic X-ray source illuminates the sample which is placed on a rotation stage. By rotating the sample from 0 to 360 degrees, 2D angular radiographs (projection images) are collected by the planar photo detector. At last, the computer treats and converts the radiographs into the 3D image normally in form of a series of virtual 2D slice images.

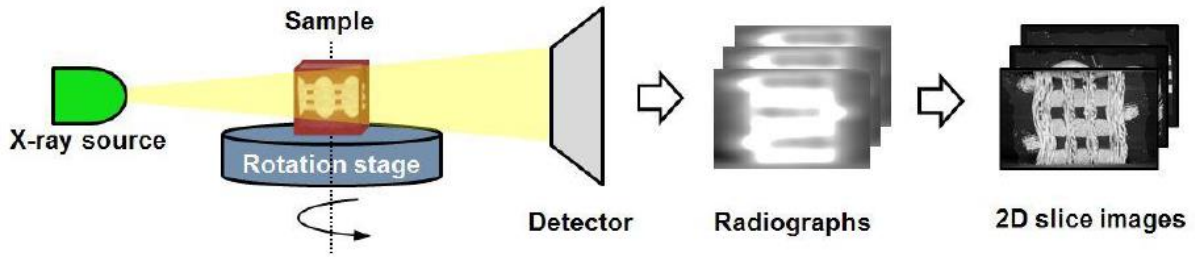


Figure 35: Schematic representation of the image acquisition by X-Ray μ CT [162].

Samples for μ CT observations were extracted as indicated in Figure 36 a). The tomographic images were acquired over the ISIS4D platform (LML/LaMcube, France). Similar scanning parameters were used for all the observations in this thesis. Each sample was scanned with 1440 projection images over a 360° rotation. A projection image was an average of six frames to reduce the random noises. The spot size of about $2\ \mu\text{m}$ was chosen to achieve the required voxel sizes. However, the μ CT slices were pre-processed (See Figure 36b)) to enhance the contrast difference between matrix and inter-yarn voids. This will be helpful for the segmentation of the μ CT data presented in Chapter 5.

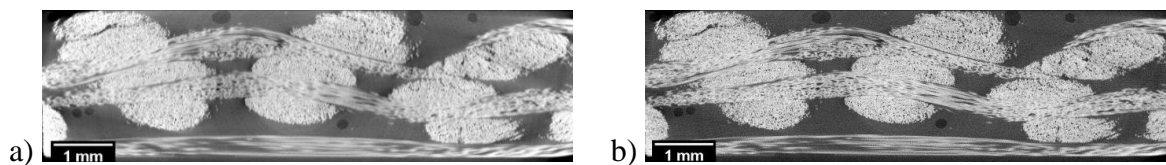


Figure 36: Slice of micro-CT data from Satin-3D a) Cross-sectional slice of the reconstructed image of satin 3D without processing the beam hardening. (b) Cross-sectional slice of the reconstructed image of satin 3D after enhancing the local contrast.

3.5 Mechanical characterization

Tensile tests were carried out in the transverse direction to the resin flow, and the tensile properties (i.e. modulus, strength, and strain at failure) of the textile composites along the direction of the weft yarn were analyzed. The tests were carried out according to the ASTM D3039 standards on Instron 1185 machine with a 100 KN load cell. Each specimen was loaded at a constant strain rate of 1mm/min until failure. The tensile test coupled with a digital image correlation technique (DIC) was carried out to measure the local strain and the modulus by using a clip-on length of 50 mm. The complete experimental setup is presented in Figure 37.

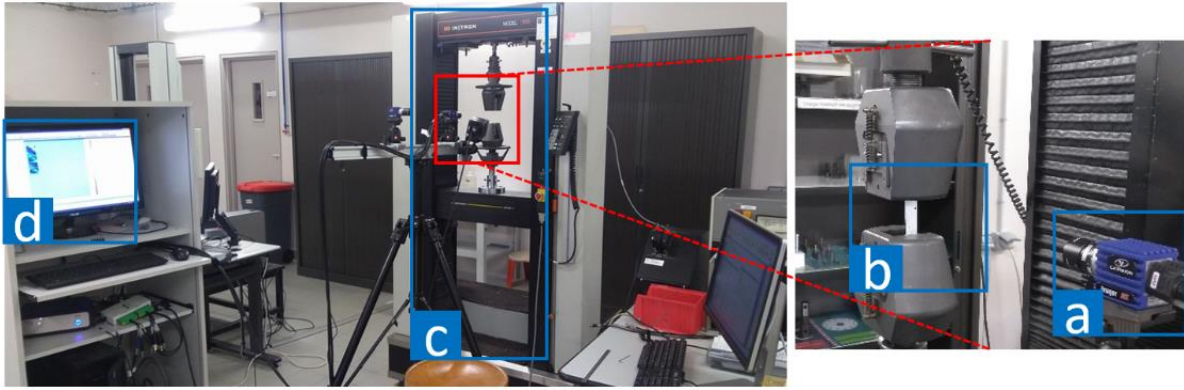


Figure 37: Experimental setup for the tensile test along with DIC a) Camera, b) Specimen mounted in the tensile testing machine, c) Instron 1185 testing machine, and d) Post-processing of images.

The specimen extraction sequence was already presented in Figure 18. The dimensions of the tensile specimen (length 160 mm, the thickness of 2.2 ± 0.1 mm and width of 2.5 mm) are provided in Figure 38. Tabs with a thickness of 1.5 mm and length of 30 mm were glued to specimens by an aeronautical graded adhesive to ensure that the failure does not occur inside the holding jaws.

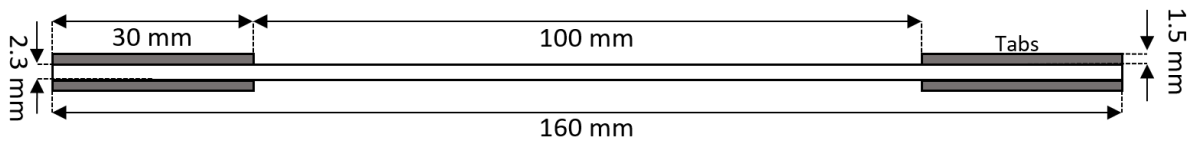


Figure 38: Dimensions of the tensile specimen.

The Allied® CMOS (Complementary Metal-Oxide-Semiconductor) camera with 2048×2048 resolution was used to record the images to obtain the deformation on the surface. The images were captured at a frequency of 10 images per second. They were treated by the DIC technique implemented by commercial software Vic-2D®. Other important parameters for a DIC are speckle pattern, size, and density. They have a direct effect on the measurement of strain resolution. Carter et al. [171] presented a comprehensive study about the effect of the speckle density and pattern on the strain resolution. Any speckle density i.e. ratio of the area occupied by speckle to the total area of the observing surface should be in the range of 23 to 58%. Deviation from this range will induce the noise in the computed strain resolution. They also presented that speckles should be of homogeneous size and have irregular shapes. Such a speckle pattern can be achieved by careful hand spray [172]. The image of the speckle pattern on the tensile specimen is presented in Figure 39. The average speckle density for the tensile specimens is 37.89%. For the post-processing of images, the users must choose a subset size and step size. Subset size is defined as the height and width of the square in the image for the analysis and step size is the distance between two subsets. A subset size of 21 with a step size of 5 was selected for this study.



Figure 39: Image to show the hand-sprayed speckle pattern on the tensile specimen.

Young's modulus and ultimate tensile strength of the specimen were measured by monotonically loading until failure. Since clip-on could be damaged during the failure of the specimen, the tensile test was carried out in two steps. In step one, clip-on was attached to the specimen and loaded until a strain of 0.4%. In step two, the system was reinitialized to the original position and the clip-on was removed and loaded until failure. Whereas the DIC measurements were performed for both steps.

In this study, there were in six tensile tests for satin architecture, six tensile tests for twill architecture, and 54 for the final 2nd twill architecture. The tensile test results for composites reinforced by satin architecture are presented in Figure 40 a) and the tensile results twill reinforcement are presented in Figure 40 b). Tensile results for 2nd twill reinforced composites manufactured with an injection pressure of 0.5 bar are presented in Figure 41 a), the results with 1.0 bar are shown in Figure 41 b) and 1.5 bar are presented in Figure 41 c).

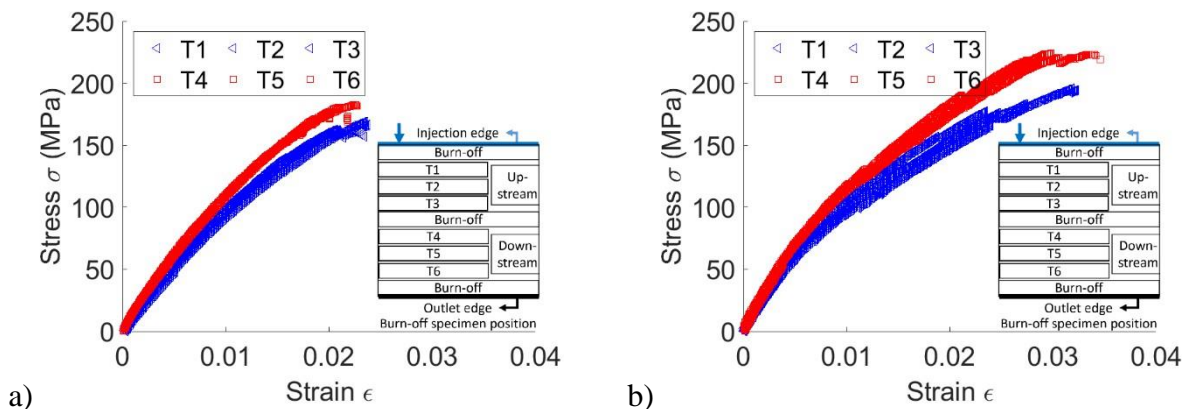


Figure 40: Stress-strain curve of tensile test on composites reinforced by a) Satin architecture and b) Twill architecture.

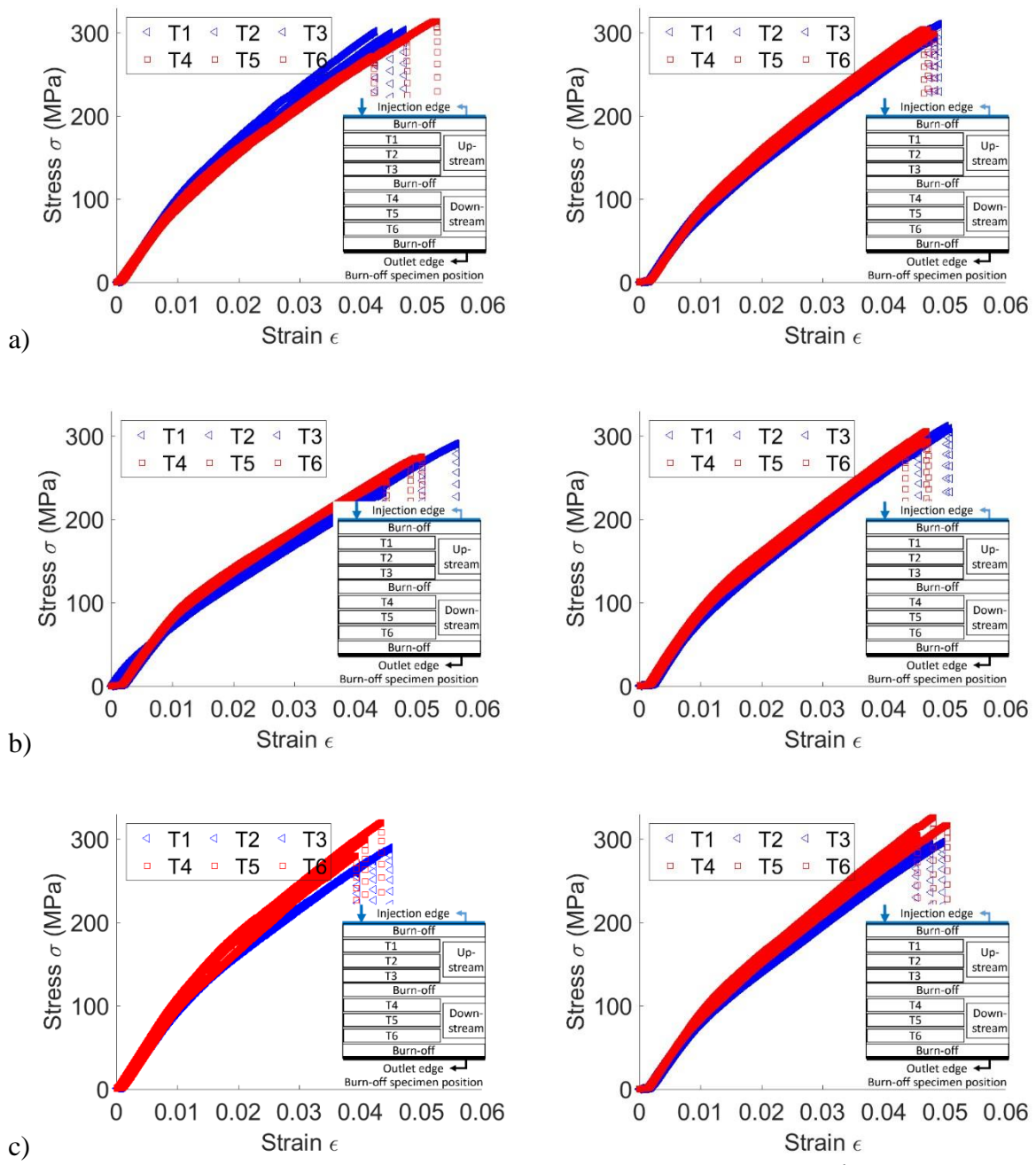


Figure 41: Stress-strain curve of tensile test on composites reinforced by 2nd twill architecture manufactured by injection pressure of a) 0.5 bar, b) 1.0 bar and c) 1.5 bar.

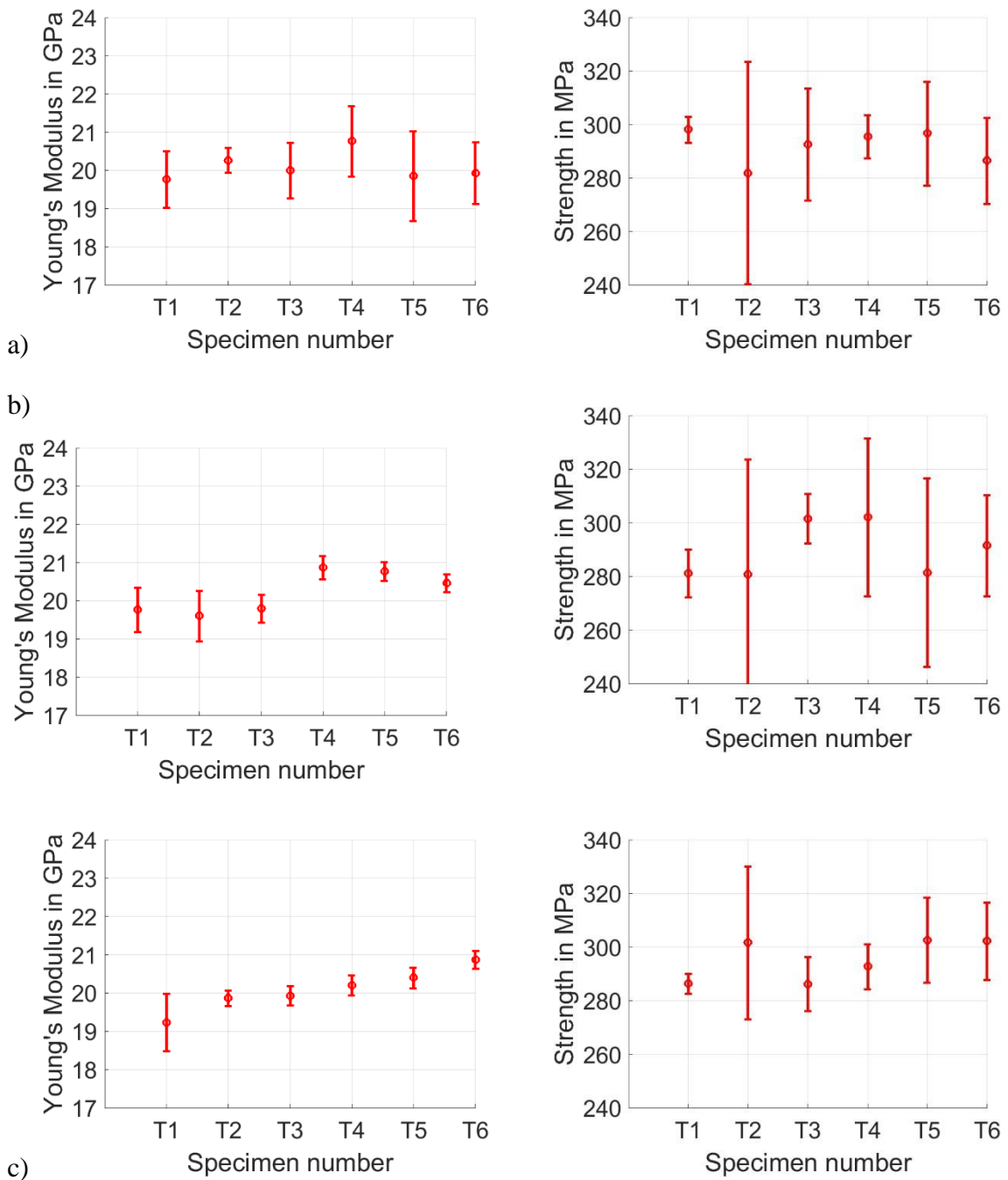


Figure 42: Variation of tensile properties from upstream to downstream in 3D textile reinforced composites manufactured at different pressures a) 0.5 bar, b) 1.0 bar and c) 1.5 bar.

The specimens from downstream (T4, T5, T6 (blue in plots)) despite having a higher total void volume fraction exhibit better mechanical behavior (higher Young's modulus, ultimate tensile strength) than the specimens from upstream (T1, T2, T3 (red in plots)).

The phenomenon described above was observed in the composite with Satin reinforcement (see Figure 40 a)) and Twill reinforcement (see Figure 40 b)). Even though this behavior was not observed in 2nd Twill composites manufactured with an injection pressure of 0.5 bar (see Figure 41 a)) it can be related to the distribution of the total void volume fraction and intra-yarn void volume fraction in upstream and downstream. However, with an increase in the injection pressure to 1.0 and 1.5 bar during manufacturing leads to better mechanical properties in the downstream (see Figure 41 b)).

Hence, the variations of Young's modulus and strength were subjected to the investigation with respect to the total void volume fraction, intra-yarn void volume fraction (see Section 3.6). The analysis with respect to the position of specimen for 2nd twill reinforced composites manufactured with an injection pressure of 0.5 bar, 1.0 bar, and 1.5 bar are presented in Figure 42. This will help us to understand the trend in the evolution of the tensile properties as a function of the manufacturing parameter (injection pressure).

The change in the mechanical properties can be correlated to the position of the voids (intra-yarn/ inter-yarn) in the composites. The results of the intra-yarn void volume fraction are presented in Section 0, and Table 9 shows that, while the total void volume fraction is lower in the upstream, the intra-yarn void content is higher and vice-versa in the downstream. Thus total void content is not always an effective parameter to analyze the effect of voids.

3.6 Results and discussion

The results of tensile tests along the weft direction for Satin, Twill, and 2nd Twill layer to layer interlock in comparison with total void volume fraction and intra-yarn void area fraction are presented in Figure 43, Figure 44, and Figure 45, respectively. For three different architectures, the evolution of Young's modulus and tensile strength are presented with respect to a) total void volume fraction, b) intra-yarn void volume fraction in warp yarns and c) intra-yarn void volume fraction in weft yarns.

For Satin reinforcement (see Figure 43), Young's modulus and strength increase by 12.54% and 13.5% with a decrease of 20.4% and 12.35% of the intra-yarn void area fraction, in the warp and weft respectively. Similarly, for Twill composites (see Figure 43), the tensile modulus and strength increase from upstream to downstream by 14.04% and 12.39% respectively. For the composites containing the 2nd Twill reinforcement (see Figure 45) the elastic modulus and strength increase from upstream to downstream by 10.4% and 9.1% respectively. The modulus and strength did not increase by the same percentage in three composites. This can be associated with the difference in the intra-yarn void fraction, the difference in architecture, and total fiber volume fraction.

In general, we can conclude that the total void volume fraction might be a limited indicator to characterize the tensile behavior of the 3D reinforced textile composites. Considering the void position (intra-yarn or inter-yarn) it has been shown that the tensile properties are more

sensitive to the intra-yarn voids which is an effective parameter to analyze the effect of the voids on the tensile behavior of the 3D textile reinforced composites. Similar behavior was observed in all three architectures. The standard deviation of the strengths is smaller than that of Young's modulus in all the reinforcements. One of the explanations for this can be that the final tensile failure of the composite is driven by fiber failure. As the fiber volume fraction is constant in all the specimens this would result in a low standard deviation in the tensile strength of the composites. The percentage of increases in Young's modulus and strength in comparison with the total void content, warp, and weft intra-yarn void content are presented in Table 10.

	E	σ	of V_{VT}	V_{vy} warp	V_{vy} weft
Trend	Increase	Increase	Increase	Decrease	Decrease
Direction	Up to down	Up to down	Up to down	Up to down	Up to down
Reinforcement					
Satin	12.54 %	13.5%	23.1%	20.4%	12.35%
Twill	14.04%	12.39%	27.5%	36.83	40.75%
2nd Twill 1.5 Bar	10.4%	9.1%	19.05%	17.53%	31.89%

Table 10: Variation of Young's modulus and strength in 3D textile composites with different reinforcement with respect to global void content, intra-yarn void content in warp and weft.

Satin architecture:

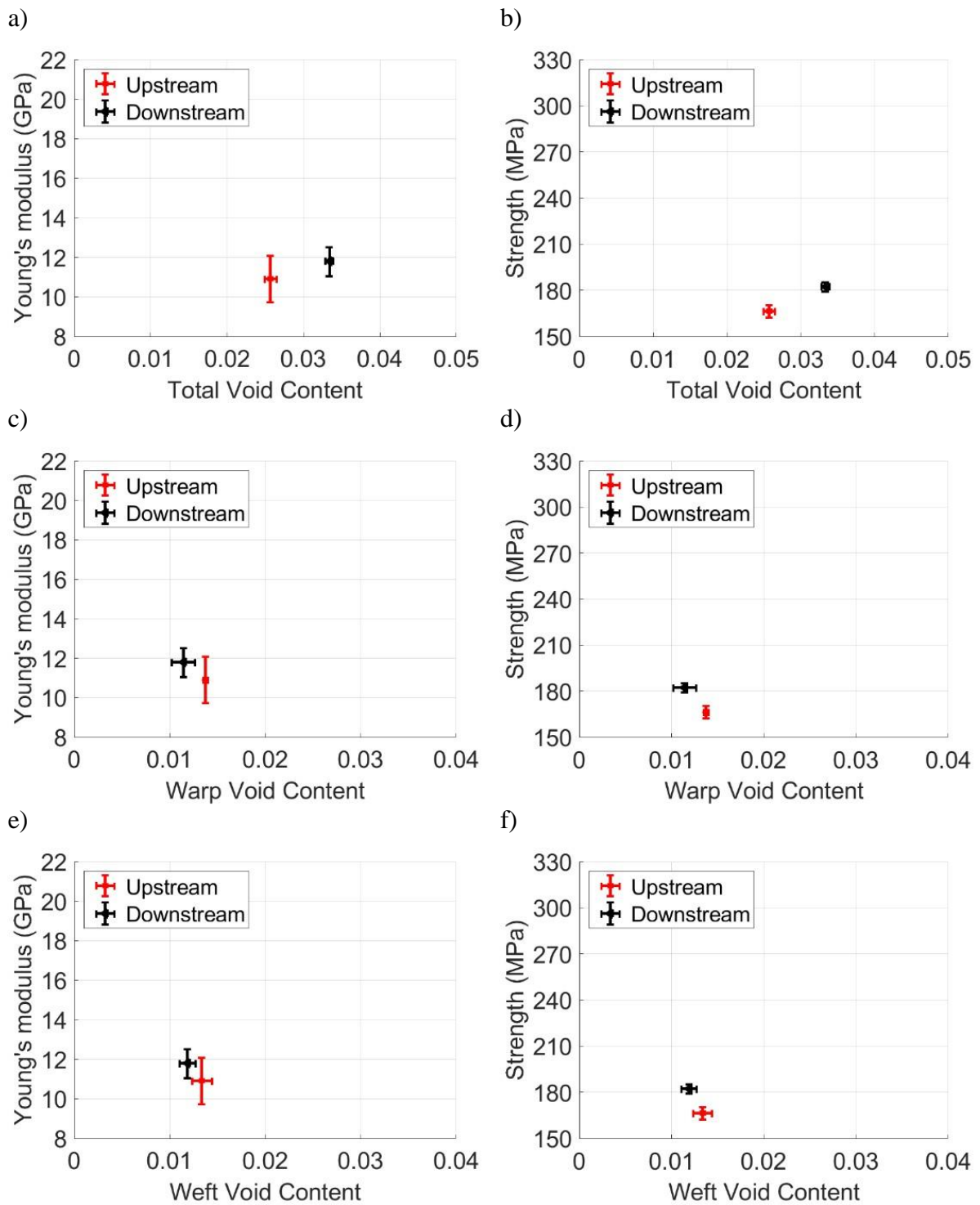


Figure 43: Tensile test results for satin architecture a) Modulus vs V_{VT} , b) Strength vs V_{VT} , c) Modulus vs warp V_{vy} , d) Strength vs warp V_{vy} , e) Modulus vs weft V_{vy} and f) Strength vs weft V_{vy} .

Twill architecture:

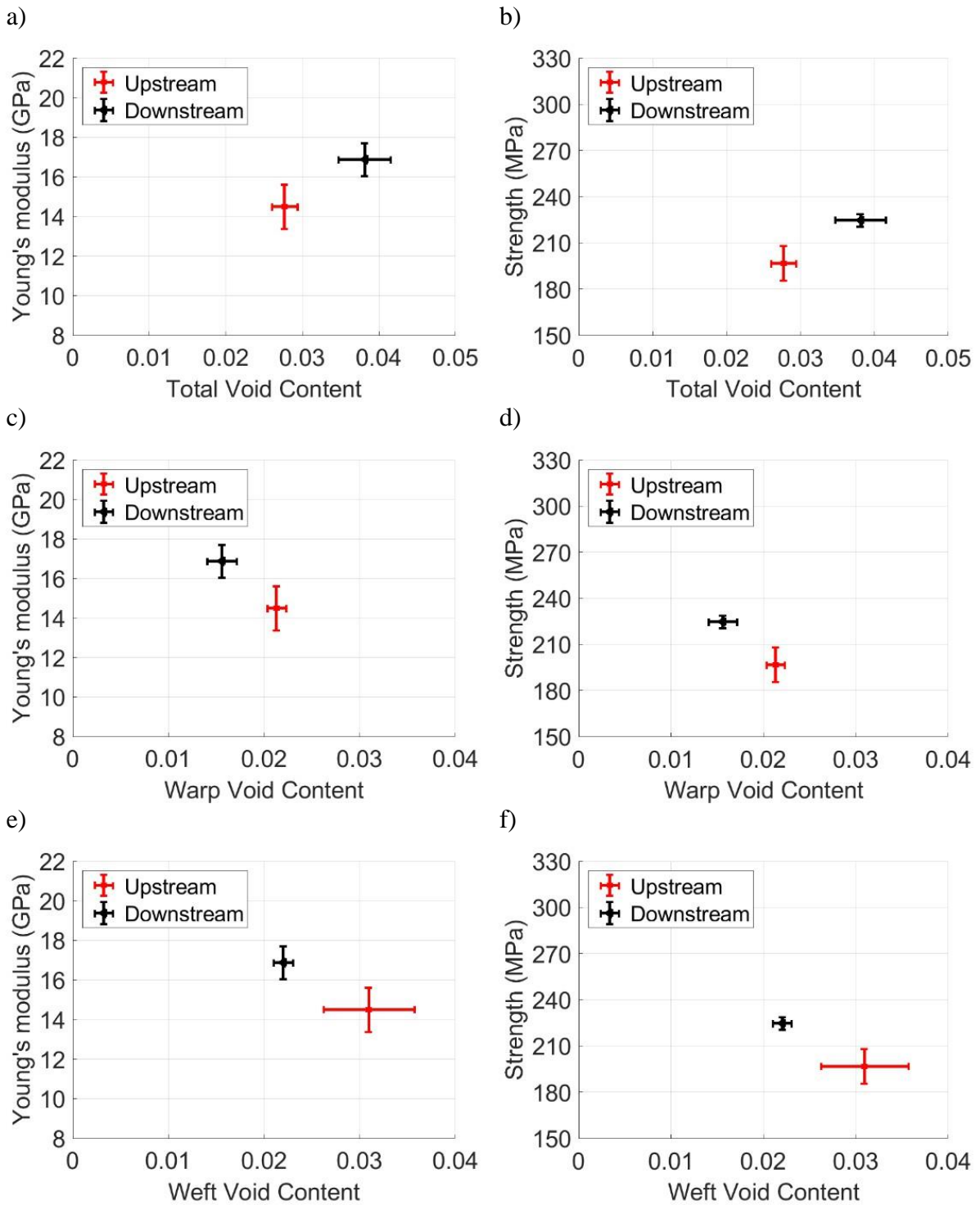


Figure 44: Tensile test results for twill architecture a) Modulus vs V_{VT} , b) Strength vs V_{VT} , c) Modulus vs warp V_{vy} , d) Strength vs warp V_{vy} , e) Modulus vs weft V_{vy} and f) Strength vs weft V_{vy} .

2nd twill architecture manufactured with injection pressure of 1.5 bar:

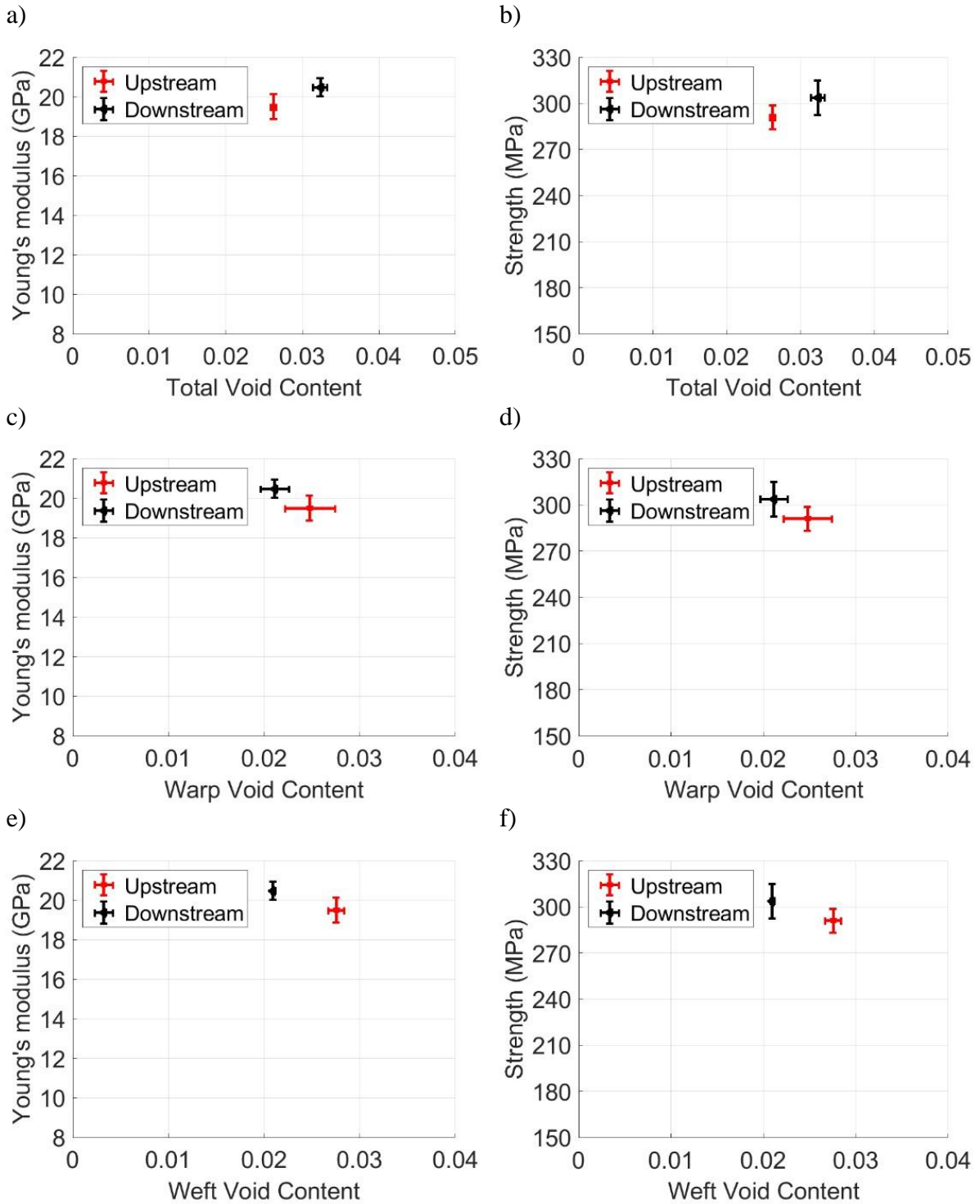


Figure 45: Tensile test results for twill 2nd architecture a) Modulus vs V_{VT} , b) Strength vs V_{VT} , c) Modulus vs warp V_{vy} , d) Strength vs warp V_{vy} , e) Modulus vs weft V_{vy} and f) Strength vs weft V_{vy} .

3.7 Conclusions

Characterization of the fiber volume fraction and void volume fraction and the mechanical behavior of 3D textile reinforced composites were presented in this chapter. Burn-off tests were conducted to obtain the total fiber volume fraction (V_{FT}) and total void volume fraction (V_{VT}). The V_{VT} in the composite plates manufactured with constant injection pressure increases from upstream to downstream. An improved Voronoi Cell Method (VCM) method was proposed in this study to calculate the local fiber packing (F_{LFP}). Intra-yarn fiber volume fraction (V_{fy}), fiber radius distribution (R_f), and inter-fibers distance (IFD) were evaluated based on the VCM. Void parameters such as size distribution and aspect ratio were evaluated by using threshold-based segmentation. For yarns, it was observed that voids occurred mainly in the regions with specific local fiber packing in the range of 0.35-0.65. These parameters will be used in Chapter 4 for the generation of the statistically representative microstructure for yarns.

For composites manufactured with an injection pressure of 0.5 bar, no specific trend in the total void volume fraction was observed. In composites manufactured with an injection pressure of 1.0 bar, the total void volume fraction increased by 24.2% from upstream (0.025 ± 0.0013) to downstream (0.033 ± 0.009). The intra-yarn void area fraction decreased from upstream to downstream. For composites manufactured with an injection pressure of 1.5 bar, the total void volume fraction increased by 18.9% from upstream (0.026 ± 0.003) to downstream (0.032 ± 0.009). The intra-yarn void area fractions in warp and weft decreased from upstream to downstream by 17.53% and 31.89 % respectively. Young's modulus and strength increased by 10.4% and 9.1% respectively. On average, the 1% increase in intra-yarn voids resulted in the 0.3-0.4% reduction of the tensile properties. Hence we can state that the intra-yarn voids have a higher influence on the tensile properties than inter-yarn voids. This phenomenon has not been reported in the literature. To completely understand the effect of the type of void on tensile properties, multiscale numerical simulations are proposed in Chapter 3 and Chapter 4.

4 Microscale modeling of yarns with void type defects

4.1 Introduction

The focus will be placed on, the microscale of the textile composites which have an approximate length scale of μm as shown in Figure 46. The estimation of the mechanical properties of yarns is the first step to evaluate the material behavior for the multiscale simulation. Calculation of the yarn behavior is possible by either an analytical approach or numerical methods [173].

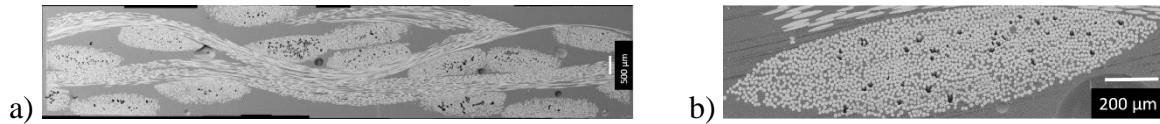


Figure 46: Scales in textile composites a) Cross-section of the 3D textile composites showing warp, weft yarns, and voids at mesoscale. b) Cross-section of yarn with fiber, void, and matrix at the microscale.

In this chapter, we provide the methodology to predict the elastic properties of the yarn with both analytical and numerical approaches. In section 4.2, an analytical approach based on stepping Mori-Tanaka methods is presented considering voids as the zero stiffness spherical inclusions. A detailed explanation of the numerical homogenization is provided in section 4.3. And the effect of void parameters such as void size, shape, and spatial distributions on the elastic properties of the unidirectional yarns is investigated. At the end of the chapter, results are presented in section 4.4.

4.2 Analytical methods to calculate the elastic properties

Analytical models have been effectively used to study the elastic properties of the dual-phase composites (fiber/particle and matrix). Empirical and phenomenological models do not consider physical aspects such as fiber shape. This will result in the deviation of the predicted elastic properties from reality, whereas the micromechanical such as Mori-Tanaka theory can overcome this drawback [174]. In 1973, Mori-Tanaka [175] formulated an analytical approach that relates the average stress and strain of stiff inclusion in an isotropic matrix. In 1987, Benveniste [176] reformulated the Mori-Tanaka's approach by applying the equivalent inclusion method to a compacted tensor, called dilution tensor which only depends on an Eshelby's tensor [94] describing the shape of the inclusions. Hence, this method is popular and called Eshelby-Mori-Tanaka's method. For a two-phase material the effective stiffness (C^{eff}) of the fiber reinforced composite can be calculated by using Equation 4.2.

$$T = [I + SC_1^{-1}(L_2 - L_1)]^{-1} \quad (4.1)$$

$$C^{eff} = C_1 + V_2\{(C_2 - C_1)T\}[V_1I + V_2\{T\}]^{-1} \quad (4.2)$$

where C_1 and C_2 are the stiffness of the matrix and the inclusion, V_1 and V_2 are respective volume fractions. Dilution tensor T can be calculated from the Eshelby's tensor S (see Equation 4.1), which depends on the shape of the inclusion, i.e. compliance tensors L_1 , L_2 of the phases. The Eshelby's tensor depends on the shape of the inclusion [176].

This method can also be extended to calculate the elastic properties of materials with more than two phases [177]. Eshelby-Mori-Tanaka's method has been employed for multi inclusion systems such as composites with coated fibers [178], [179]. This method was also applied for the materials with different inclusion shapes that are ellipsoidal or irregular. The effect of the aspect ratio of the ellipsoidal inclusion for a transversely isotropic composite as an application to the short fiber-reinforced composites was studied by Tandon et al. [180]. Closed-form solution of Eshelby's integral in the isotropic material was developed by Weng et al. [181]. Y.M Wang et al. [182] studied the elastic properties of the material with spherical inclusions and penny shaped.

In this thesis, we propose the application of Eshelby inclusion based Mori- Tanaka's method for homogenization of the fiber-reinforced composites with the manufacturing defects such as voids presented in Figure 47. A review on analytical homogenization methods for the material with multiple stiff inclusions was done by Klusemann B et al. [183]. There are no works dedicated to the homogenization of the material with voids. The main reason for this rises from the fact that the homogenized stiffness tensor calculated by the M-T scheme tends to become unsymmetrical when applied for multiple inclusions. This problem was addressed in the literature and likely to be unavoidable in the multiphase homogenization especially with inclusions of different aspect ratios such as spherical and cylindrical. Benvenitne et al. [184] showed that a predicted effective stiffness tensor satisfies the symmetric condition only for a two-phase (matrix and inhomogeneity) composite and a multi-phase composite whose inclusions have a similar shape and the same orientation. Similar findings were also mentioned in the literature [185–187].

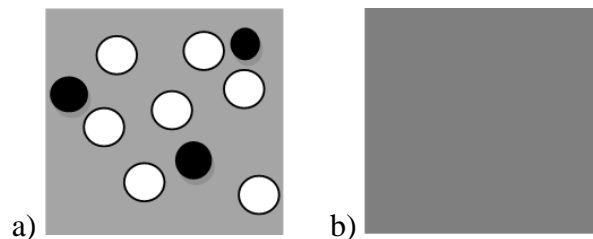


Figure 47: Schematic representation of homogenization at microscale a) Representation of the fiber (white) reinforced composite material with voids (voids) and b) Homogenized material.

To overcome this problem, a stepping scheme was proposed by Yang Q-S et al. [188] and this method can be applied to n number of inclusions and can be extended to any micromechanical approaches. Now, we present the stepping scheme to homogenize the elastic properties of the composite with cylindrical fibers and spherical voids.

4.2.1 Stepping scheme for multiple inclusion

The fundamental idea of the stepping scheme is to use one type (shape) of inclusion at one step and the homogenized material properties will be the matrix at the next inclusion. Such process is repeated until all the inclusions are considered. Thus the number of steps in the stepping scheme will be equal to the number of inclusion types in the material. To complete the understanding of the stepping scheme a few auxiliary definitions should be presented.

True inclusion fraction: It means the fraction of the volume occupied by the i^{th} inclusion in the total volume of the material. The true inclusion fraction (v_i) for the inclusion of volume V_i is calculated as:

$$v_i = \frac{V_i}{V_1 + V_2 + V_3 + \dots + V_n} \quad (4.3)$$

Instantaneous inclusion fraction: It indicates the volume fraction of the current inclusion by neglecting the inclusions that have already been used in the homogenization. It can be calculated by:

$$v'_i = \frac{V_i}{V_1 + V_2 + V_3 \dots + V_i} \quad (4.4)$$

Now, we present the application of the stepping scheme to a UD composite with cylindrical fibers and spherical voids:

Step 1: In the first step of homogenization, the material can be considered as a two-phase composite with the spherical voids and matrix then the homogenized properties can be calculated by Equation 4.2. The new homogenized material can be called an effective matrix.

Step 2: Before the application of the M-T scheme for the 2nd inclusions (cylindrical fibers), one should recalculate the Eshelby's tensor (S) and dilution tensor (T) for the second inclusion which depends on the shape of inclusion and the properties of the new effective matrix. Also, the volume fraction should be corrected by instantaneous inclusion fraction as the material after step one contains one less phase.

The formulations used for the stepping scheme are presented in Table 11. Consider a composite with isotropic matrix, fiber, and voids. C_m, C_f, C_v, C_{eff} are stiffness tensor for matrix, fiber, voids, and yarn respectively. S_s, S_c are the Eshelby tensors for spherical and cylindrical inclusions respectively. The formulation of Eshelby tensors for spherical and cylindrical inclusions can be found in Annexe (see Section 7.3). v_m, v_f, v_v are the volume fractions of the matrix, fiber, and voids respectively.

Step	Process	Comments
Input	C_m, C_f, C_v & v_m, v_f, v_v & S_s, S_c	Voids are modeled as a material with zero stiffness.
Step-1	$T = [I + SC_M^{-1}(L_V - L_M)]^{-1}$ $C_{VM} = C_V + V_v\{(C_V - C_M)T\}[V_M I + V_v\{T\}]^{-1}$	Recalculate the elastic properties of the effective matrix.
Step-2	$T = [I + SC_{VM}^{-1}(L_f - L_{VM})]^{-1}$ $C^{eff} = C_{VM} + V_f\{(C_f - C_{VM})T\}[V_M I + V_f\{T\}]^{-1}$	Calculate the tensor T
Output	C^{eff}	Calculate the properties from stiffness tensor

Table 11: Formulation for stepping Mori-Tanka scheme for yarn with cylindrical fibers and spherical voids.

S is the Eshelby tensor which should be calculated depending on the shape of the inclusions (ANNEXE B) and T is the dilution tensor and operation $[\]^{-1}$ represents the inverse of the corresponding matrix. L_V , L_f , and L_m are compliance tensor for the void, fiber, and matrix respectively.

In the case of the single inclusion problem, the stepping scheme should match Mori-Tanka's model. The proposed M-T scheme was verified by Abaimov et al. [189] where they used the Mori-Tanka scheme to predict the elastic properties of the unidirectional composite. The results are presented in Table 13. In this thesis, direction 1 represents the longitudinal direction (along the fiber direction) and direction 2 represents the transverse direction. The mechanical properties of the glass fiber, epoxy, and void are given in Table 12.

Material	Young's modulus (GPa)	Poisson's ratio
E-Glass fiber [189]	72	0.22
Epoxy [189]	3.3	0.375
Void [69]	10^{-9}	10^{-9}

Table 12: Elastic properties of each phase.

	E_{11} (Gpa)	E_{22} (Gpa)	ν_{12}, ν_{13}	ν_{23}	G_{12}, G_{13} (Gpa)	G_{23} (Gpa)
Abaimov [189]	41.1	9.89	0.282	0.492	3.67	3.31
Present work	41.1	9.89	0.282	0.492	3.67	3.31

Table 13: Validation of the stepping Mori-Tanka scheme presented in this work by Abaimov et al. [189].

The results for different study cases with fiber volume fractions of 0.40, 0.50, and 0.60 with a void volume fraction of varying from 0-0.05 were considered to observe the evolution of elastic properties with respect to void volume fraction. The results are presented in the following section.

4.2.2 Results for stepping Mori- Tanaka's scheme

To validate the stepping scheme, the predictions of the transverse properties are compared with the experimental results presented in the reference [105] (see Figure 48 a). A maximum of three percentage error was recorded at a void fraction (V_v) of 0.098 and the error in the prediction becomes higher as the void volume fraction increases (see Figure 48 b). The increase in error percentage can be due to the fact that stepping scheme is constructed assuming that voids are spherical and at higher V_v , the voids tend to have a higher aspect ratio which will increase error.

All the elastic properties tend to decrease linearly with an increase in the void fraction. The gradient of reduction depends on the orientation of the fiber. The properties in the fiber direction such as the Young's modulus in the fiber direction reduced 0.5% (see Figure 49 a) whereas the transverse modulus recorded 18% (see Figure 49 b) reduction for 4% void volume fraction. In comparison the shear properties are highly affected in the presence of voids. Notably, stepping MT predicts unreal value of the in-plane Poisson's ratio (see Figure 49 e, f) and this kind of behavior was also recorded in the literature [190–192].

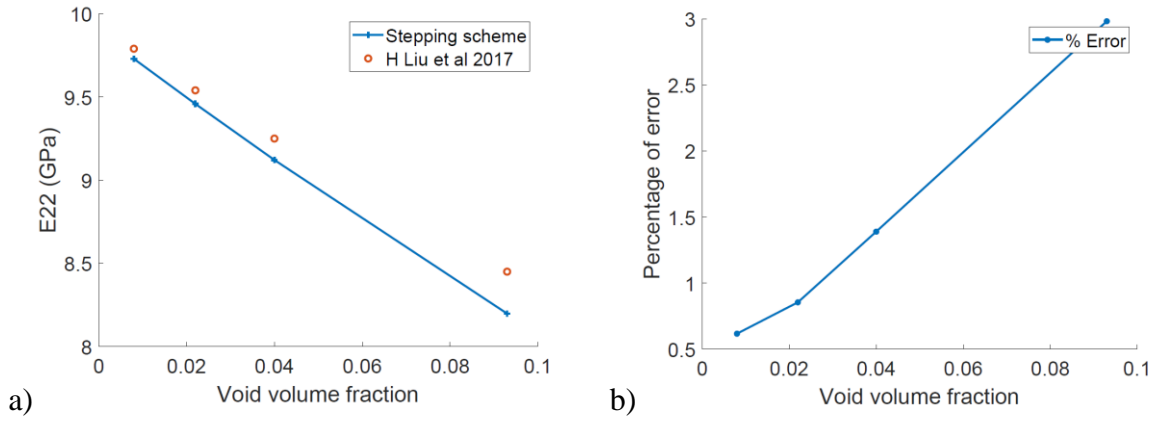
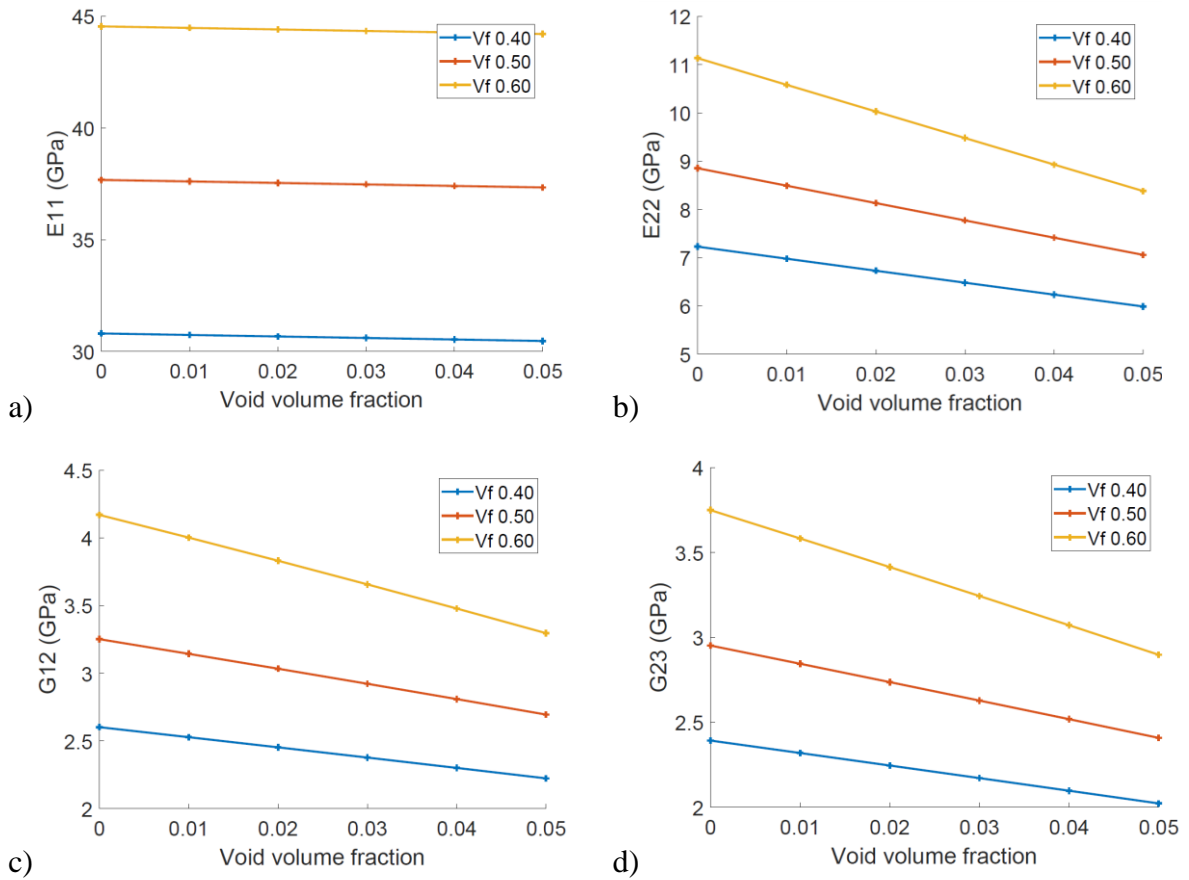


Figure 48: Comparison of stepping scheme with the experimental results of Haolong et al. [105].

Very quickly analytical solutions find their limits. Analytical approaches fail to explain the effect of void distribution and morphology on the elastic properties of the UD yarns composites. This serves as one of the motivations for the development of a numerical simulation scheme that can improve the capability to predict the elastic properties of the composites. This will be further explained in the following sections.



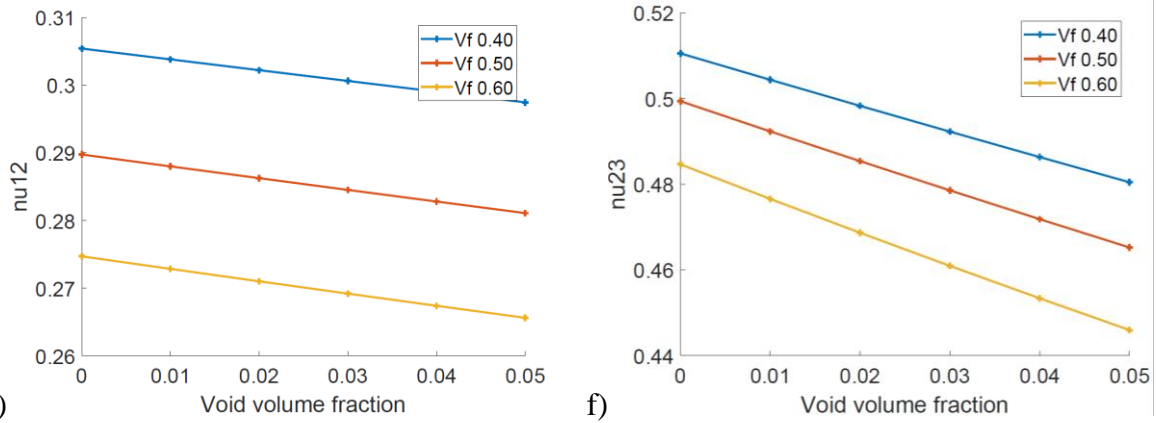


Figure 49: Evolution of elastic properties in glass fiber composites with void a) Longitudinal young's modulus, b) Transverse Young's modulus, c) In-plane shear, d) Out-of-plane shear, e) Out-of-plane Poisson's ratio and f) In-plane Poisson's ratio.

4.3 Numerical homogenization

The basic steps in the numerical homogenization are the generation of microstructure, determining mesh parameters, and application of the boundary condition and homogenization as presented in Figure 50.

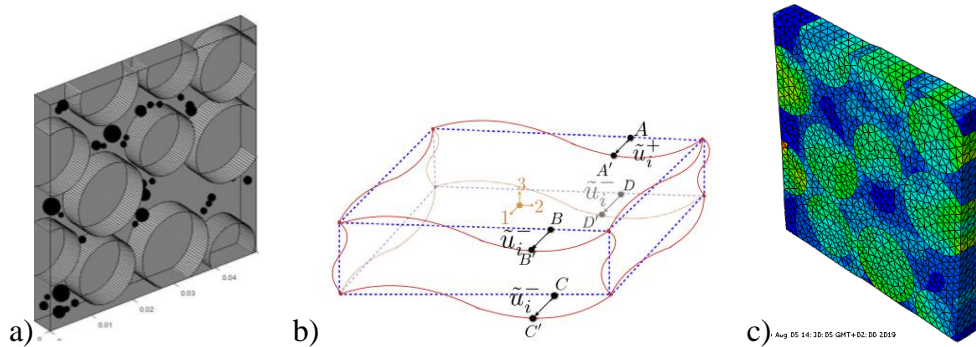


Figure 50: Steps for numerical homogenization. a) Generation of microstructure, b) Meshing and boundary conditions and c) Calculation of elastic properties.

4.3.1 Generation of microstructure

At the microscale, it refers to the process of arranging the constituents (fiber/voids) inside a matrix domain. The initially suggested approaches were based on the hard-core models, also known as Random Sequential Adsorption (RSA) models, which follow the sequential placement of fibers in a given space [104]. The main limitation of RSA is the maximum fiber volume fraction, which is around 55% [104,193]. A few works identified a solution to overcome this limitation by decreasing the RVE size to as small as 5-10 times the fiber radius to achieve higher fiber volume fractions (65%), facilitating the analysis of high-performance composites [194,195]. On the other hand, the RSA was modified by adding an intermediate step where the fibers are steered towards the matrix-rich regions, thus increasing the maximum fiber volume fraction to 65% for a large RVE. This approach was further modified by considering the variability of fiber diameters and inter-fiber distances (IFD), but this led to a

drop in the fiber volume fraction to 55% [196]. To reproduce the same fiber distribution and the fiber volume fraction of a domain of interest in a micrograph, image-based reconstruction can be used, but these methods are proven to be computationally costly and the accuracy of the results depends on the quality of the image [197,198].

Although these values of maximum fiber volume fraction may seem reasonable in several practical applications (mostly high-performance applications), it was observed that the tow fiber volume fraction could reach a value of 75% [199,200], which most of the current algorithms are not able to generate. Furthermore, as previously mentioned, most of the approaches do not consider the statistical equivalency between a real microstructure and a generated microstructure. This disregard may lead to the misinterpretations of local failure strains and damage estimations.

Thus, this work aims at developing an algorithm which fulfills both limits to fiber volume fraction and the statistical equivalency of an RVE containing long aligned cylinders. The generation algorithm is similar to the Nearest Neighbor Algorithm [158] but with specific changes leads to greater computational efficiency and a higher fiber volume fraction. The detailed description of the algorithm is presented in the subsequent section 0, followed by the assessment of randomness and statistical equivalence of generated RVE. Finally, predictions of the elastic properties of generated RVE are compared with experimental results found in the literature.

Generation of fibers

In this work, the RVE is supposed to be a square with side L , and the cross-section on which all the fibers are circular shaped. The inputs of the algorithm constitute the target fiber volume fraction ($V_{target,f}$), the statistical parameters of fiber radius distribution (r_f), and the inter-fiber distances. These parameters are obtained from micrographs (see Chapter 2). From the observation made on micrographs, the inter-fiber distance has log-normal distribution, and the fiber radius has a normal distribution. The current algorithm is similar to that of a classical NNA [158] but with a small yet significant variation which is presented in Figure 52. The step by step functioning of the algorithm is presented below:

Step 1: The initiation of the algorithm is carried out by providing the IFD distributions, fiber radius distributions, and the domain size (δ). An average value of r_f is calculated and the boundaries of a square microstructure with a side length ' L ' ($L = \delta \times r_f$) are defined. A random point (x_1, y_1) is created within a square domain. A radius ' r_f ' is randomly chosen from the normal distribution provided as input by the user.

Step 2: Once the position of the first fiber is validated, the algorithm can identify the maximum of three nearest neighbors based on IFD distributions and allocates the fiber radii to the three new fiber centers. These new fiber centers are oriented at a random angle θ_i where $0 \leq \theta_i \leq 2\pi$ and $\theta_i \neq \theta_{i+1}$ ($i=1,2,3$) as presented in Figure 51. A compatibility check is carried out to confirm that there is no overlap between existing fibers and new fibers. If so, fibers are reassigned with new placement angles to obtain new centers. This local search is repeated for about 30 times, and if the algorithm is unable to find a new center, it simply places two fibers or even one. This

is usually the case when the domain is filled up to 80% of the target fiber volume fraction. Also, if the fiber centers are generated out of the boundary of RVE, that fiber center is omitted from the accepted list of centers.

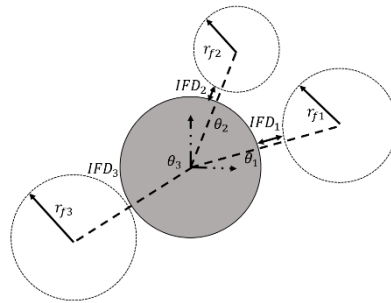


Figure 51: Definition of random angle θ , fiber radius, and inter-fiber distance IFD.

Step 3: The algorithm then moves onto the next fiber and assigns its first, second and third neighbors for which the fiber diameters, placement angle, and IFDs are assigned in a similar way described in Step 2. This is repeated until the $V_{target,f}$ is reached.

The fiber volume fraction at the end of each iteration is calculated based on the pixel method. Since the periodicity is not imposed on the fibers, this approach was more convenient and simple, rather than calculating the fiber volume fraction using the total number of fibers placed. The entire domain is discretized into pixels with the size $0.1 \times 0.1 \mu\text{m}^2$. The fibers are assigned with a color label of white, and black colors, which is assigned to the matrix. The algorithm then estimates the fiber volume fraction based on the number of white pixels within the domain.

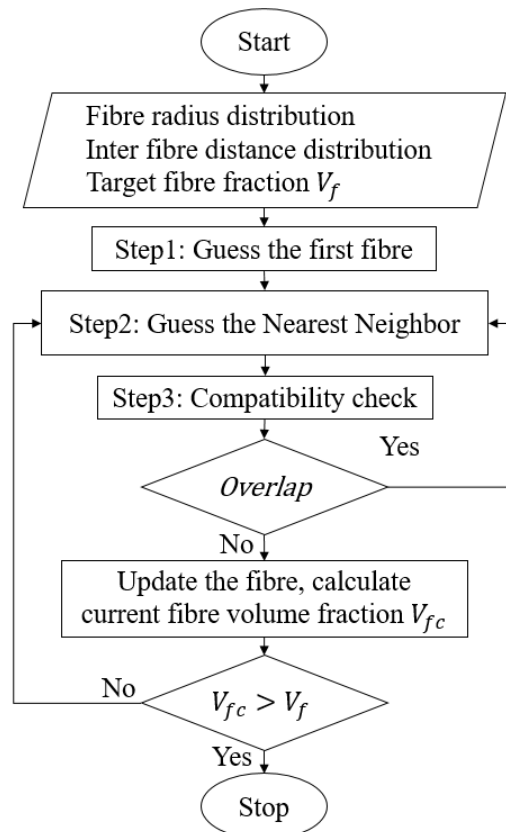


Figure 52: Flowchart for modified NNA.

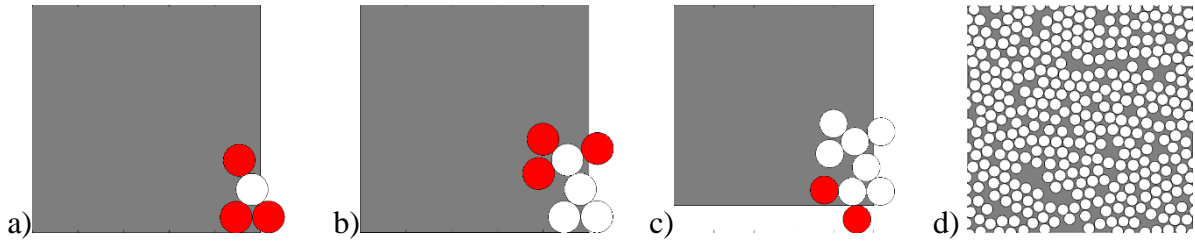


Figure 53: Generation of microstructure using modified NNA. a) Placing of three near neighbors, b-c) Packing the next set of fibers based on near neighbor distances, d) An example of generated microstructure with $V_f=65\%$ and $\delta=50$.

Computational efficiency of fiber generation algorithm

The algorithm in this work is implemented using MATLAB® on an Intel® i5 Processor. The microstructures generated using the current algorithm are presented in Figure 53 d) (more microstructures are presented in Annexe 7.4). It can be noticed that these microstructures are not periodic, but the periodicity can be imposed if necessary. The execution time is defined as the time taken for the algorithm to produce a list of fiber positions from the moment of initiation. In Figure 54 a), it can be noticed that with the increase in the domain size, the RVE generation time increases exponentially. However, even for an RVE of size $\delta=80$, the generation time is only about 800 seconds. To further appreciate the efficiency of this algorithm, a comparison is made between the existing well-known generation algorithms in the literature [201–205] and the current algorithm. It can be noticed straight away that the current algorithm is much faster even after considering all possible statistical inputs. For lower values of δ , i.e. 20, 30 and 40, the execution time is much shorter than 110 seconds. Furthermore, at a fixed domain size of $\delta=40$, the execution time for the current algorithm for 70% fiber volume fraction is only about 40 seconds with a minimal discrepancy (see Figure 54 b)). The computational efficiency of this algorithm allows the user to generate several hundreds of RVE to carry out statistical analysis or other studies demanding large data sets. The efficiency of this algorithm can be further improved by parallelizing the algorithm using GPUs. This algorithm proved the unique ability to impose exact microstructure parameters such as fiber size distribution and Inter-fiber distance (IFD) distribution during the generation. The comparison between the experimentally measured parameters and numerically generated parameters is presented in Figure 60.

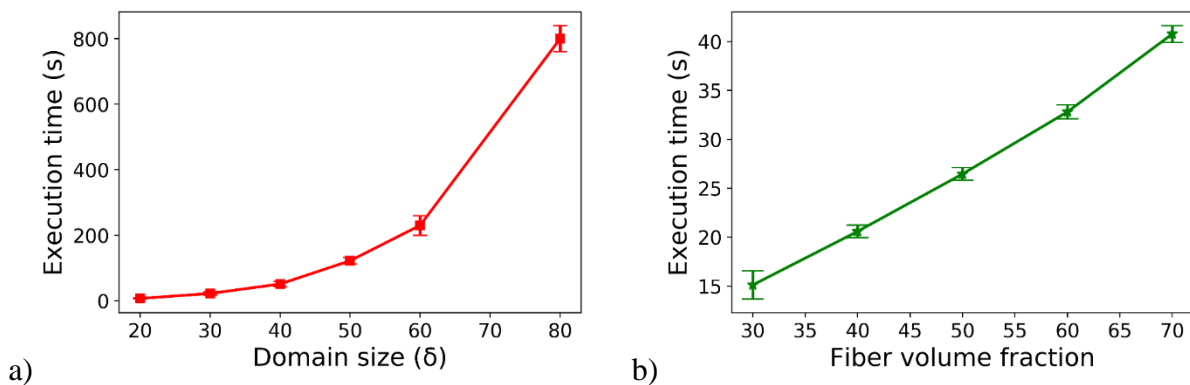


Figure 54: Computational efficiency of the algorithm a) Execution time for various domain sizes $V_f=65\%$ and b) For domain size of $\delta =40$.

Algorithm	Time (seconds)
RAND_uStru_GEN [205]	198.6±9.60
Melro et al. [201]	432±27
Catalanotti [204]	36900
Herràez et al. [202]	1e6
Bailey [203]	6456
This work	120±20

Table 14: Computational efficiency, Comparison with existing algorithms at $V_f=65\%$.

Different statistical descriptors are proposed which characterize the spatial point patterns [206] and these can be applied to the microstructural arrangement in composite materials by considering the fiber centers as a spatial point pattern. Two descriptors mostly used in the literature are Ripley's K function and pairwise distribution function [158,207]. The evaluation of these statistical descriptors is presented in subsequent sections.

Ripley's K-function is one of the spatial analysis methods used to describe the degree of dispersion of points within a domain of interest [208]. It is defined as the ratio between the number of points (in this case, fiber centers) within an observing radius ' r ' that can be incremented about an arbitrary point to the total number of points in a unit area as follows.

$$K(r) = \frac{A}{N^2} \sum_i \sum_{j \neq i} \frac{I(d_{i,j} \leq r)}{w(l_i, l_j)} \quad (4.5)$$

where A is the area of RVE, N is the number of fibers, $d_{i,j}$ is the distance between two points i, j . I is a conditional indicator which equals to 1 if the condition holds or 0 if false. $w(l_i, l_j)$ denotes the circumference of the circle within $d_{i,j}$. For an RVE which is completely random (CSR), Ripley's K-function becomes πr^2 . This can be used as a reference to understand how regular packing such as hexagonal packing fluctuates, whereas random packing approaches around CSR for higher values of r are presented in Figure 55.

$$L(r) = \sqrt{\frac{K(r)}{\pi}} \quad (4.6)$$

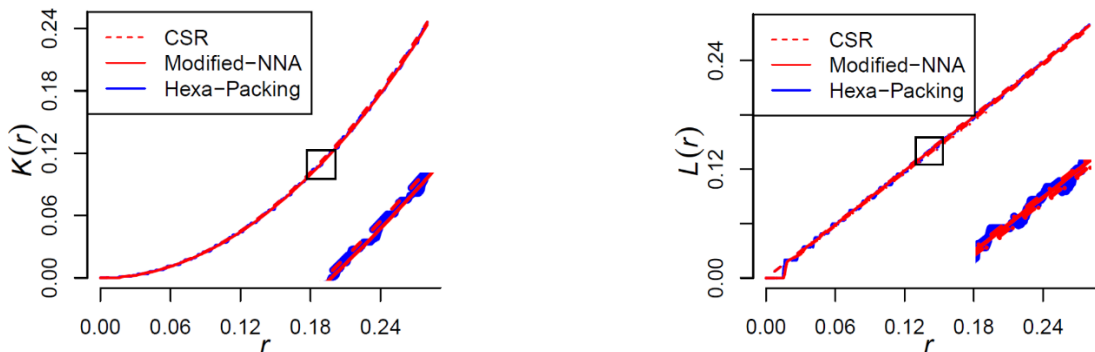


Figure 55: Ripely's K-function and modified L-function calculated at a different radius to analyze the randomness of the microstructure.

Pair-wise distribution function (PCF) also termed as g -function which is a derivative of the K -function is defined in Equation 4.7. In this work $g(r)$ can be calculated directly from a $K(r)$ whereas a special formulation can be adopted from [206].

$$g(r) = \frac{K'(r)}{2\pi r} \quad (4.7)$$

The function $g(r)$ provides information about, at which distance from any arbitrary point of a domain the distribution tends to be completely CSR. For the definition of $g(r)$, the PCF will be one for complete spatial random distribution, $g(r) > 1$ indicates the clustering and $g(r) < 1$ means the distribution is abnormal. In Figure 56, the dashed red line indicates the CSR as mentioned $g(r) = 1$, and the solid blue and red lines indicate the regular Hexa-packing and microstructure developed by modified-NNA respectively. It is observed that at an annulus radius of 0.1mm the microstructure tends to be approaching CSR whereas the regular packing has high fluctuation.

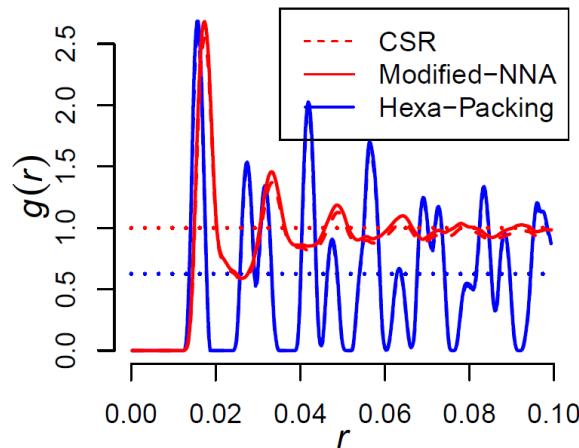


Figure 56: Pairwise correlation function calculated of CSR, Hexa, and Random packing.

Local fiber packing fraction (F_{LFP}^i) is calculated based on the Delaunay triangulation method. The reason for selecting this approach is to emphasize the fiber clustering and identify resin-rich areas as shown in the reference [209]. The calculation of F_{LFP}^i using the approach of Delaunay triangulation is implemented using a MATLAB® script. Once the microstructure is generated, it is directly fed to this script as input, where the domain is discretized into several small triangles with fiber centers as vertices. Then, the fiber volume fraction of each triangle is calculated by sectoring the fibers lying inside of the triangle. The calculation process for the **local fiber packing** (F_{LFP}^i) and **local fiber density** (T_{LFD}^i) was already explained in Section 3.3.2. The difference between F_{LFP}^i and T_{LFD}^i is shown in Figure 57.

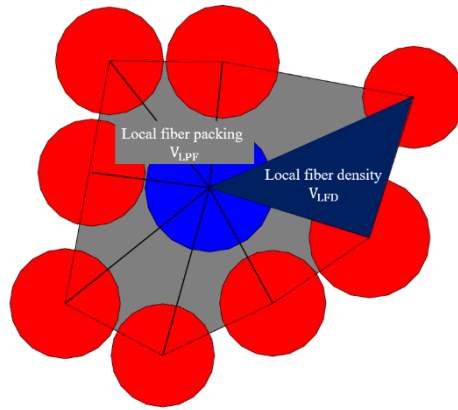


Figure 57: Figure to explain the local fiber packing fraction and local fiber density.

This is repeated for every fiber thus providing us the information regarding the fiber clusters and resin-rich zones as shown in Figure 58. In Figure 59, a clear distinction between conventional hexagonal packing and random packing can be observed. The Delaunay triangles for hexagonal arrangement are almost of the same area whereas the Delaunay triangles in an RVE exhibit varied areas. In Figure 60, the peaks in red represent the highest local fiber volume fraction which is around 0.69 while there are regions where F_{LFP}^i is 0.39.

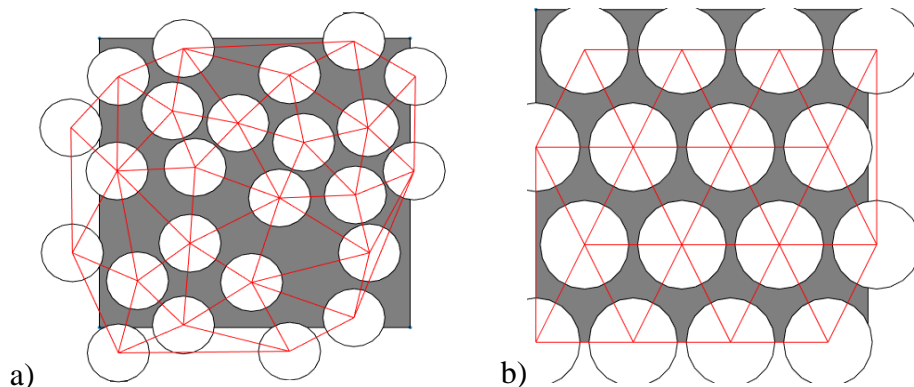


Figure 58: Delaunay triangulation of a) Random fiber arrangement and b) Regular hexagonal arrangement.

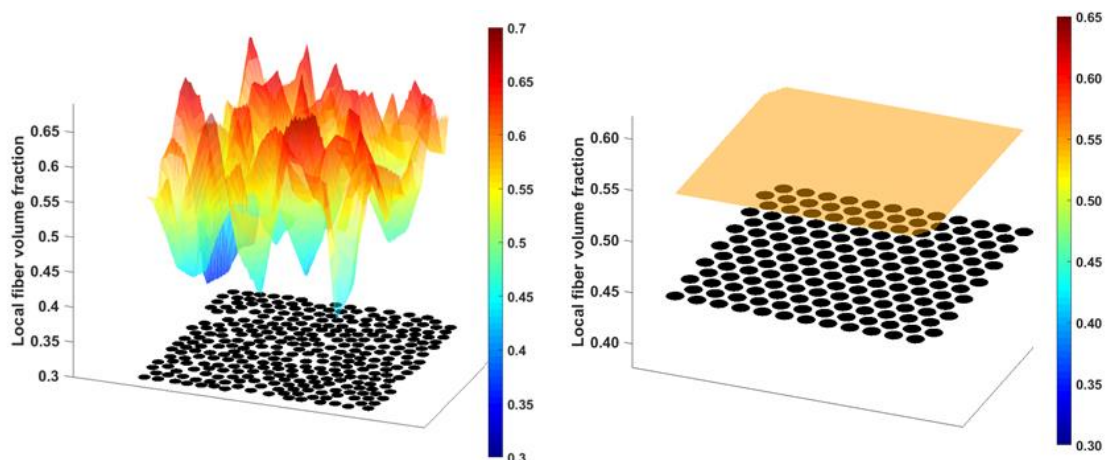


Figure 59: Variation in local fiber volume fraction for Random fiber arrangement and Regular hexagonal arrangement.

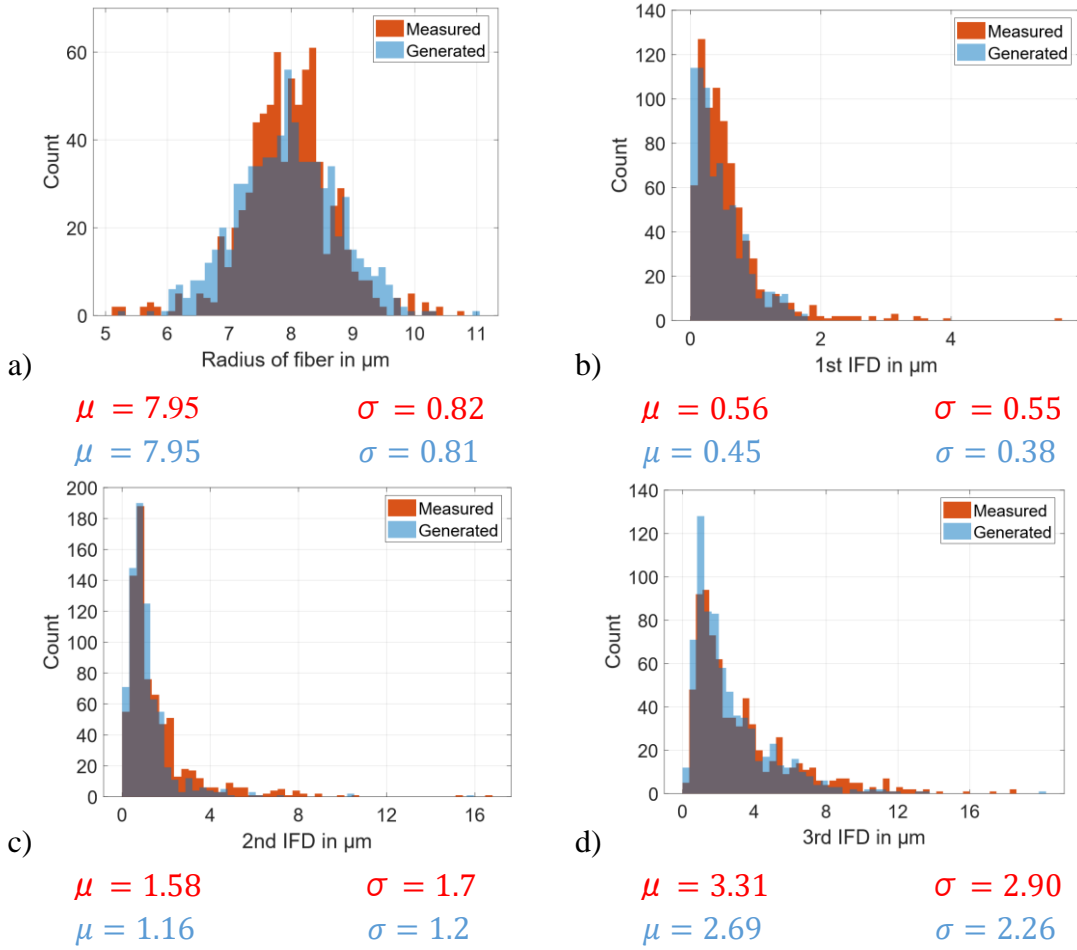


Figure 60: Comparison of statistical data of fibers for experimentally observed and generated RVE: a) Fiber radius distribution and b)-d) 1st, 2nd, and 3rd nearest neighbor distance respectively.

Generation of spherical voids by Double NNA

As introduced in Section 2.4 the intra-yarn voids have a complex shape and the present algorithms do not have systematic provision to generate the microstructure with voids. Hence in this thesis, we propose two different algorithms for void generation.

- The microstructure with spherical voids.
- The microstructure with the realistic void shapes to accommodate the statistical parameters such as void shape and void location based on the local fiber packing fraction.

At first, the algorithm for the generation of spherical voids is explained. The spherical voids are packed based on the presented NNA algorithm including some modifications such that the spheres cannot overlap on spherical voids and cylindrical fibers. Hence this algorithm is called Double Near Neighbor Algorithm (DNNA). The void generation is based on three kinds of spatial distributions (i.e. homogeneous, random, and clusters). The algorithm for packing spherical voids in the cylindrical fibers domain is presented in Figure 61. The position of the first void is selected randomly in the domain. This position is only accepted if the void does not overlap with the other fibers. The void volume fraction (V_V) in the RVE is calculated after

positioning each void. If the V_v is greater than or equal to the target V_v , the loop will be terminated and all the void information will be saved in a data file. This data will later be used in the generation of the microstructure for FEM simulations. An example of different spatial distributions of the spherical voids is presented in Figure 62.

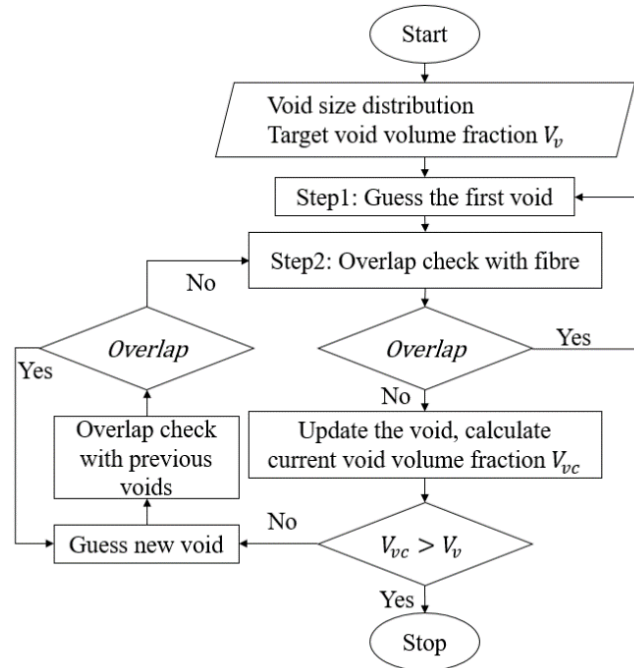


Figure 61: DNNA for voids generation inside the yarn with fixed fiber configuration.

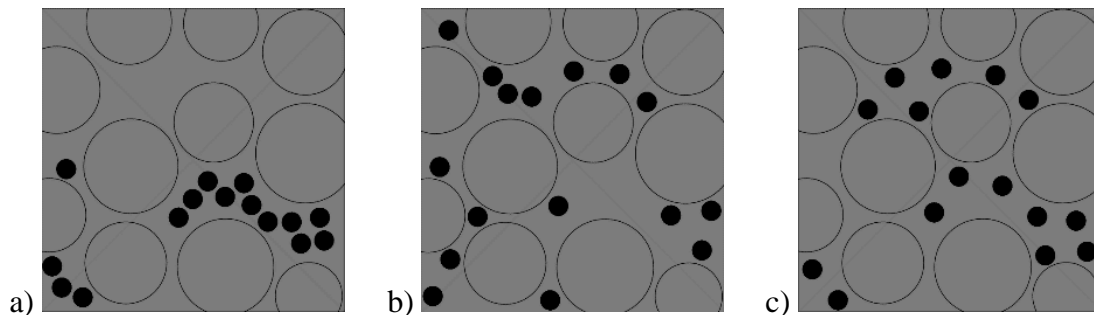


Figure 62: RVE with different void distributions a) Clusters, b) Random, and c) Homogeneous.

Generation void with realistic shapes

Consider an RVE with a fiber volume fraction of 0.60 generated by the NNA. The generation of the RVE with realistic voids can be done in three steps. 1) The first void is initiated in the zone of specified packing fraction. 2) The void is propagated to the neighboring fiber cluster. 3) Once the void area has reached the limit then propagation is terminated and a new void is initiated.

Void initiation: It is based on a general assumption that voids are formed in the local regions with specified packing that can be measured from microscopy images. After the calculation of the local fiber packing (F_{LFP}^i) in yarn, the highest probability of void formation is assigned for

the cluster with the desired packing. As we know the cluster is a collection of adjacent triangles, now to initiate the void from one of the triangles in the cluster, a triangle with high T_{LFD}^i is chosen as shown in Figure 63. The triangle with a red face-color represents the cluster of the triangles and the black triangle represents the highly packed Delaunay triangle in the cluster.

Void propagation: Initial void positioned with respect to the local fiber packing only represents the fraction of the total void content. Thus, the void size is allowed to increase based on the neighbor triangle packing. All the possible neighbor triangles are listed and the void is grown into the triangle with the next highest fiber density T_{LFD}^i . The detailed explanation for the void propagation is described in Figure 64.

Once the initial void is placed, it can have three neighboring triangles that share the common edge (a), clusters attached to the vertices of the void (b), and all the neighbor triangles along with triangles in the previous clusters (c). For the sake of easy understanding, all the neighboring triangles are shaded in blue color. The neighbor triangles list will keep appending until the void is terminated. For the propagation of the void to the next triangle, all the possible neighbors will be considered as presented in Figure 65.

Termination: The void propagation can be terminated in two conditions, either the global void volume fraction has reached the limiting void volume fraction (see Figure 66), or the void area fraction has reached the limit area fraction selected from the calculated statistical data.

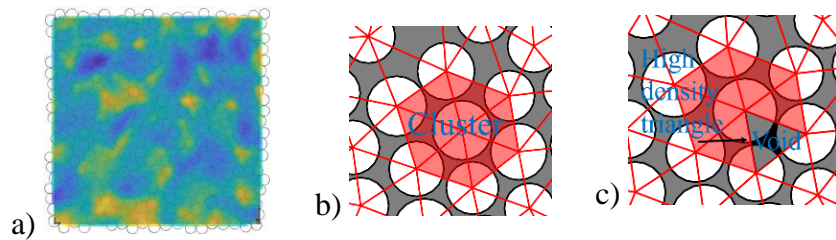


Figure 63: Initiation of the void in the cluster, based on local packing of the fibers: a) Fiber fraction calculated at each fiber, b) Identification of the high packing cluster and c) Initiation of void in the cluster.

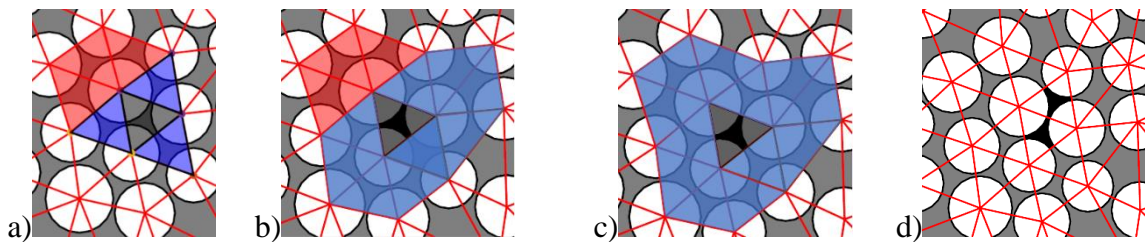


Figure 64: Propagation of the void into the neighbor triangle with highest fiber density: a) Neighbor triangles sharing common sides; b) Neighbor triangle clusters sharing vertices; c) All the neighbor triangles of the void and d) Propagation of the void to a neighbor triangle.

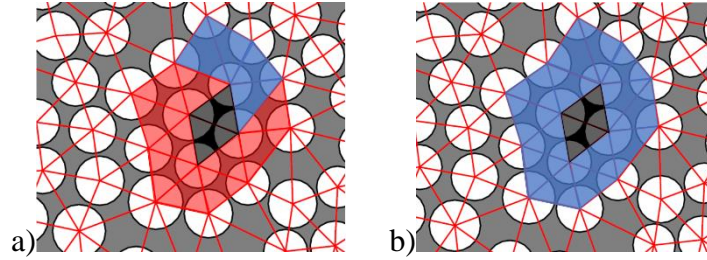


Figure 65: Near neighbor triangles for the 3rd void propagation step: a) New neighbors in the blue and previous list of neighbors in red and b) All the neighbor triangles of the void for next propagation.

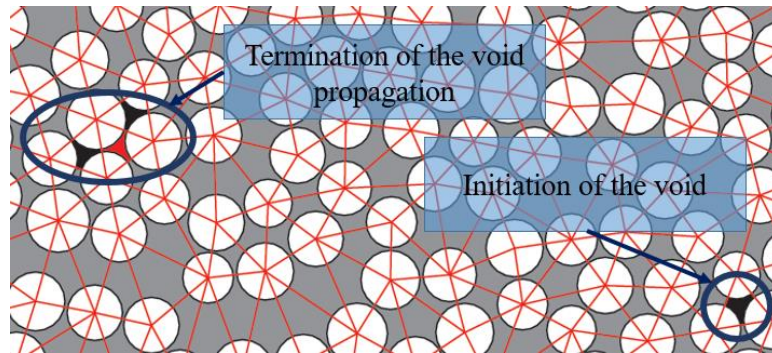


Figure 66: Termination of void and initiation of the new void.

4.3.2 FE simulations

Numerical homogenization is carried out on the generated microstructures to calculate the effective elastic properties [76]. The convergence and computational time of the solution depend on mesh type, finite element size, boundary conditions, and length of an RVE. It also depends on the material model. For example, the introduction of plasticity or damage will substantially increase the computational time. Hence, a study was performed to analyze the dependency of the elastic properties on the element size and it is observed that a tetrahedron element type (C3D4) size below $1\mu\text{m}$ does not affect the solution. In the literature, it is suggested that an RVE should be greater than 40 to 50 times of fiber radius to achieve the convergence, but this statement is only valid for kinematic uniform boundary conditions [158], [103]. Hence, this method needs a larger RVE which leads to higher computational time. On the other hand, periodic boundary conditions (PBC) can converge even at smaller RVE's [210]. However, the applications of PBC requires a periodic microstructure with a periodic mesh. This condition can be bypassed by utilizing approximate periodic boundary conditions (APBC) [211]. Schneider et al. [160] studied the effect of boundary conditions on the homogenized properties of periodic and non-periodic structures and found that APBC is a better choice for a non-periodic structure. The elastic properties are calculated using the Hill-Mandel theorem [212], [103]. which is based on volume average stress and strain and the detail of this study can be found in the literature [213].

Mesh convergence study

The choice of mesh size and element type has a determinant effect on the homogenized properties. Hence an ideal element type and mesh size should be selected based on the

convergence study [151]. The selection of element type depends on the geometrical complexity of the microstructure. For a microstructure with spherical voids, tetrahedral elements are more versatile in terms of meshing complex geometries [214]. And for the selection of mesh element a unit cell has meshed with different mesh sizes from 0.5 to 5 microns and the evolution of the homogenized properties is observed concerning for mesh size. The result presented in Figure 67 indicates that mesh size smaller than or equal to 1 micron does not affect the homogenized properties. Hence, 1 micron is selected as the mesh size for this study. After the meshing is performed, the next step in FE-simulation is the application of boundary conditions, which is presented in the following section.

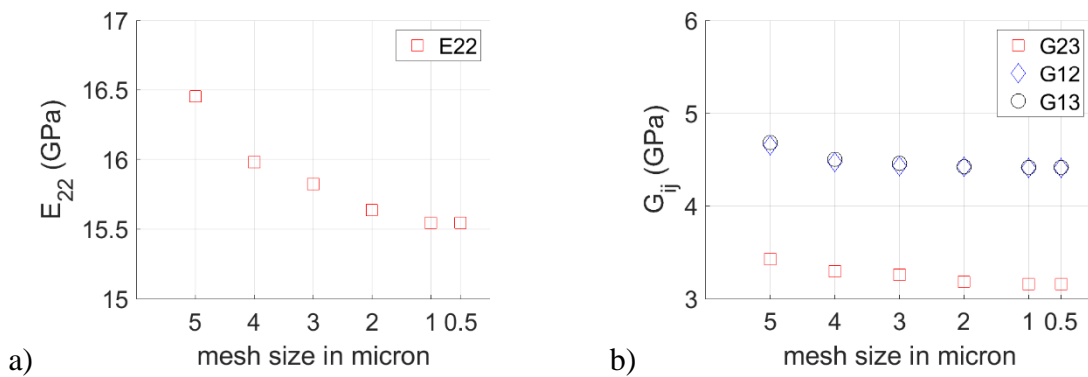


Figure 67: Mesh size convergence study for elastic properties a) E_{11} and b) G_{ij} .

Boundary conditions

The periodic boundary conditions are commonly used for the evaluation of the elastic properties of a microstructure. However, the enforcement of PBC needs a periodic mesh that cannot always be achieved. The non-periodic mesh can be due to the structure is non-periodic and sometimes FE-mesh techniques do not enforce periodicity. For such conditions, approximate periodic boundary conditions can be applied, and in the literature, this method was used by some researchers [215]. There are several methods for implementation of PBC on a non-periodic structure. Nguyen et al. [216] developed an interpolation-based method to relate the displacement of the opposite faces. This method is difficult to implement on commercial FE-solver. Hence the dummy node method used by Garoz et al. [211] was implemented by using an ABAQUS python interface.

Dummy node method implementation for a 2D model is explained in Figure 68. Similarly, it can be extended to a 3D model. The nodes from one of the faces are copied to the corresponding opposite face. Now a tie constraint (yellow) is applied on the copied nodes to the current face and copied nodes in x and y direction act as master nodes. PBC is applied between the copied nodes and current nodes on the opposite face.

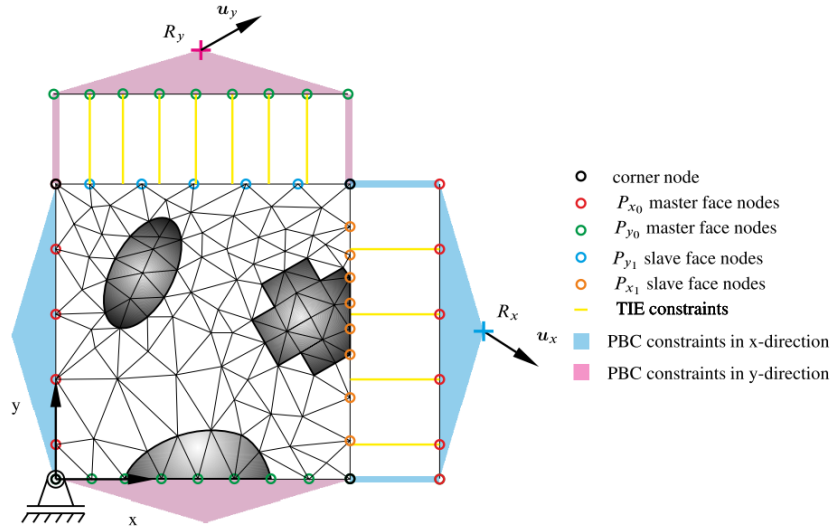


Figure 68: Schematic representation for the application of approximate periodic boundary conditions (APBC) on a 2D model [160].

To validate that APBC does not affect the homogenization, a periodic unit-cell with glass fiber and epoxy matrix, was meshed to generate two models 1) with periodic mesh and 2) with non-periodic mesh. The fiber volume fraction of the unit-cell is 0.6 and the properties of glass fiber and matrix are provided in Table 12. The comparative results are presented in Table 15. It was observed that the application of APBC does not affect homogenized properties.

Mesh type-BC	Periodic mesh-PBC	Non-Periodic mesh-APBC
E11 (GPa)	44.47	44.46
E22 (GPa)	12.05	12.047
E33 (GPa)	12.061	12.057
G12 (GPa)	4.184	4.185
G13 (GPa)	4.180	4.181
G23 (GPa)	3.985	3.986
ϑ_{12}	0.271	0.271
ϑ_{13}	0.272	0.272
ϑ_{23}	0.441	0.441

Table 15: Validation of approximate periodic boundary condition with periodic boundary condition.

Another significant parameter to be quantified is the dimensions of the RVE. They should be chosen concerning the type of boundary conditions applied. A boundary condition should not have any effect on the homogenized properties concerning the RVE dimensions. Hence to choose the RVE size, we performed the homogenization on RVE with the side dimension of 50, 100, 150 microns with APBC. The results of the numerical simulation are presented in Figure 69. It is observed that RVE as small as 50 microns can be representative for elastic behavior and the usage of this RVE size is also found in the literature [217]. Hence, this RVE size of 50 microns or greater will be used in this study.

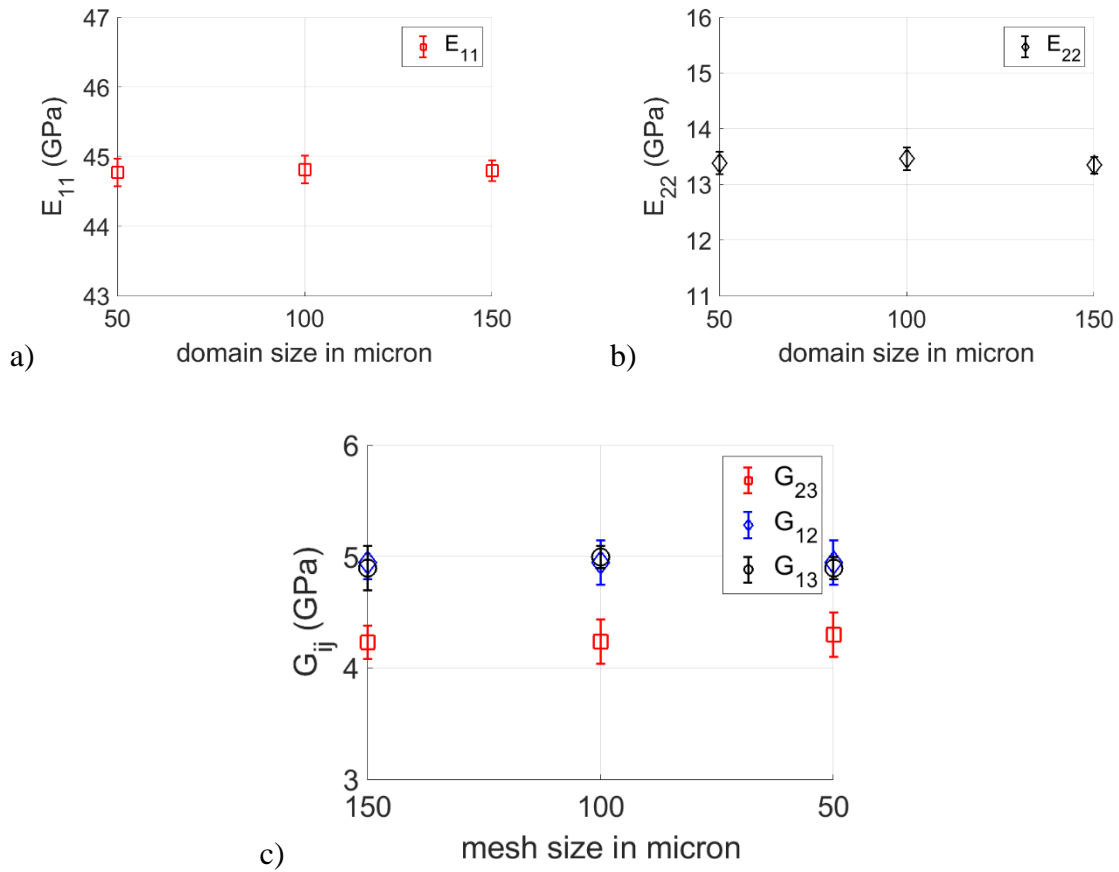


Figure 69: Dependence of elastic properties on the domain size.

Numerical homogenization is carried out by using averaging theorems following Hill-Mandel's macro homogeneity conditions. This was already presented in Chapter 1. The formulation for calculating the elastic properties is presented in Annexe 7.1.

4.4 Results and discussion

Validation of microstructure based on experimental data: A microstructure with a fiber radius of $6.6\mu\text{m}$ and fiber volume fraction of 60% with dimensions $\delta=40$, is generated into a Finite Element (FE) model using a Python interface for ABAQUS. In ABAQUS, a 3D FE model is constructed using hexahedral elements (C3D8R). The mesh element size of $1.5\mu\text{m}$ was chosen based on a mesh convergence study. Using this 3D FE model, moduli in three directions (E_{11} , E_{22} , E_{33}), shear moduli (G_{12} , G_{23} , G_{13}), and Poisson's ratio (ν_{12} , ν_{13}) are calculated. The average material constants estimated using FE analysis are provided in Table 16 and are compared with the experimental results [218]. The numerical estimation exhibited a little variation in the elastic properties when compared to the experimental results and the error percentage is in the limit of the experimental standard deviations. Furthermore, the generated RVEs exhibited the transverse isotropy with $E_{22}/E_{33} = 1.01$ and $\nu_{23}/\nu_{32} = 0.988$.

Property	FEM	[218]	Error (%)
E_{11} (GPa)	43.82	44.7	1.96
$E_{33} = E_{22}$ (GPa)	12.90	12.7	1.55
G_{23} (GPa)	4.66	4.5	3.55
$G_{12} = G_{13}$ (GPa)	4.85	-	-
ν_{12}	0.28	0.29	3.44
ν_{23}	0.42	-	-

Table 16: A comparison of numerical estimation and experimental results of elastic properties.

Voids: Intrayarn voids in a 3D textile composites have irregular shapes based on the observations made on the micrographs and statistical data such as void size and fiber size distribution. We proposed an algorithm based on local fiber packing fraction to create realistic voids either in fiber-rich zones or in matrix rich zones. An extension for a classical NNA was developed to generate spherical voids with three different sizes (i.e. $0.2 \times$ fiber radius (R_f), $0.25 \times R_f$, and $0.3 \times R_f$) and three different spatial distributions (i.e. homogeneous, random, and clusters) for each size.

Spherical voids: Reduction of elastic properties for different void sizes are presented in Figure 70. 4.0-4.5% of spherical voids results in an 8-9% reduction of transverse tensile modulus and 10% of out of plane shear modulus. Observations on the global properties do not efficiently present the effect of the void spatial distribution (homogeneous, random, and void clustering). Hence a detailed analysis of the reduction of the properties with respect to different void parameters is also presented.

Figure 71 a), c) indicate the reduction of mechanical properties when the void percentage is 1% and b), d) for 4% voids, respectively. The red dots represent the clustering, the blue squares for the random, and the green rhombi for the homogeneous void distribution. For 1% voids smaller voids ($0.2 \times R_f$) result in a 4% reduction in out-of-plane shear modulus, whereas the large voids ($0.3 \times R_f$) result in a 2% reduction. A similar trend is also observed for transverse Young's modulus. However, when the void content is increased to 4% out-of-plane shear modulus in both the microstructures with large and small size voids has been reduced by 11%. Hence, we can state that at lower V_v RVE with large size voids showed higher mechanical properties than the RVE's with smaller voids.

Clustering of void results in a higher reduction of elastic properties and orthotropic behavior of the microstructure. A cluster of bigger voids reduces (2.3%) the elastic modulus higher than clusters of the smaller voids. However, at a higher void volume fraction greater than 3%, void size and spatial distribution showed no effect and elastic properties monotonically decrease with an increase in void volume fraction.

Hence, It can be concluded that at lower void volume fractions (<3%) the void size and spatial distribution affect the matrix dominant properties. Whereas void content higher than 3% the effect of the void characteristics can be neglected and void volume fraction can be a good parameter to represent the effect of void on mechanical properties.

Realistic voids: At any given V_v , an RVE with voids in fiber-rich zones (FRV) have ineffective stress transfer and results in lower elastic properties than voids in a matrix rich zone (MRV) (see Figure 74). The matrix voids are bigger and have a high aspect ratio resulting in the orthotropic behavior of the microstructure. At maximum void content of 4.5%, MRV results in 30% of elastic properties, and FRV causes a 45% reduction of elastic properties (see

a) Voids in matrix rich zone b) Voids in fiber-rich zone c) The percentage of variation
Figure 73).

Size of void $R_v = 0.2R_f$

Size of void $R_v = 0.25R_f$

Size of void $R_v = 0.3R_f$

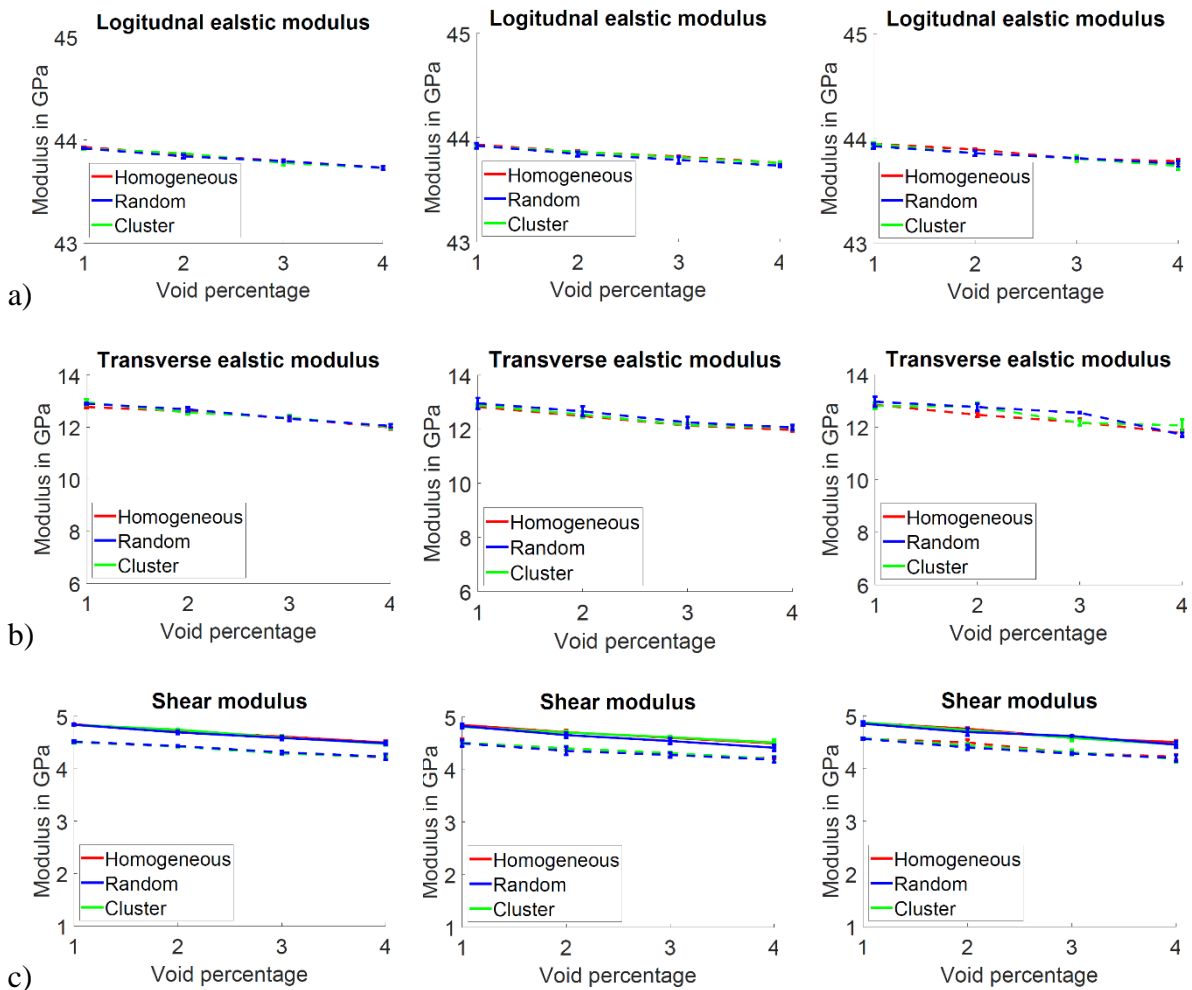


Figure 70: Reduction of elastic properties due to spherical voids of different sizes and distribution a) E11, b) E22, c) G12 (solid line), and G23 (dashed line).

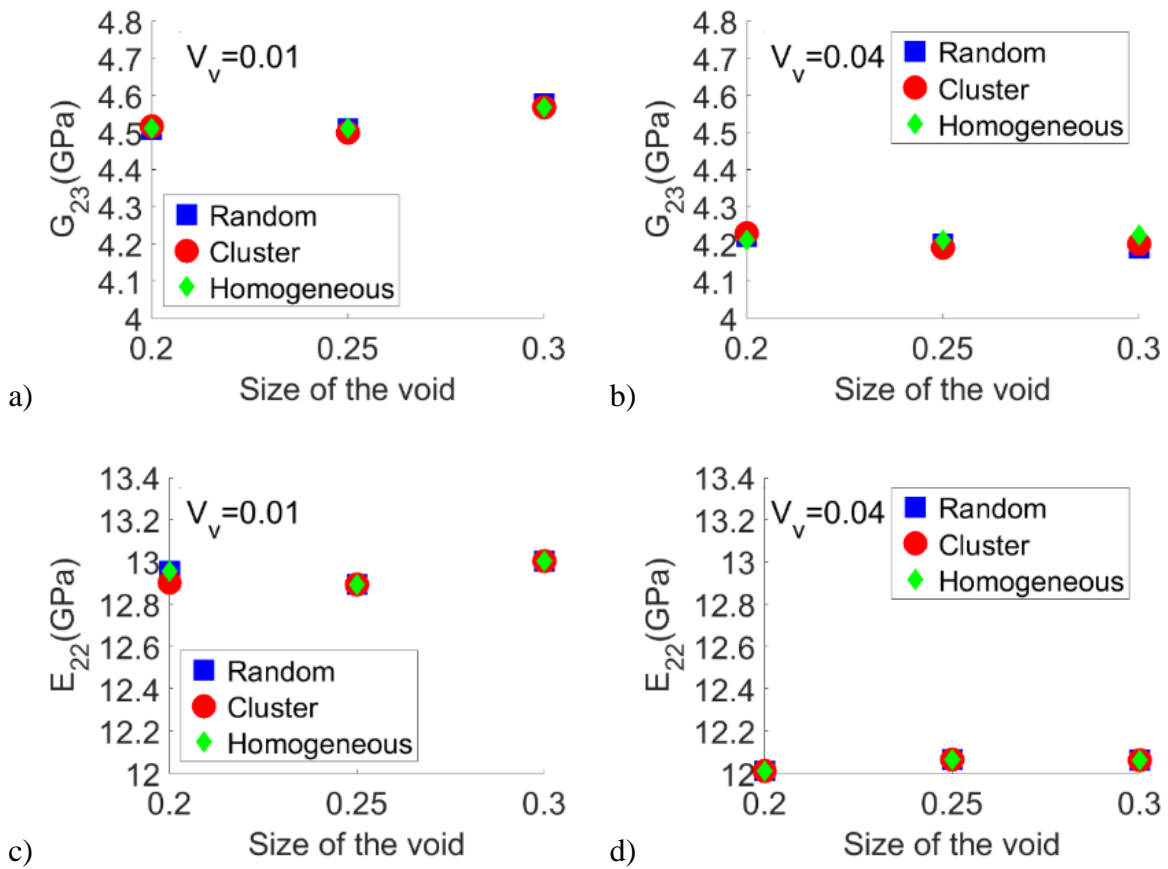


Figure 71: Variation of a) & c) G_{23} & E_{22} for $V_v=0.01$ b) & d) G_{23} & E_{22} for $V_v=0.04$.

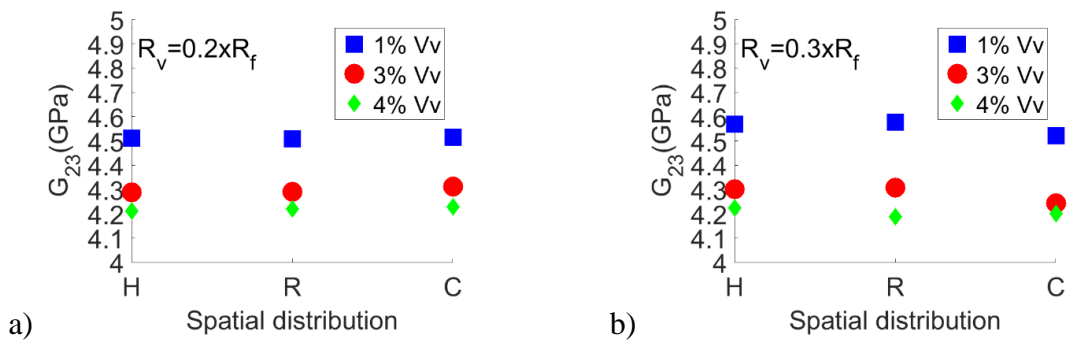
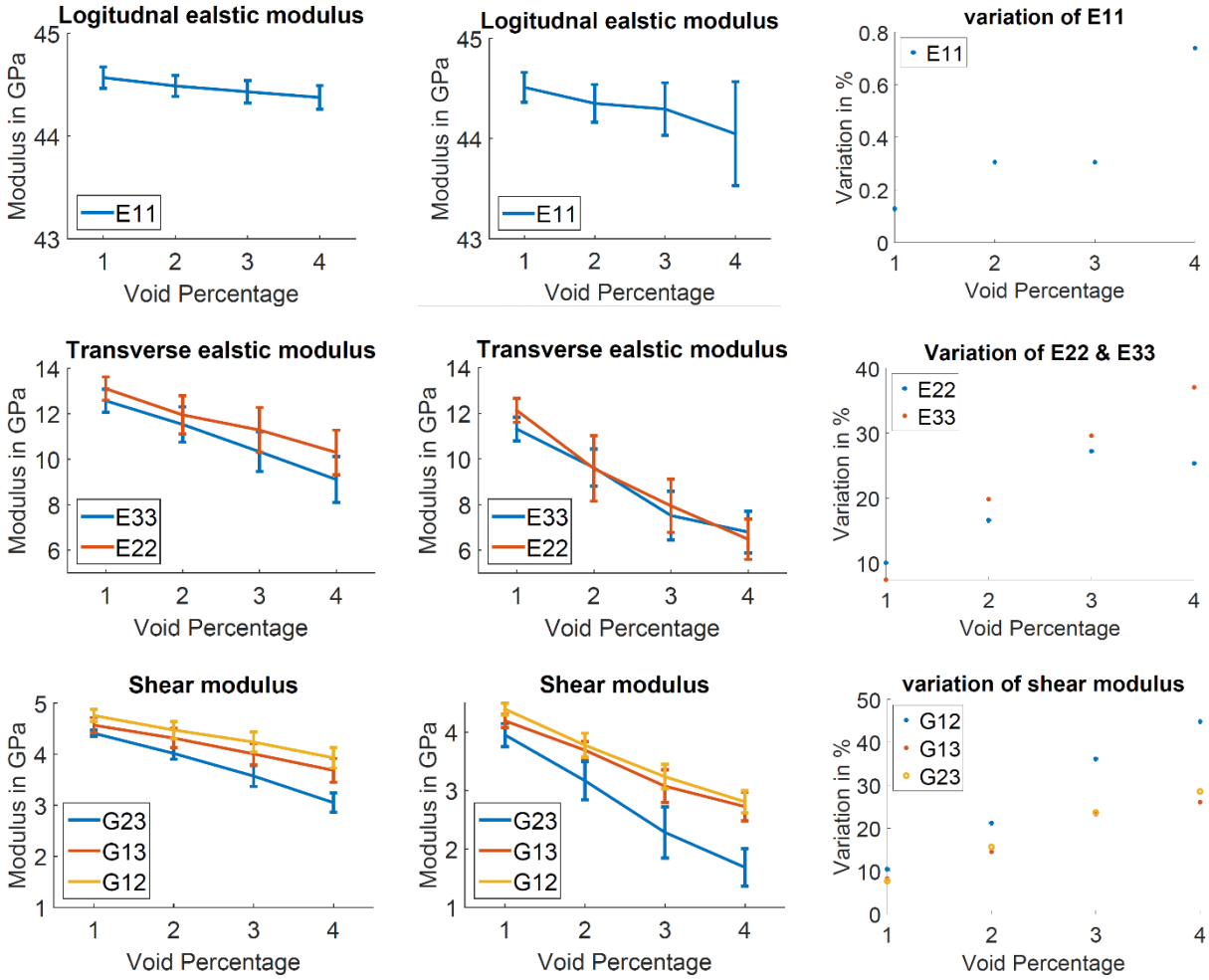


Figure 72: Variation of G_{23} to the spatial distribution of voids a) Smaller voids ($R_v=0.2R_f$) and b) Bigger voids ($R_v=0.3R_f$).



a) Voids in matrix rich zone b) Voids in fiber-rich zone c) The percentage of variation
 Figure 73: Reduction of elastic properties to voids in a) MRV & b)FRV zone and c) The percentage of variation in elastic properties in FRV to MRV.

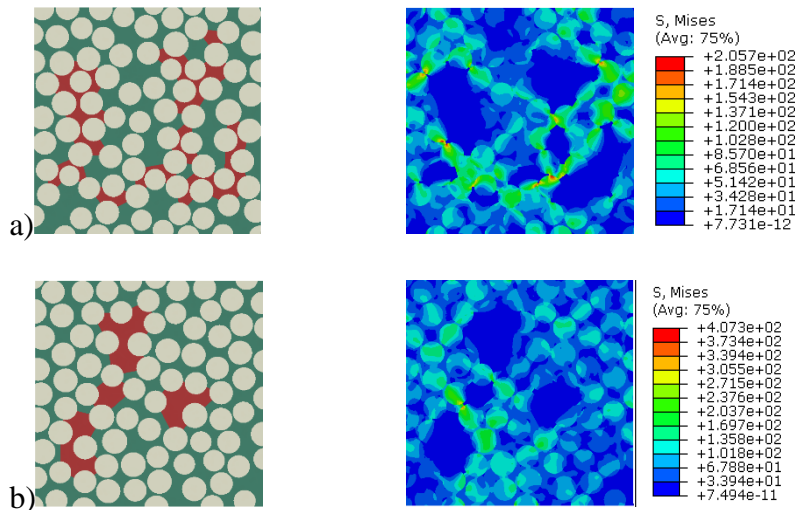


Figure 74: Reduction of stress transfer in RVE with a) Voids in the fiber-rich zone when compared to b) Voids in matrix rich zone.

Comparison between analytical method and FEM: Analytical stepping scheme over predicts the elastic properties as they do not consider the parameters such as the void distribution and irregular void shapes. This phenomenon was conclusively observed in this study when the realistic void shapes are considered. This comparison of the mechanical properties to the void shape is presented in Figure 75. The blue markers represent the stepping Mori-Tanaka scheme, and the red the FEM solution considering voids homogeneously distributed and shaped like spheres. The green and magenta represent the MRV and FRV respectively. It is conclusive to state that, considering the void shapes to be spherical, the numerical simulation and analytical modeling have similar behaviors. However, in the literature, it was found that at a given void percentage of 4% the in-plane shear modulus can be reduced by 18 to 30% [63] which was observed in the MRV. The case of FRV was not realistic and experimentally it is observed that void does not occur in these regions. Thus, MRV is a better choice to estimate the elastic properties of the yarns or UD composites. This technique will later be used to estimate the elastic properties of the 3D yarn to perform a full-scale multiscale simulation.

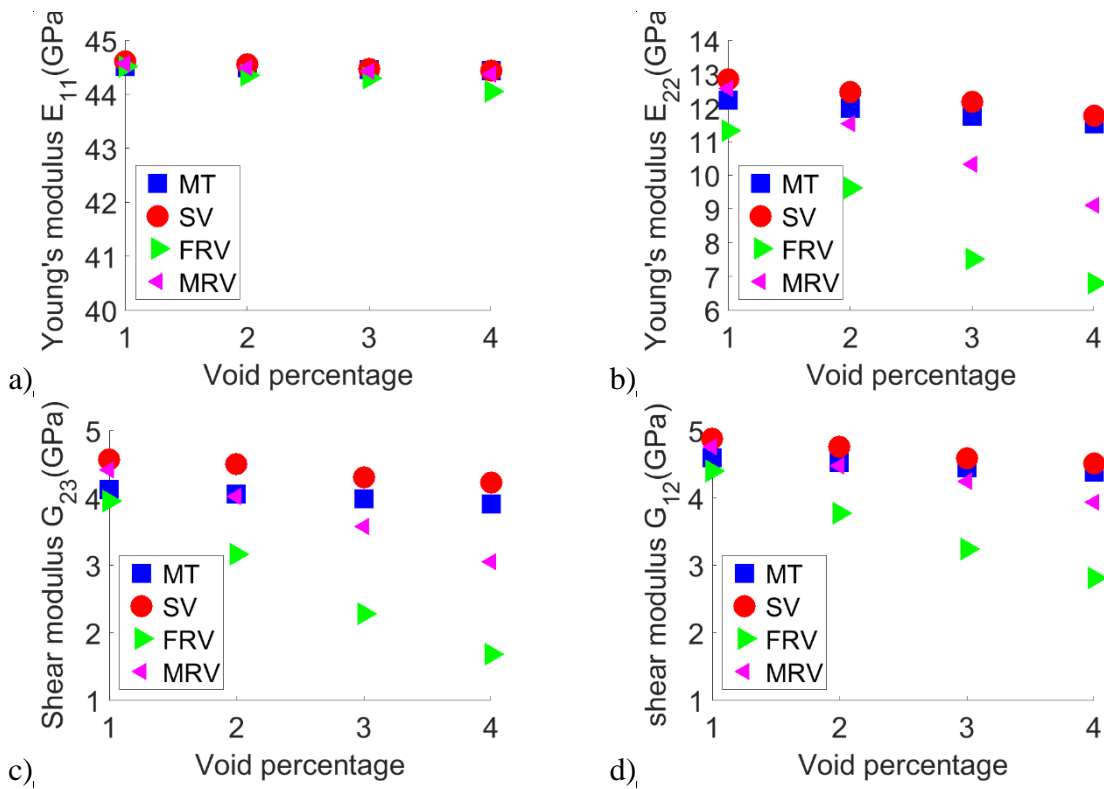


Figure 75: Comparison of analytical and FEM results for different void shapes a) Longitudinal elastic modulus, b) Transverse modulus, c) In-plane shear modulus, and d) Out-of-plane shear modulus.

4.5 Conclusions

This chapter presented the analytical method and numerical solutions to homogenize the yarn's elastic properties. First considering that yarns have only cylindrical fiber and spherical voids, we proposed a stepping scheme for Eshelby inclusion based Mori-Tanaka approach. For the analytical method, the error in predicting the elastic properties increases with an increase in the total void volume fraction. The error was correlated to the approximation of the void morphology considered in the calculation. Hence, we proposed the numerical simulation as a better approach to predict the elastic properties of the yarns in textile composites.

Also, we proposed three novel algorithms to generate the microstructure of the yarn for numerical simulation:

1. We developed an algorithm to generate a statistically equivalent RVE for the textile composite yarns (only fibers). For this, the user must provide the measurement data of the fiber radius distribution and inter-fiber distance distribution. The maximum packing fraction of the algorithm was found to be 0.83. The proposed algorithm is one of the fastest RVE generators respecting the fiber radius and spatial distribution.
2. Double near neighbor algorithm was proposed to pack the spherical voids with different radius (0.2, 0.25, and 0.3 times of fiber radius) in the RVE. Using this approach the user can adjust the spacing between the adjacent voids. This facilitates the generation of the void clusters in the RVE.
3. An algorithm based on the local fiber packing was proposed to generate realistic voids in the RVE. Using this, the user can choose to generate the voids in the desired location, having a specific local fiber packing fraction.

We conducted a parametric study to analyze the effect of void shape, radius, and spatial distribution on the elastic properties of yarn. After a convergence study, the element size of $1\mu\text{m}$ was selected for the numerical simulations. Tetrahedron elements were chosen for the RVE with spherical voids to facilitate the mesh generation. For RVEs with realistic voids, we decided to use the hexahedron mesh. After a converge study on the size of the RVE, the size of the RVE for spherical voids was $50\mu\text{m}$ and $150\mu\text{m}$ in the case of realistic voids. Approximate periodic boundary conditions were applied to the RVE for the numerical simulation. The homogenization was carried out within the framework of Hill-Mandel's theory of macro-homogeneity.

We observed that transverse properties are highly affected due to voids. On the contrary, voids have a negligible effect on Young's modulus in the fiber direction. The reduction of transverse Young's modulus was not the same for all the void shapes. In spherical voids, the elastic modulus was reduced by 11%, 17.56 % for matrix rich voids, and 33.3% for voids in fiber-rich zones. This behavior was directly related to the difference in the void shapes for the three cases. Voids with a higher aspect ratio (for the case of FRV) resulted in a higher reduction of the elastic properties. These observations were confirmed following the studies in the literature [34,63] where they observed the decline of the elastic properties with an increase of the void aspect ratio.

The spatial distribution of spherical voids affects the elastic properties when the void volume fraction is smaller than 0.03. Clustering of bigger voids results in a faster reduction (2.3%) of the elastic properties. In contrast, the clustering of smaller voids does not have any impact on the elastic properties. And also, at lower void content, the RVE with $0.3 \times R_f$ spherical voids 4% exhibits better elastic properties than the RVE with a void size of $0.2 \times R_f$.

We conclude that void aspect ratio, radius, and spatial distribution play an essential role in the yarns' elastic properties. Compared with the literature, the elastic properties predicted by the MRV showed a realistic reduction of the elastic properties. Spherical void underestimates the effect of the void, whereas the FRV overestimates. Hence, we propose the MRV based realistic voids to calculate the elastic properties of the yarn for the multi-scale simulation to be carried out in Chapter 5.

5 Mesoscale reconstruction and Multiscale Modeling

5.1 Introduction

We finalize this study focusing on the meso-scale simulations. In this chapter, we present the segmentation techniques to reconstruct the realistic microstructure from micro-CT data in Section 5.2. The statistics (void volume distribution) of the inter-yarn voids are presented in Section 5.3. Elastic properties of the composite are predicted by multi-scale numerical simulation and validated with experimental results in Section 5.4. At the end, the conclusions are presented in Section 5.5.

5.2 Creation of the voxel models

The advantage of realistic voxel models over the ideal models has been discussed in Section 2.6.4. Hence, here we present the methodology to perform segmentation to generate a voxel model from μ CT data by using VoxTex. The distribution of the material constituents (matrix/yarns/voids) in the voxel model is the result of the segmentation of the μ CT data. In the segmentation process, the total material is subdivided into sets of non-overlapping sub-domains. In other words, it is the process of mapping/classification of a voxel into a particular finite set. The classification of the voxel is carried based on the feature vector which is calculated over every voxel. A feature vector for a segmentation process can be defined based on the required type of classification. For example, if the segmentation involving the separation of warp and weft yarns based on the material orientation angle can be defined in the feature vector. Otherwise, the degree of anisotropy is enough to segment reinforcement and matrix. In this work, the material consists of four different subsets (matrix, voids, warp, and weft). Hence, the feature vector consists of structural anisotropy (β), average gray value (g), and orientation angle (φ). The calculation of these key parameters is explained below.

The calculation of the feature vector utilizes the structure tensor method. This method is widely used in the field of image processing for the detection of edges [219] and image segmentation [220]. For a 3D image ($I(x_1, x_2, x_3)$) the structure tensor ($S(p)$) is defined as follows.

$$S(p) = \int_{w(p)} s'(r) dr \quad (5.1)$$

and $s'(r)$ is calculated by Equation 5.2.

$$s'(x_1, x_2, x_3) = \begin{bmatrix} \left(\frac{\partial I}{\partial x_1}\right)^2 & \frac{\partial I}{\partial x_1} \frac{\partial I}{\partial x_2} & \frac{\partial I}{\partial x_1} \frac{\partial I}{\partial x_3} \\ & \left(\frac{\partial I}{\partial x_2}\right)^2 & \frac{\partial I}{\partial x_2} \frac{\partial I}{\partial x_3} \\ Sym & & \left(\frac{\partial I}{\partial x_3}\right)^2 \end{bmatrix} S(p) = \int_{w(p)} s'(r) dr \quad (5.2)$$

In Equation 5.2 $w(p)$ is the window of the integration, which is defined by the parameter w_r . Window size $w(p): \forall \{x_1, x_2, x_3\} (|x_1 - p_1| \leq w_r, |x_2 - p_2| \leq w_r, |x_3 - p_3| \leq w_r)$. Where p represents the current position in the integration window and r is a vector with points (x_1, x_2, x_3) in the image I , relative to the integration window. The actual size of the integration window is given by $2w_r + 1$ pixels (see Figure 76).

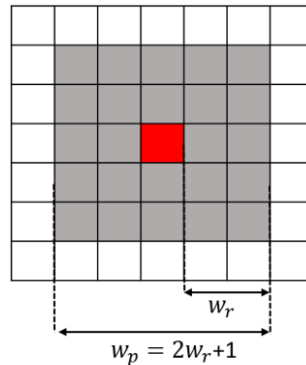


Figure 76: Figure to explain the window of integration $w(p)$ and window size w_r .

The $\frac{\partial I}{\partial x_i}$ can be solved by using the five points finite difference scheme as presented in Equation 5.3, with h , the discretization window, or the size of the integration window. In the equation, the summation is presented only for direction 1. However, the derivatives along the other coordinates can be calculated by changing the corresponding indices in equation.

$$\frac{\partial I}{\partial x_1} = \frac{I(x_1 - 2h, x_2, x_3) - 8I(x_1 - h, x_2, x_3) + 8I(x_1 + h, x_2, x_3) - I(x_1 + 2h, x_2, x_3)}{12h} \quad (5.3)$$

The structure tensor of the complete 3D image I can now be calculated as the discrete sum of the $s'(x_1, x_2, x_3)$.

Now the fiber orientation vector at every voxel can be investigated from the eigenvalue problem for structure tensor S as presented in Equation 5.4. Let $\lambda_1, \lambda_2, \lambda_3$ be the three eigenvalues corresponding to their eigenvectors v_1, v_2, v_3 , indicates the three principal orientations. Then, the eigenvector corresponding to the smallest eigenvalue is the fiber orientation. After the construction of the structure tensor, we can define the feature vector containing structural anisotropy (β), average gray value (g), and orientation angle(φ) at each voxel to perform the segmentation.

$$Sv_i = \lambda_i v_i \quad (5.4)$$

Structural anisotropy (β): It is also termed as anisotropy (β). It is a scalar quantity defined as the ratio of eigenvalues of the structure tensor. If λ_i for $i=1, 2, 3$ are eigenvalues such that $\lambda_1 \leq \lambda_2 \leq \lambda_3$, then β can be calculated by Equation 5.5. By the definition, the value of β approaches zero for the isotropic voxels (matrix, voids). For the anisotropic materials like fiber yarns, the β will be smaller than one.

$$\beta = \begin{cases} 1 - \frac{\lambda_1}{\lambda_3}, & \lambda_3 > 0 \\ 0, & \lambda_3 = 0 \end{cases} \quad (5.5)$$

Average gray value ($g(p)$): It is a scalar value represented by $g(p)$ defined as the average intensity of the image $I(r)$ for window $w(p)$. It can be calculated as the discrete sum of the intensity over an integration window $w(p)$ Equation 5.6. It is also referred to as the density of the voxel. This parameter helps to segment the image into a set of matrix, void, and yarns.

$$g(p) = \int_{w(p)} I(r) dr \quad (5.6)$$

Azimuthal angle: It is represented as φ (Phi), can be calculated by Equation 5.7. This variable consists of information about the local fiber orientation. φ is the angular description of the fiber orientation in the spherical coordinate system that coincides with the plane of the textile. This is an essential parameter to segment the warp and weft yarns in the material. This technique for segmentation of the yarns was also used by Yang et al [162], to perform the segmentation on the 3D-orthogonal composite.

$$\varphi = \tan^{-1} \frac{v_x}{v_y} \quad (5.7)$$

where v_x and v_y are the orientation vectors in the Cartesian coordinates.

The histogram showing the mutual distribution of anisotropy and density is presented in Figure 77 a). This statistical information would be sufficient to segment the μ CT data into a set of matrix and yarns. However, to segment μ CT data to the individual constituents (warp, weft, matrix, and voids) the feature vector containing the statistical data of density, anisotropy, and fiber orientation angle should be utilized. The statistical distribution of these parameters in the feature vector is presented in Figure 77 b). The result of the application of this procedure to a μ CT acquired on a Twill-3D upstream is shown in Figure 78.

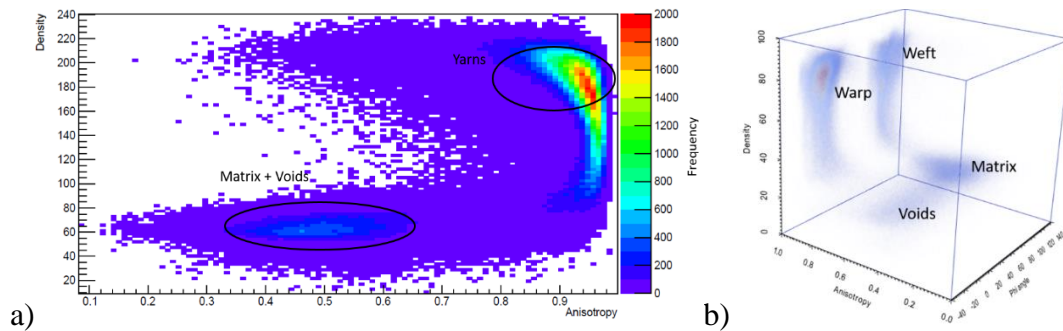
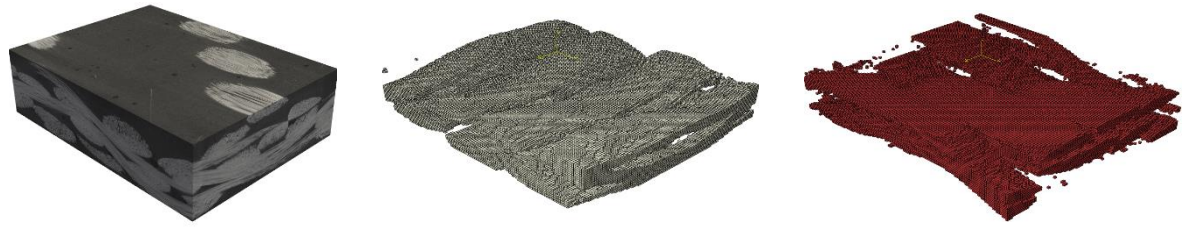
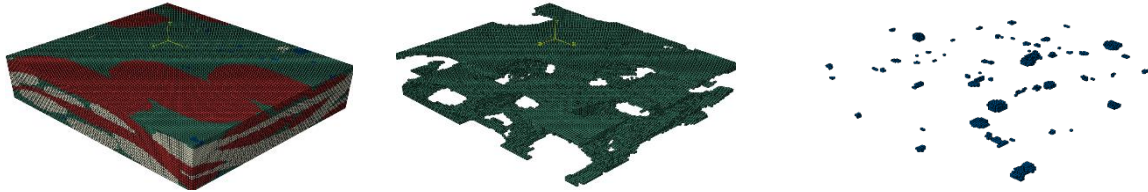


Figure 77: Statistical parameters of feature vector a) Histogram of the structural anisotropy and average gray value for the μ CT data acquired on Twill-3D and b) Three-dimensional histogram of structural anisotropy, average gray value, and fiber orientation angle.



Raw Data	Warp volume fraction	0.2908	Weft volume fraction	0.3398
----------	----------------------	--------	----------------------	--------



Voxel model	Matrix volume fraction	0.3526	Void volume fraction	0.0168
-------------	------------------------	--------	----------------------	--------

Figure 78: A voxel model of a 3D glass/epoxy Twill composite (upstream).

The next step is to select the size of the integration window, such that the segmentation parameters should not have any effect on the constituent volume fractions and calculated properties.

5.2.1 Convergence study

The choice of integration window will have a direct effect on the segmentation of the μ CT data and the mechanical behavior of the composite. Hence, two convergence studies are carried out. The first one is a comparison between numerically measured fiber volume fraction after segmentation to the experimental fiber volume fraction. The second one is the convergence of the mechanical properties to the size of the integration window. Since the calculation of the elastic properties is based on the average stress, the integration window will have a significant influence on the calculated elastic properties. Five sizes for the integration window ranging from 5 to 20 are chosen for this study. The variation of the total, warp, and weft fiber volume fractions and matrix volume fraction concerning the window size for Twill-3D downstream is presented in Table 17. It was observed that the segmentation with window size smaller than 10 has a good convergence to the experimental fiber volume fraction and total void volume fraction.

	Voxel size μm	Weft V_f	Warp V_f	Total V_f	Inter-yarn-void V_{vm}	Matrix V_m
Size-20	176.21	0.3048	0.3289	0.3833	0.03415	0.3322
Size-15	132.16	0.3025	0.3207	0.3769	0.03325	0.3436
Size-10	88.11	0.2974	0.3186	0.3726	0.03321	0.3508
Size-8	70.49	0.2961	0.3138	0.3689	0.03286	0.3683
Size-5	44.05	0.2960	0.3031	0.3671	0.03251	0.3684
Experimental				0.36 ± 0.015		

Table 17: Variation of constituent volume fraction concerning voxel size.

The results of the convergence study for the elastic properties to the window size is presented in Figure 79. The variation in the elastic property (E_{11} and E_{22}) is about 2.3% from the window size of 20 to 5. However, the window smaller than 8 does not affect the elastic properties. Hence, we select the window size of 8 as an optimal voxel size for segmentation and homogenization of the elastic properties.

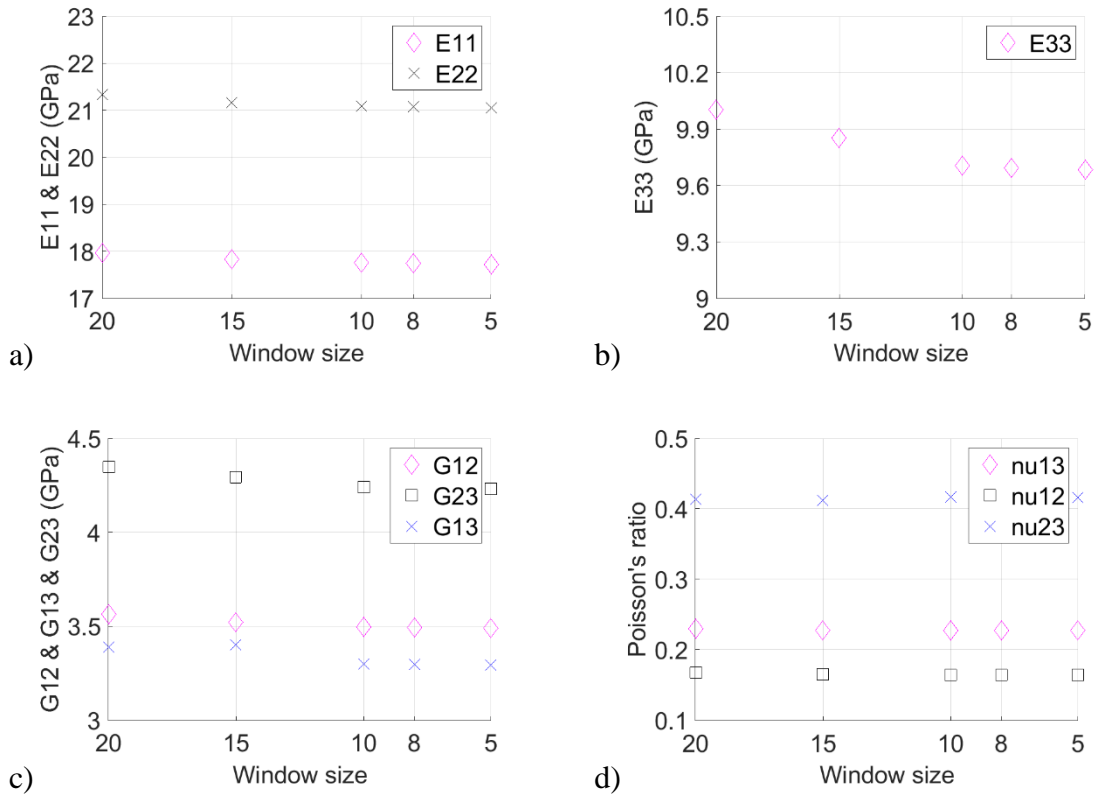


Figure 79: Convergence study on elastic properties concerning voxel size.

5.2.2 Results of segmentation

The μ CT observations were performed on Satin and Twill reinforced composites. The specimen extraction was described in Section 3.2.3. Two tomography observations were conducted on each composite plate, the one in the upstream and the second in the downstream. Based on the convergence results from section 5.2.1 the window size of ($H=8$) will be utilized for future calculations. The segmentation results of satin-3D composite by Vox-Tex are presented in Figure 80, and twill-3D is presented in Figure 81. The constituent volume fractions such as warp volume fraction (V_{warp}), weft volume fraction (V_{weft}), and the inter-yarn volume fraction are presented in Table 18.

Satin 3D

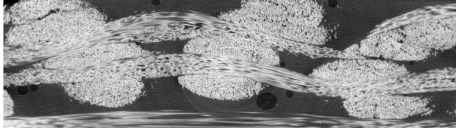
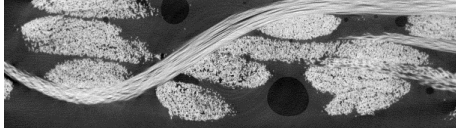
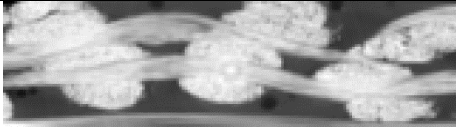
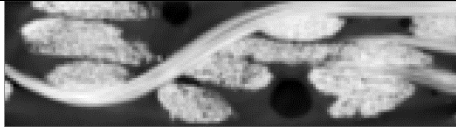


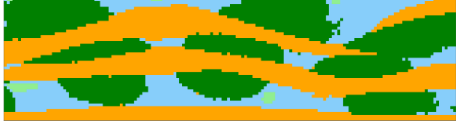

Position	Upstream	Downstream
Raw image		
Density		
Anisotropy		
Voxel model		

Figure 80: Segmentation of Satin-3D micro-CT data from upstream and downstream.

Twill 3D

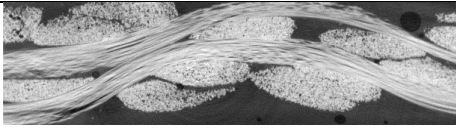
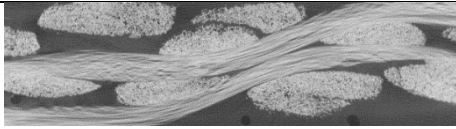
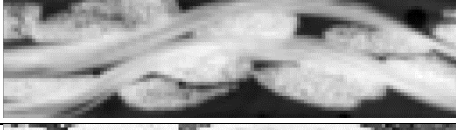
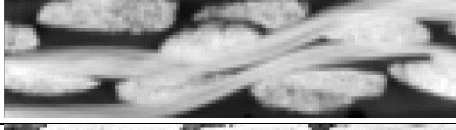
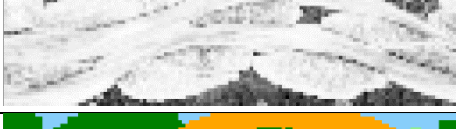
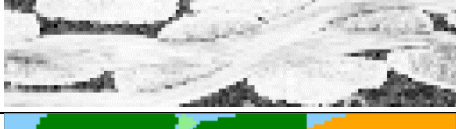

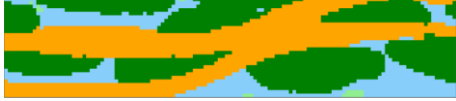
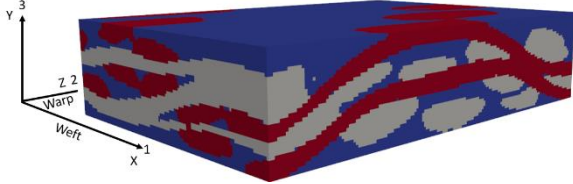
Position	Upstream	Downstream
Raw image		
Density		
Anisotropy		
Voxel model		

Figure 81: Segmentation of Twill-3D micro-CT data from upstream and downstream.

Based on the intra-yarn fiber volume fraction in warp ($V_{yf-warp}$) and weft ($V_{yf-weft}$) for composites measured from micrography observation as presented in Chapter-2. Thus, the total fiber volume fraction (V_{FT}) can be calculated based on the rule of mixtures as presented in Equation 5.8.

$$V_{FT} = V_{warp}V_{yf-warp} + V_{weft}V_{yf-weft} \quad (5.8)$$



Volume fractions		Warp	Weft	Inter-yarn voids	Matrix	Fiber
Twill	Upstream	0.2968	0.3031	0.0109	0.3893	0.359
	Downstream	0.2898	0.3015	0.0268	0.3819	0.354
Satin	Upstream	0.2908	0.3398	0.0168	0.3526	0.363
	Downstream	0.2960	0.3031	0.0325	0.3684	0.367

Table 18: Constituent volume fraction after segmentation in composites made of reinforcements satin-3D and Twill-3D.

After the segmentation, the voxel model can be exported from VoxTex to ABAQUS in a .inp format. To create a .inp file for ABAQUS the material properties for each constituent (warp, weft, matrix, and voids) and the element type should be provided. The segmented voxel model can also be saved as a text file where every voxel is indexed. Later the segmented model is imported to MATLAB to analyze the size and aspect ratio of the inter-yarn voids.

5.3 Characteristics of inter-yarn voids (meso-voids)

The statistics of the void volume distribution and the aspect ratio are presented in this section. After the segmentation was performed the results were saved in an indexed text file and the voxel model was reconstructed in MATLAB. An in-house code was developed to conduct the particle analysis on inter-yarn voids. The statistical analysis was carried out using regionprops3 an inbuilt MATLAB function [221]. For this, a binarized 3D image containing only inter-yarn voids and matrix was reconstructed from the labeled text file generated by VoxTex. The distribution of the void volume was presented in Figure 82, and the aspect ratio to describe the void shape is presented in Figure 83. The total number of inter-yarn voids in the upstream (32-Satin, 26-Twill) is smaller than that of in the downstream (154-Satin, 138-Twill). The maximum void size also increased from upstream ($42992.8 \mu\text{m}^3$ -Satin, $15717.04 \mu\text{m}^3$ -Twill) to downstream ($233993.6 \mu\text{m}^3$ -Satin, $259789.28 \mu\text{m}^3$ -Twill). However, the minimum void size in up-stream and down-stream have very similar values blow $200 \mu\text{m}^3$.

The average aspect ratio of the inter-yarn voids in the up-stream (1.34-Satin and 1.486-Twill) is 14% smaller than the average aspect ratio of the inter-yarn voids in the downstream (1.60-Satin and 1.806-Twill). Based on the statistics of the aspect ratio, we can state that the inter-yarn voids have near-spherical shapes. However, the distribution of the aspect ratio changes, (see Figure 83 c, d) the number of voids with an aspect ratio greater than two is greater in the downstream than in the upstream. It can be concluded that the voids are more elongated in the downstream and most of the void have near-spherical shapes in the upstream. A similar trend is also observed in the statistical data of inter-yarn voids for the satin reinforced composite, the statistical data on aspect ratio is presented in Figure 83 a), b).

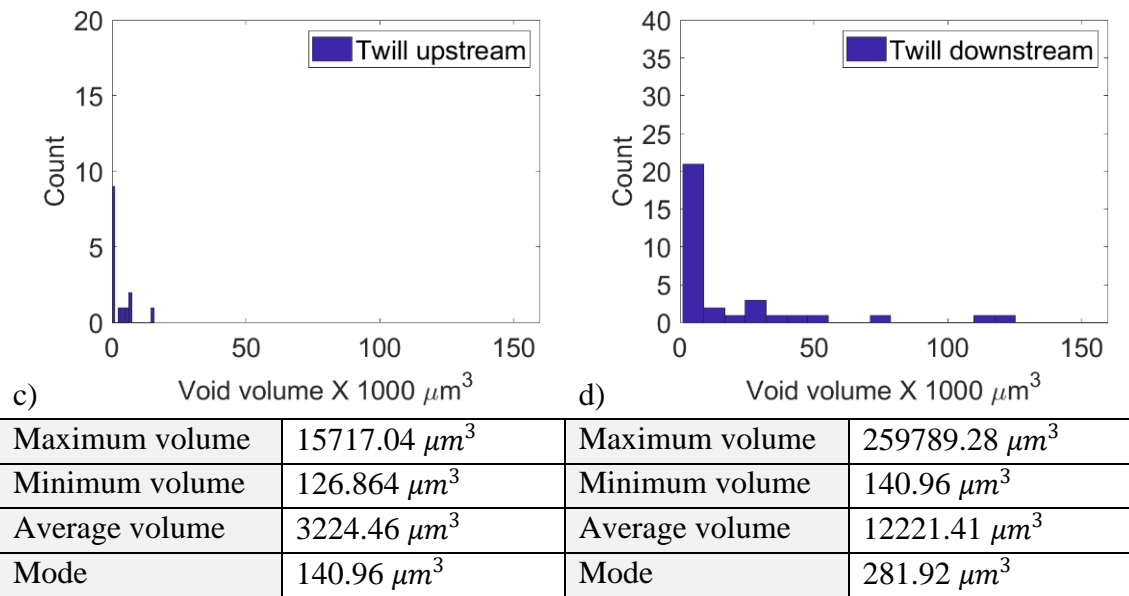
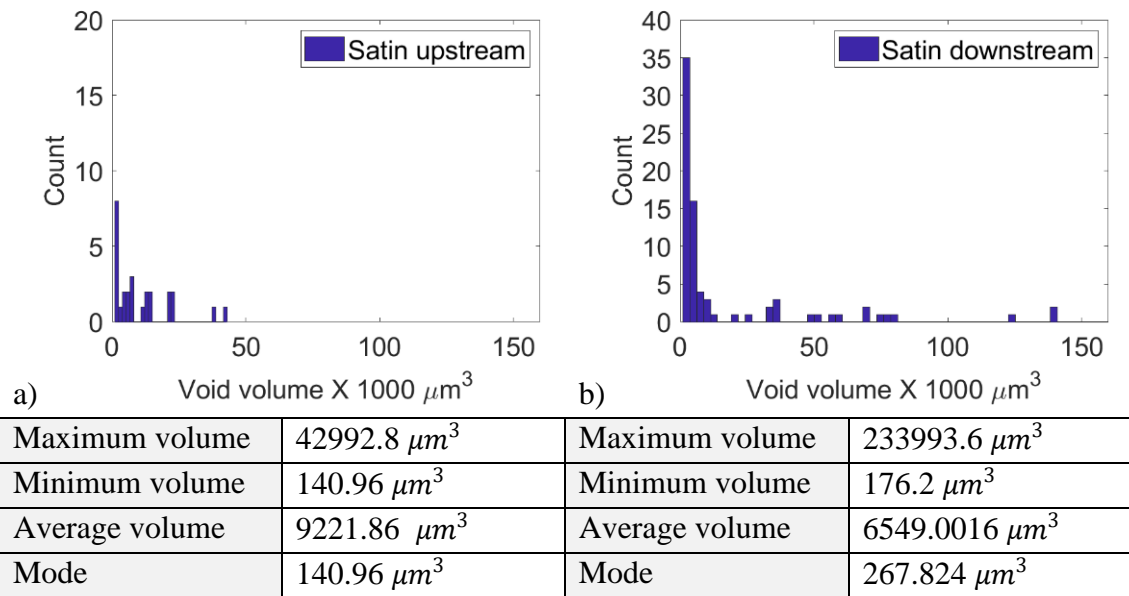


Figure 82: Size distribution of the inter-yarn voids in up and down-stream in a) Satin -3D, upstream, downstream, and b) Twill-3D, up-stream, and downstream.

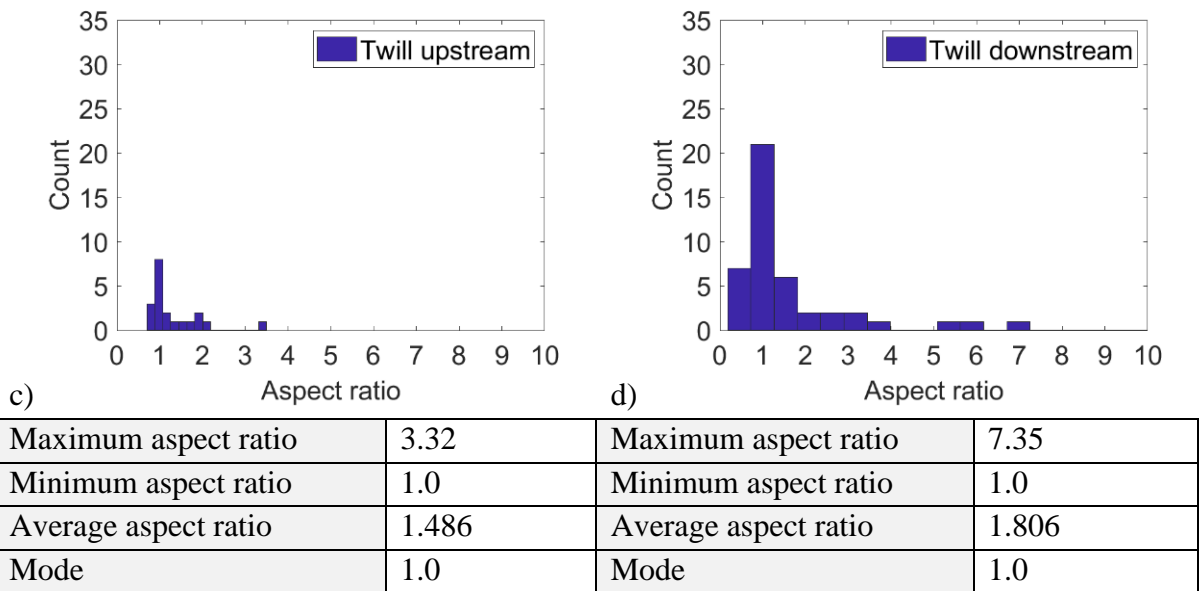
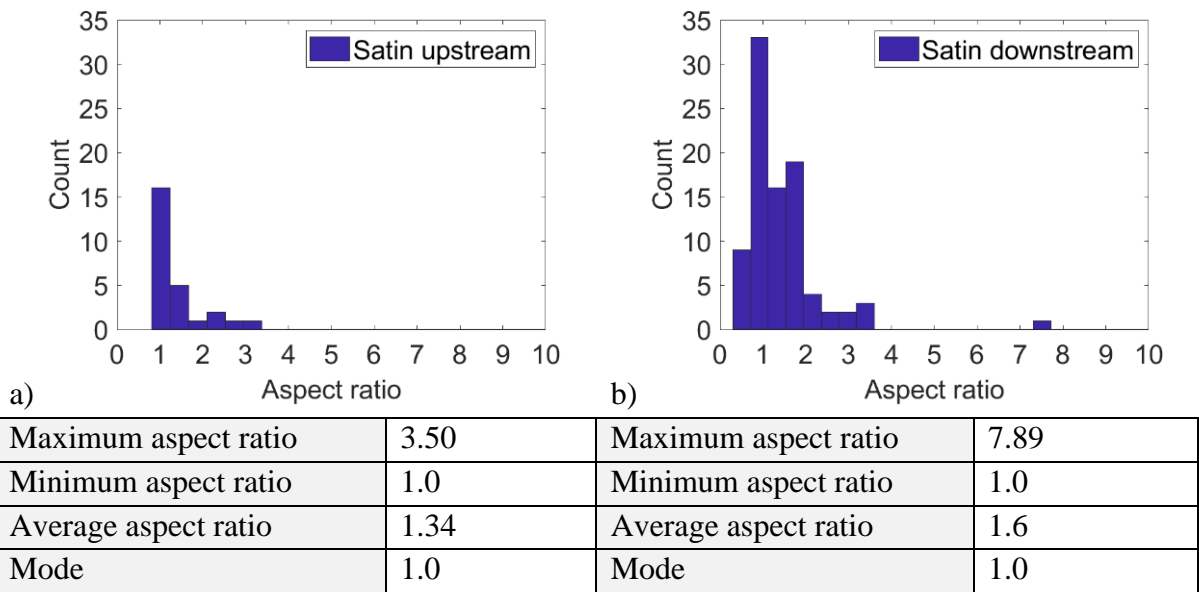


Figure 83: Aspect ratio distribution of the inter-yarn voids in up and down-stream in a) Satin-3D (up-stream, down-stream) and b) Twill-3D (up-stream and down-stream).

5.4 Multiscale simulation to analyze the effect of voids on elastic properties

5.4.1 Finite element model description

A complete finite element multi-scale simulation was performed for all the four meso-scale voxel models (Satin upstream and downstream, Twill upstream and downstream) generated from the μ CT data. The complete numerical simulation has three steps 1) generation of the geometry, 2) assigning material properties, and 3) application of boundary condition and FE-simulation. The window size of 8, resulted in the element size of 70.48 microns for the model reconstructed from Twill-3D and 90.68 microns for the satin-3D. For all the models a C3D8 brick element was chosen. The next step, in the numerical homogenization, is assigning material properties of the warp, weft yarns, matrix, and voids. The properties of the matrix and void are taken from Chapter-3 table-2. However, the elastic properties of the yarns are assigned either by Chamis micromechanics model or by numerical homogenization of the yarn RVE (following the process presented in chapter 3). As VoxTex can only export the voxel model to ABAQUS with the element types C3D8 and C3D20, the choice of element type is important to accelerate the computational time for FE-solution [222]. Since C3D8 have less computational time than C3D20, it is selected as the element type in this study. To conduct the numerical homogenization, periodic boundary conditions are applied with six different loading conditions the detail of the numerical homogenization are presented in Annexe 7.1.

Moreover, a parametric study was conducted to investigate the effect of the inter-yarn void, intra-yarn voids on the elastic properties of the 3D textile composites. The list of the test cases and the results of the parametric study are presented in Section 5.4.2.

5.4.2 Parametric study on the sensitivity of elastic properties concerning intra & inter-yarn voids

From the experimental results presented in Section 3.5 it is observed that intra-yarn voids have a higher influence than inter-yarn voids on the tensile properties of the textile reinforced composites. Hence, a parametric study was conducted with three different cases to completely understand the effect of void location on the elastic properties:

1. Voids only in the matrix.
2. Voids only in the warp yarns.
3. Void only in the weft yarns.

For all the cases the void volume fraction in the respective constituent is varied such that the total void volume fraction remains constant. A list of test cases with the constant total void volume fraction is presented in Table 19.

To conduct the parametrical study, artificial voids inter-yarn voids are generated by post-processing the segmented image from VoxTex in MATLAB. Once the '.inp' file with the matrix, warp, and weft yarns is generated it is feed to the void generation algorithm developed in MATLAB. The algorithm is presented in Figure 84 and facilitates the generation of meso-structure with two different types of inter-yarn voids: randomly distributed and spherical.

Void volume fraction in	Matrix	Warp	Weft	Total
Voids only in the matrix				
Test case-1	0.036	0	0	0.01
Test case-2	0.072	0	0	0.02
Test case-3	0.108	0	0	0.03
Test case-4	0.144	0	0	0.04
Test case-5	0.180	0	0	0.05
Void only in the warp yarns				
Test case-1	0	0.0254	0	0.01
Test case-2	0	0.0508	0	0.02
Test case-3	0	0.0764	0	0.03
Test case-4	0	0.1016	0	0.04
Test case-5	0	0.1270	0	0.05
Voids only in the weft yarns				
Test case-1	0	0	0.0303	0.01
Test case-2	0	0	0.0606	0.02
Test case-3	0	0	0.0909	0.03
Test case-4	0	0	0.1213	0.04
Test case-5	0	0	0.1516	0.05

Table 19: Test cases for parametric study to evaluate the effect of void position on the elastic properties of the 3D reinforced textile composite.

The algorithm needs input on the void volume fraction and for the case of spherical voids, it requires an additional input on the distribution of the void radius.

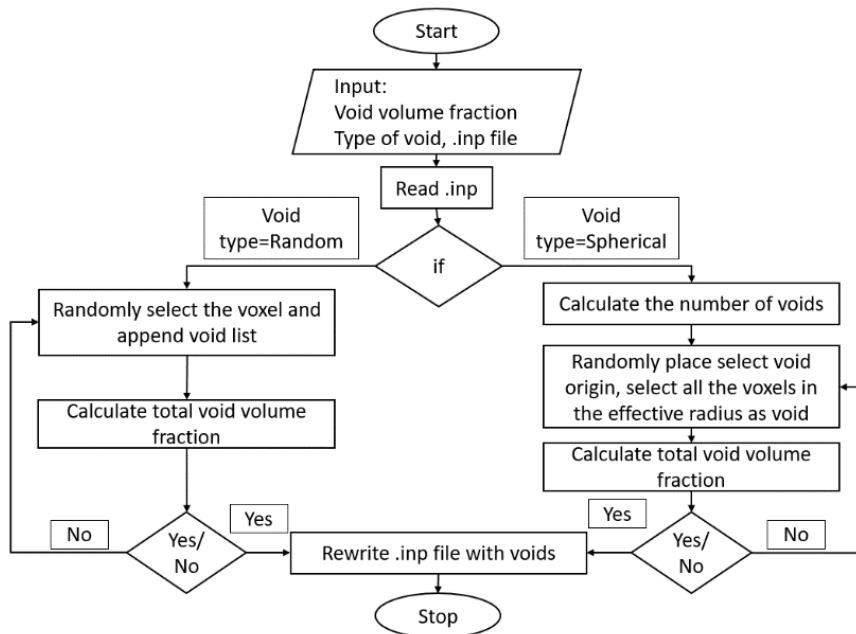


Figure 84: Algorithm for generation of the inter-yarn voids in segmented μ CT data.

Steps for random voids generation

Step 1: The 3D mesh of the segmented μ CT data was reconstructed in Matlab based on the “.inp” generated by VoxTex. Then all the mesh elements belong to the matrix were recognized and appended to a separate list.

Step 2: Random voxel in the matrix list would be selected and the elastic properties are reduced following Table 12. Then the mesh element number is appended to an array containing the list of voids.

Step 3: After the selection of every new voxel as void, the algorithm will calculate the total current void volume fraction. If it is less than the required void volume fraction (V_{vr}) the algorithm will continue to append the void list following **step 2** or else the loop can be terminated and continued to **step 4**.

Step 4: All the element numbers in the list of void were identified and the new input file for FE-simulation in ABAQUS will be written.

In literature, this kind of meso-structure with voxel void was used for an FE simulation by Shigang et al, [69] and Qian et al, [68]. The microstructures with randomly distributed voxel voids are presented in Figure 85. However, the random voxel kind of voids is not observed in the reality. Hence, meso-structures with spherical shaped inter-yarn voids are also analyzed in this study.

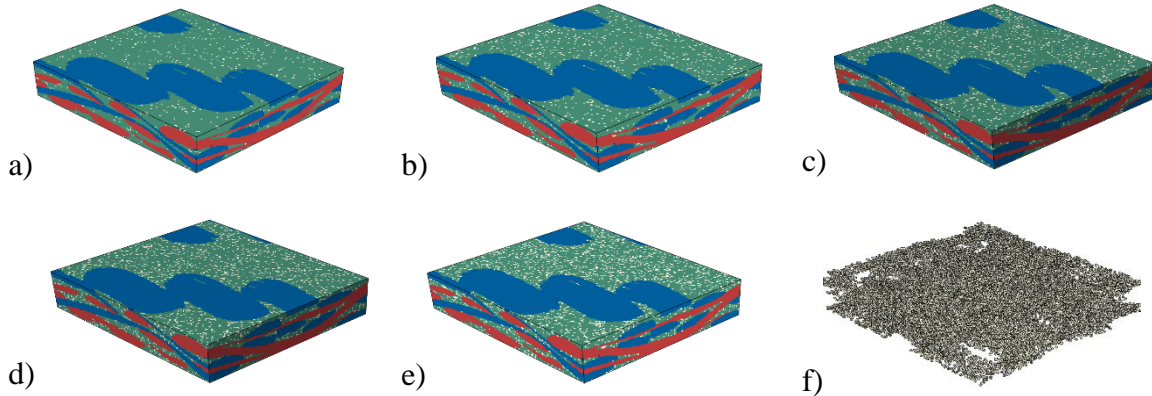


Figure 85: Generated meso-structures with random voxel void generated by using MATLAB script: a) 0.01, b) 0.02, c) 0.03, d) 0.04, and e) 0.05 of inter-yarn void volume fraction, f) Voxel voids for the total void volume fraction of 0.05.

Steps of spherical void generation

Step 1: This step was similar to **step 1** in **random voids**. The “.inp” file was read and all mesh elements that belong to the matrix were recognized and appended to a separate list.

Step 2: Based on the input value for the void volume distribution the minimum number of required voids (N) to be created for the required total void volume fraction (V_{vr}) was calculated by the equation given below.

$$N = \frac{V_{vr}}{\text{mean}(\text{void volume distribution})} \quad (5.9)$$

Step 3: A random element from the matrix array was selected as the void center and the algorithm will start to increase the void radius. At every increment, the void radius will be increased by the size of the element (voxel size). For better understanding, the 2D-schematic representation of the increase in void radius at every increment is presented in Figure 86. In reality, it happens in 3D so circles are replaced with spheres. The radius increment will continue until the void volume increases to the required void volume provided by the user (~ 46 voxels in this case). During this process, the algorithm cannot always find an element for the corresponding neighbor in every direction. This can be due to two conditions.

- The next neighboring element belongs to warp/ weft (see Figure 87 case 1)
- The void has reached the boundary of the mesostructure. (see Figure 87 case 2)

Then the algorithm will stop the increment of the void radius in direction of no neighbors and keeps increasing it in the other direction as shown in Figure 87, for i^{th} and $i + 1^{th}$ radius increment the elements belong to warp/weft was not selected (case 1) and as the void reaches the boundary element the void radius will start increasing only in other directions (case 2).

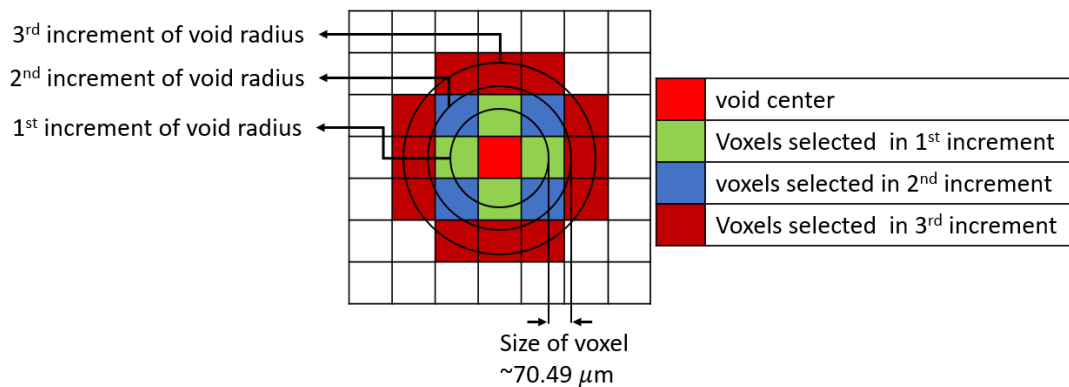


Figure 86: 2D schematic representation of the increase in void radius to create artificial voids in the segmented voxel model.

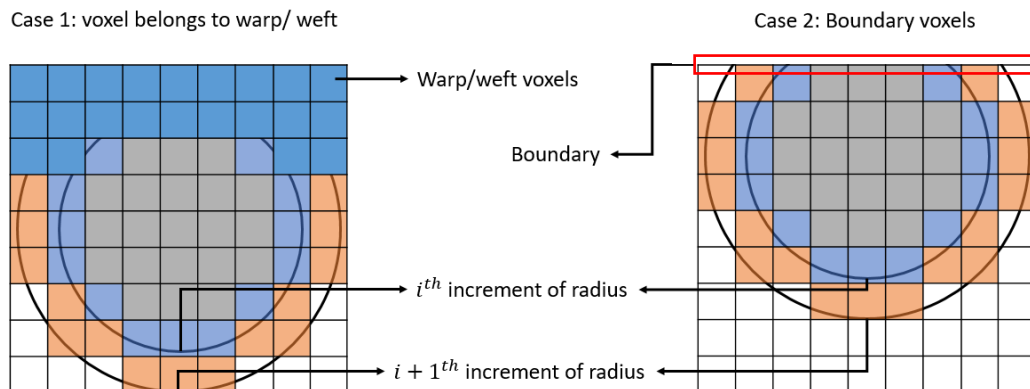


Figure 87: Schematic representation in 2D, the two different cases that can occur during the increment of the void radius.

Step 4: Once the void volume equals the input provided by the user, the algorithm will add the list of all the elements assigned as voids into a new list and removes them from the matrix array. This will ensure there will be no reselection of the element. **Step 3** and **step 4** were repeated until the total number of voids (N) was placed.

Step 5: All the element numbers in the list of void were identified and the new input file for FE-simulation in ABAQUS will be written.

For the case of simplicity, all the voids in this study have the same effective radius. Hence the number of void decreases proportionally to the reduction in total void volume fraction, such that the volume of each void remains constant. The mean void volume is 46 voxels. The microstructures containing spherical voids are presented in Figure 88.

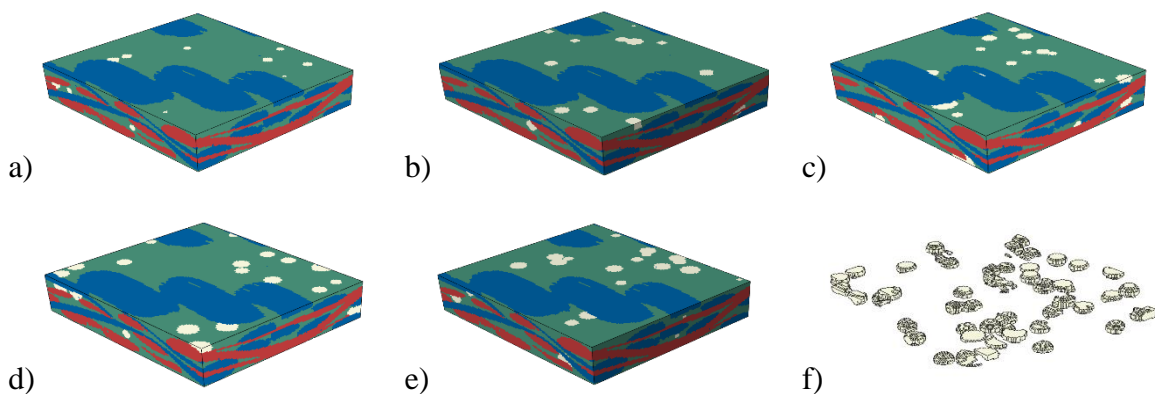


Figure 88: Microstructures containing spherical voids generated by MATLAB from a) 0.01, b) 0.02, c) 0.03, d) 0.04, and e) 0.05 of inter-yarn void volume fraction, f) Voxel voids for void volume fraction of 0.03.

For the parametric study, the elastic properties of the yarns were calculated by the modified Chamis micromechanical model proposed in [223] to obtain the elastic properties of UD composites with voids. The results of the FE-homogenization at meso-scale for all the test cases (see Table 19) are presented in Figure 89.

The FE-homogenization at meso-scale with random voxel voids has a high dispersion of the properties. This kind of behavior was also observed in the studies of [68], where they generated random voids in the 3D braided composite. Hence, an average of 5 simulations was presented for E_{11} , E_{22} , and E_{33} with their dispersion in Figure 89 b), c), d). Considering the average over five simulations the random voids come closer to the behavior of meso-model with spherical voids.

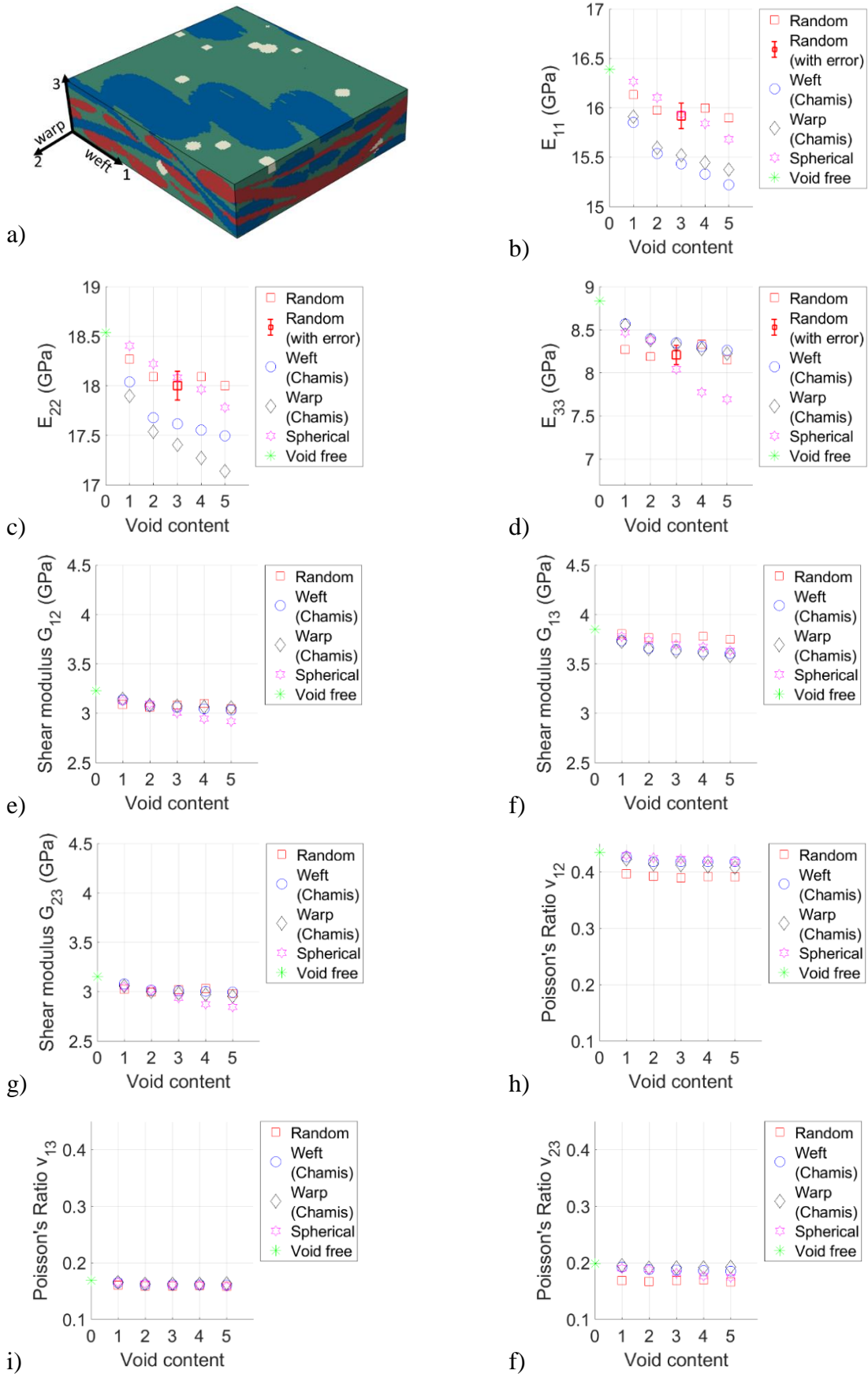


Figure 89: Variation of elastic properties of Twill - 3D textile reinforced composite concerning to the voids in the channel, only in the warp, only in the weft.

The overall observation, except E_{33} , implies that the elastic properties of the textile composites are more sensitive to intra-yarn voids than to inter-yarn voids. The percentage of reduction of the elastic properties is presented in Table 20. For test case 1, the inter-yarn void volume fraction of 0.18 equivalent to 0.05 total void volume fraction resulted in the 4.3% reduction of E_{11} (weft direction), 5.6% E_{22} (warp direction) and 12.01% reduction of E_{33} (out-of-plane). However, the intra-yarn voids in the warp resulted in the 6.1% reduction of E_{11} , 7.5% reduction of E_{22} and 6.9% reduction in E_{33} and the intra-yarn voids in the weft resulted in the 7.2% reduction of E_{11} , 5.6% reduction of E_{22} and 6.49% reduction in E_{33} .

Shear moduli are more sensitive to inter-yarn voids than to the intra-yarn voids. The 0.05 total void volume fraction for the case of inter-yarn void only, resulted in 9.6%, 9.8%, and 9.7% percent reduction in G_{12} , G_{13} and G_{23} respectively. The intra-yarn voids lead to an average reduction of 6%. Hence, we can conclude that the effect of the intra-yarn void play a crucial role in determining the in-plane tensile properties. Conversely, the out-of-plane tensile modulus and shear modulus are highly influenced by inter-yarn voids.

Reduction	E_{11} %	E_{22} %	E_{33} %	G_{12} %	G_{13} %	G_{23} %	ν_{12} %	ν_{13} %	ν_{23} %
Random	2.5	2.4	8.9	6.5	5.6	6.3	1.2	4.81	5.7
Spherical	4.3	4.6	12.01	9.6	9.8	9.7	3.16	2.31	4.7
Warp	6.1	7.5	6.9	5.9	6.4	4.9	1.7	1.7	3.3
Weft	7.2	5.6	6.49	5.2	6.9	5.2	3.7	2.06	6.1

Table 20: Reduction of the elastic properties with respect to inter-yarn and intra-yarn voids equivalent to the total void volume fraction of 0.05.

5.4.3 Validation of FE-solution with experimental results

The elastic properties were predicted by complete multi-scale numerical homogenization for Twill-3D as shown in Table 22. The properties of the warp and weft yarns were calculated by the FE-homogenization at the microscale (following the process presented in Chapter-3). The details on the geometrical properties of the yarn microstructure, intra-yarn fiber volume fraction, and intra-yarn void volume fraction are provided in Figure 90, and the calculated elastic properties are presented in Table 21.

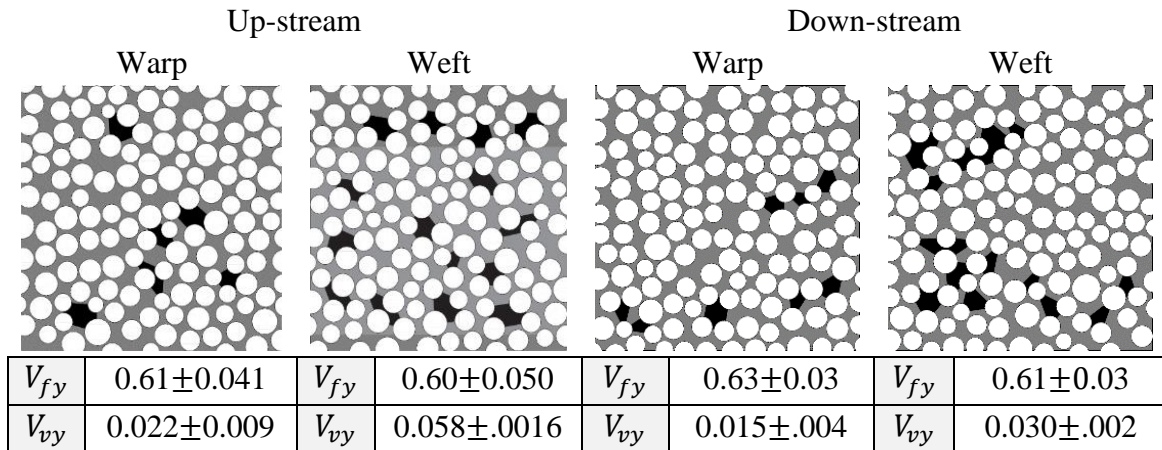


Figure 90: Microstructure for FE-simulation at microscale with the intra-yarn fiber volume fraction and intra-yarn void volume fraction.

The resolution of the voxel model for upstream and downstream was (139 X 123 X 34) and (140 x 126 x 34) respectively and the resolution for each voxel model was 70.48 micrometers. The thickness of the model after reconstruction was 2.396 mm for both upstream and downstream which deviated by 0.1% from the actual thickness of the composite and was a negligible error smaller than the standard deviation of the plate over all thickness. Both the simulations were carried on a Dell precision workstation with Intel(R) Xenon(R) CPU E5 with 16 GB RAM. For completing the numerical homogenization it took 4hr:36±20min. The time was counted from the start of the application of periodic boundary conditions to the end of numerical homogenization.

	Up-stream		Down-stream	
	Warp	Weft	Warp	Weft
E_{11} (GPa)	44.9	43.6	46.70	44.45
E_{22} (GPa)	12.5	9.8	13.42	11.37
E_{33} (GPa)	12.3	10.2	13.75	10.36
ν_{12}	0.26	0.26	0.24	0.25
ν_{13}	0.27	0.27	0.26	0.26
ν_{23}	0.36	0.36	0.38	0.37
G_{12} (GPa)	4.72	3.62	5.17	4.07
G_{13} (GPa)	4.34	4.00	5.21	4.53
G_{23} (GPa)	4.17	3.41	4.68	3.80

Table 21: Input for the yarn properties predicted by FE-homogenization, for up-stream and down-stream.

	Twill-3D Upstream		Twill-3D Downstream	
	FE-simulation	Experimental	FE-simulation	Experimental
E_{11} (GPa)	13.54	13.72±0.857	15.22	15.31±0.97
E_{22} (GPa)	15.98	-	16.68	-
E_{33} (GPa)	8.10	-	7.98	-
ν_{12}	0.212	-	0.20	-
ν_{13}	0.321	-	0.312	-
ν_{23}	0.378	-	0.362	-
G_{12} (GPa)	3.07	-	3.08	-
G_{13} (GPa)	2.87	-	2.987	-
G_{23} (GPa)	2.61	-	2.6	-

Table 22 Elastic properties of the Twill-3D composites predicted by complete multi-scale FE-simulation.

The predicted Young's modulus by the FE-simulation in the upstream was 1.3% lower than the experimental average Young's modulus. For the downstream, the FE-simulation deviates only by 0.58%. The error in both cases is less than the experimental standard deviation. Based on this we can validate that the proposed FE-based multi-scale simulation can predict the elastic properties of the 3D textile composites within a range of acceptable error.

5.5 Conclusions

In this chapter, we presented the structure tensor-based image segmentation method to generate the voxel model from the micro-CT data of textile composite with voids. The segmentation was performed using the VoxTex software. The results showed that the inter-yarn void volume fraction increased from upstream to downstream in the case of both Twill-3D textile composite and Satin-3D textile composite. The statistics of the void, such as void volume distribution and aspect ratio of the inter-yarn voids were measured by using the in-house developed MATLAB code. For Satin-3D, it was observed that the average inter-yarn void volume in down-stream was 1.41 times greater than in upstream and 3.79 times for Twill-3D. In Satin-3D and Twill-3D composites, the aspect ratio of voids in the downstream is 1.19 and 1.215 times larger than the voids in the upstream respectively. This shows that the increase of total void volume fraction in composite from upstream to downstream should be the direct contribution of the inter-yarn voids.

A parametric study was carried out to investigate the effect of the intra-yarn voids and inter-yarn voids on the elastic properties of the 3D textile composites. The observation on the results from FE-homogenization showed that the mechanical properties of the yarns play a determining role on the in-plane tensile properties of the composite. For a test case with voids only matrix, the total void volume fraction of 0.05 resulted in a 4.3 % reduction of Young's modulus in the direction of the warp (E_{22}), whereas 5% inter-yarn void in warp and weft resulted in a 7.2 % and 6.9 % reduction respectively. However, the through-thickness tensile modulus and the shear modulus are more sensitive to the intra-yarn void content.

In the last section, we presented a complete FE-based multi-scale simulation to predict the elastic properties of the 3D textile composite. The predicted Young's modulus in the weft direction (E_{11}) was validated with respect to the experimental result. The error between the prediction and experimental results was smaller than the experimental standard deviation. Hence, we propose that the FE-based multi-scale simulation can be effectively utilized to predict the elastic properties of the textile composite.

6 Conclusions and perspectives

At the beginning of this thesis (Chapter 1), we presented the main objective and motivation of the research. The structure of the whole thesis and the contents of the subsequent chapters were provided.

In the second chapter, the literature survey on the different types of process-induced defects and their influence on the mechanical properties of composite materials was presented. In particular, the experimental techniques for voids characterization and the analytical or numerical modelling approaches to predict the mechanical properties of composites containing void defects were presented. We discussed different process-induced defects that can occur in composites, emphasizing the void type defects and the mechanism of void formation during autoclave and RTM processes. Understanding the parameters used in the literature to describe the void characteristics such as void volume fraction, size, shape, and spatial distribution, the state of the art was presented concerning the influence of these parameters on the composite properties. Because of the dual scale porosity in textile composites, they pose a unique challenge to understand the mechanical behavior under the influence of voids. Based on the state of the art homogenization methods, remarks were noted on the used techniques (analytical and numerical) and different void characteristics studied in the literature to relate the composite behaviors with voids. A detailed study on the homogenization techniques to predict the elastic properties of the textile composites emphasized the importance of the multi-scale numerical simulation. In a numerical simulation, the accuracy of the prediction will be influenced by the geometry of the model and boundary conditions. Hence, this study provided a strong motivation to construct the complete numerical multi-scale simulation, which can replicate the realistic geometry of the composite at both micro-scale and meso-scale. To achieve this task, we chose the 3D-textile composites in this study.

In Chapter 3 we explained, the manufacturing technique to produce 3D textile composites with a controlled void volume fraction. This technique resulted in a different intra-yarn void and inter-yarn void distribution in the composite part. Tensile tests were carried out to quantify the effect of voids on Young's modulus and tensile strength. Burn-off tests were conducted to measure the distribution of the void volume fraction as a function of injection pressure. Image-based characterization was performed to evaluate the yarn characteristics. An improved Voronoi cell method was proposed to measure the fiber radius distribution, inter-fiber distances, and local fiber area fraction. Intra-yarn void area fraction was quantified by pixel counting method, and improved VCM was applied to measure the local void area fraction. Void characteristics such as area fraction and aspect ratio distribution were analyzed in warp and weft yarns in composite plates at the upstream and downstream of the resin flow. Local fiber area fraction and void area fraction of yarns were compared to determine the correlation between void occurrence and local packing fraction of yarns. Micro-computed tomography was conducted on the samples collected from two locations to reconstruct the realistic meso-structure for numerical homogenization. In the end, Young's modulus and strength's sensitivity to the total void volume fraction, intra-yarn area fraction in warp and weft was presented.

Chapter 4 was dedicated to the study on the effect of intra-yarn void and their characteristics on the yarns' elastic properties. A stepping Mori-Tanaka method based on the Eshelby inclusion was developed to analyze the effect of spherical voids on the mechanical properties of yarns. A numerical approach was presented to minimize the error in the prediction of the yarn's elastic properties. Three new algorithms were proposed during this study to produce a microstructure containing fibers and voids. A modified Nearest Neighbour Algorithm was proposed to generate the fibers respecting the statistical parameters measured in the yarns. It allowed us to produce the exact fiber radius distribution and inter-fiber distances, thus respecting the local fiber packing fraction. A Double Nearest Neighbour Algorithm was developed to pack the spherical voids of a different radius in between the fibers with different spatial distributions (homogeneous, random, and clusters). A new algorithm based on the local fiber packing was proposed to construct an RVE with realistic void shapes and area fractions. A parametric study was conducted to analyze the effect of void shapes, size, and distribution on the yarns' elastic response.

In the final chapter of the main manuscript (Chapter 5), a structure-tensor based segmentation method was adopted to develop a meso-structure from μ CT data. A parametric study was conducted to select acceptable segmentation parameters. Particle analysis was conducted to quantify the distribution of volume and aspect ratio for the inter-yarn voids. Artificial inter-yarn voids were created by treating segmented images in MATLAB. This process assists in generating the meso-structure with voxel voids or spherical inter-yarn voids. A parametric study was conducted to understand the sensitivity of elastic properties to the inter-yarn void, intra-yarn voids in warp and weft. Finally, the 3D textile composite's elastic properties predicted by a multi-scale numerical scheme were validated by comparison with the experimental results for textile composites.

Perspectives

- As the elastic properties only in the weft direction were analyzed in this study, more experiments can be conducted to characterize the other elastic properties such as in-plane shear modulus, tensile modulus in the direction of the warp, etc. The sensitivity of these properties can be validated with the parametric study conducted at the meso-scale which showed that the specific type of voids highly influences the particular elastic response of the 3D textile composites.
- The robustness of the proposed multiscale scheme can be verified by applying this technique to the composite containing various reinforcements. For example, laminated textile composites can be an interesting choice of study because the through-thickness properties of 2D textile laminate composites are highly sensitive to the inter-yarn voids. Similarly, this method can also be verified for cross-ply composites. Since the presented method is not dependent on the manufacturing process, its robustness can be tested for the composites manufactured by other processes such as autoclave, compression molding, infusion, etc.
- We use the experimentally measured local fiber packing fraction in yarns as an effective parameter to determine the void creation's probabilistic zone. However, the input for

the void generation zone can be numerically predicted with the help of the flow simulations. Thus, this method will help us to realize actual void shapes and distribution without carrying the experiments.

- The present microscale void generation can be further developed to generate 3D void shapes. However, this would require statistical information with the depth of the voids. This can be achieved either by μ CT or by collecting multiple micrographs of the yarn cross-section along the fiber direction.
- Estimation of the yarn strengths and their sensitivity to the void characteristics can be carried out. Even though certain void characteristics do not affect the elastic properties, they can significantly affect the strengths of composites. The recent studies conducted by Alden Hyde et al. [224] showed that the strengths of UD composites were more sensitive to void shapes than elastic properties. The effect of void spatial distribution is still an open question. This can be effectively addressed by using the generation algorithms developed during this study. Similarly, the strength simulations can be carried out at the mesoscale to understand the non-linear behavior of composite in the presence of voids.
- Conformal mesh at meso-scale can be developed by utilizing the new state-of-the-art techniques developed by Wintiba et al. [116], Anna Madra et al. [225].

7 ANNEXES

7.1 A: Numerical homogenization

In numerical homogenization, the heterogeneous microstructure was modeled as a homogeneous orthotropic medium with certain effective properties that describe the average material properties of the composite. To describe this macroscopically homogeneous medium, Hill-Mandel's macro-homogeneity condition was applied. According to this, the stress and strain in the equivalent homogeneous media can be calculated as the volumetric average stress and strains in the microstructure.

Average stress theorem: At each point on boundary surface ∂S , such that the traction vector $t_i = \sigma_{ij}n_j$ with a constant σ_{ij} is applied. For which, the volume average of the stresses inside the structure must be equal to the boundary stress tensor, i.e.

$$\bar{\sigma}_{ij} = \frac{1}{V} \int_V \sigma_{ij} dV$$

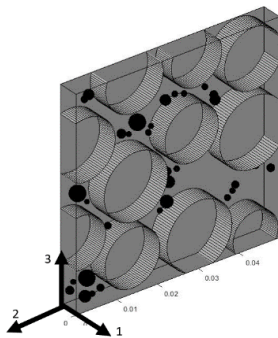
Average strain theorem: Consider at each point of the boundary surface ∂S , the displacement vector $u_i = \varepsilon_{ij}x_j$ with ε_{ij} constant is applied. Then, the volume average of the strains inside the structure is equal to the boundary strain tensor, i.e.

$$\bar{\varepsilon}_{ij} = \frac{1}{V} \int_V \varepsilon_{ij} dV$$

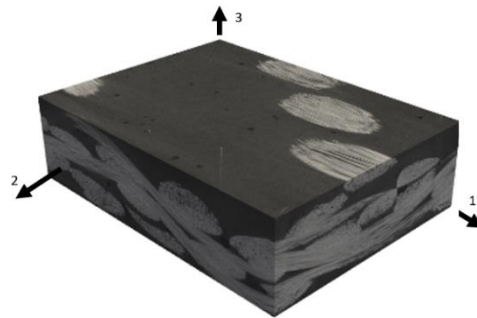
Let ε_{ij} be a kinematically admissible strain and σ_{ij} be a statically admissible stress at macroscopic scale. Then they satisfy the micro-macro energy equivalence such that, the following equation is true.

$$\frac{1}{V} \int_V \sigma_{ij} \varepsilon_{ij} = \bar{\sigma}_{ij} \bar{\varepsilon}_{ij}$$

From the generalized Hooke's law the, relationship between the $\bar{\sigma}_i$ and $\bar{\varepsilon}_j$ can be given with help of a stiffness tensor \bar{C}_{ij} . The axis system utilized to define the orientation of the material in microscale and mesoscale is presented in the following figure.



Microscale

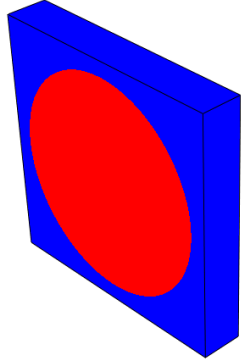


Mesoscale

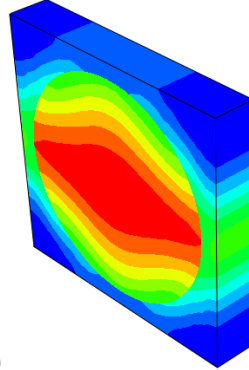
$$\begin{Bmatrix} \bar{\sigma}_1 \\ \bar{\sigma}_2 \\ \bar{\sigma}_3 \\ \bar{\sigma}_4 \\ \bar{\sigma}_5 \\ \bar{\sigma}_6 \end{Bmatrix} = \begin{bmatrix} \bar{C}_{11} & \bar{C}_{12} & \bar{C}_{13} & & & \\ \bar{C}_{21} & \bar{C}_{22} & \bar{C}_{23} & & & \\ \bar{C}_{31} & \bar{C}_{32} & \bar{C}_{33} & & & \\ & & & \bar{C}_{44} & 0 & 0 \\ & & & 0 & \bar{C}_{55} & 0 \\ & & & 0 & 0 & \bar{C}_{66} \end{bmatrix} \begin{Bmatrix} \bar{\varepsilon}_1 \\ \bar{\varepsilon}_2 \\ \bar{\varepsilon}_3 \\ \bar{\gamma}_4 \\ \bar{\gamma}_5 \\ \bar{\gamma}_6 \end{Bmatrix}$$

The elastic properties of the orthotropic material can be back-calculated if the stiffness tensor was evaluated. Hence, to calculate the stiffness tensor we need six different boundary conditions. The six boundary conditions and the calculation of the corresponding element in the stiffness tensor are presented below.

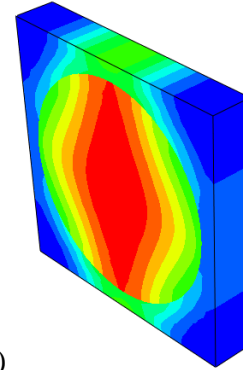
S.No	Boundary condition
1	$u_1 = 0.001 \times L_1; u_2 = 0; u_3 = 0$
2	$u_2 = 0.001 \times L_2; u_1 = 0; u_3 = 0$
3	$u_3 = 0.001 \times L_3; u_2 = 0; u_1 = 0$
4	$u_1 = 0.005 \times L_1; u_2 = 0.005 \times L_2; u_3 = 0$
5	$u_1 = 0.005 \times L_1; u_3 = 0.005 \times L_3; u_2 = 0$
6	$u_2 = 0.005 \times L_2; u_3 = 0.005 \times L_3; u_1 = 0$



1)

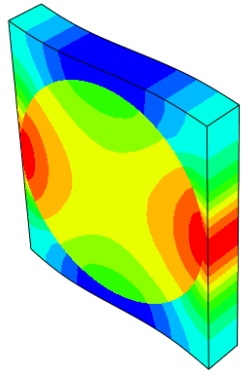


2)

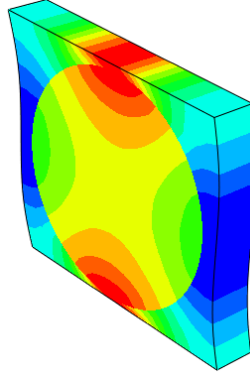


3)

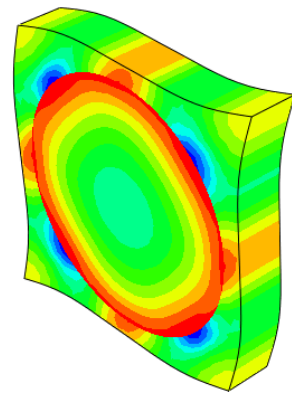
C_{11}	C_{21}	C_{31}	C_{12}	C_{22}	C_{32}	C_{13}	C_{23}	C_{66}
$= \frac{\bar{\sigma}_1}{\bar{\varepsilon}_1}$	$= \frac{\bar{\sigma}_2}{\bar{\varepsilon}_1}$	$= \frac{\bar{\sigma}_3}{\bar{\varepsilon}_1}$	$= \frac{\bar{\sigma}_1}{\bar{\varepsilon}_2}$	$= \frac{\bar{\sigma}_2}{\bar{\varepsilon}_1}$	$= \frac{\bar{\sigma}_3}{\bar{\varepsilon}_1}$	$= \frac{\bar{\sigma}_1}{\bar{\varepsilon}_3}$	$= \frac{\bar{\sigma}_2}{\bar{\varepsilon}_3}$	$= \frac{\bar{\sigma}_6}{\bar{\gamma}_6}$



4)



5)



6)

$C_{44} = \frac{\bar{\sigma}_4}{\bar{\gamma}_4}$	$C_{55} = \frac{\bar{\sigma}_5}{\bar{\gamma}_5}$	$C_{66} = \frac{\bar{\sigma}_6}{\bar{\gamma}_6}$
--	--	--

Now all the nine elastic constants for the orthotropic material can be calculated from the stiffness tensor as follows

$$E_{11} = C_{11} - \frac{2C_{12}^2}{C_{22} + C_{23}}$$

$$E_{22} = [C_{11}(C_{22} + C_{23}) - 2C_{12}^2] \frac{C_{22} - C_{23}}{C_{11}C_{22} - C_{12}^2}$$

$$E_{33} = [C_{11}(C_{33} + C_{23}) - 2C_{13}^2] \frac{C_{11} - C_{23}}{C_{33}C_{11} - C_{13}^2}$$

$$\nu_{12} = \frac{C_{12}}{C_{22} + C_{23}}$$

$$\nu_{13} = \frac{C_{13}}{C_{33} + C_{23}}$$

$$\nu_{23} = \frac{C_{11}C_{23} - C_{12}^2}{C_{11}C_{22} - C_{12}^2}$$

$$G_{23} = C_{44}$$

$$G_{12} = C_{55}$$

$$G_{13} = C_{66}$$

7.2 B: Burn-off test

Before carrying burn-off test a density test must be performed to determine the density of the composite specimen. In the literature there are two standards available to measure the density of solid objects, 1) Water Buoyancy Test (WBT) ASTM 0792 and 2) Density Gradient Technique (DGT) ASTM 01505. We use WBT to calculate the density of the specimen because it is easy to conduct. Steps followed in measuring the density of the composite specimen are described below.

This technique gives the measure of density by weighing material once in the air the (m_{ca}) and other time in liquid (m_{cl}). Any non-reactive liquid of known density (ρ_l g/cm³) can be used in the test. A laboratory balance with a sensitivity of ± 0.0001 g must be used in the experiment. Now the density of the composite (ρ_c g/cm³) is given as follows.

$$\rho_c = \frac{(m_{ca} - m_{cl})}{m_{ca}} \times \rho_l$$

Burn off test follows ISO 1172:1996 and ASTM D2734-09[226] standard, popularly known as the calcination test. This test applies to prepregs, molding compounds and laminates for calculation of constituent volume fraction.

Sampling: The determination of constituent volume fraction shall be carried out in parallel in 3 tests and the average of the value is considered only if the deviation is less than 5%.

Preparation of specimen: The minimum mass of the specimen must be 2-20 grams, the specimen must be free from moisture and surface porosity.

Apparatus required for the test:

- Balance with a least count of 0.1mg.
- An aluminum crucible of suitable size.
- Muffle furnace.
- Desiccator.
- Ventilated drying oven.

Process: Clean and measure the crucible, now place the crucible into the oven at 450 degrees C temperature for 10 min. Weight the empty crucibles after 10 min takes the crucible out and lets them cool to room temperature.

The dry weight of crucible: m_1 mg

Place the specimen in a crucible and keep them in the oven at 105° for 5 minutes to remove any moisture from the composite specimen. And now record the mass of the specimen along with crucible

The dry weight of crucible + specimen: m_2 mg

Place the crucible and specimen in the oven at [450°-500°] C for 4 hours. The matrix must degrade at such high temperatures leaving just fibers back in the crucible. Switch off the oven

and wait until the specimen reaches room temperature. Now measure the mass of the crucible along with the fibers.

The mass of crucible with fibers after calcination: m_3 mg

Now the mass fraction of the fibers can be calculated by using the equation given below

$$M_f = 1 - \frac{(m_2 - m_3)}{(m_2 - m_1)} \times 100$$

$$M_m = 1 - M_f$$

From the above information the global void volume fraction (V_v) in the composite can be calculated by the following equation.

$$V_v = 1 - \rho_c \times \left(\frac{M_m}{\rho_m} + \frac{M_f}{\rho_f} \right)$$

Where ρ_m and ρ_f are the density of matrix and fiber respectively.

7.3 C: Eshelby tensor for cylindrical and spherical inclusions

The Eshelby tensor for a geometrical inclusion with a cylindrical shape is presented below

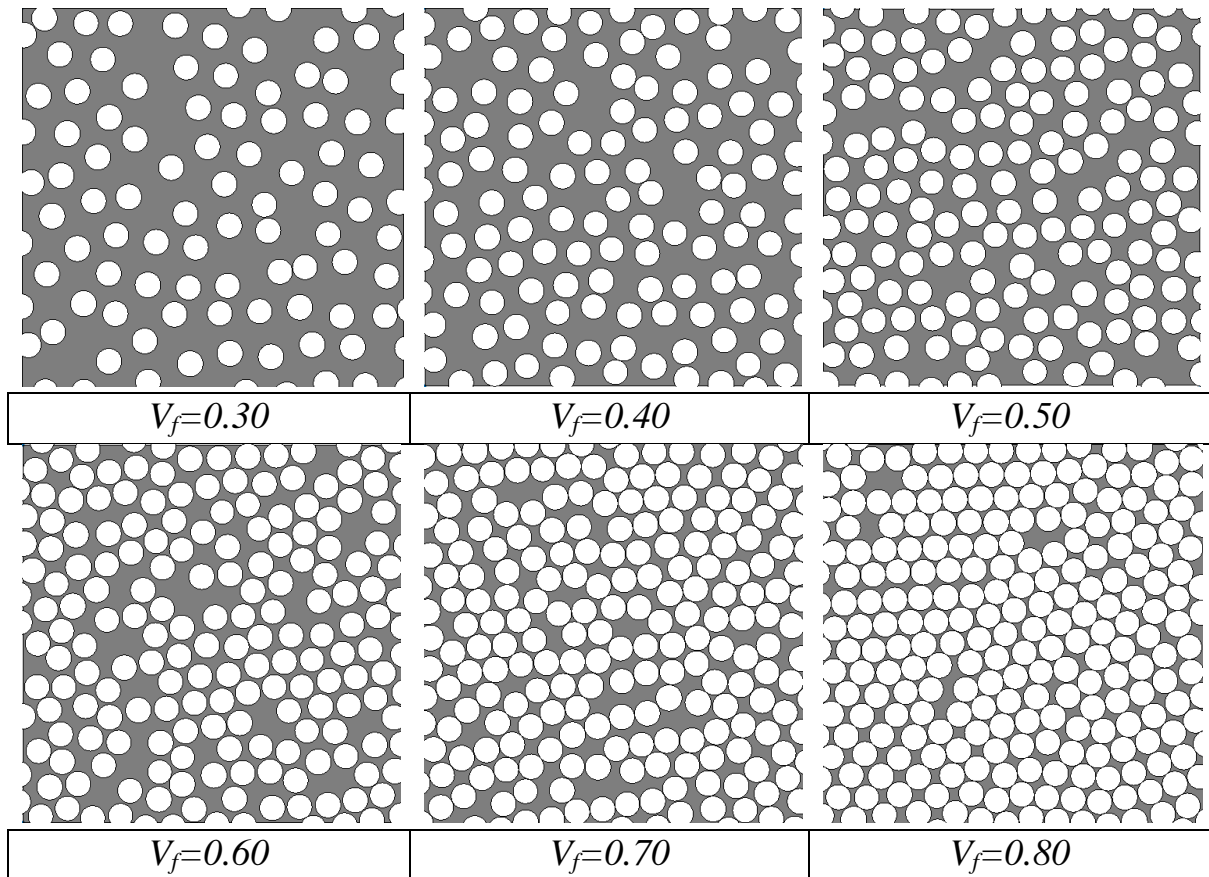
$$\begin{bmatrix} \frac{0}{v_m} & \frac{0}{5-4v_m} & \frac{0}{4v_m-1} & & & \\ \frac{2(1-v_m)}{v_m} & \frac{8(1-v_m)}{4v_m-1} & \frac{8(1-v_m)}{5-4v_m} & & & \\ \frac{v_m}{2(1-v_m)} & \frac{4v_m-1}{8(1-v_m)} & \frac{5-4v_m}{8(1-v_m)} & & & \\ & & & 0 & & \\ & & & & \frac{3-4v_m}{8(1-v_m)} & 0 & 0 \\ & & & & 0 & 1/4 & 0 \\ & & & & 0 & 0 & 1/4 \end{bmatrix}$$

The Eshelby tensor for a geometrical inclusion with a spherical shape is presented below

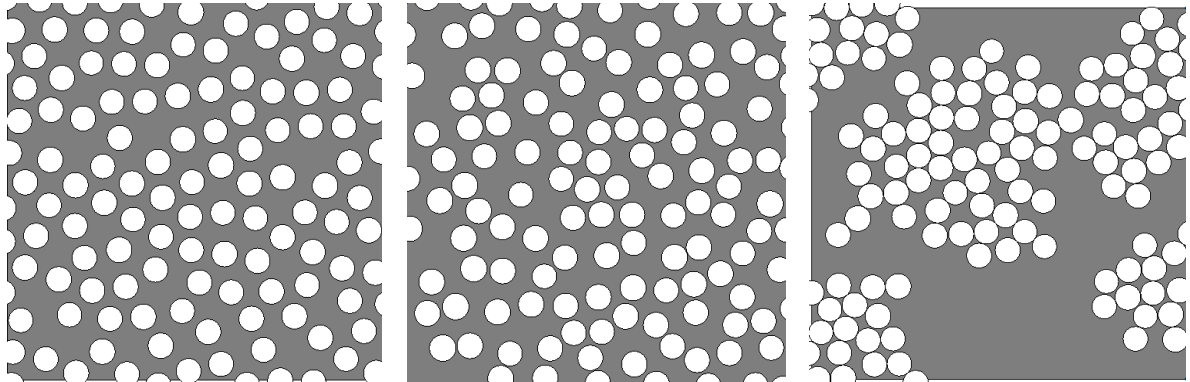
$$\frac{1}{15(1-v_m)} \begin{bmatrix} 7-5v_m & 5v_m-1 & 5v_m-1 & & & \\ 5v_m-1 & 7-5v_m & 5v_m-1 & & & \\ 5v_m-1 & 5v_m-1 & 7-5v_m & & & \\ & & & 0 & & \\ & & & & 4-5v_m & 0 & 0 \\ & & & & 0 & 4-5v_m & 0 \\ & & & & 0 & 0 & 4-5v_m \end{bmatrix}$$

7.4 D: Microstructures that can be generated by modified NNA

Microstructures with different fiber volume fractions (V_f) from 0.30 to 0.80

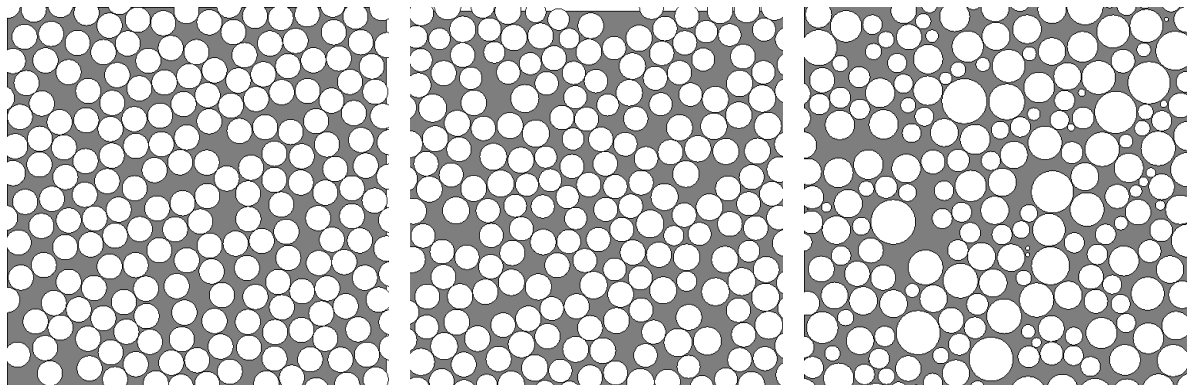


Microstructures with different spatial distribution with fiber volume fraction of 0.40.



Homogeneous	Random	Clusters
-------------	--------	----------

High variation in fiber radius



R_{mean}	7.85 μm	R_{mean}	7.85 μm	R_{mean}	7.85 μm
STD	0.0 μm	STD	0.12 μm	STD	2.5 μm

8 Bibliography

- [1] Hamidi YK, Altan MC. Process induced defects in liquid molding processes of composites. *Int Polym Process* 2017;32:527–44. <https://doi.org/10.3139/217.3444>.
- [2] Boussu F, Cristian I, Nauman S. General definition of 3D warp interlock fabric architecture. *Compos Part B Eng* 2015;80:171–88. <https://doi.org/10.1016/j.compositesb.2015.07.013>.
- [3] Talreja R. Manufacturing defects in composites and their effects on performance. *Polym. Compos. Aersp. Ind.*, Elsevier Inc.; 2015, p. 99–113. <https://doi.org/10.1016/B978-0-85709-523-7.00005-0>.
- [4] Campbell FC. *Manufacturing Processes for Advanced Composites*. vol. 1. Elsevier Science; 2003. <https://doi.org/10.1016/B978-1-85617-415-2.X5000-X>.
- [5] Abraham D, Matthews S, McIlhagger R. A comparison of physical properties of glass fibre epoxy composites produced by wet lay-up with autoclave consolidation and resin transfer moulding. *Compos Part A Appl Sci Manuf* 1998;29:795–801. [https://doi.org/10.1016/S1359-835X\(98\)00055-4](https://doi.org/10.1016/S1359-835X(98)00055-4).
- [6] Laurenzi S, Marchetti M. *Advanced Composite Materials by Resin Transfer Molding for Aerospace Applications*. *Compos. Their Prop.*, InTech; 2012. <https://doi.org/10.5772/48172>.
- [7] Liu L, Zhang BM, Wang DF, Wu ZJ. Effects of cure cycles on void content and mechanical properties of composite laminates. *Compos Struct* 2006;73:303–9. <https://doi.org/10.1016/j.compstruct.2005.02.001>.
- [8] Ruiz E, Achim V, Soukane S, Trochu F, Bréard J. Optimization of injection flow rate to minimize micro/macro-voids formation in resin transfer molded composites. *Compos Sci Technol* 2006;66:475–86. <https://doi.org/10.1016/j.compscitech.2005.06.013>.
- [9] Rojek J, Joannès S, Teissedre J-C, Laiarinandrasana L, Bunsell A, Teissèdre J-C, et al. Effect of through-thickness compressive stress and porosity on the tensile strength of carbon-fibre reinforced composites. *ICCM Int. Conf. Compos. Mater.*, ICCM22; 2019.
- [10] Gagauz I, Kawashita LF, Hallett SR. Effect of Voids on Interlaminar Behaviour of Carbon / Epoxy Composites. *Eur. Conf. Compos. Mater.*, 2016, p. 26–30.
- [11] Rohatgi V, Patel N, James Lee L. Experimental investigation of flow-induced microvoids during impregnation of unidirectional stitched fiberglass mat. *Polym Compos* 1996;17:161–70. <https://doi.org/10.1002/pc.10601>.
- [12] Hayward JS, Harris B. The effect of vacuum assistance in resin transfer moulding. *Compos Manuf* 1990;1:161–6. [https://doi.org/10.1016/0956-7143\(90\)90163-Q](https://doi.org/10.1016/0956-7143(90)90163-Q).
- [13] Grunenfelder LK, Nutt SR. Void formation in composite prepregs - Effect of dissolved moisture. *Compos Sci Technol* 2010;70:2304–9. <https://doi.org/10.1016/j.compscitech.2010.09.009>.

- [14] Vaxman A, Narkis M, Siegmann A, Kenig S. Void formation in short-fiber thermoplastic composites. *Polym Compos* 1989;10:449–53. <https://doi.org/10.1002/pc.750100609>.
- [15] Lundstrom TS, Gebart BR, Lundemo CY. Void Formation in RTM. *J Reinf Plast Compos* 1993;12:1339–49. <https://doi.org/10.1177/073168449301201207>.
- [16] Patel N, Lee LJ. Modeling of void formation and removal in liquid composite molding. Part II: Model development and implementation. *Polym Compos* 1996;17:104–14. <https://doi.org/10.1002/pc.10595>.
- [17] Lawrence JM, Neacsu V, Advani SG. Modeling the impact of capillary pressure and air entrapment on fiber tow saturation during resin infusion in LCM. *Compos Part A Appl Sci Manuf* 2009;40:1053–64. <https://doi.org/10.1016/j.compositesa.2009.04.013>.
- [18] Chen D, Arakawa K, Xu C. Reduction of void content of vacuum-assisted resin transfer molded composites by infusion pressure control. *Polym Compos* 2015;36:1629–37. <https://doi.org/10.1002/pc.23071>.
- [19] Leclerc JS, Ruiz E. Porosity reduction using optimized flow velocity in Resin Transfer Molding. *Compos Part A Appl Sci Manuf* 2008;39:1859–68. <https://doi.org/10.1016/j.compositesa.2008.09.008>.
- [20] Gueroult S, Lebel-Lavacry A, Park CH, Bizet L, Saouab A, Bréard J. Analytical modeling and in situ measurement of void formation in liquid composite molding processes. *Adv Compos Mater* 2014;23:31–42. <https://doi.org/10.1080/09243046.2013.862383>.
- [21] Park CH, Lebel A, Saouab A, Bréard J, Lee W II. Modeling and simulation of voids and saturation in liquid composite molding processes. *Compos Part A Appl Sci Manuf* 2011;42:658–68. <https://doi.org/10.1016/j.compositesa.2011.02.005>.
- [22] Park CH, Woo L. Modeling void formation and unsaturated flow in liquid composite molding processes: a survey and review. *J Reinf Plast Compos* 2011;30:957–77. <https://doi.org/10.1177/0731684411411338>.
- [23] Mehdikhani M, Gorbatiikh L, Verpoest I, Lomov S V. Voids in fiber-reinforced polymer composites: A review on their formation, characteristics, and effects on mechanical performance. *J Compos Mater* 2019;53:1579–669. <https://doi.org/10.1177/0021998318772152>.
- [24] de Almeida SFM, Neto Z dos SN. Effect of void content on the strength of composite laminates. *Compos Struct* 1994;28:139–48. [https://doi.org/10.1016/0263-8223\(94\)90044-2](https://doi.org/10.1016/0263-8223(94)90044-2).
- [25] Guerdal Z, Tomasino AP, Biggers SB. Effects of processing induced defects on laminate response: Interlaminar tensile strength. *SAMPE J* 1991;27:39–49.
- [26] Abdelal N, Donaldson SL. Comparison of methods for the characterization of voids in glass fiber composites. *J Compos Mater* 2017;002199831771008. <https://doi.org/10.1177/0021998317710083>.
- [27] Little JE, Yuan XW, Jones MI. Voids characterisation in carbon fibre/epoxy composite laminates. 18th Int. Conf. Compos. Mater., 2011.

- [28] Mehdikhani M, Straumit I, Gorbatiikh L, Lomov S V. Detailed characterization of voids in multidirectional carbon fiber/epoxy composite laminates using X-ray micro-computed tomography. *Compos Part A Appl Sci Manuf* 2019;105532. <https://doi.org/10.1016/J.COMPOSITESA.2019.105532>.
- [29] Rubin AM, Jerina KL. Evaluation of porosity in composite aircraft structures. *Compos Eng* 1993. [https://doi.org/10.1016/0961-9526\(93\)90085-X](https://doi.org/10.1016/0961-9526(93)90085-X).
- [30] Chambers AR, Earl JS, Squires CA, Suhot MA. The effect of voids on the flexural fatigue performance of unidirectional carbon fibre composites developed for wind turbine applications. *Int J Fatigue* 2006;28:1389–98. <https://doi.org/10.1016/j.ijfatigue.2006.02.033>.
- [31] Agius SL, Magniez KJC, Fox BL. Cure behaviour and void development within rapidly cured out-of-autoclave composites. *Compos Part B Eng* 2013;47:230–7. <https://doi.org/10.1016/j.compositesb.2012.11.020>.
- [32] Hsu DK, Uhl KM. A Morphological Study of Porosity Defects in Graphite-Epoxy Composites. *Rev. Prog. Quant. Nondestruct. Eval., Springer US*; 1987, p. 1175–84. https://doi.org/10.1007/978-1-4613-1893-4_134.
- [33] CA Howe, RJ Paton AG. A comparison between voids in RTM and prepreg carbon/epoxy laminates. *ICCM Int. Conf. Compos. Mater., vol. IV, 1997, p. 46–54*.
- [34] Iryna Gagauz LFK and SRH. Understanding the effect of void morphology and characteristics on laminate mechanical properties. *ICCM Int. Conf. Compos. Mater., 2017*.
- [35] Drach B, Drach A, Tsukrov I. Characterization and statistical modeling of irregular porosity in carbon/carbon composites based on X-ray microtomography data. *ZAMM - J Appl Math Mech / Zeitschrift Für Angew Math Und Mech* 2013;93:346–66. <https://doi.org/10.1002/zamm.201100190>.
- [36] Hamidi YK, Aktas L, Altan MC. Formation of microscopic voids in resin transfer molded composites. *J Eng Mater Technol* 2004;126:420–6. <https://doi.org/10.1115/1.1789958>.
- [37] Hernández S, Sket F, Molina-Aldareguía JM, González C, Llorca J. Effect of curing cycle on void distribution and interlaminar shear strength in polymer-matrix composites. *Compos Sci Technol* 2011;71:1331–41. <https://doi.org/10.1016/j.compscitech.2011.05.002>.
- [38] Sisodia SM, Garcea SC, George AR, Fullwood DT, Spearing SM, Gamstedt EK. High-resolution computed tomography in resin infused woven carbon fibre composites with voids. *Compos Sci Technol* 2016;131:12–21. <https://doi.org/10.1016/j.compscitech.2016.05.010>.
- [39] Ravey C, Ruiz E, Trochu F. Determination of the optimal impregnation velocity in Resin Transfer Molding by capillary rise experiments and infrared thermography. *Compos Sci Technol* 2014;99:96–102. <https://doi.org/10.1016/j.compscitech.2014.05.019>.
- [40] Drach B, Drach A, Tsukrov I. Prediction of the effective elastic moduli of materials with irregularly-shaped pores based on the pore projected areas. *Int J Solids Struct*

- 2014;51:2687–95. <https://doi.org/10.1016/J.IJSOLSTR.2014.03.042>.
- [41] Nikishkov Y, Airoidi L, Makeev A. Measurement of voids in composites by X-ray Computed Tomography. *Compos Sci Technol* 2013;89:89–97. <https://doi.org/10.1016/J.COMPSCITECH.2013.09.019>.
- [42] Lundström TS, Gebart BR. Influence from process parameters on void formation in resin transfer molding. *Polym Compos* 1994;15:25–33. <https://doi.org/10.1002/pc.750150105>.
- [43] Yoshida H, Ogasa T, Hayashi R. Statistical approach to the relationship between ILSS and void content of CFRP. *Compos Sci Technol* 1986;25:3–18. [https://doi.org/10.1016/0266-3538\(86\)90018-7](https://doi.org/10.1016/0266-3538(86)90018-7).
- [44] Zhan-Sheng Guo, Ling Liu, Bo-Ming Zhang, Shanyi Du. Critical Void Content for Thermoset Composite Laminates. *J Compos Mater* 2009;43:1775–90. <https://doi.org/10.1177/0021998306065289>.
- [45] Costa ML, Almeida SFM d., Rezende MC. The influence of porosity on the interlaminar shear strength of carbon/epoxy and carbon/bismaleimide fabric laminates. *Compos Sci Technol* 2001;61:2101–8. [https://doi.org/10.1016/S0266-3538\(01\)00157-9](https://doi.org/10.1016/S0266-3538(01)00157-9).
- [46] Tang JM, Lee WI, Springer GS. Effects of Cure Pressure on Resin Flow, Voids, and Mechanical Properties. *J Compos Mater* 1987;21:421–40. <https://doi.org/10.1177/002199838702100502>.
- [47] Jeong H. Effects of voids on the mechanical strength and ultrasonic attenuation of laminated composites. *J Compos Mater* 1997;31:276–92. <https://doi.org/10.1177/002199839703100303>.
- [48] Lambert J, Chambers AR, Sinclair I, Spearing SM. Damage characterisation and the role of voids in the fatigue of wind turbine blade materials. *ICCM Int. Conf. Compos. Mater.*, 2011.
- [49] Carraro PA, Maragoni L, Quaresimin M. Influence of manufacturing induced defects on damage initiation and propagation in carbon/epoxy NCF laminates. *Adv Manuf Polym Compos Sci* 2015;1:44–53. <https://doi.org/10.1179/2055035914Y.0000000004>.
- [50] Seon G, Makeev A, Nikishkov Y, Lee E. Effects of defects on interlaminar tensile fatigue behavior of carbon / epoxy composites. *Compos Sci Technol* 2013;89:194–201. <https://doi.org/10.1016/j.compscitech.2013.10.006>.
- [51] Olivier P, Cottu JP, Ferret B. Effects of cure cycle pressure and voids on some mechanical properties of carbon/epoxy laminates. *Composites* 1995;26:509–15. [https://doi.org/10.1016/0010-4361\(95\)96808-J](https://doi.org/10.1016/0010-4361(95)96808-J).
- [52] Judd NCW and Wright. Voids and their effects on mechanical-properties of composites. *Sampe J* 1978;14: 10–14.
- [53] Ghiorse SR. Effect of void content on the mechanical properties of carbon/epoxy laminates. *SAMPE Q* 1993;24:54–9.
- [54] RYSHKEWITCH E. Compression Strength of Porous Sintered Alumina and Zirconia: 9th

- Communication to Ceramography. *J Am Ceram Soc* 1953;36:65–8. <https://doi.org/10.1111/j.1151-2916.1953.tb12837.x>.
- [55] Wisnom MR, Reynolds T, Gwilliam N. Reduction in interlaminar shear strength by discrete and distributed voids. *Compos Sci Technol* 1996;56:93–101. [https://doi.org/10.1016/0266-3538\(95\)00128-X](https://doi.org/10.1016/0266-3538(95)00128-X).
- [56] Kousourakis A, Mouritz AP, Bannister MK. Interlaminar properties of polymer laminates containing internal sensor cavities. *Compos Struct* 2006;75:610–8. <https://doi.org/10.1016/j.compstruct.2006.04.086>.
- [57] Uhl KM, Lucht B, Jeong H, Hsu DK. Mechanical Strength Degradation of Graphite Fiber Reinforced Thermoset Composites Due to Porosity. *Rev. Prog. Quant. Nondestruct. Eval.*, Boston, MA: Springer US; 1988, p. 1075–82. https://doi.org/10.1007/978-1-4613-0979-6_24.
- [58] Goodwin AA, Howe CA, Paton RJ. The Role of Voids in Reducing the Interlaminar Shear Strength of RTM Laminates. *Proc. ICCM–11*, 1997, p. 11–9.
- [59] Harper BD, Staab GH, Chen RS. A Note on the Effects of Voids Upon the Hygral and Mechanical Properties of AS4/3502 Graphite/Epoxy. *J Compos Mater* 1987;21:280–9. <https://doi.org/10.1177/002199838702100306>.
- [60] Li SJ, Zhan LH, Chen R, Peng WF, Zhang YA, Zhou YQ, et al. The influence of cure pressure on microstructure, temperature field and mechanical properties of advanced polymer-matrix composite laminates. *Fibers Polym* 2014;15:2404–9. <https://doi.org/10.1007/s12221-014-2404-0>.
- [61] Stamopoulos A, Tserpes K, Prucha P, Vavrik D. Evaluation of porosity effects on the mechanical properties of carbon fiber-reinforced plastic unidirectional laminates by X-ray computed tomography and mechanical testing. *J Compos Mater* 2016;50:2087–98. <https://doi.org/10.1177/0021998315602049>.
- [62] Selmi A. Void Effect on Carbon Fiber Epoxy Composites. *2nd Int. Conf. Emerg. Trends Eng. Technol.*, International Institute of Engineers; 2014, p. 179–83. <https://doi.org/10.15242/IIE.E0514613>.
- [63] Huang H, Talreja R. Effects of void geometry on elastic properties of unidirectional fiber reinforced composites. *Compos Sci Technol* 2005;65:1964–81. <https://doi.org/10.1016/j.compscitech.2005.02.019>.
- [64] Varna J, Joffe R, Berglund LA, Lundström TS. Effect of voids on failure mechanisms in RTM laminates. *Compos Sci Technol* 1995;53:241–9. [https://doi.org/10.1016/0266-3538\(95\)00024-0](https://doi.org/10.1016/0266-3538(95)00024-0).
- [65] Broucke B Van Den, Hegemann J, Das R, Oster R, Hackl K. Modelling of textile reinforced composites using finite element tools and investigation of influence porosity on mechanical properties. *Finite Elem Model Text Text Compos* 2007;49:26–8.
- [66] Zhu H, Wu B, Li D, Zhang D, Chen Y. Influence of Voids on the Tensile Performance of Carbon/epoxy Fabric Laminates. *J Mater Sci Technol* 2011;27:69–73. [https://doi.org/10.1016/S1005-0302\(11\)60028-5](https://doi.org/10.1016/S1005-0302(11)60028-5).

- [67] Naganuma T, Naito K, Kyono J, Kagawa Y. Influence of prepreg conditions on the void occurrence and tensile properties of woven glass fiber-reinforced polyimide composites. *Compos Sci Technol* 2009. <https://doi.org/10.1016/j.compscitech.2009.06.012>.
- [68] Xu K, Qian X. An FEM analysis with consideration of random void defects for predicting the mechanical properties of 3d braided composites. *Adv Mater Sci Eng* 2014;2014. <https://doi.org/10.1155/2014/439819>.
- [69] Shigang A, Daining F, Rujie H, Yongmao P. Effect of manufacturing defects on mechanical properties and failure features of 3D orthogonal woven C/C composites. *Compos Part B Eng* 2015;71:113–21. <https://doi.org/10.1016/j.compositesb.2014.11.003>.
- [70] Hancox NL. The effects of flaws and voids on the shear properties of CFRP. *J Mater Sci* 1977;12:884–92. <https://doi.org/10.1007/BF00540969>.
- [71] Nikopour H. A virtual frame work for predication of effect of voids on transverse elasticity of a unidirectionally reinforced composite. *Comput Mater Sci* 2013. <https://doi.org/10.1016/j.commat.2013.05.049>.
- [72] Rubin AM, Jerina KL. Evaluation of porosity in composite aircraft structures. *Mech Compos Mater* 1995;30:587–600. <https://doi.org/10.1007/BF00821276>.
- [73] Farouk A, Langrana NA, Weng GJ. Modulus prediction of a cross-ply fiber reinforced fabric composite with voids. *Polym Compos* 1992;13:285–94. <https://doi.org/10.1002/pc.750130406>.
- [74] Qi L, Chao X, Tian W, Ma W, Li H. Numerical study of the effects of irregular pores on transverse mechanical properties of unidirectional composites. *Compos Sci Technol* 2018;159:142–51. <https://doi.org/10.1016/j.compscitech.2018.02.020>.
- [75] Dong J, Huo N. A two-scale method for predicting the mechanical properties of 3D braided composites with internal defects. *Compos Struct* 2016;152:1–10. <https://doi.org/10.1016/J.COMPSTRUCT.2016.05.025>.
- [76] Lomov S V., Ivanov DS, Verpoest I, Zako M, Kurashiki T, Nakai H, et al. Meso-FE modelling of textile composites: Road map, data flow and algorithms. *Compos Sci Technol* 2007;67:1870–91. <https://doi.org/10.1016/j.compscitech.2006.10.017>.
- [77] Choudhry RS, Sharif T, Khan KA, Khan SZ, Hassan A, Khan MA. Predicting the effect of voids on mechanical properties of woven composites. *IOP Conf. Ser. Mater. Sci. Eng.*, vol. 406, 2018, p. 012007. <https://doi.org/10.1088/1757-899X/406/1/012007>.
- [78] Yanjun C, Guiqiong J, Bo W, Wei L. Elastic behavior analysis of 3D angle-interlock woven ceramic composites. *Acta Mech Solida Sin* 2006;19:152–9. <https://doi.org/10.1007/s10338-006-0618-4>.
- [79] Ansar M, Xinwei W, Chouwei Z. Modeling strategies of 3D woven composites: A review. *Compos Struct* 2011;93:1947–63. <https://doi.org/10.1016/j.compstruct.2011.03.010>.
- [80] Hage C El, Younès R, Aboura Z, Benzeggagh ML, Zoeter M. Analytical and numerical modeling of mechanical properties of orthogonal 3D CFRP. *Compos Sci Technol*

- 2009;69:111–6. <https://doi.org/10.1016/j.compscitech.2007.10.048>.
- [81] Naik NK, Sridevi E. An Analytical Method for Thermoelastic Analysis of 3D Orthogonal Interlock Woven Composites. *J Reinf Plast Compos* 2002;21:1149–91. <https://doi.org/10.1177/073168402128987716>.
- [82] Dong C. Effects of Process-Induced Voids on the Properties of Fibre Reinforced Composites. *J Mater Sci Technol* 2016;32:597–604. <https://doi.org/10.1016/j.jmst.2016.04.011>.
- [83] Hyde A, He J, Cui X, Lua J, Liu L. Effects of microvoids on strength of unidirectional fiber-reinforced composite materials. *Compos Part B Eng* 2020;187:107844. <https://doi.org/10.1016/j.compositesb.2020.107844>.
- [84] E W, Engquist B, Li X, Ren W, Vanden-Eijnden E. Heterogeneous Multiscale Methods: A Review. *Commun Comput Phys Commun Comput Phys* 2007;2:367–450.
- [85] Sendeckyj G, Wang S, Steven Johnson W, Stinchcomb W, Chamis C. Mechanics of Composite Materials: Past, Present, and Future. *J Compos Technol Res* 1989;11:3. <https://doi.org/10.1520/CTR10143J>.
- [86] Aboudi J, Arnold S, Bednarczyk B. *Micromechanics of Composite Materials*. Elsevier; 2013. <https://doi.org/10.1016/C2011-0-05224-9>.
- [87] Ishikawa T, Chou T-W. Elastic Behavior of Woven Hybrid Composites. *J Compos Mater* 1982;16:2–19. <https://doi.org/10.1177/002199838201600101>.
- [88] Ishikawa T, Chou TW. Stiffness and strength behaviour of woven fabric composites. *J Mater Sci* 1982;17:3211–20. <https://doi.org/10.1007/BF01203485>.
- [89] Hallal A, Younes R, Fardoun F, Nehme S. Improved analytical model to predict the effective elastic properties of 2.5D interlock woven fabrics composite. *Compos Struct* 2012;94:3009–28. <https://doi.org/10.1016/j.compstruct.2012.03.019>.
- [90] Zhou Y-X, Huang Z-M. A bridging model prediction of the ultimate strength of composite laminates subjected to triaxial loads. *J Compos Mater* 2012;46:2343–78. <https://doi.org/10.1177/0021998312449491>.
- [91] Naik NK, Ganesh VK. Prediction of on-axes elastic properties of plain weave fabric composites. *Compos Sci Technol* 1992;45:135–52. [https://doi.org/10.1016/0266-3538\(92\)90036-3](https://doi.org/10.1016/0266-3538(92)90036-3).
- [92] Hallal A, Younes R, Fardoun F. Review and comparative study of analytical modeling for the elastic properties of textile composites. *Compos Part B Eng* 2013;50:22–31. <https://doi.org/10.1016/j.compositesb.2013.01.024>.
- [93] Gommers B, Verpoest I, Van Houtte P. The Mori-Tanaka method applied to textile composite materials. *Acta Mater* 1998;46:2223–35. [https://doi.org/10.1016/S1359-6454\(97\)00296-6](https://doi.org/10.1016/S1359-6454(97)00296-6).
- [94] Eshelby JD. The Determination of the Elastic Field of an Ellipsoidal Inclusion, and Related Problems. *Proc R Soc A Math Phys Eng Sci* 1957;241:376–96. <https://doi.org/10.1098/rspa.1957.0133>.

- [95] Lomov SV, Gusakov AV, Huysmans G, Prodromou A, Verpoest I. Textile geometry preprocessor for meso-mechanical models of woven composites. *Compos Sci Technol* 2000;60:2083–95. [https://doi.org/10.1016/S0266-3538\(00\)00121-4](https://doi.org/10.1016/S0266-3538(00)00121-4).
- [96] Prodromou AG, Lomov S V., Verpoest I. The method of cells and the mechanical properties of textile composites. *Compos Struct* 2011;93:1290–9. <https://doi.org/10.1016/j.compstruct.2010.09.022>.
- [97] Raju B, Hiremath SR, Roy Mahapatra D. A review of micromechanics based models for effective elastic properties of reinforced polymer matrix composites. *Compos Struct* 2018;204:607–19. <https://doi.org/10.1016/J.COMPSTRUCT.2018.07.125>.
- [98] Ramakrishna S. Characterization and modeling of the tensile properties of plain weft-knit fabric-reinforced composites. *Compos Sci Technol* 1997;57:1–22. [https://doi.org/10.1016/S0266-3538\(96\)00098-X](https://doi.org/10.1016/S0266-3538(96)00098-X).
- [99] Chen Y, Vasiukov D, Gélébart L, Park CH. Fast Fourier transform solver for damage modeling of composite materials. *JMST Adv* 2019;1:49–55. <https://doi.org/10.1007/s42791-019-0004-2>.
- [100] Vasiukov D, Parvathaneni KK, Lomov S V., Park CH. Multi-scale modelling of 3D textile composites with different orthogonal mesostructures including the influence of the composite manufacturing process. *ECCM 2018 - 18th Eur Conf Compos Mater 2018*.
- [101] Liu Y, Straumit I, Vasiukov D, Lomov S V., Panier S. Multi-scale material model for 3D composite using Micro CT Images geometry reconstruction. *ECCM 2016 - Proceeding 17th Eur. Conf. Compos. Mater.*, 2016.
- [102] Fish J. *Multiscale Methods*. vol. 44. Oxford University Press; 2009. <https://doi.org/10.1093/acprof:oso/9780199233854.001.0001>.
- [103] Geers MGD, Kouznetsova VG, Brekelmans WAM. Multi-scale computational homogenization: Trends and challenges. *J Comput Appl Math* 2010;234:2175–82. <https://doi.org/10.1016/J.CAM.2009.08.077>.
- [104] Torquato S, Uche OU, Stillinger FH. Random sequential addition of hard spheres in high Euclidean dimensions. *Phys Rev E - Stat Nonlinear, Soft Matter Phys* 2006;74:061308. <https://doi.org/10.1103/PhysRevE.74.061308>.
- [105] Liu H, Cui H, Wen W, Su X, Kang H, Engler-Pinto C. The effect of voids on the quasi-static tensile properties of carbon fiber/polymer-laminated composites. *J Compos Mater* 2017;002199831773782. <https://doi.org/10.1177/0021998317737827>.
- [106] Masmoudi M, Kaddouri W, Kanit T, Madani S, Ramtani S, Imad A. Modeling of the effect of the void shape on effective ultimate tensile strength of porous materials: Numerical homogenization versus experimental results. *Int J Mech Sci* 2017;130:497–507. <https://doi.org/10.1016/J.IJMECSCI.2017.06.011>.
- [107] Matveeva A, Garoz D, Sevenois RDB, Zhu M, Pyl L, Van Paepegem W, et al. Effect of intra-ply voids on the homogenized behavior of a ply in multidirectional laminates. *IOP Conf Ser Mater Sci Eng* 2018;406. <https://doi.org/10.1088/1757-899X/406/1/012009>.
- [108] Wu L, Chung CN, Major Z, Adam L, Noels L. From SEM images to elastic responses: A

- stochastic multiscale analysis of UD fiber reinforced composites. *Compos Struct* 2018;189:206–27. <https://doi.org/10.1016/j.compstruct.2018.01.051>.
- [109] Melro AR, Camanho PP, Pinho ST. Influence of geometrical parameters on the elastic response of unidirectional composite materials. *Compos Struct* 2012;94:3223–31. <https://doi.org/10.1016/j.compstruct.2012.05.004>.
- [110] Hale RD, Villa M. Influence of opposing wave nesting in compression-loaded composites. *J Compos Mater* 2003;37:1149–66. <https://doi.org/10.1177/0021998303037013002>.
- [111] Woo K, Suh YW. Low Degree of Homogeneity Due to Phase Shifts for Woven Composites. *J Compos Technol Res* 2001;23:239–46. <https://doi.org/10.1520/ctr10996j>.
- [112] Kashani MH, Milani AS. Damage Prediction in Woven and Non-woven Fabric Composites. *Non-woven Fabr., InTech*; 2016. <https://doi.org/10.5772/61511>.
- [113] Le Page BH, Guild FJ, Ogin SL, Smith PA. Finite element simulation of woven fabric composites. *Compos. Part A Appl. Sci. Manuf.*, vol. 35, Elsevier; 2004, p. 861–72. <https://doi.org/10.1016/j.compositesa.2004.01.017>.
- [114] Dixit A, Mali HS. Modeling techniques for predicting the mechanical properties of woven-fabric textile composites: A Review. *Mech Compos Mater* 2013;49:1–20. <https://doi.org/10.1007/s11029-013-9316-8>.
- [115] Isart N, El Said B, Ivanov DS, Hallett SR, Mayugo JA, Blanco N. Internal geometric modelling of 3D woven composites: A comparison between different approaches. *Compos Struct* 2015;132:1219–30. <https://doi.org/10.1016/j.compstruct.2015.07.007>.
- [116] Wintiba B, Sonon B, Ehab Moustafa Kamel K, Massart TJ. An automated procedure for the generation and conformal discretization of 3D woven composites RVEs. *Compos Struct* 2017;180:955–71. <https://doi.org/10.1016/j.compstruct.2017.08.010>.
- [117] Sherburn M. Geometric and Mechanical Modelling of Textiles. Phd Thesis 2007.
- [118] Lomov SV, Verpoest I. Model of shear of woven fabric and parametric description of shear resistance of glass woven reinforcements. *Compos Sci Technol* 2006;66:919–33. <https://doi.org/10.1016/j.compscitech.2005.08.010>.
- [119] Wendling A, Hivet G, Vidal-Sallé E, Boisse P. Consistent geometrical modelling of interlock fabrics. *Finite Elem Anal Des* 2014;90:93–105. <https://doi.org/10.1016/j.finel.2014.05.010>.
- [120] Badel P, Vidal-Sallé E, Maire E, Boisse P. Simulation and tomography analysis of textile composite reinforcement deformation at the mesoscopic scale. *Compos Sci Technol* 2008;68:2433–40. <https://doi.org/10.1016/j.compscitech.2008.04.038>.
- [121] Lomov S V., Huysmans G, Verpoest I. Hierarchy of Textile Structures and Architecture of Fabric Geometric Models. *Text Res J* 2001;71:534–43. <https://doi.org/10.1177/004051750107100611>.
- [122] Lomov S V., Verpoest I. Compression of Woven Reinforcements: A Mathematical

- Model. *J Reinf Plast Compos* 2000;19:1329–50. <https://doi.org/10.1106/50RF-DQJ7-9RN3-6CPX>.
- [123] Ha-minh C, Provost B, Boussu F, Coutellier D, Ha-minh C, Provost B, et al. Vers la géométrie réelle d'un tissu 3D interlock sur la précision de la simulation numérique à l'impact. 2018.
- [124] Roirand Q. Modélisation multiéchelle du comportement et de l'endommagement de composites tissés 3D. Développement d'outils numériques d'aide à la conception des structures tissées. 2018.
- [125] Sonon B, Massart TJ. A level-set based representative volume element generator and XFEM simulations for textile and 3D-reinforced composites. *Materials (Basel)* 2013;6:5568–92. <https://doi.org/10.3390/ma6125568>.
- [126] Piezel B, Mercatoris BCN, Trabelsi W, Laiarinandrasana L, Thionnet A, Massart TJ. Bending effect on the risk for delamination at the reinforcement/matrix interface of 3D woven fabric composite using a shell-like RVE. *Compos Struct* 2012;94:2343–57. <https://doi.org/10.1016/j.compstruct.2012.03.015>.
- [127] Piezel B, Laiarinandrasana L, Thionnet T. A multilevel finite element analysis of a textile composite. *ICCM Int Conf Compos Mater* 2009.
- [128] Perie G, Lomov S V, Verpoest I, Marsal D. Meso-scale modelling and homogenization of interlock reinforced composite. *ICCM Int. Conf. Compos. Mater.*, 2009.
- [129] Lin H, Sherburn M, Crookston J, Long AC, Clifford MJ, Jones IA. Finite element modelling of fabric compression. *Model Simul Mater Sci Eng* 2008;16:035010. <https://doi.org/10.1088/0965-0393/16/3/035010>.
- [130] Cox BN, Dadkhah MS, Morris WL. On the tensile failure of 3D woven composites. *Compos Part A Appl Sci Manuf* 1996;27:447–58. [https://doi.org/10.1016/1359-835X\(95\)00053-5](https://doi.org/10.1016/1359-835X(95)00053-5).
- [131] Mahadik Y, Hallett SR. Effect of fabric compaction and yarn waviness on 3D woven composite compressive properties. *Compos Part A Appl Sci Manuf* 2011;42:1592–600. <https://doi.org/10.1016/j.compositesa.2011.07.006>.
- [132] Wang Y, Sun X. Digital-element simulation of textile processes. *Compos Sci Technol* 2001;61:311–9. [https://doi.org/10.1016/S0266-3538\(00\)00223-2](https://doi.org/10.1016/S0266-3538(00)00223-2).
- [133] El Said B, Green S, Hallett SR. Kinematic modelling of 3D woven fabric deformation for structural scale features. *Compos Part A Appl Sci Manuf* 2014;57:95–107. <https://doi.org/10.1016/j.compositesa.2013.11.006>.
- [134] Durville D. Finite Element Simulation of the Mechanical Behaviour of Textile Composites at the Mesoscopic Scale of Individual Fibers. *Comput. Methods Appl. Sci.*, vol. 8, Springer; 2008, p. 15–34. https://doi.org/10.1007/978-1-4020-6856-0_2.
- [135] Green SD, Long AC, El Said BSF, Hallett SR. Numerical modelling of 3D woven preform deformations. *Compos Struct* 2014;108:747–56. <https://doi.org/10.1016/j.compstruct.2013.10.015>.

- [136] Faes JC, Rezaei A, Van Paepegem W, Degrieck J. Accuracy of 2D FE models for prediction of crack initiation in nested textile composites with inhomogeneous intra-yarn fiber volume fractions. *Compos Struct* 2016;140:11–20. <https://doi.org/10.1016/j.compstruct.2015.12.024>.
- [137] Wintiba B, Vasiukov D, Panier S, Lomov S V, Moustafa Kamel, K E, Massart TJ. Automated reconstruction and conformal discretization of 3D woven composite CT scans with local fiber volume fraction control. *Compos Struct* 2020;112438. <https://doi.org/10.1016/j.compstruct.2020.112438>.
- [138] Naouar N, Vidal-Salle E, Schneider J, Maire E, Boisse P. 3D composite reinforcement meso F.E. analyses based on X-ray computed tomography. *Compos Struct* 2015;132:1094–104. <https://doi.org/10.1016/j.compstruct.2015.07.005>.
- [139] Straumit I, Lomov S V., Wevers M. Quantification of the internal structure and automatic generation of voxel models of textile composites from X-ray computed tomography data. *Compos Part A Appl Sci Manuf* 2015;69:150–8. <https://doi.org/10.1016/J.COMPOSITESA.2014.11.016>.
- [140] Liu Y, Straumit I, Vasiukov D, Lomov S V., Panier S. Prediction of linear and non-linear behavior of 3D woven composite using mesoscopic voxel models reconstructed from X-ray micro-tomography. *Compos Struct* 2017;179:568–79. <https://doi.org/10.1016/j.compstruct.2017.07.066>.
- [141] Mühlstädt M, Seifert W, Arras MML, Maenz S, Jandt KD, Bossert J. 3D model of intra-yarn fiber volume fraction gradients of woven fabrics. *Compos Struct* 2017;180:944–54. <https://doi.org/10.1016/j.compstruct.2017.08.049>.
- [142] Kurashiki T, Zako M, Hirosawa S, Lomov S V, Verpoest I. Estimation of a mechanical characterization for woven fabric composites by FEM based on damage mechanics. *Proc. ECCM-12, 2004*.
- [143] Pierreux G, Van Hemelrijck D, Massart TJ. Automated generation of 3D orthogonal woven composites RVEs including yarn cross-section variations. *Compos Sci Technol* 2019;176:90–102. <https://doi.org/10.1016/j.compscitech.2019.03.023>.
- [144] Laiarinandrasana L, Morgeneyer TF, Proudhon H, N’Guyen F, Maire E. Effect of multiaxial stress state on morphology and spatial distribution of voids in deformed semicrystalline polymer assessed by X-ray tomography. *Macromolecules* 2012;45:4658–68. <https://doi.org/10.1021/ma3005247>.
- [145] Gigliotti M, Pannier Y, Gonzalez RA, Lafarie-Frenot MC, Lomov S V. X-ray micro-computed-tomography characterization of cracks induced by thermal cycling in non-crimp 3D orthogonal woven composite materials with porosity. *Compos Part A Appl Sci Manuf* 2018;112:100–10. <https://doi.org/10.1016/j.compositesa.2018.05.020>.
- [146] Rojek J, Breite C, Swolfs Y, Laiarinandrasana L. Void growth measurement and modelling in a thermosetting epoxy resin using SEM and tomography techniques. *Contin Mech Thermodyn* 2020;32:471–88. <https://doi.org/10.1007/s00161-020-00865-5>.
- [147] Hurmane A, Mavel A, Paulmier P, Laurin F. Combined experimental and modelling

- approaches for strength analysis of 3D woven composites: from elementary coupons to complex aeronautical structures. *AerospaceLab J* 2016;1–11. <https://doi.org/10.12762/2016.AL12-03>.
- [148] Médeau V. Rupture des composites tissés 3D : de la caractérisation expérimentale à la simulation robuste des effets d'échelle 2019.
- [149] Hill R. Elastic properties of reinforced solids: Some theoretical principles. *J Mech Phys Solids* 1963;11:357–72. [https://doi.org/10.1016/0022-5096\(63\)90036-X](https://doi.org/10.1016/0022-5096(63)90036-X).
- [150] Pastore CM, Bogdanovich AE, Gowayed YA. Applications of a meso-volume-based analysis for textile composite structures. *Compos Eng* 1993;3:181–94. [https://doi.org/10.1016/0961-9526\(93\)90041-H](https://doi.org/10.1016/0961-9526(93)90041-H).
- [151] Kim HJ, Swan CC. Voxel-based meshing and unit-cell analysis of textile composites. *Int J Numer Methods Eng* 2003;56:977–1006. <https://doi.org/10.1002/nme.594>.
- [152] Hollister SJ, Riemer BA. Digital-image-based finite element analysis for bone microstructure using conjugate gradient and Gaussian filter techniques. In: Wilson JN, Wilson DC, editors. *Math. Methods Med. Imaging II*, vol. 2035, SPIE; 1993, p. 95–106. <https://doi.org/10.1117/12.146616>.
- [153] Doitrand A, Fagiano C, Irisarri FX, Hirsekorn M. Comparison between voxel and consistent meso-scale models of woven composites. *Compos Part A Appl Sci Manuf* 2015;73:143–54. <https://doi.org/10.1016/j.compositesa.2015.02.022>.
- [154] Fang G, El Said B, Ivanov D, Hallett SR. Smoothing artificial stress concentrations in voxel-based models of textile composites. *Compos Part A Appl Sci Manuf* 2016;80:270–84. <https://doi.org/10.1016/j.compositesa.2015.10.025>.
- [155] Espadas-Escalante JJ, van Dijk NP, Isaksson P. A study on the influence of boundary conditions in computational homogenization of periodic structures with application to woven composites. *Compos Struct* 2017;160:529–37. <https://doi.org/10.1016/J.COMPSTRUCT.2016.10.082>.
- [156] Zhang YC, Harding J. A numerical micromechanics analysis of the mechanical properties of a plain weave composite. *Comput Struct* 1990;36:839–44. [https://doi.org/10.1016/0045-7949\(90\)90154-T](https://doi.org/10.1016/0045-7949(90)90154-T).
- [157] Byström J, Jekabsons N, Varna J. An evaluation of different models for prediction of elastic properties of woven composites. *Compos Part B Eng* 2000;31:7–20. [https://doi.org/10.1016/S1359-8368\(99\)00061-X](https://doi.org/10.1016/S1359-8368(99)00061-X).
- [158] Vaughan TJ, McCarthy CT. A combined experimental–numerical approach for generating statistically equivalent fibre distributions for high strength laminated composite materials. *Compos Sci Technol* 2010;70:291–7. <https://doi.org/10.1016/J.COMPSCITECH.2009.10.020>.
- [159] Kouznetsova VG. Computational homogenization for the multi-scale analysis of multi-phase materials. 2002. <https://doi.org/10.6100/IR560009>.
- [160] Schneider K, Klusemann B, Bargmann S. Fully periodic RVEs for technological relevant composites: not worth the effort! *J Mech Mater Struct* 2017;12:471–84.

- <https://doi.org/10.2140/jomms.2017.12.471>.
- [161] Bodaghi M, Costa R, Gomes R, Silva J, Correia N, Silva F. Experimental comparative study of the variants of high-temperature vacuum-assisted resin transfer moulding. *Compos Part A Appl Sci Manuf* 2020;129:105708. <https://doi.org/10.1016/j.compositesa.2019.105708>.
- [162] LIU Y. Multi-Scale damage modelling of 3D textile reinforced composites including microstructural variability generation and meso-scale reconstruction. IMT Lille Douai, 2017.
- [163] Todeschini R, Consonni V. *Molecular Descriptors for Chemoinformatics*. vol. 2. 2010. <https://doi.org/10.1002/9783527628766>.
- [164] Haeri M, Haeri M. ImageJ Plugin for Analysis of Porous Scaffolds used in Tissue Engineering. *J Open Res Softw* 2015;3. <https://doi.org/10.5334/jors.bn>.
- [165] Mesquita A, Pereira J, Jenny A. Streamlined particle quantification (SParQ) plug-in is an automated fluorescent vesicle quantification plug-in for particle quantification in Fiji/ImageJ. *Autophagy* 2020;16:1711–7. <https://doi.org/10.1080/15548627.2019.1695400>.
- [166] Karahan M, Lomov S V., Bogdanovich AE, Mungalov D, Verpoest I. Internal geometry evaluation of non-crimp 3D orthogonal woven carbon fabric composite. *Compos. Part A Appl. Sci. Manuf.*, vol. 41, 2010, p. 1301–11. <https://doi.org/10.1016/j.compositesa.2010.05.014>.
- [167] Amirkhosravi M, Pishvar M, Hamidi YK, Altan MC. Accurate characterization of fiber and void volume fractions of natural fiber composites by pyrolysis in a nitrogen atmosphere. *AIP Conf. Proc.*, vol. 2205, American Institute of Physics Inc.; 2020, p. 020032. <https://doi.org/10.1063/1.5142947>.
- [168] Bostanabad R, Zhang Y, Li X, Kearney T, Brinson LC, Apley DW, et al. Computational microstructure characterization and reconstruction: Review of the state-of-the-art techniques. *Prog Mater Sci* 2018. <https://doi.org/10.1016/j.pmatsci.2018.01.005>.
- [169] Arganda-Carreras I, Kaynig V, Rueden C, Eliceiri KW, Schindelin J, Cardona A, et al. Trainable Weka Segmentation: a machine learning tool for microscopy pixel classification. *Bioinformatics* 2017;33:2424–6. <https://doi.org/10.1093/bioinformatics/btx180>.
- [170] Mehdikhani M, Straumit I, Gorbatiikh L, Lomov S V. Detailed characterization of voids in multidirectional carbon fiber/epoxy composite laminates using X-ray micro-computed tomography. *Compos Part A Appl Sci Manuf* 2019:105532. <https://doi.org/10.1016/J.COMPOSITESA.2019.105532>.
- [171] Carter JLW, Uchic MD, Mills MJ. Impact of Speckle Pattern Parameters on DIC Strain Resolution Calculated from In-situ SEM Experiments. *Conf. Proc. Soc. Exp. Mech. Ser.*, vol. 66, 2015, p. 119–26. https://doi.org/10.1007/978-3-319-06977-7_16.
- [172] Correlated Solutions. Application Note AN -1701 Speckle Pattern Fundamentals. 2017.
- [173] Angioni SL, Meo M, Foreman A. A comparison of homogenization methods for 2-D

- woven composites. *Compos Part B Eng* 2011;42:181–9. <https://doi.org/10.1016/J.COMPOSITESB.2010.10.004>.
- [174] Vignoli LL, Savi MA, Pacheco PMCL, Kalamkarov AL. Comparative analysis of micromechanical models for the elastic composite laminae. *Compos Part B Eng* 2019;174. <https://doi.org/10.1016/j.compositesb.2019.106961>.
- [175] Mori T, Tanaka K. Average stress in matrix and average elastic energy of materials with misfitting inclusions. *Acta Metall* 1973;21:571–4. [https://doi.org/10.1016/0001-6160\(73\)90064-3](https://doi.org/10.1016/0001-6160(73)90064-3).
- [176] Benveniste Y. A new approach to the application of Mori-Tanaka's theory in composite materials. *Mech Mater* 1987;6:147–57. [https://doi.org/10.1016/0167-6636\(87\)90005-6](https://doi.org/10.1016/0167-6636(87)90005-6).
- [177] Skrzat, A., Stachowicz F. Determination of Effective Properties of Fiber-Reinforced. *ASTRJ* 2014;8:56–9. <https://doi.org/10.12913/22998624.1105167>.
- [178] Liu H, Catherine Brinson L. A hybrid numerical-analytical method for modeling the viscoelastic properties of polymer nanocomposites. *J. Appl. Mech. Trans. ASME*, vol. 73, American Society of Mechanical Engineers Digital Collection; 2006, p. 758–68. <https://doi.org/10.1115/1.2204961>.
- [179] Li Y, Waas AM, Arruda EM. A closed-form, hierarchical, multi-interphase model for composites Derivation, verification and application to nanocomposites. *J Mech Phys Solids* 2011;59:43–63. <https://doi.org/10.1016/j.jmps.2010.09.015>.
- [180] Tandon GP, Weng GJ. The effect of aspect ratio of inclusions on the elastic properties of unidirectionally aligned composites. *Polym Compos* 1984;5:327–33. <https://doi.org/10.1002/pc.750050413>.
- [181] Weng GJ. Some elastic properties of reinforced solids, with special reference to isotropic ones containing spherical inclusions. *Int J Eng Sci* 1984;22:845–56. [https://doi.org/10.1016/0020-7225\(84\)90033-8](https://doi.org/10.1016/0020-7225(84)90033-8).
- [182] Wang YM, Weng GJ. The influence of inclusion shape on the overall viscoelastic behavior of composites. *J Appl Mech Trans ASME* 1992;59:510–8. <https://doi.org/10.1115/1.2893753>.
- [183] Klusemann B, Böhm HJ, Svendsen B. Homogenization methods for multi-phase elastic composites with non-elliptical reinforcements: Comparisons and benchmarks. *Eur J Mech A/Solids* 2012;34:21–37. <https://doi.org/10.1016/j.euromechsol.2011.12.002>.
- [184] Benveniste Y, Dvorak GJ, Chen T. On diagonal and elastic symmetry of the approximate effective stiffness tensor of heterogeneous media. *J Mech Phys Solids* 1991;39:927–46. [https://doi.org/10.1016/0022-5096\(91\)90012-D](https://doi.org/10.1016/0022-5096(91)90012-D).
- [185] Ferrari M. Asymmetry and the high concentration limit of the Mori-Tanaka effective medium theory. *Mech Mater* 1991;11:251–6. [https://doi.org/10.1016/0167-6636\(91\)90006-L](https://doi.org/10.1016/0167-6636(91)90006-L).
- [186] Qiu YP, Weng GJ. On the application of Mori-Tanaka's theory involving transversely isotropic spheroidal inclusions. *Int J Eng Sci* 1990;28:1121–37.

- [https://doi.org/10.1016/0020-7225\(90\)90112-V](https://doi.org/10.1016/0020-7225(90)90112-V).
- [187] Castañeda PP, Willis JR. The effect of spatial distribution on the effective behavior of composite materials and cracked media. *J Mech Phys Solids* 1995;43:1919–51. [https://doi.org/10.1016/0022-5096\(95\)00058-Q](https://doi.org/10.1016/0022-5096(95)00058-Q).
- [188] Yang Q-S, Tao X, Yang H. A stepping scheme for predicting effective properties of the multi-inclusion composites. *Int J Eng Sci* 2007;45:997–1006. <https://doi.org/10.1016/J.IJENGSCI.2007.07.005>.
- [189] Abaimov SG, Khudyakova AA, Lomov S V. On the closed form expression of the Mori-Tanaka theory prediction for the engineering constants of a unidirectional fiber-reinforced ply. *Compos Struct* 2016;142:1–6. <https://doi.org/10.1016/j.compstruct.2016.02.001>.
- [190] Liu L, Huang Z. A Note on mori-tanaka's method. *Acta Mech Solida Sin* 2014;27:234–44. [https://doi.org/10.1016/S0894-9166\(14\)60033-1](https://doi.org/10.1016/S0894-9166(14)60033-1).
- [191] Desrumaux F, Meraghni F, Benzeggagh ML. Generalised Mori-Tanaka scheme to model anisotropic damage using numerical Eshelby tensor. *J Compos Mater* 2001;35:603–24. <https://doi.org/10.1106/NNKC-VVM2-D78W-4KA5>.
- [192] Saadat F, Birman V, Thomopoulos S, Genin GM. Effective elastic properties of a composite containing multiple types of anisotropic ellipsoidal inclusions, with application to the attachment of tendon to bone. *J Mech Phys Solids* 2015;82:367–77. <https://doi.org/10.1016/J.JMPS.2015.05.017>.
- [193] Zhou J, Qi L, Gokhale AM. Generation of three-dimensional microstructure model for discontinuously reinforced composite by Modified Random Sequential Absorption Method. *J Eng Mater Technol* 2016;138:021001. <https://doi.org/10.1115/1.4032152>.
- [194] Chen X, Papathanasiou TD. The transverse permeability of disordered fiber arrays: A statistical correlation in terms of the mean nearest interfiber spacing. *Transp Porous Media* 2008;71:233–51. <https://doi.org/10.1007/s11242-007-9123-6>.
- [195] Gommer F, Endruweit A, Long AC. Influence of the micro-structure on saturated transverse flow in fibre arrays. *J Compos Mater* 2018;52:2463–75. <https://doi.org/10.1177/0021998317747954>.
- [196] Wang W, Dai Y, Zhang C, Gao X, Zhao M. Micromechanical modeling of fiber-reinforced composites with statistically equivalent random fiber distribution. *Materials (Basel)* 2016;9:1–14. <https://doi.org/10.3390/ma9080624>.
- [197] Jeong G, Lim JH, Choi C, Kim SW. A virtual experimental approach to evaluate transverse damage behavior of a unidirectional composite considering noncircular fiber cross-sections. *Compos Struct* 2019;228. <https://doi.org/10.1016/j.compstruct.2019.111369>.
- [198] Romanov V, Lomov S V., Swolfs Y, Orlova S, Gorbatiikh L, Verpoest I. Statistical analysis of real and simulated fibre arrangements in unidirectional composites. *Compos Sci Technol* 2013;87:126–34. <https://doi.org/10.1016/J.COMPSCITECH.2013.07.030>.
- [199] Gommer F, Endruweit A, Long AC. Quantification of micro-scale variability in fibre

- bundles. *Compos Part A Appl Sci Manuf* 2016;87:131–7. <https://doi.org/10.1016/J.COMPOSITESA.2016.04.019>.
- [200] Catalanotti G. On the generation of RVE-based models of composites reinforced with long fibres or spherical particles. *Compos Struct* 2016;138:84–95. <https://doi.org/10.1016/j.compstruct.2015.11.039>.
- [201] Wongsto A, Li S. Micromechanical FE analysis of UD fibre-reinforced composites with fibres distributed at random over the transverse cross-section 2005;36:1246–66. <https://doi.org/10.1016/j.compositesa.2005.01.010>.
- [202] Liu Y, Vasiukov D, Panier S. A numerical approach to reconstruct mesoscopic yarn section of textile composites based upon X-ray. 23ème Congrès Fr. Mécanique, Lille: 2017, p. 1–9.
- [203] Pathan MV, Tagarielli VL, Patsias S, Baiz-Villafranca PM. A new algorithm to generate representative volume elements of composites with cylindrical or spherical fillers. *Compos Part B Eng* 2017;110:267–78. <https://doi.org/10.1016/J.COMPOSITESB.2016.10.078>.
- [204] Trias D, Costa J, Turon A, Hurtado JE. Determination of the critical size of a statistical representative volume element (SRVE) for carbon reinforced polymers. *Acta Mater* 2006;54:3471–84. <https://doi.org/10.1016/j.actamat.2006.03.042>.
- [205] Melro AR, Camanho PP, Pinho ST. Generation of random distribution of fibres in long-fibre reinforced composites. *Compos Sci Technol* 2008;68:2092–102. <https://doi.org/10.1016/j.compscitech.2008.03.013>.
- [206] Bailey T. Statistical Analysis of Spatial Point Patterns. *Int J Geogr Inf Sci* 2004;18:105–6. <https://doi.org/10.1080/13658810310001620870>.
- [207] Catalanotti G. On the generation of RVE-based models of composites reinforced with long fibres or spherical particles. *Compos Struct* 2016;138:84–95. <https://doi.org/10.1016/J.COMPSTRUCT.2015.11.039>.
- [208] Hambly B, Stoyan D, Stoyan H. Fractals, Random Shapes and Point Fields. *J R Stat Soc Ser A (Statistics Soc)* 1996;159:194. <https://doi.org/10.2307/2983497>.
- [209] Ghayoor H, Hoa S V., Marsden CC. A micromechanical study of stress concentrations in composites. *Compos Part B Eng* 2018;132:115–24. <https://doi.org/10.1016/j.compositesb.2017.09.009>.
- [210] Omairey SL, Dunning PD, Sriramula S. Development of an ABAQUS plugin tool for periodic RVE homogenisation. *Eng Comput* 2019;35:567–77. <https://doi.org/10.1007/s00366-018-0616-4>.
- [211] Garoz D, Gilabert FA, Sevenois RDB, Spronk SWF, Van Paepegem W. Consistent application of periodic boundary conditions in implicit and explicit finite element simulations of damage in composites. *Compos Part B Eng* 2019;168:254–66. <https://doi.org/10.1016/j.compositesb.2018.12.023>.
- [212] Kouznetsova VG. Computational homogenization for the multi-scale analysis of multi-phase materials. 2002. <https://doi.org/10.6100/IR560009>.

- [213] Kari S, Berger H, Rodriguez-Ramos R, Gabbert U. Computational evaluation of effective material properties of composites reinforced by randomly distributed spherical particles. *Compos Struct* 2007;77:223–31. <https://doi.org/10.1016/j.compstruct.2005.07.003>.
- [214] Benzley SE, Perry E, Merkley K, Clark B, Sjaardema G. A Comparison of All-Hexahedral and All-Tetrahedral Finite Element Meshes for Elastic and Elasto-Plastic Analysis. 4th Int Meshing Roundtable, Sandia Natl Lab 1995:179–91.
- [215] Xia Z, Zhang Y, Ellyin F. A unified periodical boundary conditions for representative volume elements of composites and applications. *Int J Solids Struct* 2003;40:1907–21. [https://doi.org/10.1016/S0020-7683\(03\)00024-6](https://doi.org/10.1016/S0020-7683(03)00024-6).
- [216] Nguyen VD, Béchet E, Geuzaine C, Noels L. Imposing periodic boundary condition on arbitrary meshes by polynomial interpolation. *Comput Mater Sci* 2012;55:390–406. <https://doi.org/10.1016/j.commatsci.2011.10.017>.
- [217] Garoz D, Gilabert FA, Sevenois RDB, Spronk SWF, Van Paepegem W. Consistent application of periodic boundary conditions in implicit and explicit finite element simulations of damage in composites. *Compos Part B Eng* 2019;168:254–66. <https://doi.org/10.1016/j.compositesb.2018.12.023>.
- [218] Barbero EJ, Cosso FA, Roman R, Weadon TL. Determination of material parameters for Abaqus progressive damage analysis of E-glass epoxy laminates. *Compos Part B Eng* 2013;46:211–20. <https://doi.org/10.1016/j.compositesb.2012.09.069>.
- [219] Sertcelik I, Kafadar O. Application of edge detection to potential field data using eigenvalue analysis of structure tensor. *J Appl Geophys* 2012;84:86–94. <https://doi.org/10.1016/j.jappgeo.2012.06.005>.
- [220] Ge Q, Wei ZH, Xiao L, Zhang J. An improved region-based model with local statistical feature. 2011 18th IEEE Int. Conf. Image Process., IEEE; 2011, p. 3341–4. <https://doi.org/10.1109/ICIP.2011.6116388>.
- [221] Lehmann G, Legland D. Efficient N-Dimensional surface estimation using Crofton formula and run-length encoding. *Insight J* 2012;January-De:1–11.
- [222] Smith M. ABAQUS/Standard User's Manual, Version 6.9. Dassault Systèmes Simulia Corp, Providence, RI.; 2009.
- [223] Chamis CC, Abdi F, Garg M, Minnetyan L, Baid H, Huang D, et al. Micromechanics-based progressive failure analysis prediction for WWFE-III composite coupon test cases. *J Compos Mater* 2013;47:2695–712. <https://doi.org/10.1177/0021998313499478>.
- [224] Hyde A, He J, Cui X, Lua J, Liu L. Effects of microvoids on strength of unidirectional fiber-reinforced composite materials. *Compos Part B Eng* 2020;187:107844. <https://doi.org/10.1016/j.compositesb.2020.107844>.
- [225] Madra A, Hajj N El, Benzeggagh M. X-ray microtomography applications for quantitative and qualitative analysis of porosity in woven glass fiber reinforced thermoplastic. *Compos Sci Technol* 2014;95:50–8. <https://doi.org/10.1016/J.COMPSCITECH.2014.02.009>.

[226] ASTM International. Standard Test Methods for Void Content of Reinforced Plastics. Astm D 2734-94 2003;08:3–5. <https://doi.org/10.1520/D2734-09.2>.

Abstract

The influence of the void type manufacturing defects on the mechanical properties of textile composites was investigated both by experimental characterization and by multiscale modeling. In particular, voids characteristics such as not only void volume fraction but also its size, shape, and distribution have been characterized for textile composites and their effect on the mechanical properties have been analyzed. Several textile composite plates were fabricated by the resin transfer molding (RTM) process where 3D interlock glass textile reinforcement was impregnated by epoxy resin under a constant injection pressure to generate different types of voids. A series of mechanical tests were performed to examine the dependency of tensile modulus and strength of composites on the total void volume fraction, intra & inter-yarn void volume fraction, and their geometrical characteristics. Microscopy observations were performed to obtain local information about fibers (diameter and distribution) and intra-yarn voids (radius, aspect ratio, and distribution). Based on these results, a novel algorithm was proposed to generate the statistically equivalent representative volume element (RVE) containing voids. Moreover, the effect of void morphology, diameter, and spatial distribution (homogeneous, random, and clustering) on the homogenized properties of the yarns was also investigated by the finite element method. X-ray micro-computed tomography was employed to extract the real meso-scale geometry and inter-yarn voids. Subsequently, this data was utilized to create a numerical model at meso-scale RVE and used to predict the elastic properties of composites containing voids. A parametric study using a multiscale numerical method was proposed to investigate the effect of each void characteristic, i.e. volume fraction, size, shape, distribution, and location on the elastic properties of composites. Thus, the proposed multiscale method allows establishing a correlation between the void defects at different scales and the mechanical properties of textile composites.

Résumé

L'influence des porosités induites par les procédés de fabrication sur les propriétés mécaniques des composites textiles a été étudiée à la fois par caractérisation expérimentale et par modélisation multi-échelle. En particulier, les porosités ont été caractérisées en termes de fraction volumique, taille, forme et distribution, et les effets de chaque caractéristique sur les propriétés mécaniques des composites textiles ont été analysés. De nombreuses plaques de composites textiles ont été fabriquées par le procédé Resin Transfer Molding (RTM). Ainsi, un renfort textile en verre interlock 3D a été imprégné par une résine époxy injectée sous une pression constante pour générer différents types de porosités. Des essais mécaniques ont été réalisés pour examiner la dépendance du module et de la résistance en traction des composites par rapport au taux de porosité total, intra-toron et inter-toron et également par rapport aux caractéristiques géométriques des porosités. Des analyses au microscope électronique ont été effectuées pour obtenir des informations locales sur les fibres (diamètre et distribution) et les porosités intra-toron (rayon, rapport d'aspect et distribution). À partir de ces résultats, un nouvel algorithme a été développé pour générer le Volume Élémentaire Représentatif (VER) qui est statistiquement équivalent au composite contenant les porosités. De plus, l'effet de la morphologie, du diamètre et de la distribution spatiale des porosités (homogène, aléatoire et concentré) sur les propriétés homogénéisées des torons a également été étudié par la méthode des éléments finis. La tomographie par rayons X a été utilisée pour extraire la géométrie méso-échelle réelle en trois dimensions et les porosités intra-toron. Ensuite, ces données ont été utilisées pour créer un modèle numérique à l'échelle mésoscopique (VER) et prédire les propriétés élastiques des composites avec porosités. Une étude paramétrique utilisant une méthode numérique multi-échelle a été effectuée pour étudier l'effet de chaque caractéristique des porosités, c.-à-d. le taux volumique, la taille, la forme, la distribution et la localisation sur les propriétés élastiques des composites. Ainsi, la méthode multi-échelle proposée permet d'établir une corrélation entre les porosités à différentes échelles et les propriétés mécaniques des composites textiles.